# Metal-Organic Framework (MOF) Membranes for Gas Separations

A thesis presented in partial fulfilment of the requirements of the degree of

Doctor of Philosophy

in

Chemistry

at Massey University, Manawatu, New Zealand

Yiming Zhang

2023

# Abstract

The study presented in this thesis involves the design, preparation and evaluation of metal-organic frameworks (MOFs) for gas separation applications, with a focus on the development of MOF membranes with both high gas permeability and good selectivity. Here, two types of membranes, including crystal glass composite membranes (CGCMs) and mixed matrix membranes (MMMs), were prepared and characterized, followed by a comprehensive evaluation of their performance for $CO_2$ separation.

Separating gases using membranes is an appealing due to their efficiency and low energy requirements. Recently, glasses have been discovered that are produced by the melt-quenching of ZIFs. In chapter 2, we propose that useful membranes can be prepared by combining ZIF glasses with MOFs. We prepared these crystal-glass composite membranes by ball milling ZIF-62 with various crystalline MOFs followed by pressing into a tablet, heating to melt the ZIF-62 into a glass, and subsequent cooling. This fabrication process delivers membranes with homogenous dispersion of crystalline MOF particles in a ZIF glass matrix. As an alternative, we show how pre-forming ZIF-62 glass allows membranes to be formed with MOFs with relatively low stability. The resulting crystal-glass composite membranes show ultrahigh $CO_2$ permeance.

MMMs offer great potential for gas separation through the integration of nanofillers into polymers with excellent processability. Among these, MOFs based MMMs have emerged as promising candidates for advanced gas separation applications. However, a major obstacle hindering their performance is the inherent interfacial incompatibility between MOFs particles and the polymer matrix. In this thesis, we present a viable solution utilizing a scalable ball milling approach to address this challenge, specifically targeting the interfacial incompatibility between MUF-16 and the polymer matrix. Significantly, our approach involves the production of MUF-16 with varying crystal sizes through ball milling prior to MMM fabrication. In chapter 3 and 4, we illustrate that the nanosizing of MUF-16 (*ns*MUF-16) enhances its dispersion within three different polymer matrices (Pebax, 6FDA-DAM and 6FDA-Durene), effectively minimizing non-selective voids around the particles. Importantly, MMMs incorporating *ns*MUF-16 consistently exhibit superior $CO_2$ separation performance compared to those utilizing micro-sized MUF-16. Overall, this study highlights a versatile methodology employing engineered approaches to develop high-performance membranes with enhanced interfacial compatibility for gas separation. Furthermore, this approach holds promise for

extending the processability of other MOF adsorbents into matrix materials, thereby broadening the scope of potential applications in gas separation technologies.

Due to the distinctive structural arrangement of MUF-15, where the phenyl rings of the ipa ligands protrude into the void space, there exists a potential for substituting the ipa ligand with various functional groups. This opens avenues for obtaining analogues of MUF-15. These functionalized variants, denoted as MUF-15-X (with X representing substituents such as F, Br, $CH_3$, and $NO_2$), offer the prospect of imbuing MUF-15 with diverse gas sorption properties. Consequently, our interest is piqued to explore the structural characteristics and gas separation capabilities of these analogues across different functional groups. In chapter 5, we present a comprehensive investigation into 6FDA-DAM-based MMMs incorporating MUF-15 and its analogues for $CO_2$ separation from $CH_4$. Notably, this study constitutes the pioneering utilization of MUF-15 analogues as fillers in MMMs specifically designed for $CO_2/CH_4$ separation. It introduces a spectrum of emerging MUF-15 derivatives as potential filler materials for MMM development and underscores the efficacy of pore structure functionalization in augmenting the separation performance of MMMs.

# Contributions

All the work in this thesis was completed by Yiming Zhang

Except:

- Elnaz Jangodaz assisted with the Maxwell fitting and analysis presented in Chapter 4.

# Acknowledgements

Over the course of my PhD journal, I would like to express my great thanks to all those who have helped me.

First of all, I would like to give my heartful thanks and respects to my supervisor, Professor Shane G. Telfer, for providing me this wonderful PhD opportunity to carry out my membrane journey in this creative group. Under your illuminating guidance and profound knowledge, I learned a lot and expanded my view not only focus on membrane field, also obtained a better understanding of MOF world. Thank you for your constant encouragement throughout my PhD journey, from the big picture all the way to technical details. Thank you for providing funding for me to attend conferences and symposiums, which have tremendously improved my presentation skills and personal confidence.

I also express my appreciation to my co-supervisor, Ben Hang Yin, for his invaluable guidance and help. Thanks for his keen insights and constant encouragement, I have learnt from him not only how to solve detailed problems but also how to perform critical thinking. He has always been a true friend to me.

I would also like to thank my another co-supervisor, Professor Mark Waterland, for his much-valued guidance. I also thank Dr. Pat Edwards for assisting in NMR experiments, and David Lun for his technical assistance. I am also extremely grateful to all my friends and teammates, Dr. Subo Lee and Dr. Macro Marco Pandullo, Bernhard Auer, Ludwig Petters, Ghadir Dahalan, Elnaz Jangodaz, Mohana Arul and other past Telfer group members, for scientific discussions, technical assistance. I also thank SNS administration and technical staff for their great assistance during my PhD research.

I would like to acknowledge the financial support from the Chinese Scholarship Council and the MacDiarmid Institute for their support with my project. I also thank the SNS postgraduate travel fund and Shane for supporting me to attend membrane conference in Melbourne.

I also want to thank to all the people who help me, care about me and wish me for the best. Last but not least, I express my loving thanks to my family, to my parents, for their unfailing support, care and love.

# Publications and thesis structure

**Publications relevant to this thesis**

**Additional publications**

1. Ashling, C. W.; Macreadie, L. K.; Southern, T. J. F.; **Zhang, Y.**; McHugh, L. N.; Evans, R. C.; Kaskel, S.; Telfer, S. G.; Bennett, T. D., Guest size limitation in metal–organic framework crystal–glass composites. *J. Mater. Chem. A* **2021**, *9* (13), 8386-8393.

# Abbreviations

| | |
|---|---|
| CCS | Carbon capture and storage |
| PSA | Pressure swing adsorption |
| TSA | Temperature swing adsorption |
| MMMs | Mixed matrix membranes |
| MOFs | Metal-organic frameworks |
| COFs | Covalent-organic frameworks |
| GO | Graphene oxide |
| MOF-CGC | MOF crystal-glass composite |
| LBL | Layer-by-layer |
| ZIFs | Zeolitic Imidazolate Frameworks |
| UiO | University of Olso |
| MILs | Materials of Institute Lavoisier |
| *Tm* | Liquid melting temperature |
| *Tg* | Glass transition temperature |
| Im | Imidazole |
| bIm | Benzimidazole |
| GMMF | Glass mixed matrix film |
| LGCF | Layered glass composite film |
| FFV | Fractional free volume |
| PI | Polyimides |
| PVDF | Poly(vinylidene fluoride) |
| PVA | Polyvinyl acetate |
| PVAm | Polyvinylamine |
| IAST | Ideal Adsorbed Solution Theory |
| NLDFT | Non-local Density Functional Theory |
| 2-mIm | 2-Methylimidazole |
| $H_2$aip | 5-amino isophthalic acid |
| DMF | N,N-dimethylformamide |
| DCM | Dichloromethane |
| MUF-16 | Massey University Framework – 16 |
| MUF-15 | Massey University Framework – 15 |
| PXRD | Power X-ray diffraction |
| TGA | Thermogravimetric analysis |
| DSC | Differential Scanning Calorimetry |

| | |
|---|---|
| SEM | Scanning Electron Microscope |
| TEM | Transmission Electron Microscope |
| ATR-FTIR | Attenuated total reflection flourier transformed infrared spectroscopy |
| ipa | Isophthalate |
| BDC | 1,4-benzene-dicarboxylate |
| $CHCl_3$ | Chloroform |

# Table of Contents

# Chapter 1 Introduction

## 1.1 The purpose of carbon capture and storage (CCS)

In recent years, the rapid development of industrialization and globalization has driven intensive energy consumption. This has inevitably led to a sharp increase in the carbon dioxide ($CO_2$) concentration in the atmosphere and an irreversible environmental damage, including melting polar ice, rising sea levels, hurricanes and droughts.[1-2] Reducing greenhouse gas emissions and mitigating the impacts of global warming has become the most urgent mission for human society. The combustion of fossil fuels, such as coal and natural gas, is the primary $CO_2$ emissions source has pushed atmospheric $CO_2$ concentrations to record levels.[3] And capturing or isolating the $CO_2$ produced by burning fossil fuels has the potential to lower the atmospheric $CO_2$ levels. As a result, $CO_2$ capture and storage (CCS) was proposed to achieve $CO_2$ reduction and carbon neutrality.[4-5] The International Energy Agency's (IEA) Blue Map scenario, for example, envisions a 19 % $CO_2$ reduction using CCS by 2050.[6] Overall, CCS plays a significant role in lowering $CO_2$ emissions and mitigating climate change.

In addition, removing $CO_2$ from natural gas is another approach to minimize $CO_2$ emissions. By removing $CO_2$ from natural gas, the resulting gas can have a lower carbon content, reducing its carbon footprint when use as a fuel. Natural gas demand has risen in the recent years because of the lower $CO_2$ emissions than burning other fossil fuels.[7] Methane ($CH_4$), the main component of natural gas, has a low carbon-to-hydrogen ratio, resulting in a lower emission of carbon.[8] However, impurities such as $CO_2$, $N_2$ and hydrocarbons also present in the natural gas. In recent years, landfill gas has become a growing source of natural gas. However, high content of undesirable gas contaminants, mainly $CO_2$, preclude landfill gas from being widely used. The industrial landfill gas contains about 40 – 60 % $CO_2$.[9] As a result, separation of $CO_2$ from natural gas can enhance the quality of the gas and minimize pipeline damage.[10-12]

## 1.2 Current $CO_2$ separation technologies

The need to lower the atmospheric $CO_2$ emissions has inspired researchers to explore strategies for efficient $CO_2$ capture. To date, $CO_2$ has been captured via oxyfuel-combustion capture, pre-combustion capture, and post-combustion technologies.[13] Oxyfuel combustion employs $O_2$ (> 95%) to generate flue gas containing just $CO_2$ and water vapor. In the pre-combustion approach, the focus of $CO_2$ separation is on the capture and removal of $CO_2$ from the syngas during the conversion of fossil fuels to syngas ($H_2$ and CO) by partial oxidation.

This process is challenging because the fuel conversion process is complicated. Post-combustion is a process that involves capturing and removing $CO_2$ from the flue gases produced during the combustion of fossil fuels, which is a more frequent approach to $CO_2$ separation. However, its flexibility and ease of operation can vary depending on specific circumstances.[14-15] Advances in technology and ongoing research may contribute to making it more efficient and cost-effective in the future. On an industrial scale, the selection of an appropriate separation process is determined by many criteria such as capital cost, efficiency, purity, and recovery, etc. For post-combustion $CO_2$ separation, numerous techniques based on physical adsorption, chemical absorption, cryogenic technology, and membrane separation are commonly employed (Fig. 1.1). The conventional separation approaches of adsorption, absorption, and cryogenic distillation dominate the current market of commercial $CO_2$ separation.[16-18] As an emerging technology, membrane separation possesses the advantages of low energy consumption and carbon footprint in contrast to the conventional methods.

For chemical absorption[19-20], liquid absorbent compounds, especially liquid amines, are frequently used. To date, diethanolamine (EDA),[21-22] methyldiethanolamine (MDEA),[23-24] monoethanolamine (MEA),[25-26] diglycolamine (DGA),[27-28] triethanolamine (TEA),[29-30] and piperazine (PZ)[31-32] et al. have been used in chemical absorption technology because they can react with $CO_2$ to create a nitrogen-substituted carbamic acid.[33] The carbamic acid decomposes at high temperatures, thus reversibly releasing $CO_2$ and regenerating the amine. In addition to this substantial energy input, certain irreversible salts can form when $SO_2$ and $NO_x$ are present, and some degraded amines can generate hazardous and corrosive mixtures.

Pressure swing adsorption (PSA) and temperature swing adsorption (TSA) are the two main physical adsorption methods used for carbon capture. PSA and TSA are appealing for $CO_2$ separation when a preferential and reversible adsorption can be achieved in the mixed gaseous compounds under pressure or temperature control.[34] In the natural gas field, physical adsorption using an adsorbent bed has been extensively employed for over half a century.[35] And researchers are working to create high-performance adsorbent materials for the PSA and TSA processes that have a large adsorption capacity and quick adsorption kinetics. Generally, an adsorbent bed is made of solid-state components, such as zeolites, carbons, etc.[36] Microporous materials with high surface area and porosity are often used as solid absorbents because of their high absorption selectivity to $CO_2$. This selective is benefit from their sieving effect or strong $CO_2$ affinity. These techniques allow $CO_2$ to remain in the adsorption column while the low affinity gases easily pass through an adsorption bed. Both PSA and TSA are widely used in industrial $CO_2$ separation by using multiple adsorption chambers or beds in

parallel. These processes enable continuous operation while allowing for adsorption and regeneration cycles to occur simultaneously.[37] Although the adsorption approach is simple to operate and could produce gas of high purity, it requires significant energy input for the regeneration of the adsorbents.

Compared to the conventional distillation methods , cryogenic distillation operates at a lower temperature for effective separation based on the difference in boiling points of mixed molecular components.[38] Cryogenic distillations for $CO_2$ separation have attracted wide attention due to the high-purity.[39] However, the entire condensation process necessitates complicated equipment and heating integration, which results in lengthy start-up and shut-down periods, and large capital costs. The majority of the expense in distillation is linked with pressurizing and chilling all the columns for gas condensation, which is the primary form of energy consumption.[40-42] Consequently, while cryogenic distillation can achieve separation with a high degree of concentration, it is unavoidably energy intensive and expensive.

Recently, membrane technology has been highlighted as the most promising candidate for advanced separation applications that can provide an energy-efficient alternative to the aforementioned conventional separation methods.[43-46] A membrane is a continuous semi-permeable barrier that can selectively isolate the target components from a mixture. Membrane separation processes is featured with low energy consumption, low capital costs, ease of operation, high efficiency, and environmental friendliness. These benefits make membrane separation technologies to be widely used in industrial separation systems, especially for gas separation.[47-48]

Until now, gas separation membranes have been widely used for separating a variety of gas pairs, such as $CO_2/N_2$ and $CO_2/CH_4$ separations.[49] The market for gas separation membrane is expected to be on a continuous and rapid grow, and it is predicted that membrane separation can alleviate environmental burden by capturing a high concentration of $CO_2$.[50]

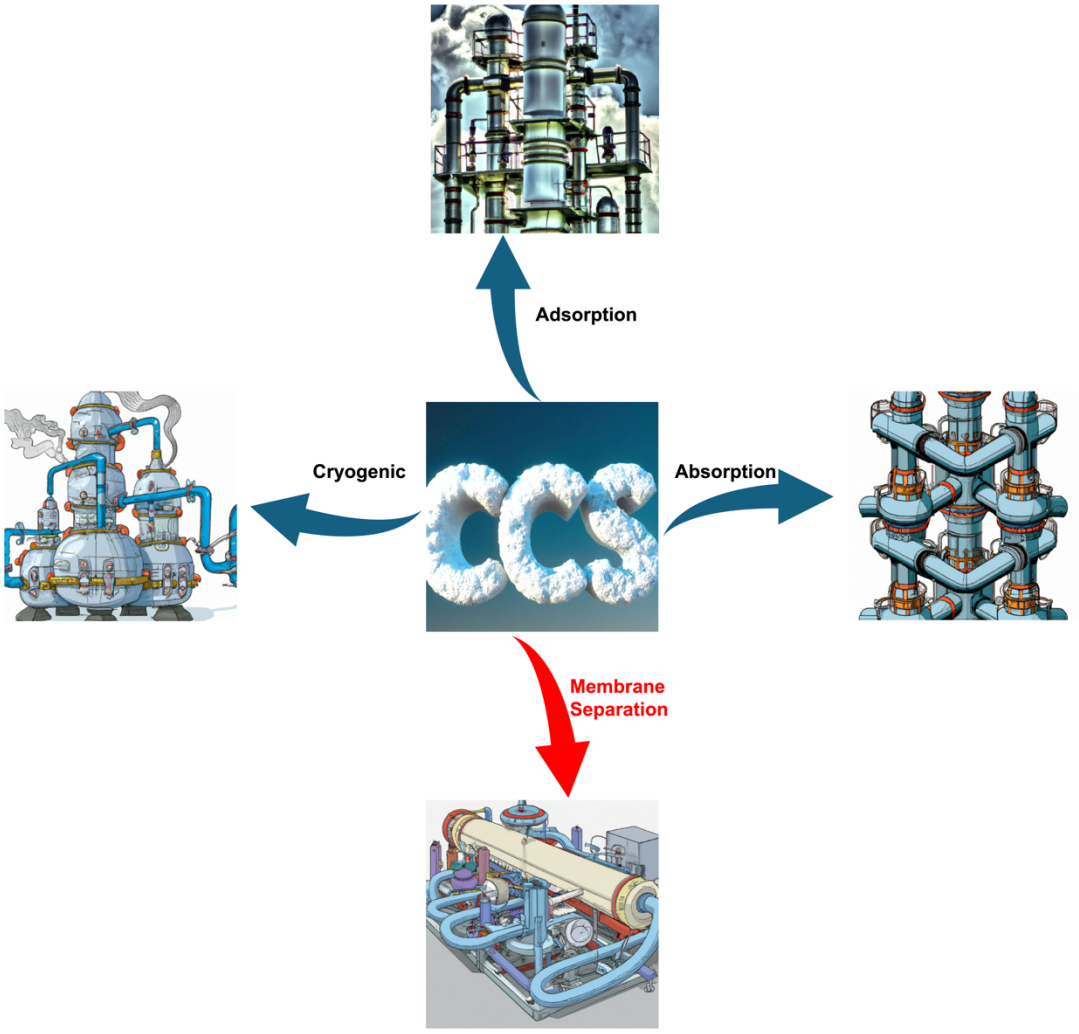


**Figure 1.1** $CO_2$ separation techniques are used in carbon capture and storage processes.

## 1.3 Gas separation membranes

### 1.3.1 Introduction to membranes

What is a membrane? A membrane is a separating barrier that can selectively allow permeable substances to pass through while blocking or selectively retaining the others. The membrane-based gas separation technology separates gas mixtures by allowing the selective permeation components of the gas mixture. The driving force in gas permeation processes results from the partial pressure difference between the feed and permeate of the respective components. As a result of this pressure differential, the more permeable gas can pass through the membrane and accumulate on the permeate side. Meanwhile, the less permeable or non-permeable gas is swept away from the membrane as a retentate stream (Fig. 1.2). Gas permeability refers to the ability of a material or membrane to allow the passage of a specific

gas through it. Gas permeability is often quantified using the permeability coefficient, which represents the rate of gas flow per unit area and per unit of pressure difference across the material. The permeability coefficient is often reported in units such as Barrer (1 Barrer = $10^{-10}$ $cm^3$ (STP)·cm/($cm^2$·s·cmHg)) or gas permeation units (1 GPU = $10^{-6}$ $cm^3$ (STP)/($cm^2$·s·cmHg)). And the selectivity of a gas separation membrane can be calculated by the ratio of the permeability of one gas to another. For example, in the case of a membrane separating gas A and gas B, the selectivity is defined as the ratio of the permeability of gas A ($P_A$) to the permeability of gas B ($P_B$).

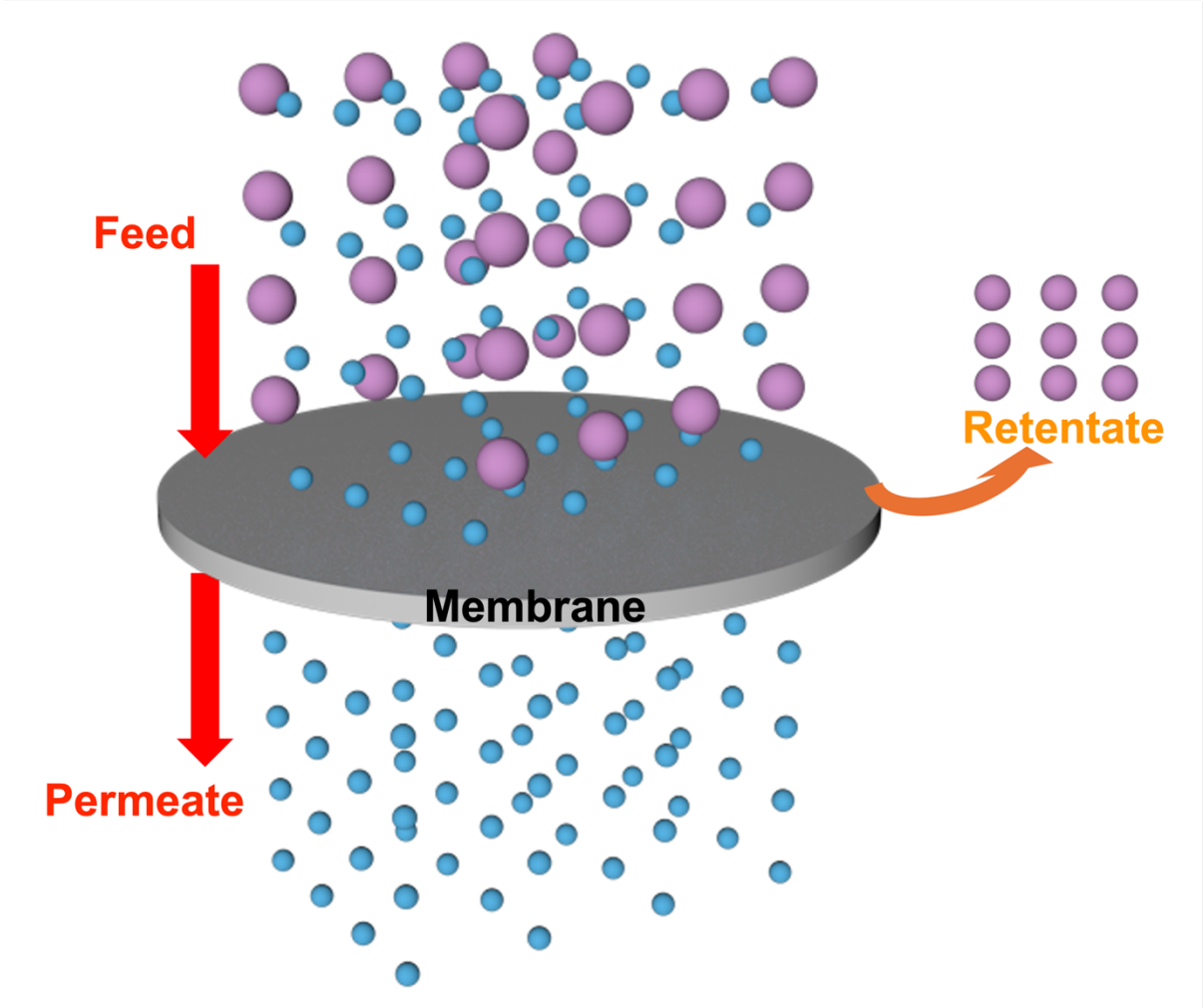


**Figure 1.2** Schematic of membrane separation. The gas with high permeability is shown as blue spheres. The gas with lower permeability is shown as purple spheres.

### 1.3.2 Categories of membrane materials

Membranes can be broadly divided into three major categories based on membrane materials, namely polymeric membranes, inorganic membranes, and mixed matrix membranes

(MMMs). Among these membranes, polymeric membranes are the most used in industry due to their advantages of solution processability, ease of manufacturing, mechanical strength, low capital consumption, and considerable separation performance.[51-52] However, polymeric membranes face the trade-off effect and some substantial challenges, especially the aging process of gas separation membranes. Furthermore, the key obstacles for polymeric membranes that should be considered include limited stability under extreme circumstances (*eg*. high temperature, serve pH value, and polar solvents). Therefore, the search for novel membrane materials that have better performance in terms of gas separation and stability than polymers is needed.

Inorganic membranes, a type of membrane material that is composed of inorganic compounds, have gained considerable interest for gas separation due to their excellent thermal and chemical stability, and the resistance to harsh operating conditions. To date, a series of materials, including carbons,[53] silicas,[54] zeolites,[55] ceramics,[56] and metal-organic frameworks (MOFs)[57] have all been employed to construct inorganic membranas for separation applications. Nevertheless, the high capital cost and brittleness have hampered their universal application on a large scale.

To address the shortcomings of inorganic and polymer membranes, MMMs incorporate organic/inorganic fillers into a polymeric matrix to combine the processability of the polymers with the high gas permeability of filler particles (Fig. 1.3).[58] MMMs are well-known for their ease of fabrication, excellent efficiency, and low cost. To date, several filler particles, including zeolites,[59-60] MOFs,[61-62] covalent-organic frameworks (COFs),[63-64] graphene oxide (GO),[65-66] carbons,[67-68] and metal oxides[69-70] have been used in the MMMs. To overcome the performance barriers, high gas permeability and selectivity can be achieved simultaneously.

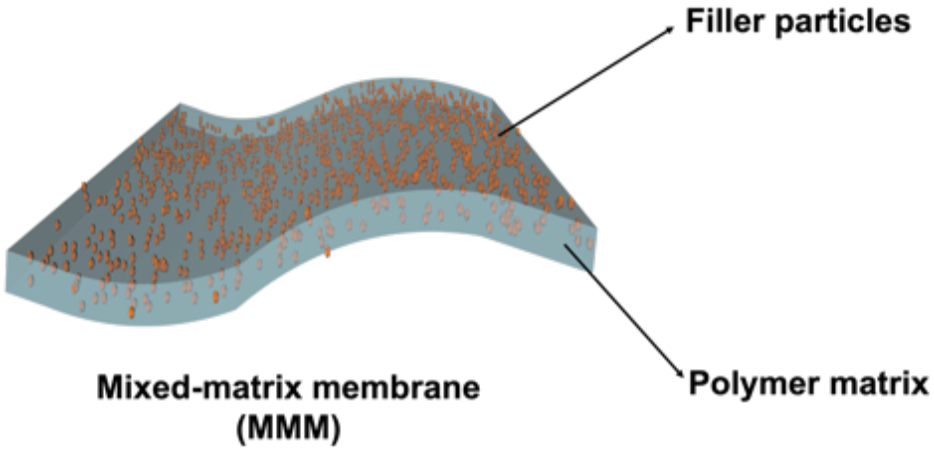


**Figure 1.3** Schematic diagram of MMMs.

### 1.3.3 Trade-off effect in polymeric membranes

From the analysis of extensive literature data, the polymeric membranes are found confronting a trade-off between gas permeability and selectivity, i.e. high gas permeability correlates with low selectivity and vice versa. This phenomenon was originally presented by Robeson in 1991, which was updated in 2008 and 2019 by Freeman.[71-73] The trade-off is depicted by the log-log plot of gas permeability ($P_A$) versus selectivity, i.e. $\log(P_A/P_B)$, which is known as the Robeson upper bound plot. And it has been established for various gas pairs. On the $CO_2/N_2$ upper bound plot, for example, if a given polymeric material has both high gas permeability and selectivity, the upper bound line may be surpassed, indicating that this type of material has outstanding gas separation performance in the 'target region' (Fig. 1.4).

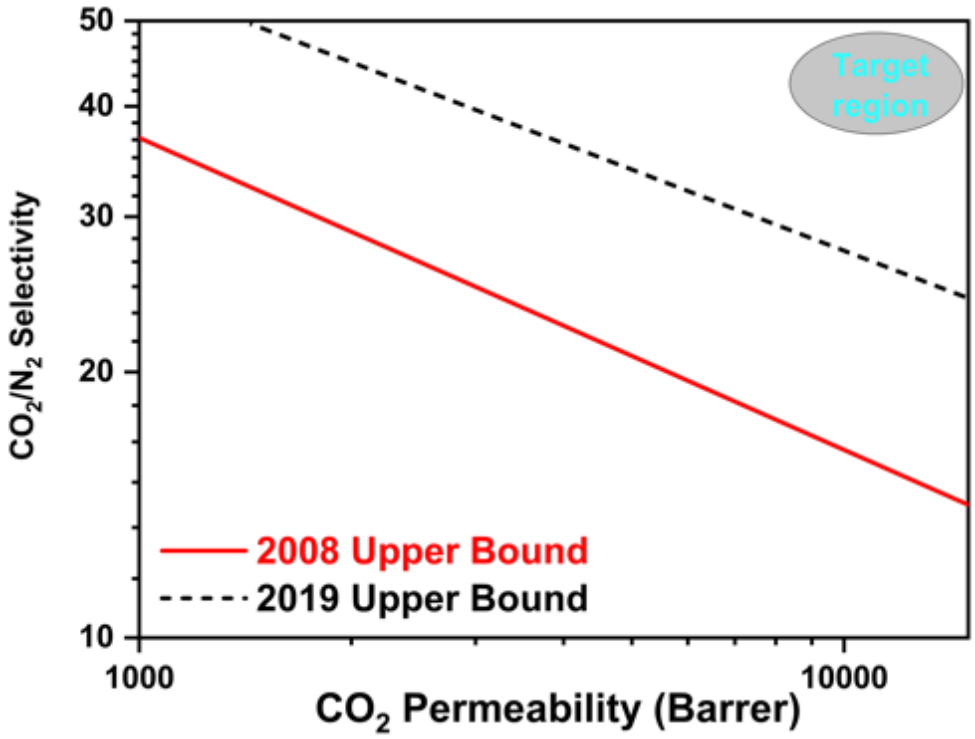


**Figure 1.4** A Robeson plot showing the upper bounds for polymer membranes for $CO_2/N_2$ separation.

### 1.4 MOFs-based membranes: Next-generation materials for advanced gas separations

MOFs, also known as porous coordinated polymers, are made of metal nodes or metal clusters that are linked together by organic linkers. Faced with the challenges of separation performance and stability issues based on polymeric membranes, new materials for membrane

separations have been explored and developed. In this regard, MOFs have been identified as one of the most promising materials for gas separation membranes.[74]

This thesis will center on three types of MOF membranes: polycrystalline MOF membranes, crystal-glass composite membranes and MOF-based MMMs (Fig. 1.5).

(i) MOF polycrystalline membranes have already showed impressive gas separation performance due to their tunable pore environment and diverse chemical functionality.

(ii) MOF glasses are a new class of porous materials with an amorphous structure that are formed by heating certain crystalline MOFs above their glass transition temperature. The porous nature of MOFs glasses makes them excellent materials for gas separation applications. Moreover, crystal-MOF glass composites have showed enhanced gas sorption capabilities, allowing them to be used as membrane materials for advanced separations.

(iii) The generally good compatibility of MOFs and polymers allows MOF particles to be used in MMMs. In this thesis, we are aiming to fabricated high-performance $CO_2$ separation MMMs with both high permeability and selectivity.

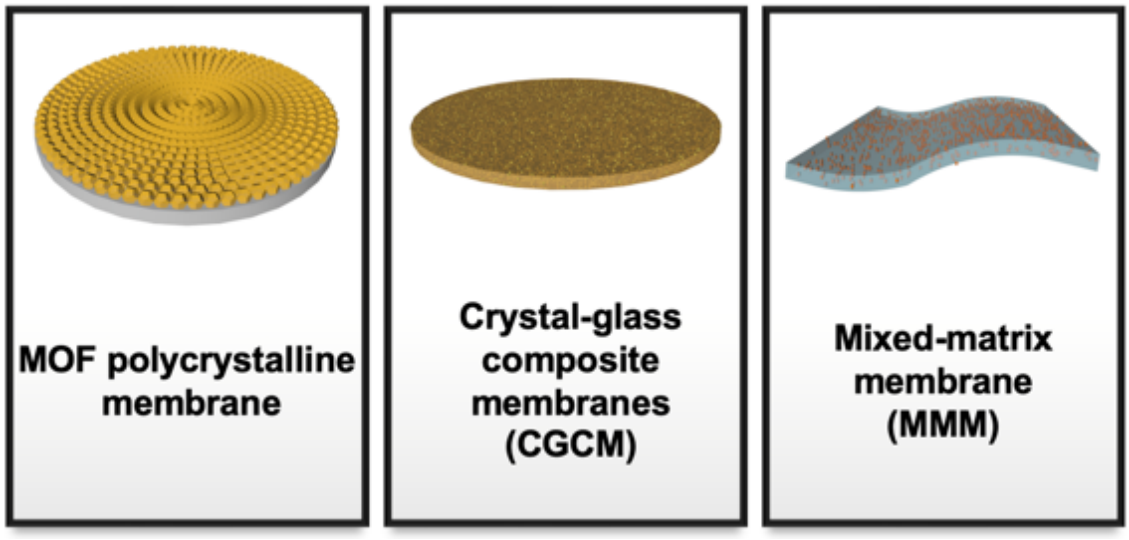


**Figure 1.5** Three types of MOF-based membranes used for gas separation.

### 1.4.1 MOF polycrystalline membranes

MOF polycrystalline membranes, in general, are composed of an intergrown layer of MOF crystals on a robust and porous substrate that provides additional mechanical strength. The produced membranes often exhibit outstanding separation performance due to the consistent pore size of crystalline MOF materials.

To date, several MOF polycrystalline membranes have been developed and applied in gas separations, including CCS,[75-78] $H_2$ purification,[79-81] hydrocarbon separation,[82-83] ion extraction[84-86] and chiral resolution.[87-89] Nevertheless, developing compact and defect-free MOF polycrystalline membranes on porous supports remains challenging due to unregulated MOF crystal growth or inadequate adhesion or bonding between the selective MOF layer and the porous support. Additionally, the existence of intercrystalline flaws in the membrane can significantly degrade the intrinsic membrane's separation ability. To address these issues, several approaches have been used and developed to construct defect-free MOF polycrystalline membranes.

(1) In situ solvothermal growth.

In situ solvothermal growth is a method used for the synthesis of MOFs directly on a substrate or support material. This approach involves the growth of MOF crystals under solvothermal conditions, typically using the same synthesis conditions as MOF crystallization in solution. By immersing a porous support in the MOF precursor solution, nucleation takes place on the porous support, followed by the production of the MOF layer (Fig. 1.6). MOF-5 membrane growth on a porous alumina support was the first polycrystalline MOF membrane created via in situ solvothermal growth.[90] However, fabricating a defect-free polycrystalline MOF membranes is difficult due to a lack of nucleation sites on the porous support. To address this issue, prior modification of the porous support is typically used to facilitate the heterogeneous MOF layer formation.

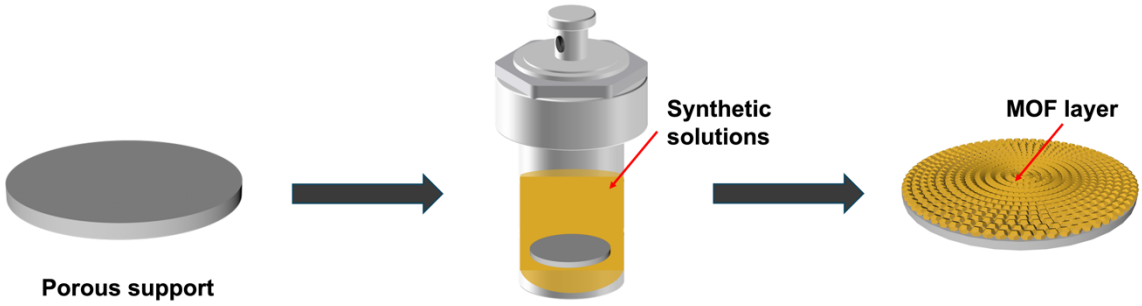


**Figure 1.6** Schematic illustration of MOF crystalline membrane fabrication via in situ solvothermal growth.

(2) Secondary growth

Secondary growth, also known as seed-assisted secondary growth, can produce thin MOF layers by increasing the number of heterogeneous nucleation sites on the membrane supports. In this process, MOF crystal seeds are first planted on porous supports, and then the porous

supports with the seeds are immersed in the MOF mother solution for secondary growth (Fig. 1.7). The seeding approach can thus offer enough nucleation sites on the support surface to generate a continuous MOF membrane. In this way, thick, defect-free MOF layers for improved molecular separations can be created. For example, Liu *et al.* used oriented secondary growth method to create a ZIF-8 membrane for $H_2$ purification.[91]

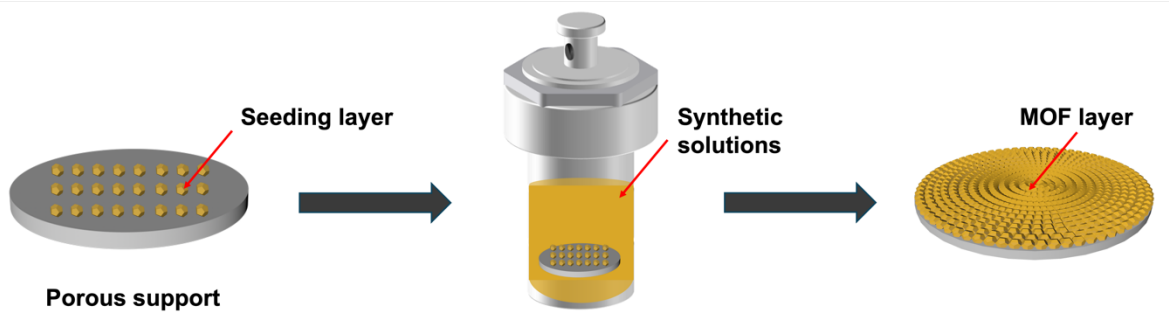


**Figure 1.7** Schematic illustration of MOF crystalline membrane fabrication via secondary growth approach.

(3) Layer-by-layer growth

Layer-by-layer (LBL) growth is a technique used to fabricate thin films or membranes with precise control over their structure and properties, which can also be adapted for the growth of MOF membranes.[92] Normally, LBL growth process can be started by alternately immersing the modified substrate in separate solutions containing the MOF building blocks. The building blocks typically consist of metal ions and organic linkers specific to the desired MOF. For each immersion step, the substrate is exposed to one of the building block solutions to form a layer on its surface. After each immersion, rinse the substrate to remove any excess or unreacted species. Then repeating the MOF layer deposition step multiple times can achieve the desired number of MOF layers. In the LBL approach, the membrane thickness can be precisely adjusted by regulating the precursor concentration and the growth cycles (Fig. 1.8). Eddaoudi et al. developed the first ZIF-8 membrane by using the LBL growth technique and controlling the growth cycles.[93] Another advantage of LBL is that it can be coupled with automated equipment to make MOF membranes, simplifying and expediting the membrane fabrication process. Hurrle and co-workers used the LBL approach and the scheduled spraying technique to manufacture large-area membranes.[94] Although the LBL approach is the most promising choice for realizing scale-up MOF membrane production, considerable volumes of solvents are often required throughout the membrane growth process. Moreover, LBL is unfavorable to MOFs synthesized in severe conditions (high temperature and high pressure).

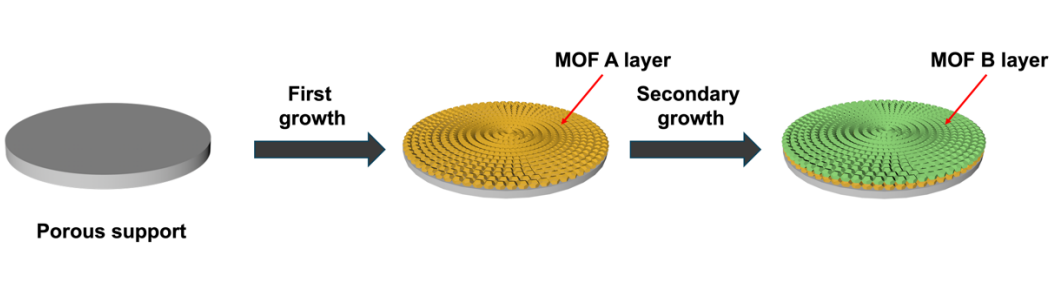


**Figure 1.8** Schematic illustration of Layer-by-layer growth for MOF crystalline membrane fabrication.

(4) Electrochemical synthesis

The electrochemical synthesis approach, which employs electrochemical principles to facilitate fast and continuous MOF layer generation by boosting ligand deprotonation, has emerged as an innovative paradigm for the fabrication of MOF membranes (Fig. 1.9). Because of the benefits of self-healing and self-inhibited growth, a continuous and defect-free MOF membrane can be created in this manner. Zhou's group reported the first current-driven synthesized ZIF-8 membrane in 2018, demonstrating fast MOF membrane fabrication within 20 min at ambient temperature using an H-shaped electrolytic cell.[95] Specifically, carbon rods were wired to the counter electrode, while a conductive porous support was connected to the cathode. $Zn^{2+}$ ions could flow towards the cathode and accumulate on the porous support surface. Simultaneously, the ZIF-8 ligand was deprotonated and then interacted with $Zn^{2+}$ ions to generate ZIF-8 on the support surface. As a result, any exposed defects on the support surface exposed to the precursor solution were healed by the production of additional ZIF-8 crystals at these bare spots. High-quality ZIF-8 membranes could be obtained due to the self-elimination of defects. This straightforward strategy represents a direct approach to other MOF membrane fabrications.[83, 96-98]

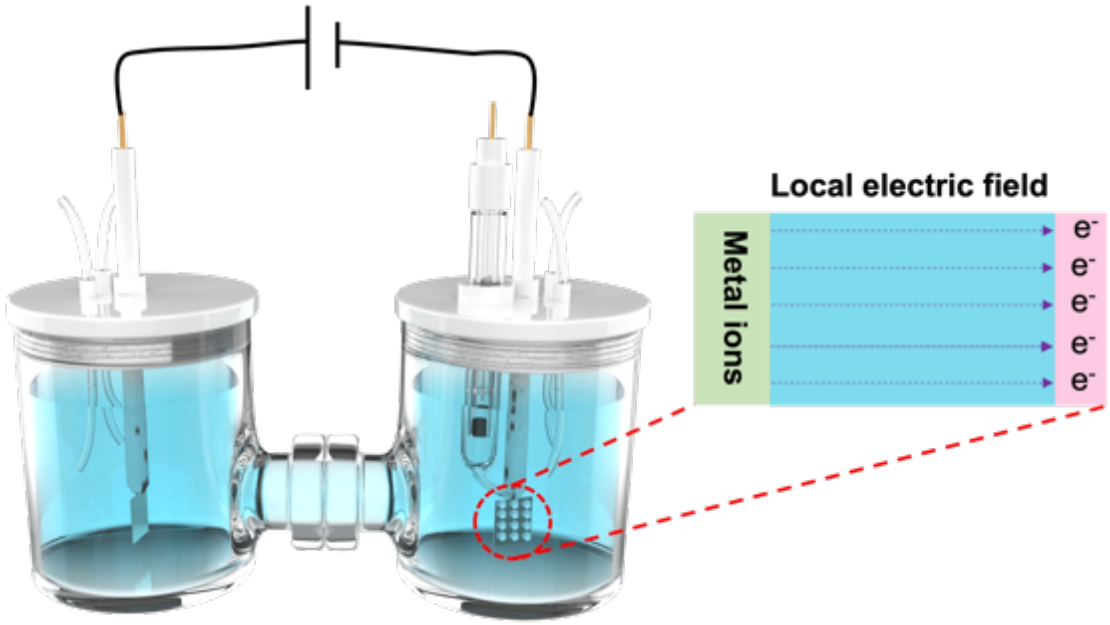


**Figure 1.9** Schematic illustration of electrochemical synthesize MOF crystalline membrane.

(5) Post-modification

Post-modification of MOF polycrystalline membrane is an effective method of strengthening MOF structures to improve the stability of membranes. Additionally, this approach demonstrates the advantages of defect healing and pore structure correction, which result in the increased membrane separation performance. For example, Lee and co-workers developed a ligand exchange strategy to produce ZIF-8 membranes.[99] This work revealed how imidazole-2-carbaldehyde (Ica) was used to substitute the ZIF-8 ligand (2-methylimidazole, mIm) to increase the pore size of resulting membrane (Fig. 1.10). The ligand exchange mostly altered the upper layer's pore size, whereas the bottom ZIF-8 layer maintained a good $C_3H_6/C_3H_8$ separation. As a result, $C_3H_6$ permeance was considerably increased while $C_3H_6/C_3H_8$ selectivity was slightly diminished. Similarly, post-modification using long-chain amines can enhance the pore size of ZIF-94 polycrystalline membranes.[100] Although the post-modification approach can increase separation performance, it usually requires lengthy operations. Moreover, the pore size modulation is difficult to regulate and can occasionally result in a noticeable drop in selectivity. Therefore, post-modification may not be the primary choice for producing MOF polycrystalline membranes.

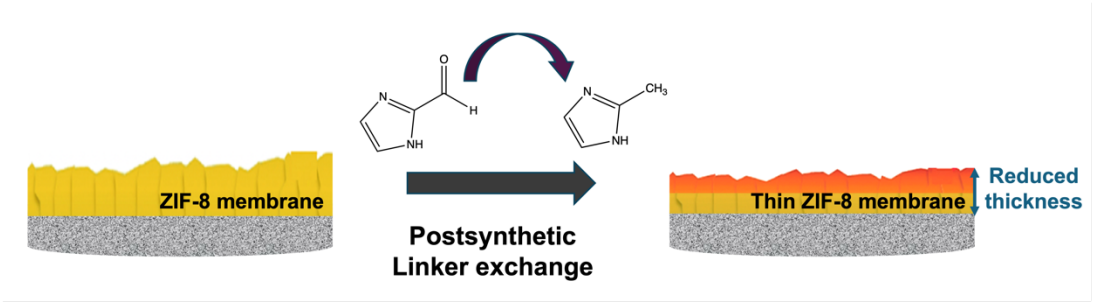


**Figure 1.10** Schematic illustration of the post-modification of ZIF-8 membrane by a ligand exchange strategy.

### 1.4.2 MOF glasses and MOF glass membranes

Recently, certain MOFs have been discovered to have the capacity to form glasses, and these glassy MOFs exhibit promise in gas separation. Normally, MOF glasses are produced by heating crystalline MOFs above their glass transition temperature (*Tg*).[101] In this approach, the highly ordered MOF becomes disordered (glassy) phase while keeping its porous nature. The generation of a liquid by melting offers benefits of processability and inter-particle defect healing. Glass-forming ability has been observed for several MOFs, including ZIF-4,[102] ZIF-62,[103] ZIF-76,[104] and TIF-4.[105] When compared to other MOF glasses, ZIF-62 has a lower melting temperature and a wider melting range prior to decomposition so it is a good option for membrane separation. To date, a pure ZIF-62 glass membrane has been successfully produced and exhibited good gas separation performance.[106] In another report, a TIF-4 glass membrane was created on the α-$Al_2O_3$ substrate using the same method as ZIF-62.[107] These MOF glass membranes demonstrated good $CO_2$ separation performance and stability. When combined with other functional materials, MOF glass composites can show enhanced gas adsorption or separation capabilities.[108-109]

Three distinct suggested configurations for glassy thin-film composites have been offered: glass mixed matrix film (GMMF), asymmetric layered glass composite film (LGCF) and crystal-MOF glass composite membrane (CGCM), as shown in Fig. 1.11. For GMMF, its separation layer has a similar configuration to MMMs as the filler particles are incorporated into a continuous glassy matrix, which is deposited onto a porous substrate. Instead, since the filler particles and glassy matrix have the same inorganic properties, it is promising to produce a good filler-matrix interface that can assure good separation performance. For example, MIL-53 was embedded into the ZIF-62 glass and the composite demonstrated improved gas uptake

due to the good contact between MIL-53 and ZIF-62.[110] This strategy can be explored for the GMMF fabrication.

It is possible to construct the LGCF configuration by developing various layers of MOF glass and composites to create an asymmetric layer. This hierarchical structure enables broader pore size variation throughout the membrane as well as stepwise reaction flow via the selective layer. Small molecule separation benefits from hierarchical pore size variations. MOF polycrystalline film with hierarchical arrangement displayed good separation performance for monovalent ions.[111] As a result, a MOF glass composite in LGCF configuration may also achieve hierarchical pore distribution in thin film. A membrane with LGCF design can be fabricated using this approach for enhanced molecular separation.

Inspired by the manufacturing principle of MMMs, we proposed a unique idea of CGCM, which can be produced by inserting MOF crystals into the glass phase. Free-standing CGCMs, like MMMs, can be fabricated by directly incorporating MOF crystals into glass-former phase. It has the potential to combine the advantages of porous MOF crystals with high gas sorption capacity and the processable MOF glass phase. As a result, free-standing CGCMs may be practical for improving the gas separation performance. In this thesis, we have prepared and analyzed the gas separations of a series of CGCMs (including ZIF-8, UiO-66, MIL-53, and MUF-16 CGCMs) and investigated their gas separation in this study.

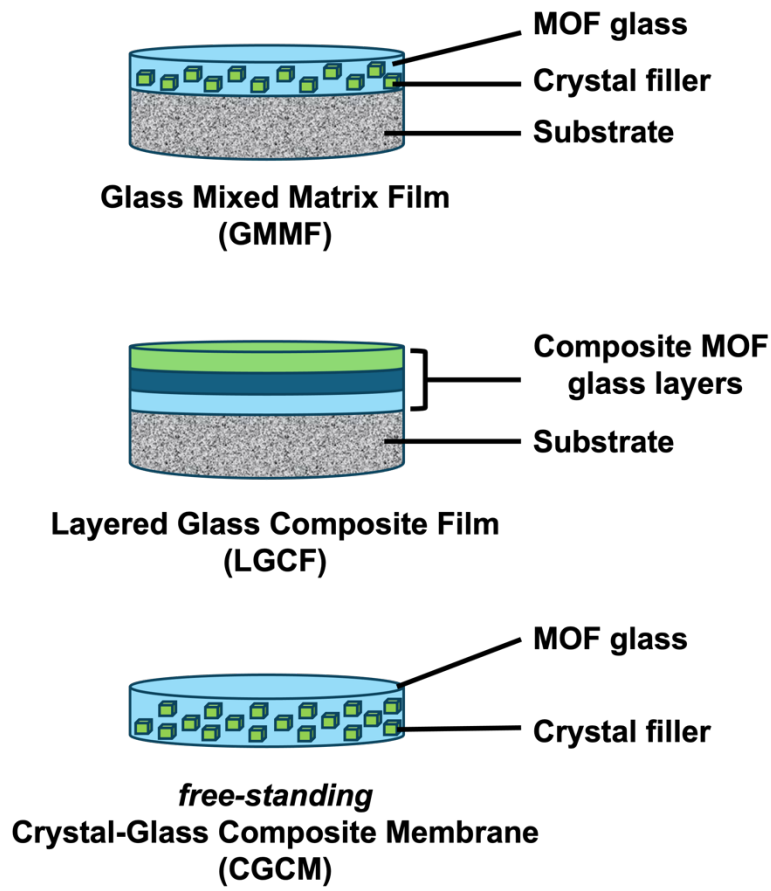


**Figure 1.11** Three suggested MOF glass composite membrane configurations (GMMF and LGCF are inspired from Ref [112].).

### 1.4.3 MOF-based MMMs

The first MMMs were developed by Paul and Kemp in 1973 by incorporating zeolite type 5A into a silicon rubber matrix.[113] Subsequently, to increase gas separation performance, a variety of filler particles have been used in the fabrication of MMMs. MOFs have attracted wide attention as a filler material because of their exceptional gas separation capabilities.[114] The incorporation of MOF particles in MMMs offers a distinct advantage in terms of the gas diffusion pathway through the membrane, this unique gas diffusion pathway can create a selectivity towards certain gas molecules. Certain gas molecules can diffuse through the porous MOF particles preferentially, resulting in a high permeability (the solubility and diffusivity contributions to the permeability are discussed later). The permeability of other gas molecules is not enhanced by the presence of MOF particles and are compelled to pass a longer and tortuous pathway around the particles. In this manner, a high selectivity can be realized (Fig. 1.12).

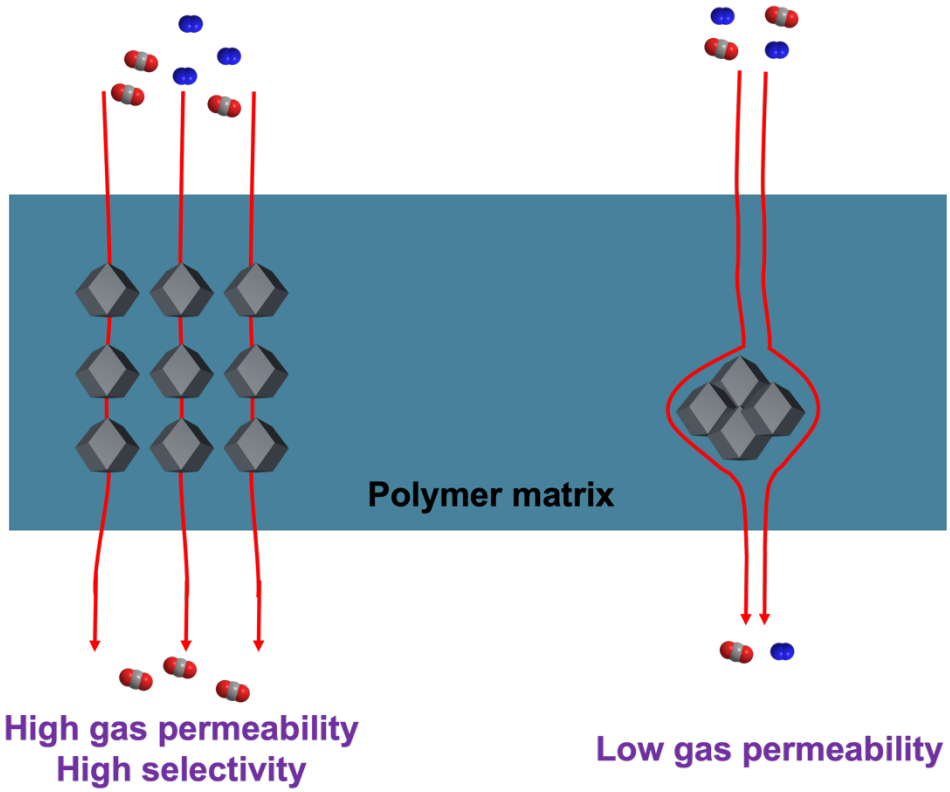


**Figure 1. 12** Gas transport pathways in MOF-based MMMs exemplified by a showing $CO_2$ with a high permeability and $N_2$ with a low permeability.

For the manufacture of gas separation MMMs, many subclass kinds of MOFs, including Zeolitic Imidazolate Frameworks (ZIFs), University of Olso (UiO) and Materials of Institute Lavoisier (MILs), have been employed (Fig. 1.13). In addition, some emerging MOFs with enhanced separation performance have been designed MUF-15 (MUF = Massey University Framework).[115] MUF-15 and its derivatives together with MUF-16 were employed in the preparation of MMMs in our study, and these MMMs all showed enhanced $CO_2$ separation performance compared to the pristine polymers, which will be presented in detail in the subsequent chapters.

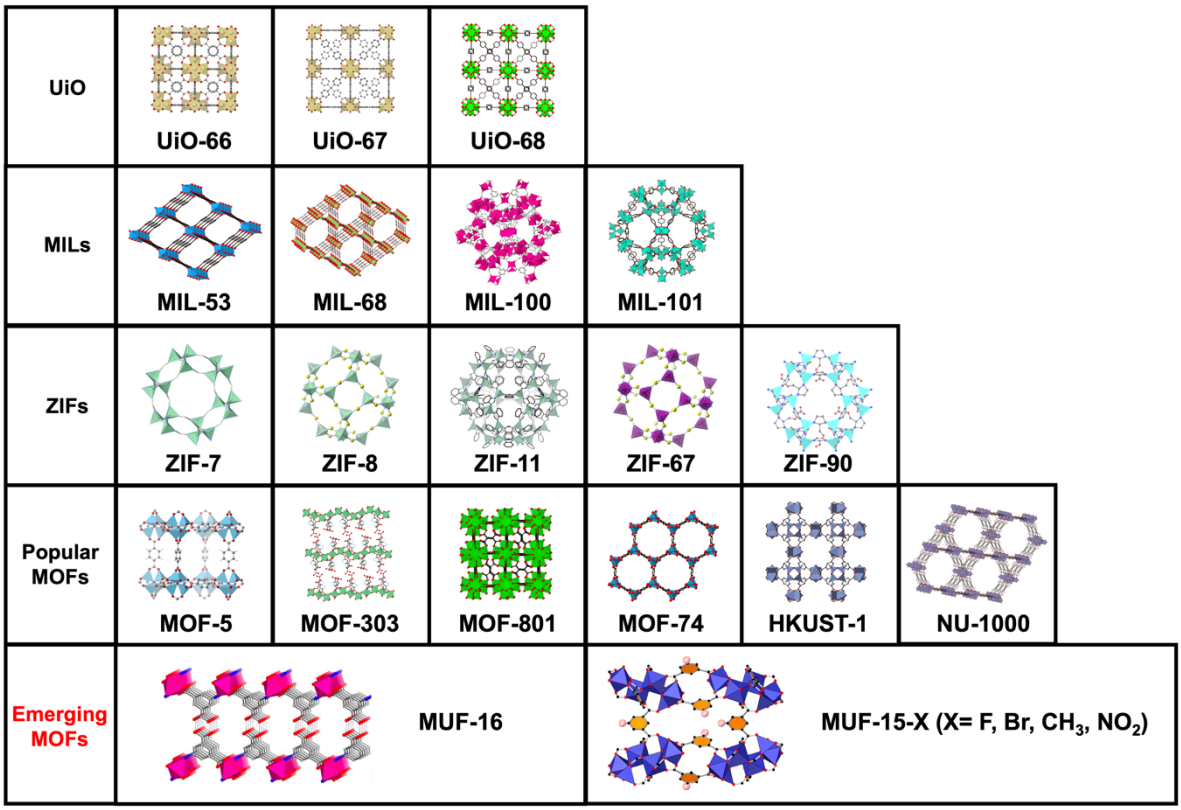


**Figure 1.13** Types of MOFs used for the fabrication of MMMs.

### 1.4.3.1 Fabrication of MOFs-based MMMs

1) In-situ growth

Two approaches are included in the in-situ growth method: in-situ growth of MOFs and in-situ polymerization (Fig. 1.14). In the first case, the polymer is first dissolved in a solvent, then the MOF fillers precursors and organic linkers are dispersed into the target solution, before being added to the polymer solution and mixed to generate the homogeneous casting solution.[116-117] The MOFs fillers can therefore be generated during the casting solution creation. A uniform membrane with well-dispersed MOF particles can be constructed. Another option is to perform in-situ polymerization by mixing MOFs fillers with polymer monomers prior to polymerization. In brief, MOFs fillers are first dispersed into solvent before being added to the polymer monomer, and then heating induces polymerization after casting. Because of the creation of creation of chemical linkages between MOFs fillers and polymer matrix during in-situ polymerization, high interfacial compatibility between MOFs fillers and polymer matrix can be obtained.

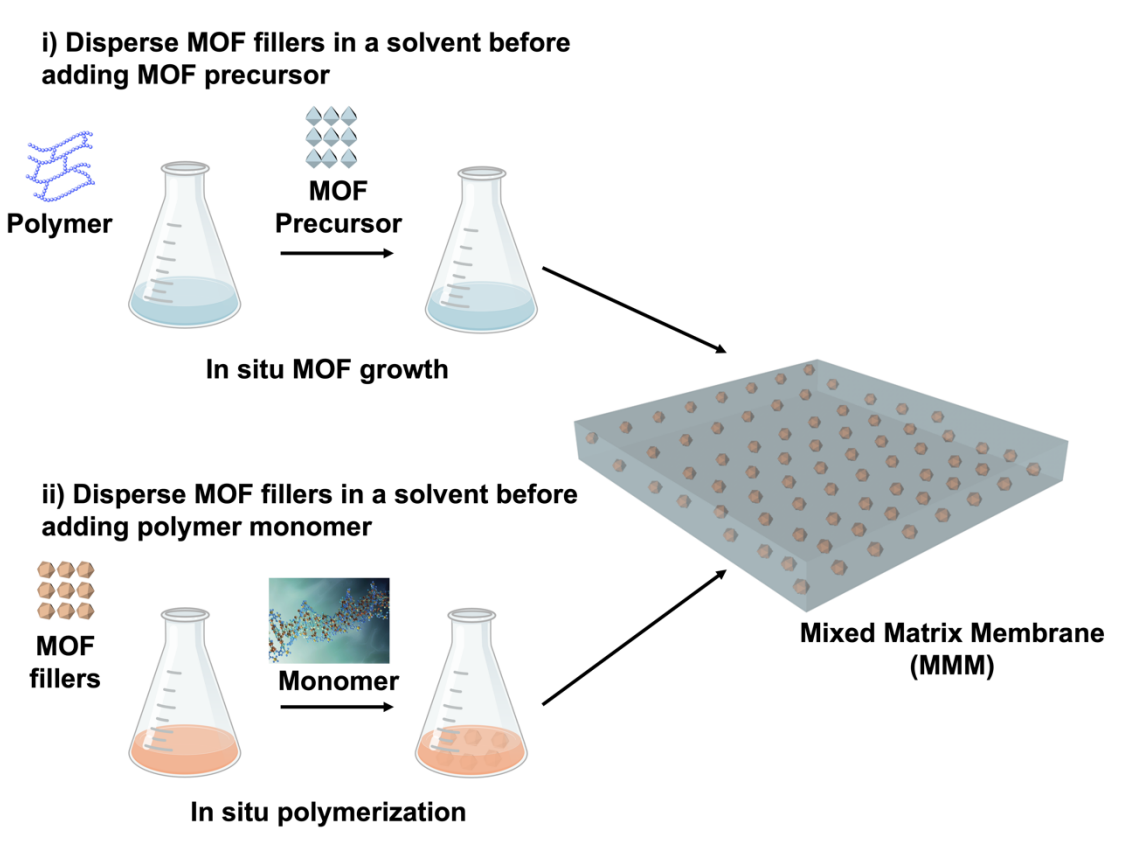


**Figure 1.14** Approaches for MOFs-based MMMs fabrication using in-situ growth method.

2) Solution mixing

In the solution mixing method, the polymer is first dissolved in solvent to form a homogeneous solution, and then the MOF fillers are added to this solution (Fig. 1.15). To minimize agglomeration, ultrasonication can aid in the separation of any clumped MOFs fillers. There are three common approaches for producing casting solutions by solution mixing: i) dispersing MOFs fillers in a solvent before adding polymer, ii) dissolving polymer in solvent before adding MOFs fillers and iii) dissolving MOFs fillers and polymer before combining them together. The solution is then poured onto a glass plate and allowed to evaporate at a certain temperature. Given its simplicity, solution mixing is the most used approach for fabricating MOFs-based MMMs.

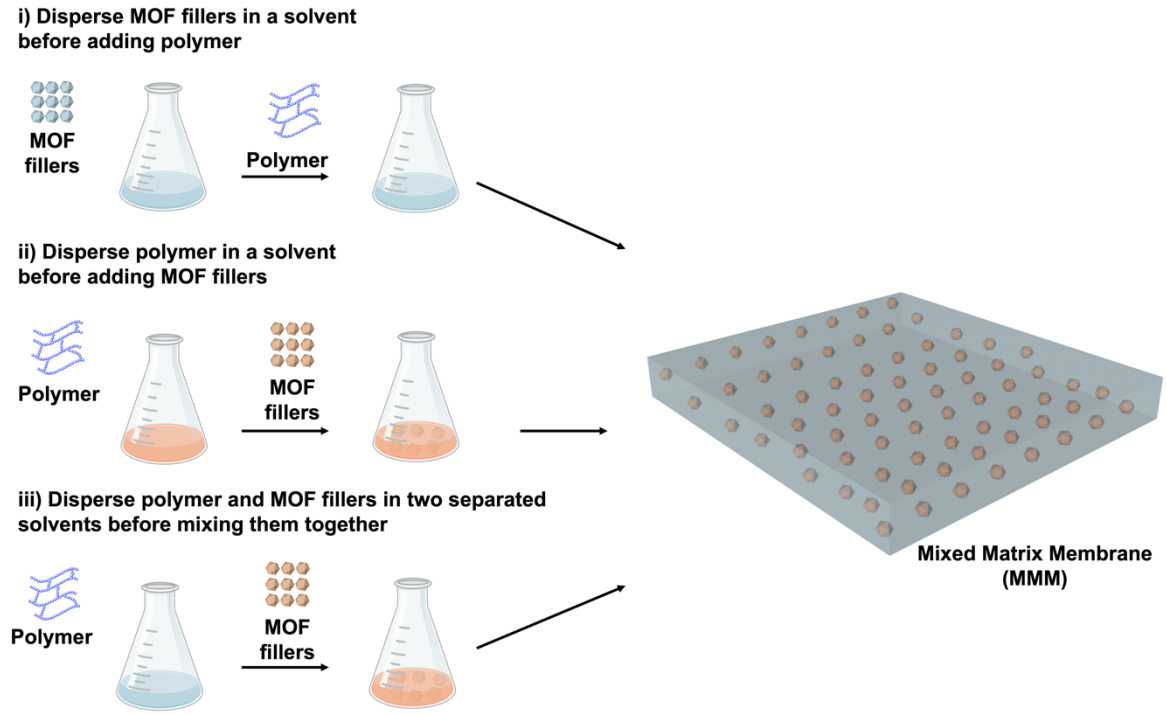


**Figure 1.15** Approaches for MOFs-based MMMs fabrication using solution mixing method.

### 1.4.3.2 Challenges in the fabrication of MOF-based MMMs

Developing MMMs with optimal separation performance is challenging due to the occurrence of non-idealities in MMMs manufacturing, which may impede the simultaneous enhancement of gas permeability and / or selectivity. In practice, problems relating to the dispersibility of MOF fillers, interfacial voids between the polymer and MOFs fillers, polymer chain rigidification around MOF fillers, and pore blockage of the MOFs by polymer chains. and MOF loadings, and particle size can result in suboptimal performance (Fig. 1.16).

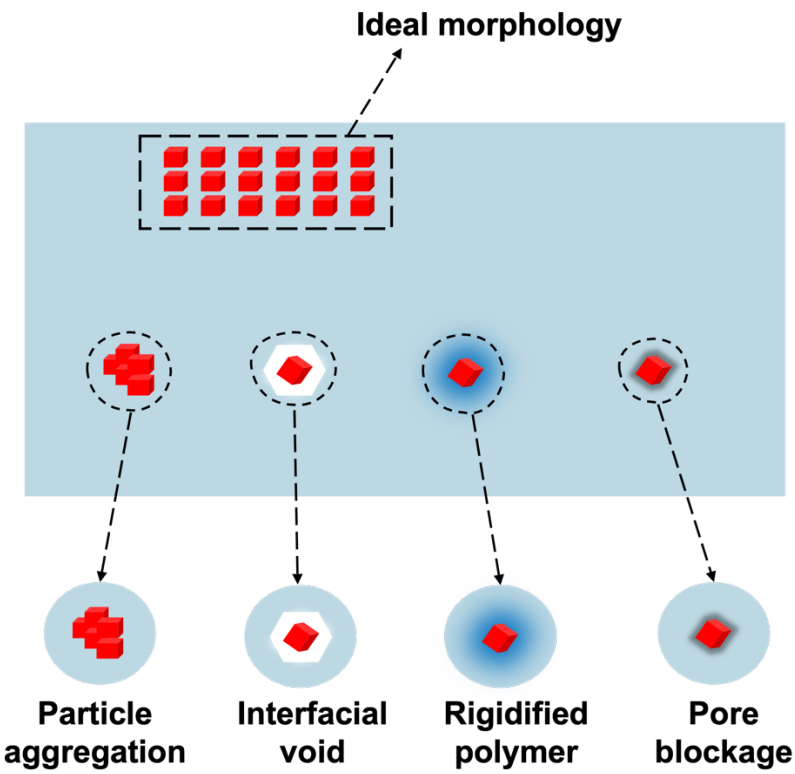


**Figure 1.16** Typical challenges of MOF dispersion states in MMMs.

Membrane permeability generally increases with increased loading of the MOF fillers. However, overloading may result in agglomeration and sedimentation. The aggregation of filler particles can cause non-selective voids and even membrane defects, undermining selectivity due to non-selective bypasses for gas molecules around the filler particles (Fig. 1.17). Meanwhile, the membrane becomes brittle at a high MOF loading. As a result, optimum MOF loading is critical to combining good separation performance and physical characteristics.

Poor MOF dispersion and polymer-MOF coexist can also result in low selectivity. The rigidification of the polymer chains around the filler particles can result in a zone of reduced free volume and chain mobility, lowering the permeability. In addition, the pore blockage by the polymer chains may reduce permeability and render the porous filler worthless if its pores are entirely blocked. In certain circumstances, particle pore blockage may boost selectivity if the decrease in pore size just matches the size of the target permeate, however, the permeability is always compromised. Moreover, controlling the degree of polymer rigidification and the extent of pore blockage is challenging. To the formation of ideal morphologies in the MMM system, polymer rigidification and pore blocking must be avoided.

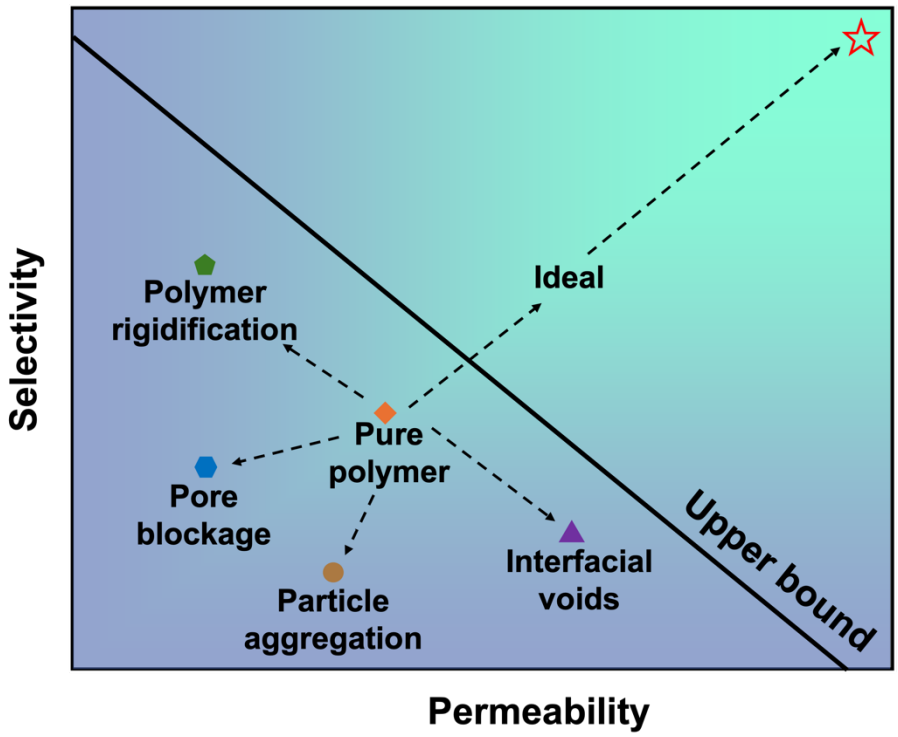


**Figure 1.17** Schematic illustration of the relationship between MOF filler dispersion status in MMMs and the corresponding membrane separation performances.

### 1.4.3.3 Strategies to improve interfacial compatibility.

To reduce interfacial voids between the polymer matrix and MOF fillers, several approaches can be employed.

(1) Functionalization of MOF fillers

The MOF particles can be modified by adding some functional groups. MOFs fillers can be functionalized with amino groups to enhance their compatibility with polymer matrix. The amino groups in MOFs can provide additional interaction sites for bonding with the polymer chains, thus improving adhesion and compatibility between MOFs and polymers.[118-119] MOFs fillers can be modified to incorporate amine functional groups using simple procedures such as reflux heating [120-121] or vigorous stirring.[122-123] As a result of the improved interaction between the dispersed modified MOFs fillers and the polymer matrix, the resultant MMMs can perform better. And the link between polymer and MOFs fillers is formed due to the presence of hydrogen-bonding, which can cause MOF fillers to the agglomerate in membrane.[124] For example, UiO-66-$NH_2$ could display enhanced stability in polymethyl methacrylate (PMMA) solution after $NH_2$ group induction in UiO-66, since it can create hydrogen bonds between the

amino groups and carbonyl groups of PMMA.[125] In other cases, even modest MOFs loading can result in unsatisfactory interfacial morphologies of prepared MMMs because the polymer and MOF are poorly compatible.[126] Therefore, selecting a good polymer-MOFs pair is critical for the preparation of MMMs.

(2) Geometry tuning

Another endeavor is to modify the morphologies of the distributed MOFs in the polymer matrix by tuning the geometry of the MOF filler particles. MOF particles can be shaped during their synthesis process by altering the conditions or the preparation procedures. To date, MOFs of various forms (rods, sheets, spherical particles etc.) have been used to fabricate MMMs. The separation performance of the same polymer-MOF combination with different MOF filler geometries may differ. For example, Deng et al. fabricated membranes embedded with three distinct ZIF forms (particles, microneedles, and sheets) and showed that the separation results correlated with the morphologies of the ZIF fillers.[127] There are two primary methods for obtaining MOF nanosheets. Bottom-up is a simple approach for changing the shape of MOF fillers by varying the reaction time or the MOF precursor ratios.[128] The top-down technique, on the other hand, is preferred due to its ease of operation, high yield and even greater membrane performance.[129-130] Besides, exfoliation method can fabricate high-quality MOF nanosheets with large lateral dimensions, and mechanical or sonication techniques are normally applied to break apart the bulk crystals into individual nanosheets.[131-132]

In addition, the size of the MOF fillers is a significant aspect that can impact the final membrane performance. Normally, when the size of the filler particles decreases, the interfacial area between the MOFs particles and the polymer rises. Smaller MOF particles have a higher surface area–to–volume ratio than large particles. The increased surface area can provide more contact points for interaction with the polymer matrix, resulting in the enhanced interfacial adhesion.[133] And the smaller MOF particles are easily to disperse into polymer matrix due to their smaller size, this enables them to migrate into regions with better MOF-polymer contact, leading to increased interfacial interaction. In this case, smaller MOF particles are present on the gas diffusion pathway to encounter more gas molecules in the membrane, thus improving the gas separation performance.[134] For example, ball milling is an excellent approach to decrease the particle size of MOFs without losing their crystalline structure. For our MUF-16, it is vital to note that the differences in MOF particle size have no effect on the aperture size and the molecular sieving characteristics.[135]

(3) Dual filler incorporation

Another way to improve interfacial compatibility is to combine MOFs with an additional filler. For example, graphene oxide (GO) is widely used in combination with MOFs due to its high compatibility with polymer matrices.[136-137] Moreover, GO has a sheet morphology, which can act as a substrate for MOFs growth or immobilization via its functional groups (epoxy, hydroxyl, carboxyl groups).[138] Also, combining MOFs with carbon nanotubes as fillers in MMMs can also increase improved interfacial characteristics and separation performance.[139]

## 1.5 Fundamentals of gas permeation through membranes

### 1.5.1 Technical terms used in gas permeation membrane science

***Diffusion***: Diffusion is the process by which molecules are move from areas of high concentration to areas of low concentration. There three important forms of diffusion in a membrane: solution diffusion, Knudsen diffusion, and molecular sieving. These will be discussed in more detail later.

Fick's law: Fick's law states that a gas will diffuse from a region of high concentration to a region of a low concentration zone. The flux is the magnitude and direction of the gas flow and this is proportional to the concentration gradient.

***Henry's law***: Henry's law is a gas law of developed by William Henry in 1803. It states that the amount of a gas dissolved in a solution is proportional to its partial pressure above the solution. The Henry constant is the name given to this proportionality factor. The concept can be transferred from liquids to membranes.

***Fractional free volume***: The free volume of a polymer refers to the unoccupied space or voids between the polymer chains. It represents the accessible space that is not filled by the polymer chains themselves. Therefore, the free volume can provide pathways and voids for gas molecules to move and diffuse within the polymer structure. Direct investigation of the pores in polymeric membranes is not feasible because the gaps occur at the molecular level. The difference between the measured experimental specific volume of polymer ($V$, $cm^3/g$), and the theoretical volume occupied by the polymer chain segments ($V_0$, $cm^3/g$) is used to determine the fractional free volume (FFV). Therefore,

$$\boldsymbol{FFV = \frac{V - V_0}{V}} \quad 1.1$$

The term $V_0$ is typically estimated using group contribution theory as described by Bondi[140]:

$$V_0 = 1.3 \sum V_w \quad 1.2$$

$V_w$ is the van der Waals volume of functionality comprising the polymer chains. Finally, FFV can be expressed as:

$$FFV = \frac{V - 1.3V_w}{V} \quad 1.3$$

***Permeability:*** Gas permeability refers to the ability of a material or membrane to allow the passage of a specific gas through it. Gas permeability is often quantified using the permeability coefficient, which represents the rate of gas flow per unit area and per unit of pressure difference across the material.

***Selectivity***: This term defines the membrane's ability to allow some components to pass through while blocking others. The membrane's capacity to separate two gases (*A* and *B*) is defined as the ratio of their permeabilities ( $\alpha_{\frac{A}{B}}$).

***Kinetic diameter***: The kinetic diameter of a gas molecule is its sphere of influence that can lead to a scattering event (Table 1.1). It can be calculated from

$$d^2 = \frac{1}{\pi l n} \quad 1.4$$

Where $l$ is the mean free path length of the molecule, $d$ is the kinetic diameter of the molecule and $n$ is the number of molecules per unit volume.

**Table 1.1** Molecular weights and kinetic diameters (Å) of common gases.

| Molecule | Molecular weight | Kinetic diameter (Å) |
|---|---|---|
| $H_2$ | 2 | 2.89 |
| $CH_4$ | 16 | 3.8 |
| $N_2$ | 28 | 3.64 |
| $O_2$ | 32 | 3.46 |
| $CO_2$ | 44 | 3.3 |
| $C_2H_2$ | 26 | 3.3 |
| $C_2H_4$ | 28 | 3.9 |
| $C_3H_6$ | 42 | 4.5 |
| $C_3H_8$ | 44 | 4.3 |

***Glassy and rubbery polymers***：The glass transition temperature is the temperature at which the first polymer chain movement begins, causing a shift from the glassy, solid, and hard state to the soft, flexible, and rubbery state.[141] The glass glass transition temperature (*Tg*) of glassy polymers is greater than their operating temperature. It should be emphasized that the glassy

temperature occurs only for the amorphous portions of the polymers and not for the crystalline regions. The polymer modules and the temperature in Fig. 1.18 illustrate the glassy transition temperature. Below their glass transition temperatures, glassy polymers are rigid and stiff. Polyimides (PI), such as 6FDA-DAM and 6FDA-Durene (used in this thesis), Matrimid and PIM-1 are commonly employed in membrane construction. In contrast, rubbery polymers operate beyond their glass transition temperature, making them soft and flexible. These polymers have a lower *Tg* as well as being fully amorphous. Poly(vinylidene fluoride) (PVDF), polyvinyl acetate (PVA) and polyvinylamine (PVAm), and Pebax-1657 (used in this thesis) are popular rubbery polymers used in membrane applications.

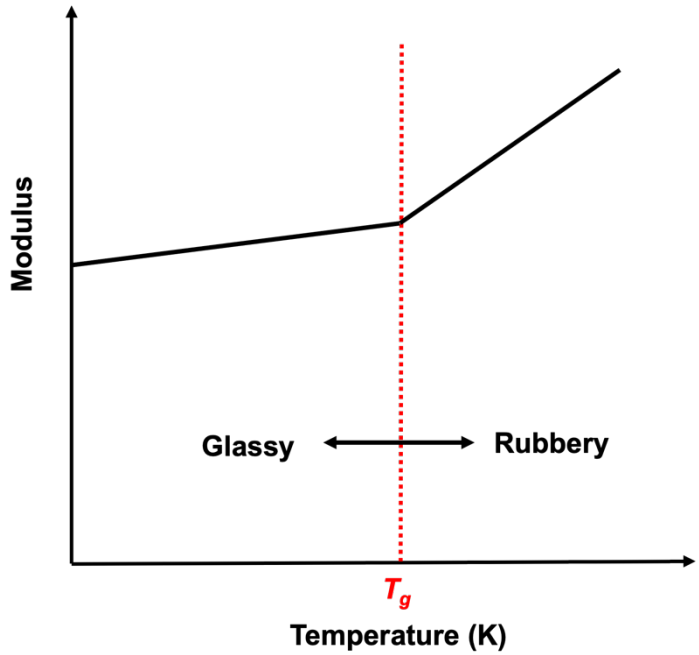


**Figure 1.18** Polymer modulus versus the temperature and occurrence of glass transition temperature ($T_g$).

**Table 1.2** Glassy transition (*Tg*) temperatures for some of the common polymeric materials.

| Polymers | | *Tg* (°C) | Ref. |
|---|---|---|---|
| Glassy | 6FDA-DAM | 391 | [142] |
| | 6FDA-Durene | 409 | [143] |
| | Matrimid | 302 | [144] |
| | PIM-1 | 371 | [145] |
| Rubbery | PVDF | -39 | [146] |
| | PVA | 52.4 | [147] |
| | Pebax-1657 | -51.7 | [148] |

### 1.5.2 Transport mechanisms for gases through membranes

The most common types of gas separation membranes in use today are still the dense polymeric membranes, where gas transport is based on Fick's law.

Fick's law describes the diffusion of molecules or particles through a media, such as a gas or liquid, which can be represented as:

$$J_i = -D_{ij}\frac{dc_i}{d_x} \quad 1.5$$

Where *Ji* is the flux of component *i* (mol/[m$^2$s], $D_{ij}$ is the diffusion coefficient (m$^2$/s), $\frac{dc_i}{d_x}$ is the concentration gradient for component *i* over the length *x* (mol/[m$^3$·m].

When applied to membrane separation, Fick's law yields $d_x = l$ (membrane thickness), and $dc_i$ = concentration difference (i.e. particle pressure differences) across the membrane. And the $D_{ij}$ varies according to the dominating transport mechanism.

The gas permeance *P/l* (mol/[m$^2$ Pa s] (SI units) for a given gas (*i*) is defined by:

$$\frac{P_i}{l} = \frac{J_i}{\Delta p_i} \quad 1.6$$

Where *P/l* can be expressed as (m$^3$[STP]/(m$^2$ bar h), $\Delta p_i$ is the partial pressure difference (bar or Pa).

Therefore, gas permeability can be expressed as:

$$P_i = \frac{J_i}{\Delta p_i}\cdot l \quad 1.7$$

Membrane permeability is typically expressed in units of Barrer:

$$1\ Barrer = 3.35 \times 10^{-16} \frac{mol \cdot m}{m^2 \cdot s \cdot Pa} = 1 \times 10^{-10} \frac{cm_{STP^3} \cdot cm}{cm^2 \cdot cm \cdot Hg} \quad 1.8$$

In addition, membrane permeance can be expressed in a unit of GPU:

$$1\ \text{GPU} = 3.35 \times 10^{-10} \frac{\text{mol}}{\text{m}^2 \cdot \text{s} \cdot \text{P}_\text{a}} \quad 1.9$$

This equation demonstrates the relation of flux between the partial pressure difference and the membrane thickness. That is, the flux through the membrane is proportional to the pressure difference across the membrane and inversely proportional to the membrane thickness. The ideal selectivity between gas components can be expressed as the ratio of the pure gas permeabilities for each gas component *i* and *j:*

$$\alpha_{ij}^{*} = \frac{P_i}{P_j} \quad 1.10$$

For mixed gases, the separation factor $\alpha_{ij}$ is expressed by the mole fractions of the components on the feed side ($x$) and the permeate side ($y$) of the membrane, respectively:

$$\alpha_{ij} = \frac{y_i / y_j}{x_i / x_j} \quad 1.11$$

Dense polymeric materials often used for gas separation membrane applications. Gas permeation through this type of membrane can be viewed as following the *solution-diffusion* mechanism. Moreover, Knudsen diffusion and molecular sieving are another two main types of gas diffusion through the membrane (Fig. 1.19).

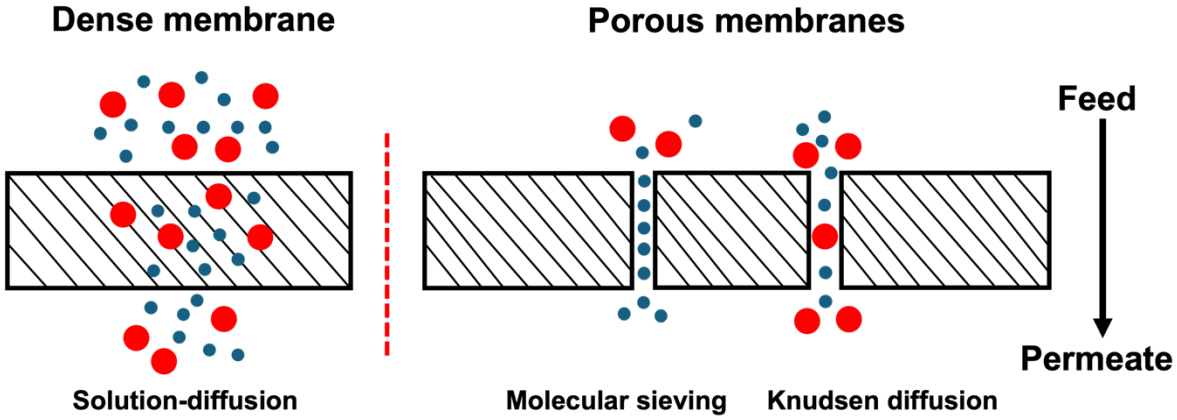


**Figure 1.19** Schematic diagram of the mechanism of gas transport through membranes.

**Solution-diffusion**

The solution-diffusion mechanism is one of the primary mechanisms used in gas separation membranes. It describes the process by which different gas molecules are dissolved in the membrane material and then diffuse through it at different rates, resulting in the selective separation of gases based on their solubility and diffusivity.

Derived from Fick's law, the gas permeability $P$ can also be written as the product of the diffusion ($D$) and solubility ($S$) of the gas passing through the membrane according to the *solution-diffusion* mechanism:

$$P = D \cdot S \tag{1.12}$$

The diffusion coefficient $D$ reflects the mobility of the individual gas molecules in the membrane materials, and the gas sorption (solubility) coefficient $S$, reflects the number of gas molecules dissolved in the membrane (in the case of a polymer) or adsorbed (in the case of a porous material).

Therefore,

$$\alpha_{ij} = \frac{P_i}{P_j} = \left[\frac{D_i}{D_j}\right] \cdot \left[\frac{S_i}{S_j}\right] \tag{1.13}$$

Where $\frac{D_i}{D_j}$ is the ratio of the diffusion coefficients of the binary gas molecules and can be considered as the mobility selectivity, reflecting the diffusivity differences of the gas molecules. And $\frac{S_i}{S_j}$ is the ratio of the sorption coefficients of two gas molecules and can be regarded as the sorption or solubility selectivity, indicating the relative solubilities of the gas molecules.

**Molecular sieving**

Molecular sieving is a transport mechanism where the pore size is comparable to the target molecular dimensions. In molecular sieving, the porous material or membrane can act as a sieve, allowing smaller molecules to diffuse through the interconnected pores, while larger molecules are unable to enter or pass through. The selectivity of this process is primarily determined by the size and geometry of the pores.

The separation can be achieved by exploiting the differences in molecular size and shape between the gas molecules.

In molecular sieving process for gas separation the following aspects are important:

(i) Adsorption. The gas mixtures contact with the porous membrane, then the gas molecules reach the surface of the pores and are adsorbed onto the pore walls due to the interactions such as van der Waals forces.

(ii) Diffusion. The adsorbed gas molecules diffuse through the interconnected pores of materials or membrane. Smaller gas molecules can easily pass through the smaller pores, while larger gas molecules are limited or excluded.

**Knudsen diffusion**

Knudsen diffusion occurs in microporous inorganic membranes or through pinholes in dense polymeric membranes. Knudsen flow is characterized by the mean free path ($\lambda$) of the diffusing molecules being larger than the pore dimensions ($d_p$).

While the exact threshold for Knudsen diffusion can vary depending on the specific gas and conditions, a common rule is that Knudsen diffusion becomes prominent when the ratio of the pore diameter to the mean free path (also known as the Knudsen number, Kn) is in the range of 0.1 to 10. Knudsen diffusion can be described as:

$$D_{K_n} = \frac{d_p}{3}\bar{V}_A = \frac{d_p}{3}\sqrt{\frac{8RT}{\pi M_A}} = 48.5 \cdot d\sqrt{\frac{T}{M_A}} \qquad 1.14$$

Where $D_{K_n}$ is the Knudsen diffusivity, $d_p$ is the average pore diameter (m), $\bar{V}_A$ is the average molecular velocity (m/s), $M_A$ is the molecular weight of gas component A (g/mol), $R$ is the gas constant, and $T$ is the temperature (K).

As a result, the selectivity of gas *i* over *j* based on Knudsen diffusion is:

$$\alpha_{\frac{i}{j},Kn} = \frac{D_{i,Kn}}{D_{j,Kn}} = \sqrt{\frac{M_j}{M_i}} \qquad 1.15$$

These selectivity values are not very high, which means that effective membrane separation processes rely on other transport processes.

**Table 1.3** Ideal Knudsen selectivity of several commonly-encountered binary gas mixtures.

| Gas mixtures | $CO_2/N_2$ | $CO_2/CH_4$ | $H_2/CO_2$ | $H_2/N_2$ | $H_2/CH_4$ | $C_3H_6/C_3H_8$ |
|---|---|---|---|---|---|---|
| Ideal Knudsen selectivity | 0.80 | 0.60 | 4.69 | 3.74 | 2.8 | 1.02 |

### 1.5.3 Modelling of gas transport properties in MMMs

Several empirical models have been used to describe the gas transport properties of MMMs, which are typically functions that combine the gas permeabilities of the continuous (polymer matrix) and dispersed (filler particles) phases.[149] The Maxwell model[150] is the most widely used model for predicting the influence of filler loading on gas permeability through MMMs,

and it can extrapolated to predict the permeability of a pure MOF from MMM permeability measurements:

$$P_{MMM} = P_P \left[ \frac{P_S + 2P_P - 2\emptyset_s(P_P - P_s)}{P_S + 2P_P + \emptyset_s(P_P - P_s)} \right] \quad 1.16$$

Where $P_{MMM}$ is the permeability of mixed matrix membrane; $P_P$ is the permeability of the polymer matrix (pure polymer); Ps is the permeability of the dispersed filler particles, and $\emptyset_s$ is the volume fraction of filler particles in mixed matrix membrane:

$$\emptyset_s = \frac{\frac{M_{fillers}}{\rho_{fillers}}}{\frac{M_{fillers}}{\rho_{fillers}} + \frac{M_{polymer}}{\rho_{polymer}}} \quad 1.17$$

## 1.6 Experimental aspects of permeability calculations

This section will introduce the equipment and method used to calculate membrane permeabilities in this thesis.

### 1.6.1 Mass spectrometer calibration

In our work, gas permeability measurements were carried out via a Wicke-Kallenbach apparatus (Fig. 1.20a). And the corresponding schematic of this apparatus is shown in Fig. 1.20b. Taking $CO_2/N_2$ mixture as an example, the mass spectrometer needs to be first calibrated for $CO_2$ and $N_2$.

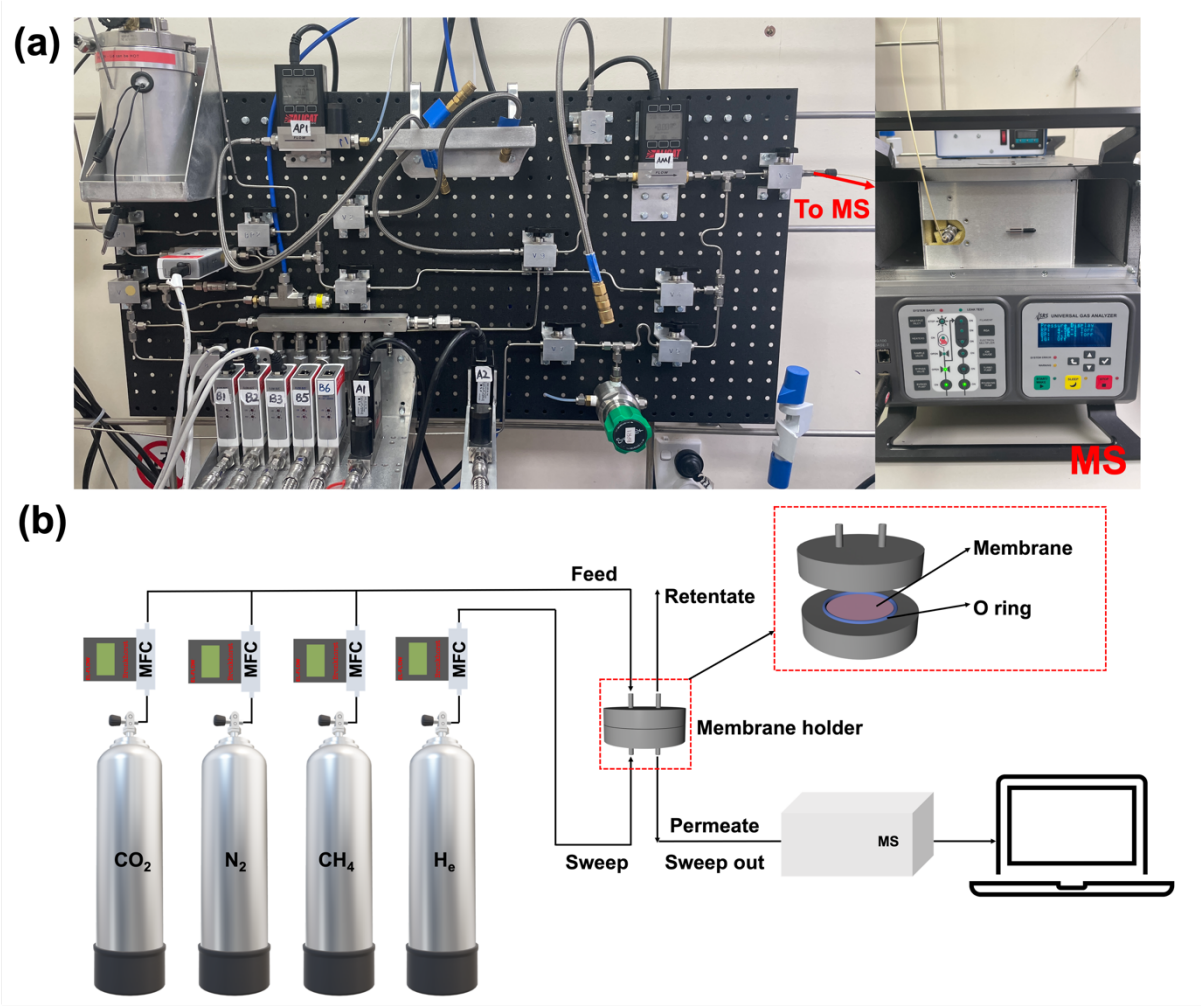


**Figure 1.20** (a) Photo of Wicke-Kallenbach apparatus for gas permeability test of membranes in our work. (b) Scheme of Wicke-Kallenbach apparatus used for gas permeation measurements in this work.

(1) $N_2$ calibration

For the calibration of $N_2$, the capillary line of MS was exposed to air. Then the sample valve was turned on, followed by clicking "sensitivity tuning" under "Head menu" on the RGA software, waiting for about 60 s.

The "mass selection" of $N_2$ was set as 28 AMU (atomic mass unit). When the environmental pressure is 760 torr, for $N_2$, 78 % accounts for the indoor air pressure. Therefore, $N_2$ pressure can be calculated: 0.78 × 760 torr =592.8 torr. In our MS, 92.6 % of $N_2$ gives a signal at AMU 28, so the reference pressure reading should be 545 torr. The sensitivity factor was measured several times to obtain a steady value. Once the calibration of $N_2$ was achieved the MS reads a pressure value of 545 torr from lab air.

As for other gases, the scale factor as shown in Table 1.4.

**Table 1.4** Scale factor of commonly used gases.

| Selected gas fragments | |
|---|---|
| Gas | % |
| $CO_2$ (44) | 78.4314 |
| $N_2$ (28) | 92.5926 |
| $H_2$ (2) | 95.2381 |
| He (4) | 100 |
| $CH_4$ (16) | 45.9348 |

(2) $CO_2$ calibration

a) A $CO_2$ and $N_2$ mixture gas of known concentration was introduced into the gas line, with precise control by the mass flow controller.

b) The MS was initiated to measure the partial pressures of $CO_2$ and $N_2$ in the mixture gas.

c) The $CO_2$ partial pressures were corrected to the known values by adjusting the scale factor/ratio to the $N_2$ partial pressure, and this scale factor was recorded in the system.

With a similar procedure, He, $H_2$, $CH_4$ and other gases can be calibrated by obtaining the corresponding scaling factors.

### 1.6.2 Gas permeability and selectivity tests

A schematic of the apparatus is shown in Fig. 1.20b. Briefly, the mass flow rate was controlled using Alicat mass flow controllers (MFC). Helium (20 sccm) was used as the carrier gas in each test. The permeate gas was analyzed via the mass spectrometer. For single (pure) gas permeation tests, $N_2$, $CH_4$, and $CO_2$ were tested in order. Each gas was tested for 30 min to reach a steady state, then the permeate gas compositions were recorded by averaging 10 sets of data points. The feed pressure was in a range of 1 bar to 5 bar, and the temperature was maintained at 20 $^oC$. To further investigate the separation performance, mixed gas permeation tests were conducted. Here the ratio of mass flow rates for $CO_2$ to $N_2$ and $CH_4$ was 2:8. The feed gases were delivered to feed side of the membrane as a mixture.

### 1.6.3 Data analysis

This section outlines how the measure data was transformed into permeability and selectivity values using $CO_2$ as an example.

(1) Background collection

The mass spectrometer was purged by He since there were often residual gases that were difficult to clean out. When the readings of each gas on RGA were sufficiently low, the background could be collected. Normally, 10 groups of data were collected, and their average value is the background.

(2) $CO_2$ real pressure = $CO_2$ raw value – $CO_2$ background value

Where $CO_2$ raw value represents the test pressure of $CO_2$ in RGA; $CO_2$ background value is the averaged $CO_2$ pressure from the He flush in RGA (see below).

| Background | | He | H2 | CH4 | N2 | O2 | CO2 | N2-14 | CH4-16 |
|---|---|---|---|---|---|---|---|---|---|
| | 50070.453 | 752.01 | 0.25343 | 0.087446 | 0.19744 | 0.035415 | 0.20691 | 0.082052 | 0.026494 |
| | 50075.469 | 755.78 | 0.25795 | 0.15033 | 0.17307 | 0.03156 | 0.22406 | 0.10085 | 0.036177 |
| | 50080.484 | 755.07 | 0.25308 | 0.11314 | 0.11105 | 0.02609 | 0.17109 | 0.10771 | 0.091317 |
| | 50085.484 | 757.46 | 0.2528 | 0.032225 | 0.22372 | 0.017663 | 0.12003 | 0.036072 | 0.038732 |
| | 50090.500 | 751.2 | 0.24101 | 0.067998 | 0.24755 | 0.052271 | 0.085354 | 0.052076 | 0.050164 |
| | 50095.516 | 758.36 | 0.24376 | 0.081058 | 0.23157 | 0.051284 | 0.34142 | 0.073669 | 0.066033 |
| | 50100.516 | 753.69 | 0.2332 | 0.1377 | 0.17686 | 0.012911 | 0.10707 | 0.1133 | 0.045591 |
| | 50105.531 | 742.03 | 0.23438 | 0.070553 | 0.20936 | 0.049222 | 0.14975 | 0.12143 | 0.058367 |
| | 50110.531 | 747.47 | 0.22663 | 0.068424 | 0.15303 | 0.022773 | 0.16385 | 0.11762 | 0.034294 |
| | 50115.547 | 746.65 | 0.24185 | 0.094402 | 0.29793 | 0.056754 | 0.081544 | 0.012702 | 0.053526 |
| Average | #DIV/0! | 751.972 | 0.243809 | 0.090328 | 0.202158 | 0.035594 | 0.165108 | 0.081748 | 0.05007 |
| | | | | | | | | | |
| Raw data | 2180.156, | 741.99 | 0.2321 | 7.17E-02 | 0.96735 | 0.25821 | 7.7057 | 0.25597 | 0.49537 |
| | 2185.172, | 740.63 | 0.23651 | 6.89E-02 | 0.93692 | 0.27938 | 7.6711 | 0.18008 | 0.53265 |
| | 2190.172, | 754.24 | 0.23712 | 0.12044 | 0.83419 | 0.26668 | 7.8188 | 0.21077 | 0.53097 |
| | 2195.188, | 752.6 | 0.24368 | 0.10196 | 0.71828 | 0.20703 | 7.3485 | 0.19888 | 0.41186 |
| | 2200.203, | 750.22 | 0.24452 | 0.067134 | 0.70839 | 0.23205 | 7.1444 | 0.2612 | 0.45305 |
| | 2205.156, | 758.9 | 0.24022 | 0.087606 | 0.75126 | 0.29747 | 7.2614 | 0.20554 | 0.41544 |
| | 2210.219, | 747.45 | 0.21608 | 8.79E-02 | 0.78423 | 0.24475 | 7.3117 | 0.17984 | 0.48876 |
| | 2215.219, | 750.36 | 0.22893 | 0.11379 | 0.86108 | 0.27592 | 7.2321 | 0.19792 | 0.4779 |
| | 2220.235, | 754.02 | 0.2257 | 0.12084 | 0.81771 | 0.43485 | 7.5818 | 0.19055 | 0.45249 |
| | 2225.250, | 752.94 | 0.2477 | 0.12922 | 0.85296 | 0.31825 | 7.8284 | 0.26049 | 0.46022 |
| Average | #DIV/0! | 750.335 | 0.235256 | 0.096938 | 0.823237 | 0.281459 | 7.49039 | 0.214124 | 0.471871 |
| real value | | | | | 0.621079 | | 7.325282 | | |

Then $CO_2$ actual pressure was used for the $CO_2$ permeability calculation.

(3) $CO_2$ permeability calculation

**Table 1.5** $CO_2$ permeability calculation.

| **$CO_2$ permeability test** | | |
|---|---|---|
| **Membrane parameters** | | |
| Dimension (mm) | 10 | |
| Thickness(um) | 65 | |
| **Testing conditions** | | |
| Feed pressure (psi) | 29 | |
| Sweep gas flow rate (sccm) | 20 | |
| **Gas compositions** | | |
| Gas | He | $CO_2$ |
| Panel reading | 7.50E+02 | 7.33E+00 |
| Fragment factor | 1.00E+00 | 7.84E-01 |
| Actual pressure (torr) | 7.50E+02 | 9.34E+00 |
| Gas compositions (%) | 9.88E+01 | 1.23E+00 |
| **Results** | | |
| Total flow (sccm) | | 2.02E+01 |
| Permeate flow (sccm) | | 2.49E-01 |
| Area ($m^2$) | | 7.85398E-05 |
| Permeate flux (mol/s·Pa) | | 6.18E-13 |
| Permeance (mol /s·Pa·$m^2$) | | 7.87E-09 |
| Permeability (mol·m/s·Pa·$m^2$) | | 5.12E-13 |
| Permeability (Barrer) | | 1.53E+03 |

$$P_i = \frac{L \times q_i}{A \times \Delta P_i} \quad 1.18$$

L: membrane thickness (average value: 65 μm, obtained from a micrometer).

A: the effective area of the membrane. The prepared membrane was sealed into an aluminum foil, the effective diameter of membrane was controlled at 10 mm (Fig. 1.21). (A=7.85398E-05 $m^2$, d = 10 mm, $S = \pi r^2$).

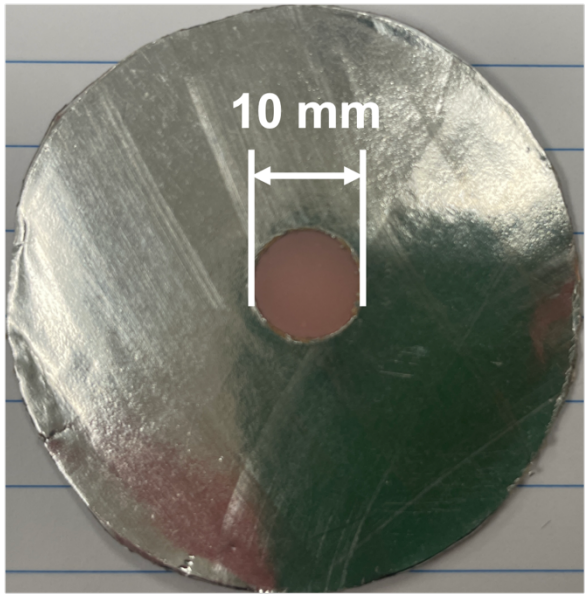


**Figure. 1.21** Photo of membrane sealed into an aluminum foil.

$\Delta P_i$: the partial pressure of component i (feed pressure set as 29.0 psi as an example).

$q_i$: the mass flow rate of the permeate $CO_2$ (sccm).

Using the sweep gas (He) to back-calculate the $CO_2$ permeate flow rate, since the flow rate of He is fixed at 20 sccm during the gas permeation test and the actual pressure of He can be read at 750 torr in the mass spectrometer. For $CO_2$, the 0.784314 of partial gas pressure can be read in the mass spectrometer. Therefore, the actual pressure of $CO_2$ could be obtained using dividing the real pressure by its fragments factor (see Table 1.4).

In this case, the $CO_2$ real pressure is 7.33 torr, therefore the actual pressure of $CO_2$ is 9.34 torr (7.33 torr / 0.784314 = 9.34 torr) (see Table 1.5).

When the actual pressure of $CO_2$ and He is determined, the corresponding gas compositions of the $CO_2$ and He could be obtained.

Therefore, the compositions of $CO_2$ and He in the permeate side could be calculated:

$$CO_2\ composition = \frac{P_{CO_2}}{P_{CO_2} + P_{He}} \quad 1.19$$

$$CO_2\ composition = \frac{9.34}{9.34 + 750}$$

$$1.23\%$$

$$He\ composition = \frac{P_{He}}{P_{CO2} + P_{He}} \quad 1.20$$

$$He\ composition = \frac{750}{9.34 + 750} = 98.78\%$$

In our test, pure He was used as the sweep gas during the test, and its gas flow rate was constant at 20 sccm, therefore the total flow rate can be obtained using sweep gas flow rate.

$$Total\ flow\ rate\ (sccm) = \frac{sweep\ gas\ flow\ rate}{He\ composition} \quad 1.21$$

$$Total\ flow\ rate\ (sccm) = \frac{20\ sccm}{98.78\%} = 20.2\ sccm$$

Afterwards, permeate flow rate of $CO_2$ can be calculated through multiplying the total flow rate by $CO_2$ composition.

$$CO_2\ Permeate\ flow\ rate\ (sccm) = Total\ flow\ rate\ \times\ CO_2\ composition \quad 1.22$$

$$CO_2\ Permeate\ flow\ rate\ (sccm) = 20.2 \times 1.23\% = 0.249\ sccm$$

Note:

$$1\ sccm = 7.45 \times 10^{-7}\ \frac{mol}{s}$$

$$1\ psi = 6894.76\ Pa \quad 1.23$$

Therefore, $CO_2$ permeate flux can be calculated using equation 1.6.

$$CO_2\ Permeate\ flux\ \left(\frac{mol}{S \cdot Pa}\right) = \frac{CO_2\ permeate\ flow\ rate\ \times\ (7.45 \times 10^{-7}) \times\ 6894.76}{(feed\ pressure + 14.7) - (14.7\ \times\ CO_2\ composition)}\left(\frac{mol}{S \cdot Psi}\right) \quad 1.24$$

Note: $\Delta P$ is the pressure difference between the two sides of the membranes (29.0 Psi as an example).

$$CO_2\ Permeate\ flux\ \left(\frac{mol}{s \cdot Pa}\right) = \frac{0.249 \times (7.45 \times 10^{-7})\ \times\ 6894.76}{(29.0 + 14.7) - (14.7 \times 0.197\%)}$$

$$= (6.18 \times 10^{-13})\left(\frac{mol}{S \cdot Psi}\right)$$

$$CO_2\ permeance\ \left(\frac{mol}{s \cdot Pa \cdot m^2}\right) = \frac{CO_2\ permeate\ flux}{membrane\ area} \quad 1.25$$

$$CO_2\ permeance = \frac{(6.18 \times 10^{-13})\left(\frac{mol}{s \cdot Pa}\right)}{(7.85398\text{E} - 05)m^2} = (7.87 \times 10^{-9})\frac{mol}{s \cdot Pa \cdot m^2}$$

$CO_2$ permeance converted to $CO_2$ permeability via multiplying $CO_2$ permeance by membrane thickness (equation 1.7).

$$CO_2\ permeability\ \left(\frac{mol \cdot m}{s \cdot Pa \cdot m^2}\right) = CO_2\ permeance\ \times\ thickness \tag{1.26}$$

$$CO_2\ permeability\ \left(\frac{mol \cdot m}{s \cdot Pa \cdot m^2}\right)$$
$$= (7.87 \times 10^{-9}) \frac{mol}{s \cdot Pa \cdot m^2} \times 65\ \mu m$$
$$= 5.12 \times 10^{-13} \left(\frac{mol \cdot m}{s \cdot Pa \cdot m^2}\right)$$

Finally, the unit of $CO_2$ permeability can be converted to barrer.

$$Since\ 1\ barrer = 3.35 \times 10^{-16} \frac{mol \cdot m}{m^2 \cdot s \cdot Pa}$$

Therefore,

$$CO_2\ permeability\ (barrer) = \frac{CO_2\ permeability\ \left(mol\ \cdot \frac{m}{m^2} \cdot s \cdot\ pa\right)}{3.35 \times 10^{-16}} \tag{1.27}$$

$$CO_2\ permeability\ (barrer) = \frac{5.12 \times 10^{-13} \left(\frac{mol \cdot m}{s \cdot Psi \cdot m^2}\right)}{3.35 \times 10^{-16}} = 1.53 \times 10^3\ barrer$$

Using the same method, $N_2$ and $CH_4$ gas permeabilities can be obtained.

Finally, the selectivity of $CO_2/N_2$ for the membrane can be calculated through equation 1.10.

### 1.6.4 Solubility (S) and diffusivity (D) calculations related to the solution-diffusion mechanism

The solubility coefficient (S) represents the thermodynamic contribution to transport. It can be measured independently by pressure-decay sorption and expressed as:

$$S_i = \frac{c_i}{f_i} \tag{1.28}$$

Where $c_i$ is the concentration of a gas adsorbed in the sample, and $f_i$ is the corresponding upstream fugacity driving force of component $i$. This can be estimated experimentally from gas adsorption isotherms.

For a rubbery polymer (such as Pebax) and its mixed matrix membranes, the adsorbed gas concentration can be described by Henry's law:

$$c_i = c_{D,i} = k_{D,i} f_i \quad 1.29$$

Where $c_{D,i}$ is dissolved gas concentration, $k_{D,i}$ is the Henry's law sorption coefficient, which can be estimated by an adsorption isotherm.

For MOF crystals, the adsorbed concentration of gases can also be described by a Henry's law equation where their adsorption isotherms are linear. For non-linear isotherms the adsorbed concentration of gas can be described by the Langmuir model:

$$c_i = c_{H,i} = \frac{c_{sat} b_i f_i}{1 + b_i f_i} \quad 1.30$$

Where $c_{H,i}$ is the dissolved gas concentration in the Langmuir mode, $c_{sat}$is the Langmuir capacity constant, and $b_i$ is the Langmuir affinity constant.

Once P and S are known, the diffusion coefficient ($D$) of the gas in the membrane can be calculated from the solution-diffusion mechanism (P = S · D):

$$D_i = \frac{P_i}{S_i} \quad 1.31$$

### 1.6.5 Apparatus validation

To validate our apparatus, a range of polymers including Pebax-1657, 6FDA-DAM and 6FDA-Durene, was used to prepare pure membranes and their gas separation performance was tested. The obtained results are close to those reported in the literature.

Taking Pebax-1657 as an example, 3.0 wt% Pebax solution (EtOH/$H_2O$) was used to prepare a pure Pebax membrane. Its permeability was tested in a sequence of $CO_2$, $N_2$ then $CH_4$ (at 20 °C with a feed pressure of 1 bar). The permeability results from our Wicke-Kallenbach apparatus are shown in Table 1.6.

**Table 1.6** Comparison of experimental separation performance of a Pebax membrane using our Wicke-Kallenbach apparatus with literature results.

| Membrane | Gas | Experimental Permeability (Barrer) | Literature value[151] |
|---|---|---|---|
| Pebax | $CO_2$ | 69.0 ± 2.07 | 71.25 |
| | $N_2$ | 1.78 ± 0.06 | 2.15 |
| | $CH_4$ | 5.54 ± 0.17 | 6.27 |
| | $CO_2/N_2$ | 38.76 ± 1.16 | 35.91 |
| | $CO_2/CH_4$ | 12.45 ± 0.37 | 12.54 |

# Chapter 2 Metal−Organic Framework Crystal-Glass Composite Membranes for Gas Separation

## 2.1 Introduction

Membrane-based separation technologies have been regarded as an attractive candidate due to their low energy consumption and environmental friendliness.[50, 152] While polymeric membranes have made remarkable progress on a commercial scale, there is still a significant market expansion in terms of their separation performance and stability challenges.[52, 153] And the trade-off effect between membrane permeability and selectivity is another obstacle to their wider application.[73] In this context, the development of novel membrane materials with superior gas separation performance is possible to address the aforementioned issues. To this end, several materials, including metal-organic frameworks (MOFs),[154-156] covalent-organic frameworks (COFs)[157-159] and zeolites[160-161] etc. have been extensively explored for advanced membrane separation in recent years. In particular, MOF membranes have demonstrated impressive gas separation performance due to their large surface area, tunable functionality, and good chemical stability.[74, 162] However, interfacial defects and/or grain boundaries present in MOF membranes caused by uncontrollable crystal size growth generally exhibit undesirable separation performance.[163] Therefore, it is still challenging to construct pure MOF membranes without interfacial defects for superior gas separation performance.

As a recently developed material, MOF glass has attracted a wide range of applications in the fields of gas sorption,[164] sensors,[165] photonics[166] and ion conduction.[167] Normally, MOF glass can be formed by melt-quenching its crystalline phase. To date, some zeolitic imidazolate frameworks (ZIFs), such as ZIF-4,[168-169] ZIF-62,[103] and ZIF-76,[170] have displayed the glass-forming ability by quenching their liquid phase at a temperature range of liquid melting ($T_m$) and glass transition ($T_g$). Notably, ZIF-62 [$Zn(Im)_{1.75}(bIm)_{0.25}$], a MOF consisting of mixed linkers of imidazole (Im, $C_3H_3N_2^-$) and benzimidazole (bIm, $C_7H_5N_2^-$), is considered as a good candidate for glass formation due to its relatively low melting temperature and high thermal stability. The advantages of high porosity and ease of fabrication enable ZIF-62 glass (*ag*ZIF-62) to be used in gas separation membranes. Jiang *et al*. first reported an *ag*ZIF-62 membrane with enhanced gas molecular sieving capability by melt-quenching crystalline ZIF-62 membrane on an alumina support.[106] This work provided a blueprint in the manufacture of gas separation membranes. Later, Li and co-workers developed a hybrid ZIF-8/ZIF-62 glass membrane via a flux-melting approach for

$C_3H_6/C_3H_8$ separation.[171] Zhong and co-workers developed free-standing *ag*ZIF-62 foam membrane for advanced $CH_4/N_2$ separations.[172]

Although these glass membranes displayed ultra-high gas permeance, the corresponding selectivity cannot meet the need for actual separation. To simultaneously achieve high gas permeance and good selectivity, MOF crystal-glass composite (MOF-CGC) membranes were developed by incorporating crystalline MOFs into a MOF glass matrix, the chemical properties of crystalline MOFs can be preserved by glassy MOFs, and the enhanced gas adsorption ability could improve the resulting selectivity.[173-174] To date, reports about the use of MOF crystal-glass composites membranes for $CO_2$ separation are rare. Similar to the manufacturing process of mixed matrix membranes (MMMs) (incorporation of filler particles into a polymer matrix), we proposed the crystal-glass composite membranes (CGCMs), which can be constructed by incorporating MOF crystals into the glass phase using pressing and quenching treatments (Fig. 2.1). To improve the $CO_2$ separation ability, we designed several CGCMs with enhanced $CO_2$ adsorption capacity by incorporating MOFs crystals into glass matrix.

Here, we have developed a series of CGCMs with different MOF crystals that are derived from different metal precursors [UiO-66 (Zr), ZIF-8 (Zn), MIL-53 (Al) and MUF-16 (Co) (Massey University Framework - 16)] and investigated their gas separation performance. Notably, these MOF crystals with varying sizes were used to investigate the interfacial cohesion with glass phase in membrane. To ensure the final CGCMs with continuous morphology without boundary voids, MOF crystals (UiO-66, ZIF-8, and MIL-53) were first homogeneously mixed with ZIF-62 via a ball mill treatment to form the composite (CGC), respectively. The resulting CGCMs were obtained after sequential tableting (CGC tablet) and melt quenching processes. As expected, the fabricated CGCMs showed improved $CO_2$ adsorption uptake, and the gas separation results of the fabricated CGCMs demonstrated improved $CO_2$ permeance compared to the pure *ag*ZIF-62 membrane. Overall, this strategy provided one promising way to fabricate high-performance membranes. In addition, another MOF with high $CO_2$ adsorption capacity (MUF-16) was combined with *ag*ZIF-62 and then re-melted to form the CGCM, further expanding the applications of MOF glasses in gas separation.

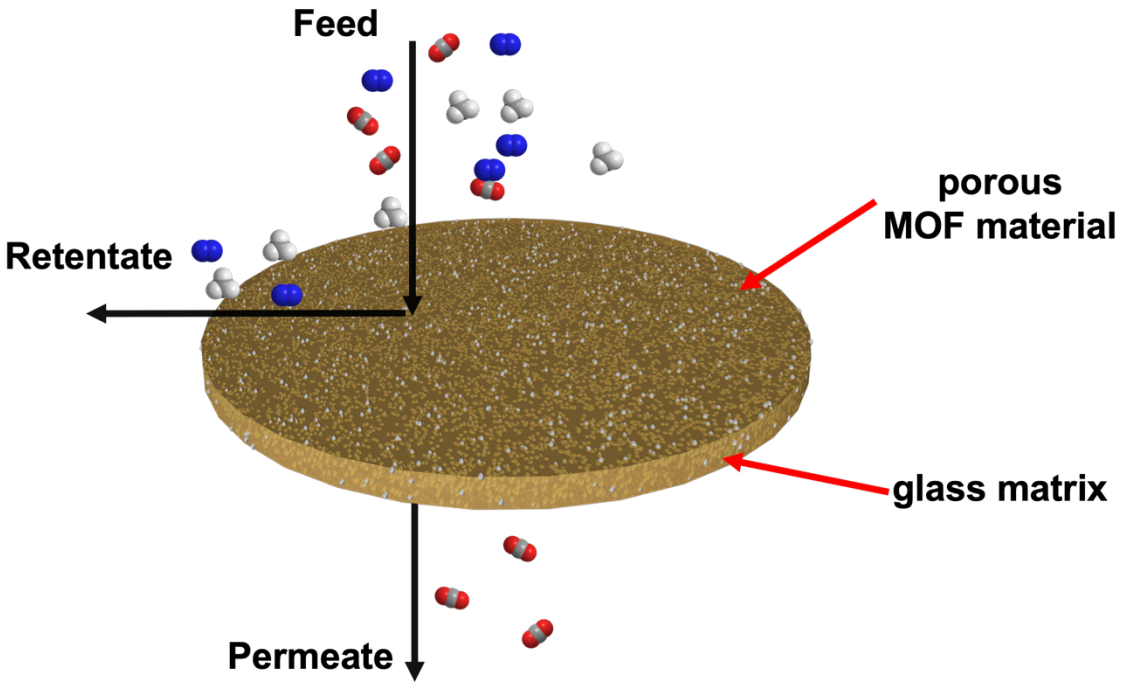


**Figure 2.1** Scheme showing the use of a crystal-glass composite membrane (CGCM) for gas separation.

## 2.2 Results and discussion

### 2.2.1 Characterization of crystalline ZIF-62 and *ag*ZIF-62

Crystalline ZIF-62 (Fig. A. 1a, Electronic Appendix) can form a glass (Fig. A. 1b, Electronic Appendix) after melt-quenching treatment. The PXRD pattern of ZIF-62 prior to melting displays its highly crystalline nature. On the other hand, the Bragg diffraction peaks of *ag*ZIF-62 are all dispersed due to the loss of the original crystalline structure after the melting process (Fig. 2.2a). In addition, compared with the sorption capacity of crystalline ZIF-62 (Fig. 2.2a), although *ag*ZIF-62 showed a reduced gas uptake volume, $CO_2$ uptake value remained at a high level, indicating the high porosity of *ag*ZIF-62 (Fig. 2.2b), which is consistent with the previous reports.[104] In addition, TGA (Fig. 2.2c) of ZIF-62 demonstrates that there is no mass loss, indicating its good thermal stability. Moreover, $^1$H NMR spectra (Electronic Appendix, Fig. A. 2) showed that *ag*ZIF-62 the organic chemical composition (benzimidazole and imidazole) of ZIF-62 after melt quenching.

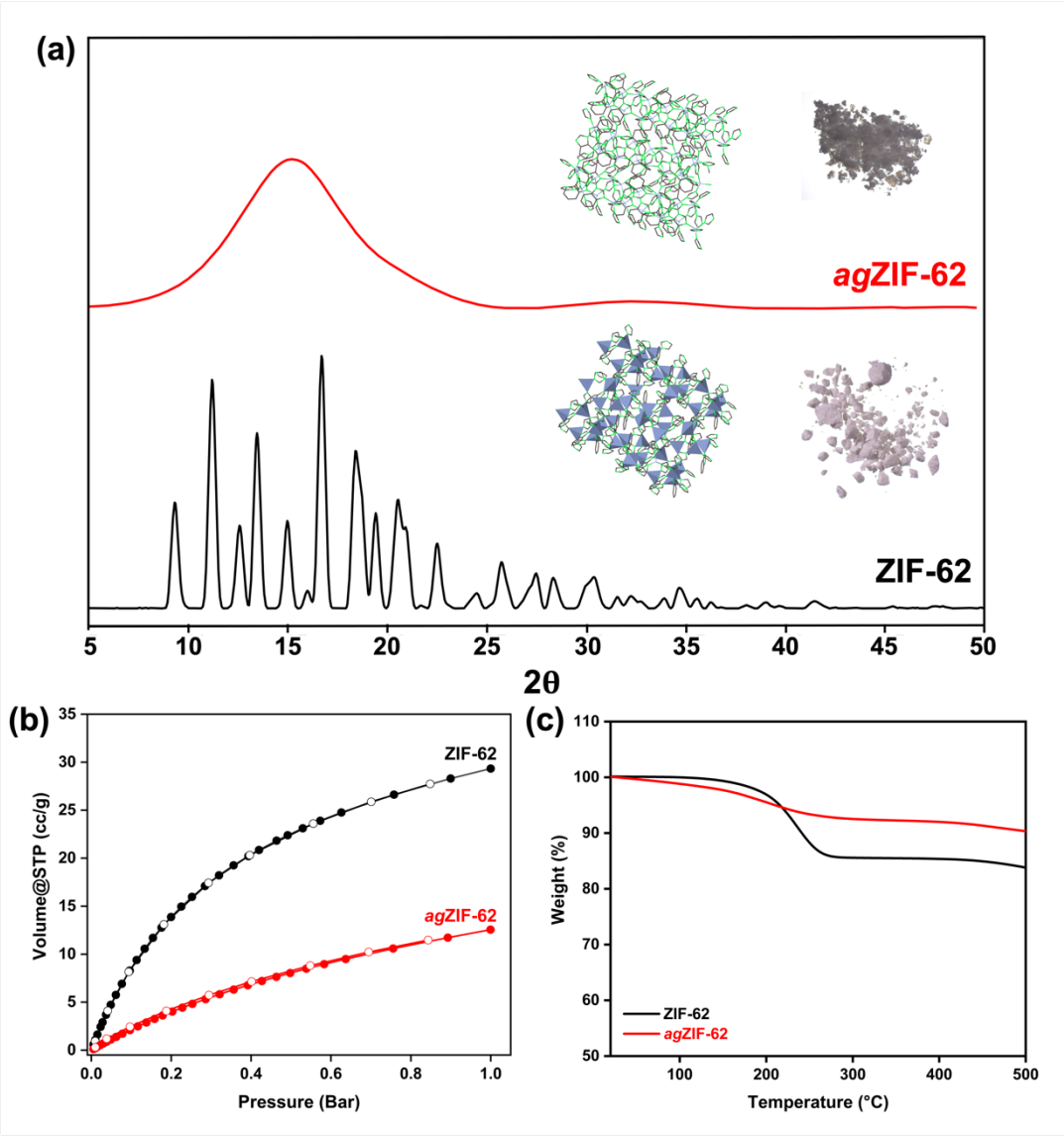


**Figure 2.2** (a) PXRD patterns of crystalline ZIF-62 (black) and *ag*ZIF-62 (red) (inserted figures are crystalline structures and micrographs of ZIF-62 and *ag*ZIF-62). (b) $CO_2$ adsorption (filled circles) and desorption (open circles) isotherms of ZIF-62 and *ag*ZIF-62 measured at 293 K. (c) TGA of ZIF-62 and *ag*ZIF-62.

### 2.2.2 Characterization of crystal fillers

The UiO-66, ZIF-8, MIL-53, and MUF-16 MOFs with crystals of different sizes were synthesized using reported methods (see experimental procedures in Electronic Appendix A, and molecular structures can be observed in Fig. A. 3). Notably, to minimize the interfacial boundaries in the resulting membranes, a microemulsion synthesis strategy was applied to fabricate nano-sized UiO-66. And MUF-16 was post-treated via a ball mill to obtain nano-sized crystals. Moreover, TEM images of crystalline ZIF-8, UiO-66, MIL-53, and MUF-16

are shown in Fig. 2.3, and the corresponding crystal size can be seen in Table. 2.1. Before fabricating CGCMs, all the synthesized crystals were first checked, and the PXRD patterns of as-synthesized MOF crystals were all in good agreement with the simulated results (Fig. A. 4, Electronic Appendix). Finally, a series of CGCMs were fabricated using these MOF crystals as described in experimental procedures (Electronic Appendix A).

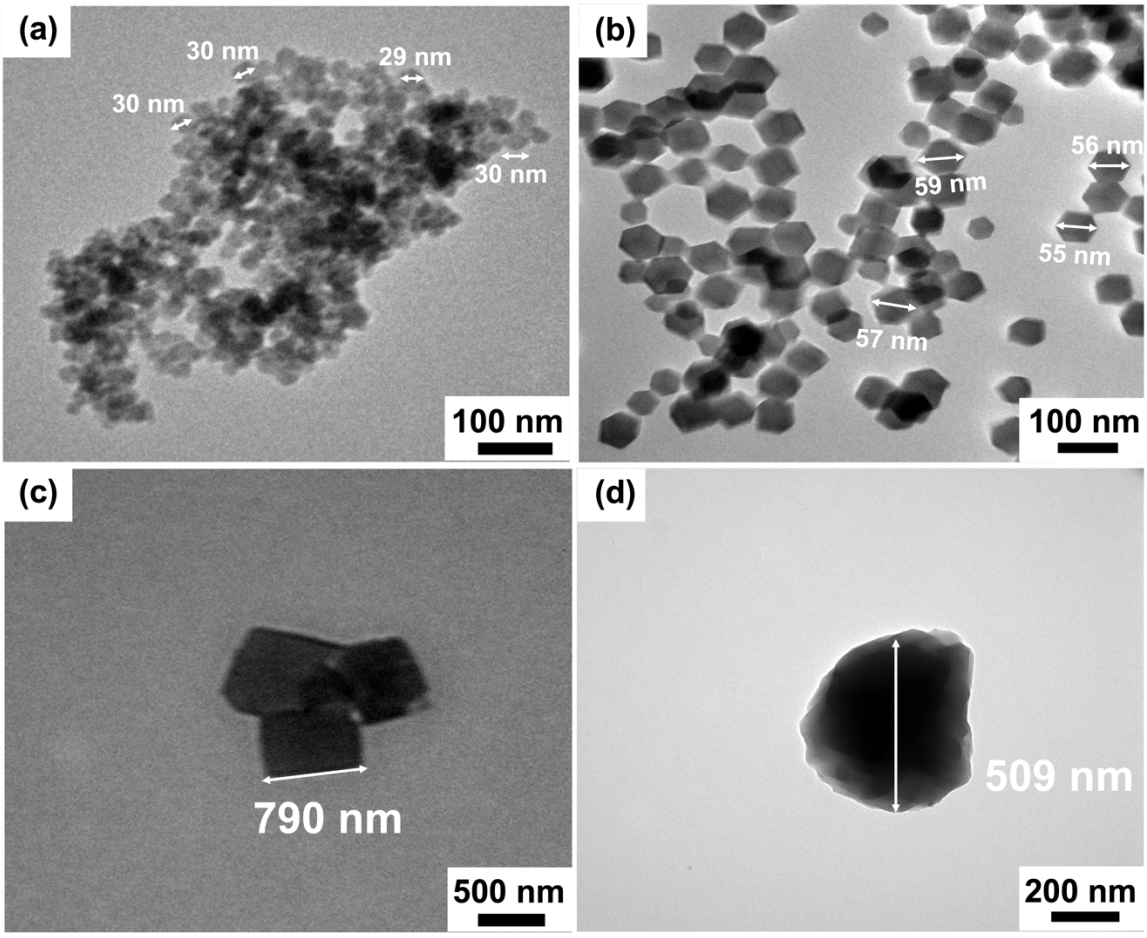


**Figure 2.3** TEM images of (a) ZIF-8, (b) UiO-66 and (c) MIL-53(Al) and (d) ball milling treated MUF-16.

**Table 2.1** Crystal size of synthesized MOF crystals in this work.

| MOF | UiO-66 | ZIF-8 | MIL-53 | MUF-16 |
|---|---|---|---|---|
| Crystal size (nm) | 30 | 55 | 790 | 500 |

### 2.2.3 CGCM fabrication process

The fabrication process for CGCMs, illustrated in Fig. 2.4a using UiO-66 as a representative case, follows a sequence of steps. First, UiO-66 crystals were blended with crystalline ZIF-62 in a ball mill to form a homogeneous composite. Subsequently, this amalgamated composite was pelletized into tablets using a mold under elevated pressure (5 tons). These tablets were then undergoing controlled heating at 409 °C within an inert atmosphere, followed by a precisely regulated quenching process. The outcomes of these processes give rise to two distinct products: the pressed composites are termed as $(UiO\text{-}66)_x(ZIF\text{-}62)_{1-x}$ tablets, while the membranes take on the designation as *ag*$[(UiO\text{-}66)_x(ZIF\text{-}62)_{1-x}]$ CGCMs. Here, *x* represents the mass fraction of incorporated UiO-66 crystals. The details of the compositions for all the CGCMs fabrication are shown in Table. S3.2 to S3.5. Through this systematic approach, UiO-66 CGCMs with different loadings were fabricated. For better comparison, the pure *ag*ZIF-62 membrane was fabricated as a blank membrane. Using the similar method, a series of CGCMs with different crystals incorporation (ZIF-8 and MIL-53) were fabricated. In addition, the details of MUF-16 CGCMs are shown in Fig. 2.4b. The composition of all CGCMs can be seen in Tables A. 1 to A. 4 in Electronic Appendix.

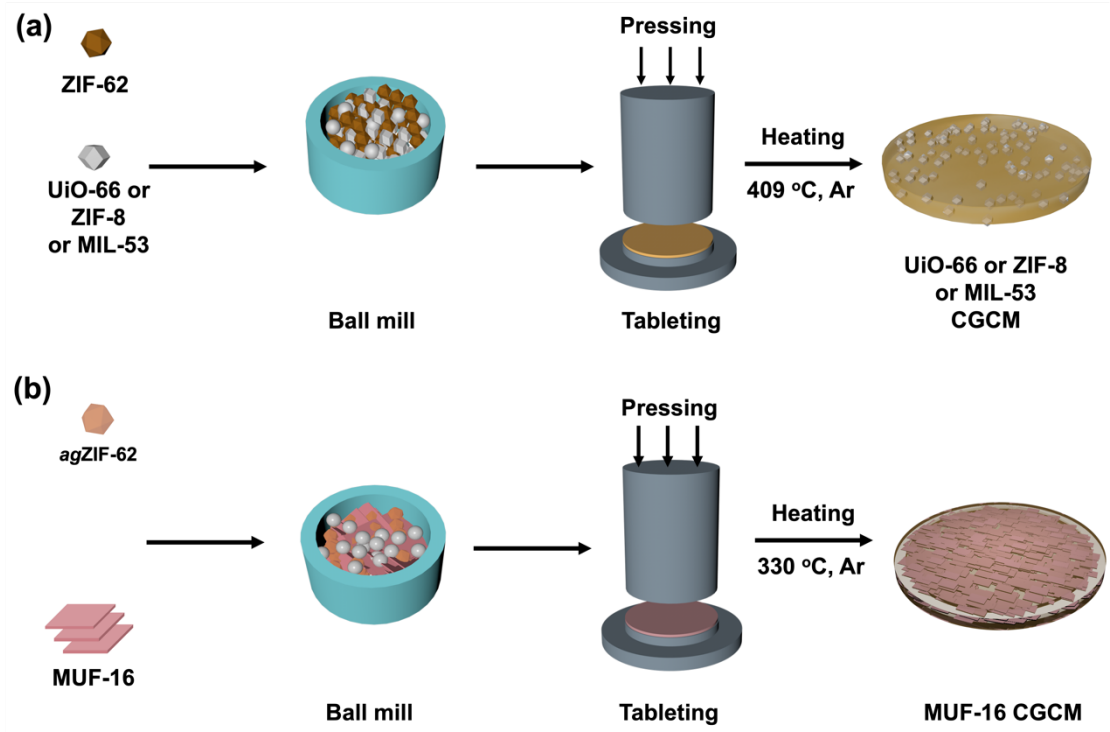


**Figure 2.4** Scheme illustration of CGC membranes fabrication process.

### 2.2.4 Characterizations of CGCM

#### PXRD of CGCMs

Detailed analysis via PXRD patterns reveals that the initial crystalline structure of ZIF-62 undergoes a transformative shift into an amorphous glass state due to the high-pressure and quenching treatment. Remarkably, the crystalline integrity of UiO-66 remains unaltered throughout this intricate procedure (Fig. 2.5a: 40 wt.% UiO-66, Fig. S2.5: all UiO-66 loadings). By following this approach, a series of UiO-66 CGCMs with varying loadings was successfully fabricated. Analogously, an array of CGCMs using diverse MOF fillers (ZIF-8, MIL-53 and MUF-16) and exhibiting a range of loadings (ranging from 10 wt.% to 40 wt.%) was also fabricated with precision.

PXRD patterns pertaining to ZIF-8 CGCMs yield a noteworthy observation, the crystalline ZIF-8 remained remarkably intact even after the rigorous quenching treatment. This intriguing finding demonstrates the absence of any significant structural alterations within ZIF-8 during the melting process (Fig. 2.5b and Fig. A. 6 in Electronic Appendix). In contrast to the scenarios in which flux melting typically occurs, an interesting facet emerges from this study. This peculiarity can be attributed to the low temperature employed for the ZIF-62 melting process. Notably, the synthesis of ZIF-62 involves a mechanochemical approach using nano-ZnO, thereby leading to a comparatively reduced melting temperature.[175] Consequently, the energy available to affect the melting of ZIF-8 crystals via the ZIF-62 flux at the elevated temperature of 409 $^{o}$C is severely limited.

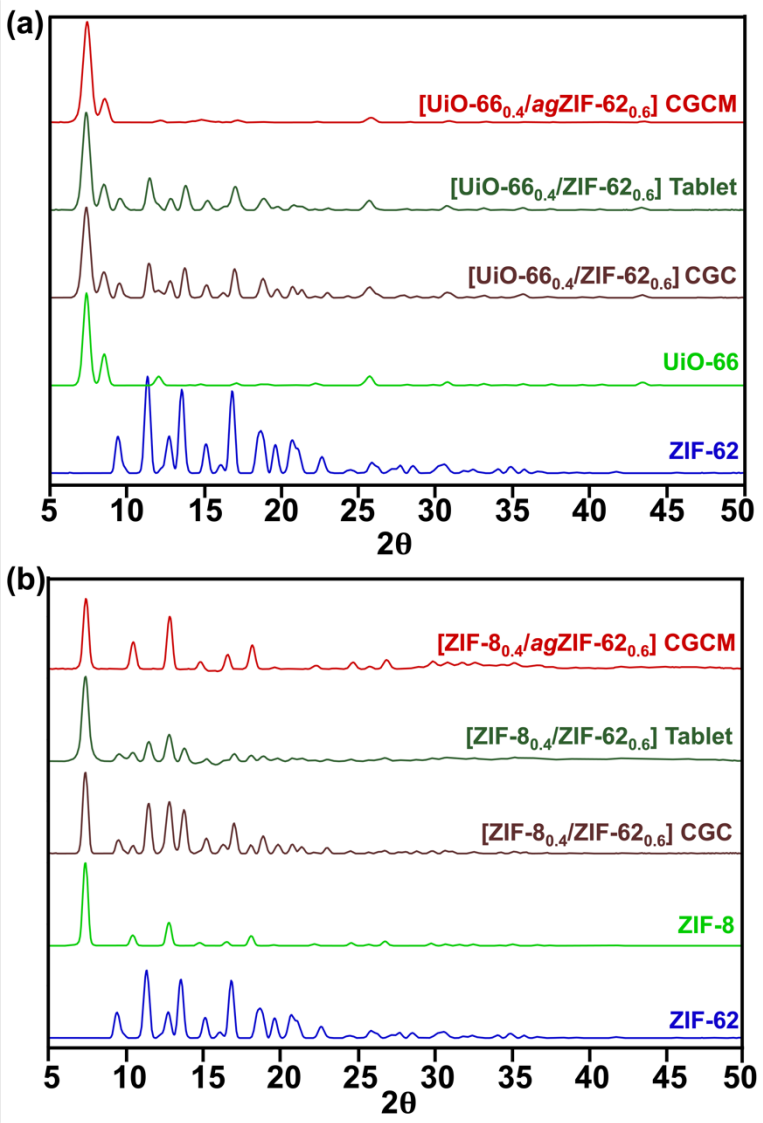


**Figure 2.5** PXRD patterns of (a) ZIF-62, UiO-66, [UiO-66$_{0.4}$/ZIF-62$_{0.6}$] CGC, [UiO-66$_{0.4}$/ZIF-62$_{0.6}$] tablet and [UiO-66$_{0.4}$/*ag*ZIF-62$_{0.6}$] CGCM. (b) ZIF-62, ZIF-8, [ZIF-8$_{0.4}$/ZIF-62$_{0.6}$] CGC, [ZIF-8$_{0.4}$/ZIF-62$_{0.6}$] tablet and [ZIF-8$_{0.4}$/*ag*ZIF-62$_{0.6}$] CGCM.

The exploration of structure disorder within the realm of MOFs presents a captivating avenue of study. MIL-53, a MOF centered around aluminum 1,4-benzenedicarboxylate (BDC) linkers. Distinguished by its three-dimensional framework, MIL-53 boasts corner-sharing $AlO_4(OH)_2$ octahedra, forming an intricate lattice.[176] A remarkable characteristic of MIL-53 is its intrinsic flexibility, exhibiting what is commonly termed as a breath effect. This phenomenon allows MIL-53 to seamlessly transition between distinct states, altering between a configuration with narrow pores (np) and another featuring expanded large pores (lp).[177] Notably, the as-synthesized MIL-53 encapsulates certain $H_2BDC$ ligands within its pore network, and these ligands can be selectively eliminated through controlled thermal

treatment. Consequently, MIL-53-as can undergo a transformation to an open-pore structure that we designate as MIL-53-lp.[178-179] In a fascinating convergence, the manufacturing process of composite membranes offers an opportunity for the integration of MIL-53-lp into the *ag*ZIF-62 matrix (Fig. A. 6a, Electronic Appendix). The structural fidelity of MIL-53-lp within these composite membranes is strikingly evident in the PXRD patterns (Fig. A. 6b, Electronic Appendix), underscoring its sustained existence within the membrane structure (all MIL-53 loading see Fig. A. 7, Electronic Appendix).

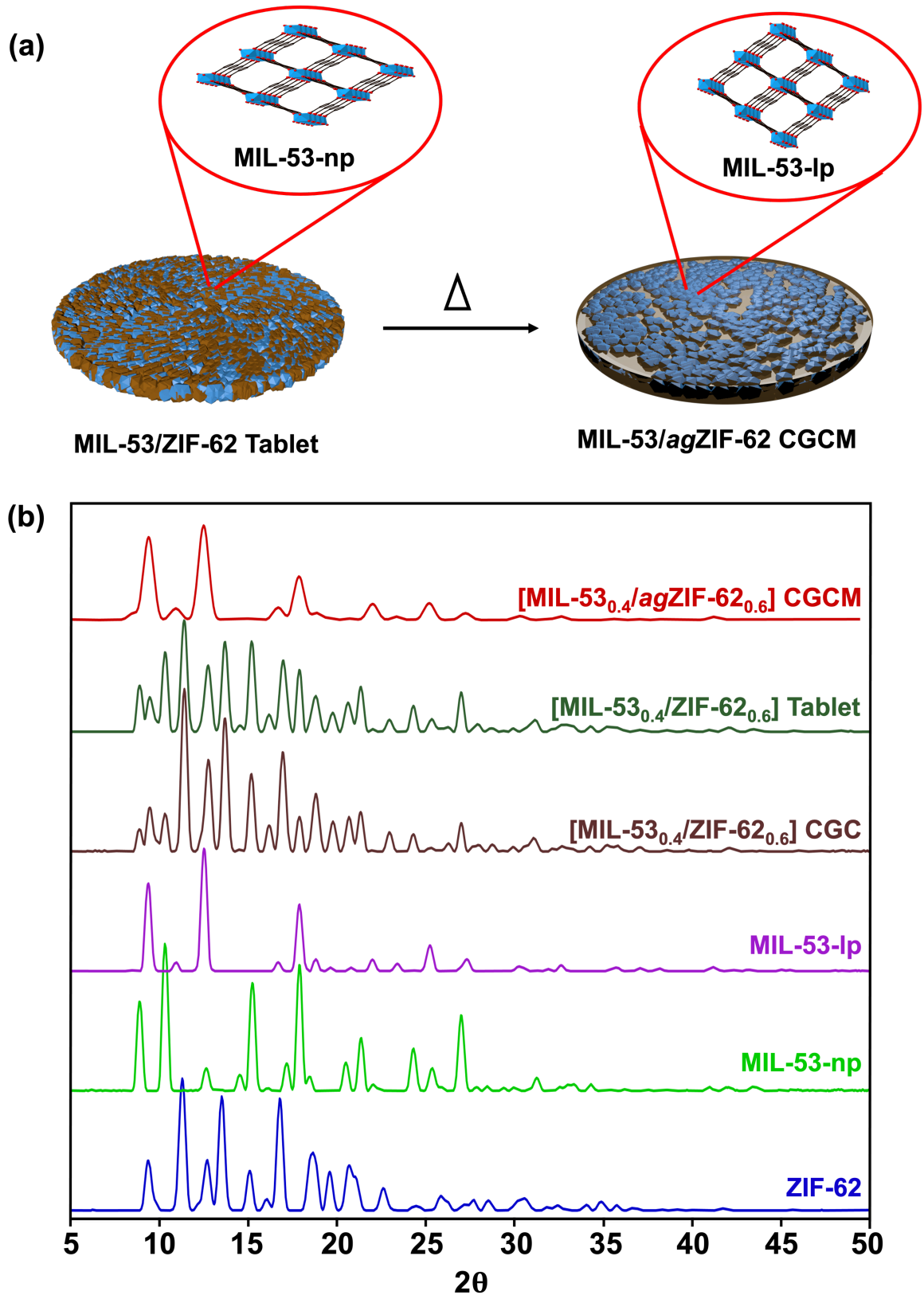


**Figure 2.6** (a) Diagram of the MIL-53 transition in the [MIL-53/*ag*ZIF-62] CGCM. (b) PXRD patterns of ZIF-62, MIL-53-as, MIL-53-lp, [MIL-53$_{0.4}$/ZIF-62$_{0.6}$] CGC, [MIL-53$_{0.4}$/ZIF-62$_{0.6}$] tablet and [MIL-53$_{0.4}$/*ag*ZIF-62$_{0.6}$] CGCM.

Furthermore, in pursuit of enhancing the $CO_2$ separation efficiency of CGCMs, the spotlight turns to a promising MOF, MUF-16. This choice is underpinned by MUF-16's remarkable attributes, including its elevated $CO_2$ adsorption capacity and its exceptional preference for $CO_2$ over other gases.[180] However, MUF-16 is susceptible to decomposition at approximately 350 °C (Fig. A. 8, Electronic Appendix). To prevent MUF-16 decomposition during the vitrification of the ZIF-62 matrix, *pre-formed ag*ZIF-62 was blended with the MUF-16 crystals to produce $(MUF\text{-}16)_x(agZIF\text{-}62)_{1-x}$ (Fig. 2.7a). This union can be achieved by subjecting the *ag*ZIF-62 matrix is then gently re-melted at a relatively low temperature of 330 °C. The final membranes are recorded as [$MUF\text{-}16_x/agZIF\text{-}62_{1-x}$] CGCM, signifying the composite membranes that stand as a statement to this amalgamation. Evidently, the crystalline nature of MUF-16 is preserved after the re-melting process (Fig. 2.7b and Fig. A. 9, Electronic Appendix) and no interfacial voids are present (Fig. A. 23, Electronic Appendix). This strategy produces ideal MUF-16 CGCMs.

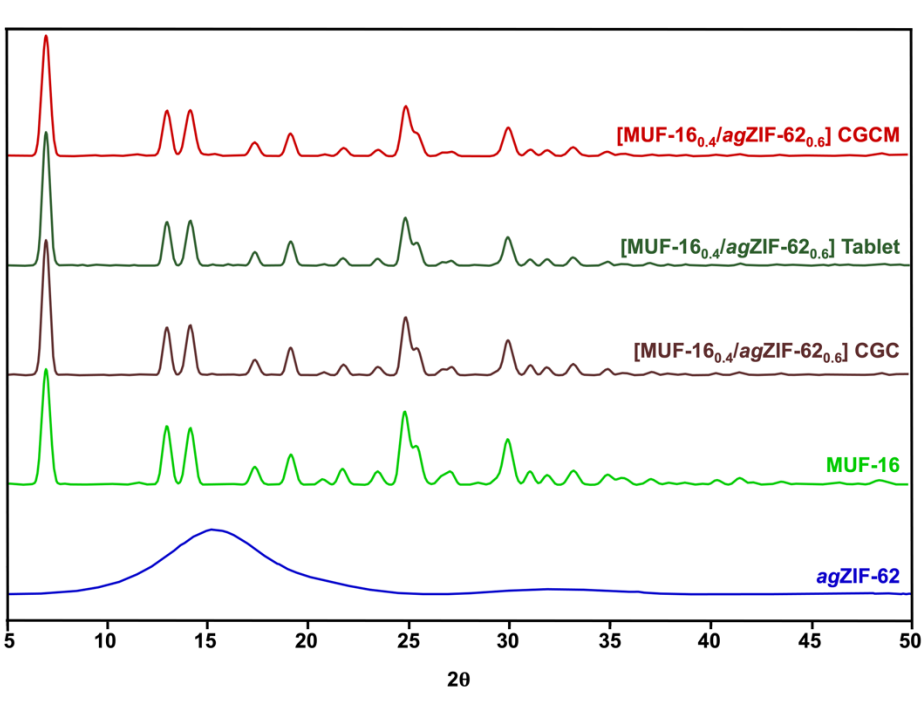


**Figure 2.7** (a) PXRD patterns of (a) *ag*ZIF-62, MUF-16, [$MUF\text{-}16_{0.4}/agZIF\text{-}62_{0.6}$] CGC, [$MUF\text{-}16_{0.4}/ZIF\text{-}62_{0.6}$] CGC tablet and [$MUF\text{-}16_{0.4}/agZIF\text{-}62_{0.6}$] CGCM.

### FTIR spectra of CGCMs

The FTIR spectrum (Fig. 2.8a) of *ag*ZIF-62 displays almost the same intermolecular vibrations as its crystalline counterpart, indicating the unchanged integrity of its organic linkers following the melt-quenching procedure. Notably, the $(UiO\text{-}66)_{0.4}(ZIF\text{-}62)_{0.6}$ tablet interweaves the vibrational signatures of both UiO-66 and ZIF-62 (Fig. 2.8a and Fig. A. 10,

Electronic Appendix). Impressively, no discernible peak shift occurs, affirming the absence of any newly-formed chemical bonds. Furthermore, the unchanged peak profiles within [UiO-66$_{0.4}$/*ag*ZIF-62$_{0.6}$] CGCM indicate the stability of organic linkers. These patterns of structural robustness extend to other CGCMs as well. [ZIF-8$_{0.4}$/*ag*ZIF-62$_{0.6}$] and [MIL-53$_{0.4}$/*ag*ZIF-62$_{0.6}$] CGCMs, along with the MUF-16 CGCMs, display the unchanged FTIR spectra (Figs. 2.8b to 2.8d, and Figs. A. 11 to A. 13, Electronic Appendix). This collective fidelity further reaffirms that the intricate membrane fabrication process leaves the chemical compositions and structures unaltered, resulting in a series of composite membranes to meet the demands of their resulting gas separation performances.

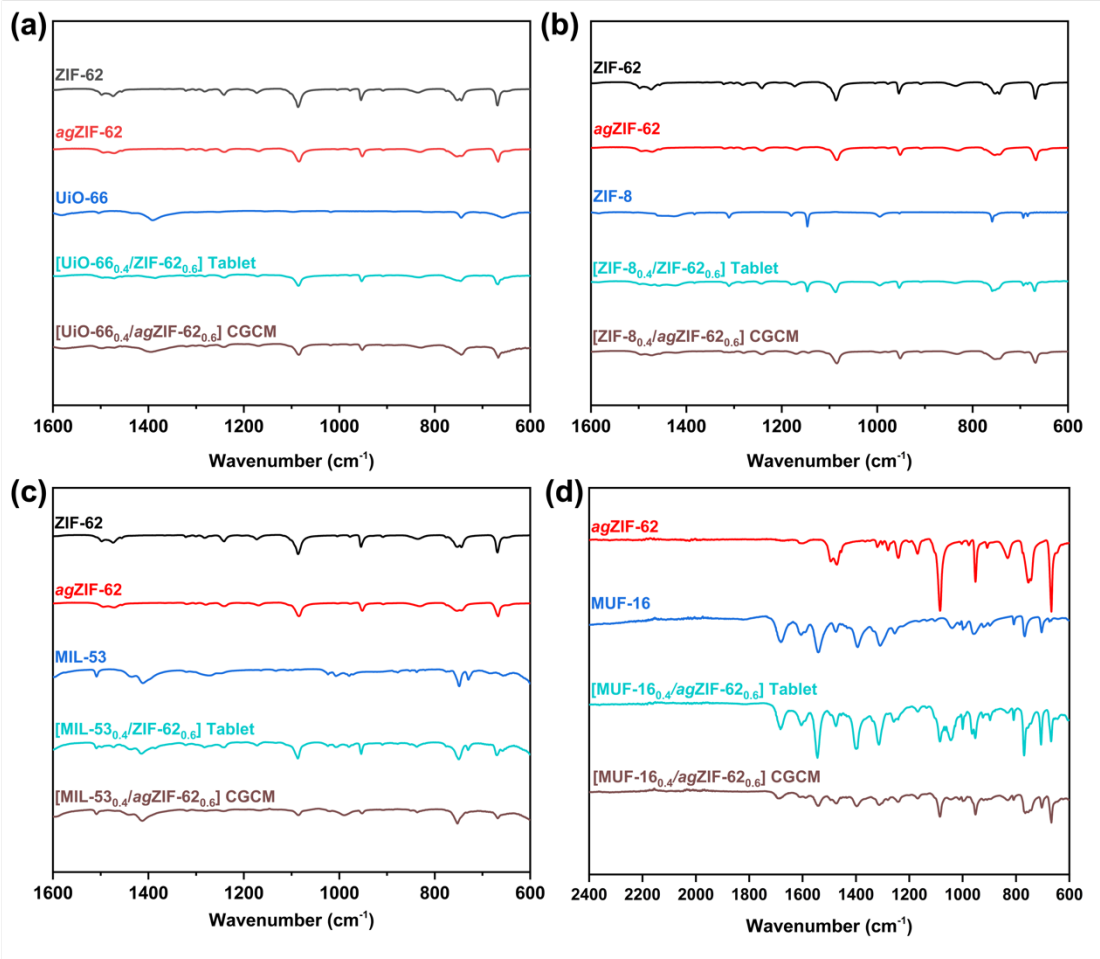


**Figure 2.8** FTIR spectra of (a) [UiO-66)$_{0.4}$/agZIF-62$_{0.6}$], (b) [ZIF-8$_{0.4}$/*ag*ZIF-62$_{0.6}$], (c) [MIL-53$_{0.4}$/ZIF-62$_{0.6}$] and (d) [MUF-16$_{0.4}$/*ag*ZIF-62$_{0.6}$] CGCM.

**TGA curves of crystal-glass composites (CGCs)**

For (UiO-66)$_x$(ZIF-62)$_{1-x}$ composite, a mass loss at around 250 °C was caused by the removal of strongly adsorbed DMF within ZIF-62 pores (Fig. 2.9). A key issue is that all (UiO-66)$_x$(ZIF-62)$_{1-x}$ CGCs display the good stability up to around 500 °C, ensuring the integrity of UiO-66 within the resulting *ag*ZIF-62 matrix. Similarly, ZIF-8 and MIL-53

CGCMs show the similar trend (Figs. A. 14 and A. 15, Electronic Appendix). Moreover, MUF-16 can be decomposed at 350 °C, so it was first mixed with *ag*ZIF-62 to produce a tablet and then *ag*ZIF-62 could be remelted at a low temperature (330 °C), which could confer the stability in the resulting membrane (Fig. A. 16, Electronic Appendix).

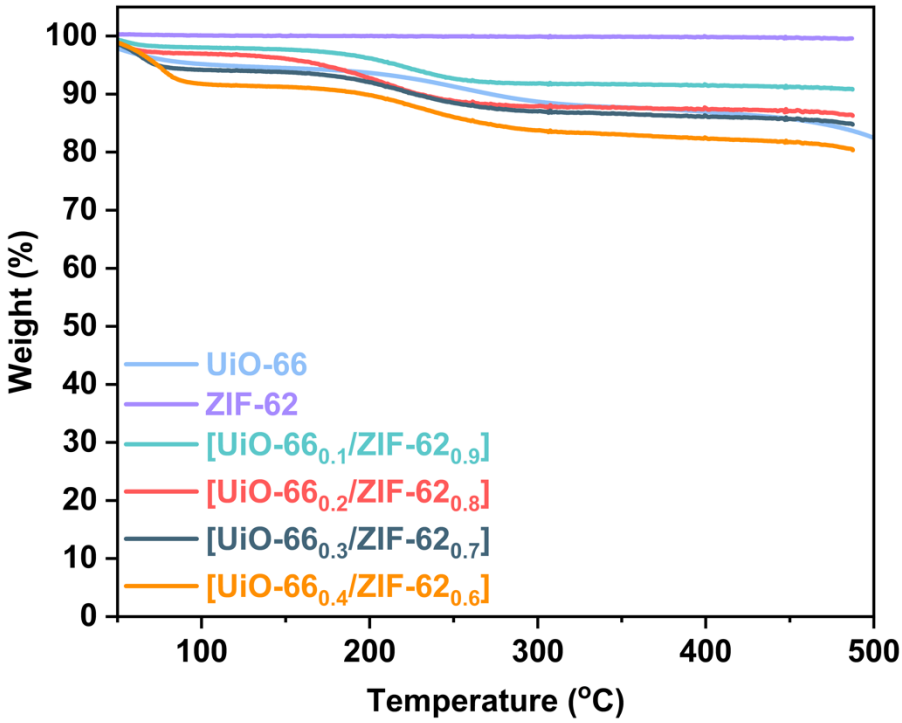


**Figure 2.9** TGA curves of [UiO-66$_x$/ZIF-62$_{1-x}$] CGCs.

**DSC curves of CGCs**

During the second DSC scan, the distinct *Tg* shift can be observed across the different CGCMs. This *Tg* variation provides a tangible understanding of the inherent glassy nature of these membranes with different crystal loadings. The incorporation of crystals, including UiO-66 (Fig. 2.10), ZIF-8 (Fig. A. 17, Electronic Appendix), and MIL-53 (Fig. A. 18, Electronic Appendix), introduces an intriguing interplay within the *ag*ZIF-62 matrix and consequently leads to the increased *Tg* along with their crystal loadings. Similarly, the incorporation of MUF-16 also yields a comparable outcome, resulting in an indelible increase in *Tg* (Fig. A. 19, Electronic Appendix). These collective observations highlight the complex interplay between the incorporated crystals and *ag*ZIF-62, which ultimately determines the thermal behavior of the resulting composite membranes.

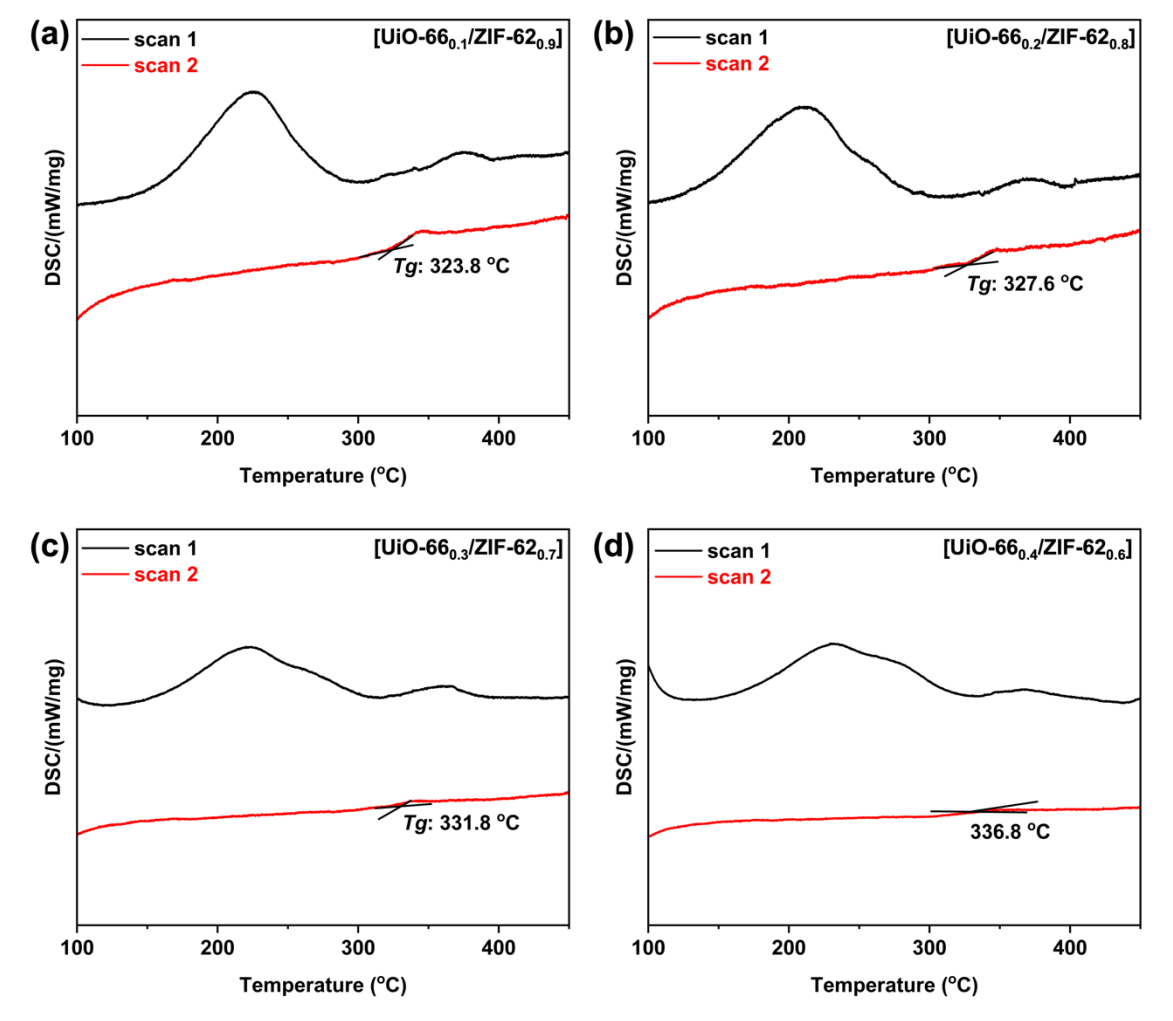


**Figure 2.10** DSC curves of (a) $(UiO\text{-}66)_{0.1}(ZIF\text{-}62)_{0.9}$, (b) $(UiO\text{-}66)_{0.2}(ZIF\text{-}62)_{0.8}$, (c) $(UiO\text{-}66)_{0.3}(ZIF\text{-}62)_{0.7}$ and (d) $(UiO\text{-}66)_{0.4}(ZIF\text{-}62)_{0.6}$ CGC.

### SEM morphologies of *ag*ZIF-62 membrane

In terms of membrane morphology, a visual assessment of the SEM images of MOF composite tablets prior to the heating process displays the pronounced gaps, cracks, and pinholes that highlight the initial state of the composite. Prior to the melting process, the cross-sectional morphology of the pure ZIF-62 tablet shows visible cracks, which is a direct consequence of the inherent grain boundaries and crystalline structure of the polycrystalline ZIF-62 crystals (Figs. 2.11a and 2.11b). Throughout the heating treatment, the molten ZIF-62 infiltrates the interstices of the polycrystalline voids and acts as a unifying agent bridging the gaps (Figs. 2.11c and 2.11d). Upon the subsequent cooling to ambient temperature, a well-integrated *ag*ZIF-62 membrane was formed with encapsulation of the structural cohesion. Therefore, this continuous *ag*ZIF-62 membrane is promising to achieve good separation performance.

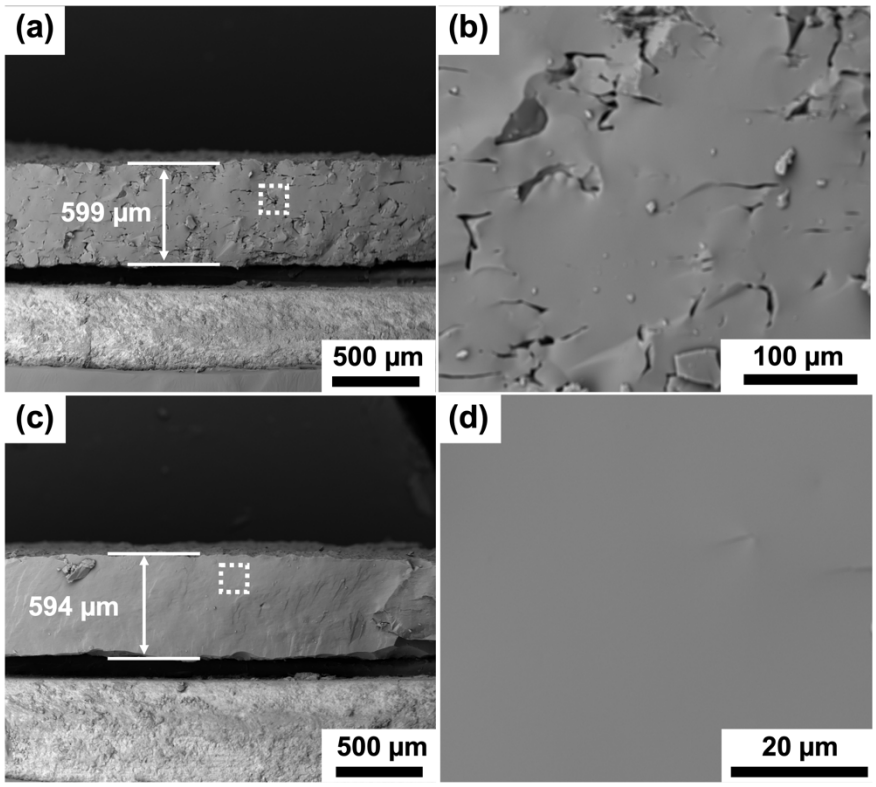


**Figure 2.11** Cross-sectional morphology of (a) pressed ZIF-62 tablet and (b) high resolution image of the white box in ZIF-62 tablet. Cross-sectional morphology of (c) *ag*ZIF-62 membrane and (d) high resolution image of the white box in *ag*ZIF-62 membrane.

**SEM morphologies of UiO-66 CGCM**

UiO-66 CGCMs reveal an excellent integrity without observable crystalline boundaries or unfavorable morphological traits even after undergoing vitrification. Moreover, there is no major difference between the UiO-66 CGCMs when the loading is increased from 10 wt.% to 30 wt.% and even up to 40 wt.% (Figs. 2.12a to 2.12d). This uniformity can be attributed to the small particle size of UiO-66 (Fig. 2.3b). This remarkable observation is supported by the analysis of the cross-sectional elemental distribution, which clearly confirms the uniform distribution of UiO-66 within the *ag*ZIF-62 phase (Fig. A. 20, Electronic Appendix). By preserving the crystalline essence of UiO-66 through integration with *ag*ZIF-62, the formation of interfacial voids between the crystals and *ag*ZIF-62 is judiciously minimized. This intricate interplay allows for the optimal gas separation performance that occurs with other CGCM counterparts. These results fit into the broader landscape of CGCM research and suggest the durability and potential of these innovative composites.

Moreover, SEM morphologies of other CGCMs with ZIF-8, MIL-53 and MUF-16 are shown in Figs. A. 21 to A. 23 (Electronic Appendix). And the Optical photographs the prepared CGCMs with UiO-66, ZIF-8, MIL-53, and MUF-16 are shown in Figs. A. 24 to A. 27 (Electronic Appendix).

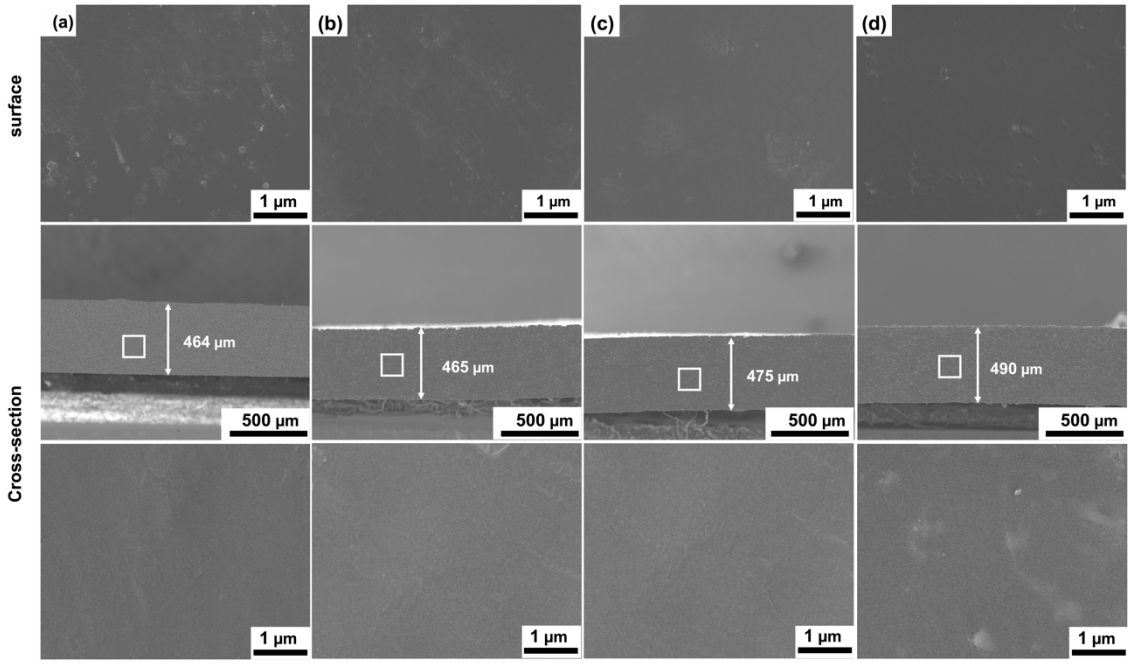


**Figure 2.12** Surface and cross-sectional SEM images of [UiO-$66_x$/*ag*ZIF-$62_{1-x}$] CGCMs with different loadings (a) 10 wt.%, (b) 20 wt.%, (c) 30 wt.% and (d) 40 wt.%. The corresponding high resolution cross-sectional SEM images from the white box are included.

**HR-TEM images of UiO-66 CGCM**

High resolution transmission electron microscopy (HR-TEM) of [UiO-$66_{0.4}$/ZIF-$62_{0.6}$] CGCM shows the lattice stripes of crystalline phase of UiO-66 in the white box regions (Fig. 2.13a). While most of the remaining regions tend to be amorphous, indicating its disordered state caused by glass transformation. And the crystal plane spacing (d = 3.49 Å) corresponds to (6,0,0) spacing for UiO-66. Importantly, the integrated structure in this region displays no interfacial voids between the crystalline UiO-66 phase and the amorphous glass phase. In addition, the [UiO-$66_{0.4}$/*ag*ZIF-$62_{0.6}$] CGCM was detected by energy dispersive X-ray (EDX) mapping to verify the distribution of crystalline UiO-66 in the glass phase, both Zn and Zr elements can be uniformly observed in the target region, demonstrating the homogeneous distribution of UiO-66 in the glass matrix (Fig. 2.13b). It is notable that these observations likely to extend their validity to other CGCMs within the study, underlining a consistent

pattern of structural soundness across the materials examined (Figs. A. 28 to A. 30, Electronic Appendix).

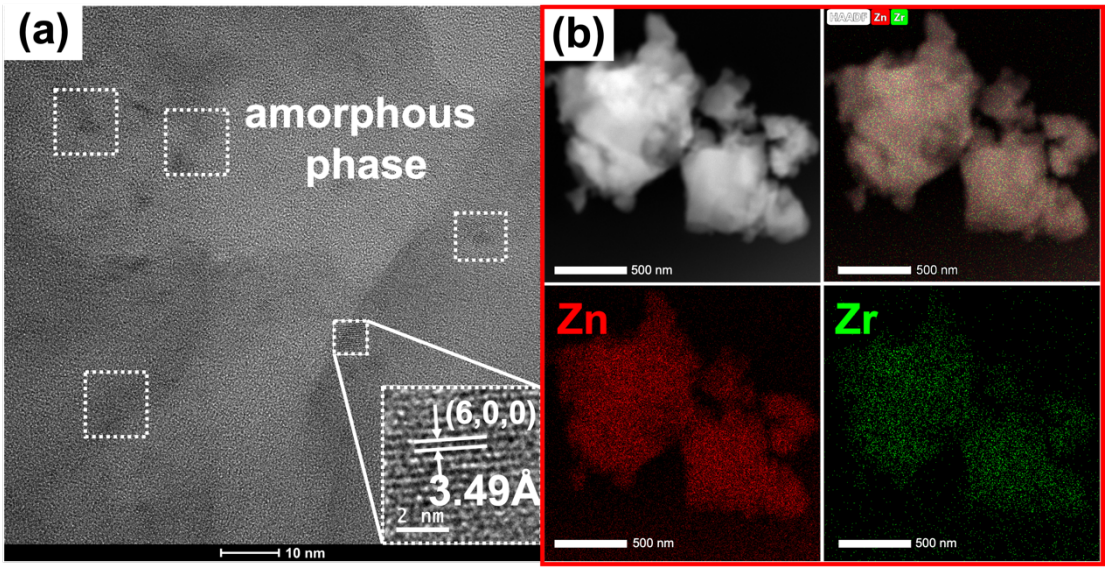


**Figure 2.13** (a) HR-TEM images of [UiO-66$_{0.4}$/*ag*ZIF-62$_{0.6}$] CGCM, the yellow dashed boxes show the crystal phase, and the other regions are the amorphous phase. And the crystal plane spacing d = 3.49 Å, corresponding to (6,0,0) spacing for UiO-66. (b) EDX mapping of Zn and Zr in [UiO-66$_{0.4}$/*ag*ZIF-62$_{0.6}$] CGCM.

### 2.2.5 Gas adsorption isotherms and IAST selectivity

The adsorption isotherms of *ag*ZIF-62 for $CO_2$ and $N_2$ illustrate the preservation of its microporosity following the quenching treatment (Fig. 2.14a, Table A. 5 in Electronic Appendix). At 293 K and 1 bar, the gas adsorption capacities for $CO_2$ and $N_2$ for *ag*ZIF-62 stand at 11.3 and 1.2 $cm^3/g$ respectively. For [UiO-66$_x$/*ag*ZIF-62$_{1-x}$] CGCMs, compared with to pure *ag*ZIF-62 membrane, as the UiO-66 loading increases, the adsorption capacity of all gases $CO_2$ and $N_2$ all increased. The doping of UiO-66 crystals into *ag*ZIF-62 matrix could improve the adsorption capacity (Figs. 2.14c to 2.14f, Table A. 5 in Electronic Appendix). This enhancement in $CO_2$ uptake also carries the potential to confer a heightened $CO_2$ permeance compared to that of the pure *ag*ZIF-62 membrane.

Interestingly, a similar trend can be observed in all ZIF-8, MIL-53, and MUF-16 CGCMs (Figs. A. 31 to A. 33, Tables A. 6 to A. 8 in Electronic Appendix). These observations further hold potential for manufacturing CGCMs that are not only adept at gas adsorption but also exhibit promise for the efficient separation of $CO_2$.

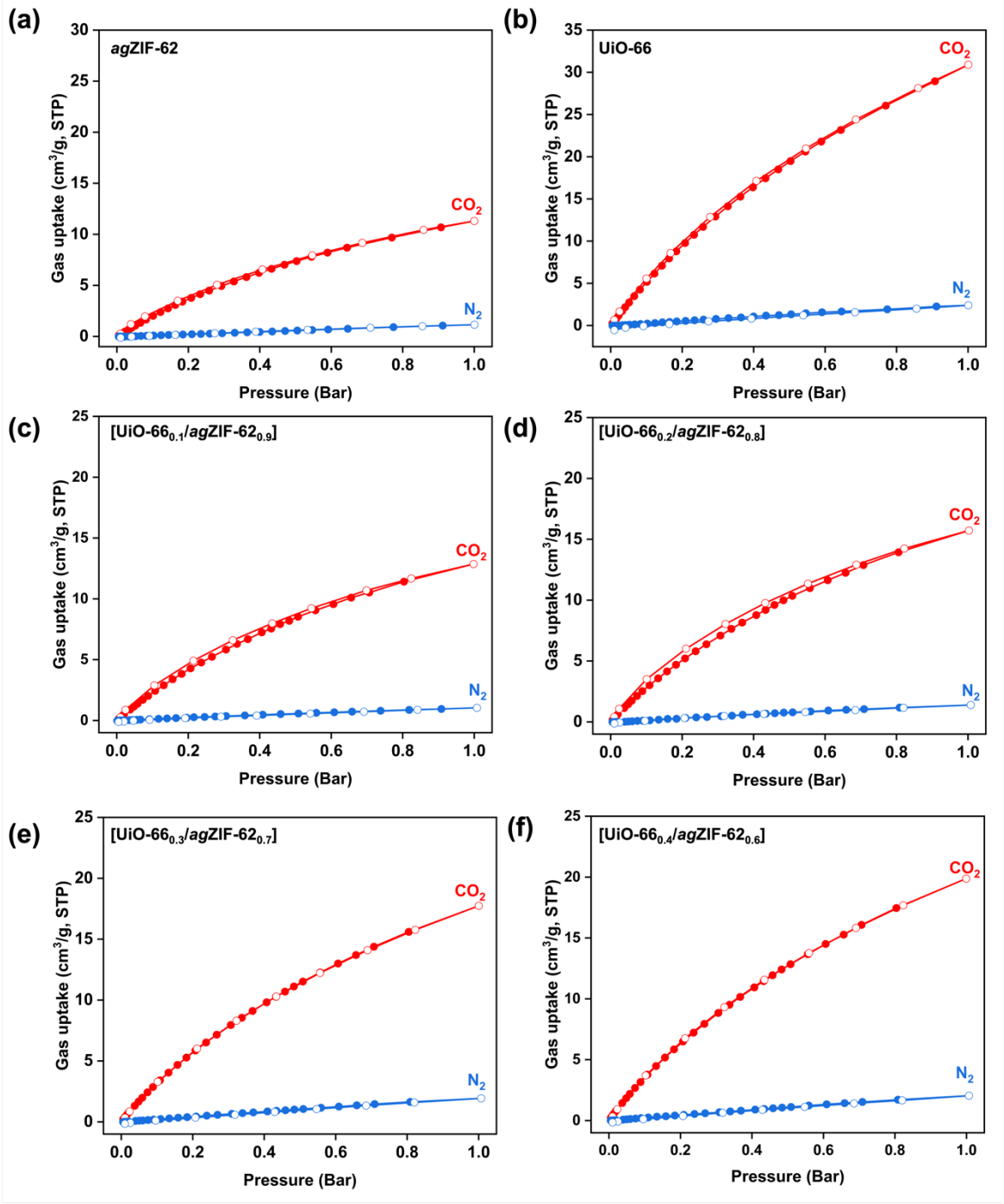


**Figure 2.14** $CO_2$ and $N_2$ adsorption (filled circles) and desorption (open circles) isotherms of (a) *ag*ZIF-62, (b) UiO-66, (c) [UiO-66$_{0.1}$/*ag*ZIF-62$_{0.9}$] CGCM, (d) [UiO-66$_{0.2}$/*ag*ZIF-62$_{0.8}$] CGCM, (e) [UiO-66$_{0.3}$/*ag*ZIF-62$_{0.7}$] CGCM and (f) [UiO-66$_{0.4}$/*ag*ZIF-62$_{0.6}$] CGCM at 293K.

Ideal Adsorbed Solution Theory (IAST) selectivities at 1 bar of the UiO-66 CGCMs (Fig. 2.15a, Table A. 5 in Electronic Appendix) were performed using adsorption isotherms at 293 K. Notably, the results showed increased selectivities in $CO_2/N_2$ binary mixtures (50/50). In

addition, the IAST results on ZIF-8 (Fig. 2.15b, Table A. 6 in Electronic Appendix) and MIL-53 (Fig. 2.15c, Table A. 7 in Electronic Appendix) CGCMs demonstrated their significant efficiency in favoring $CO_2$ separation. MUF-16 CGCMs also exhibited the commendable $CO_2$ selectivity, which is attributed to their porous structure which facilitates the higher $CO_2$ adsorption capacity than $N_2$ (Fig. 2.15d, Table A. 8 in Electronic Appendix).

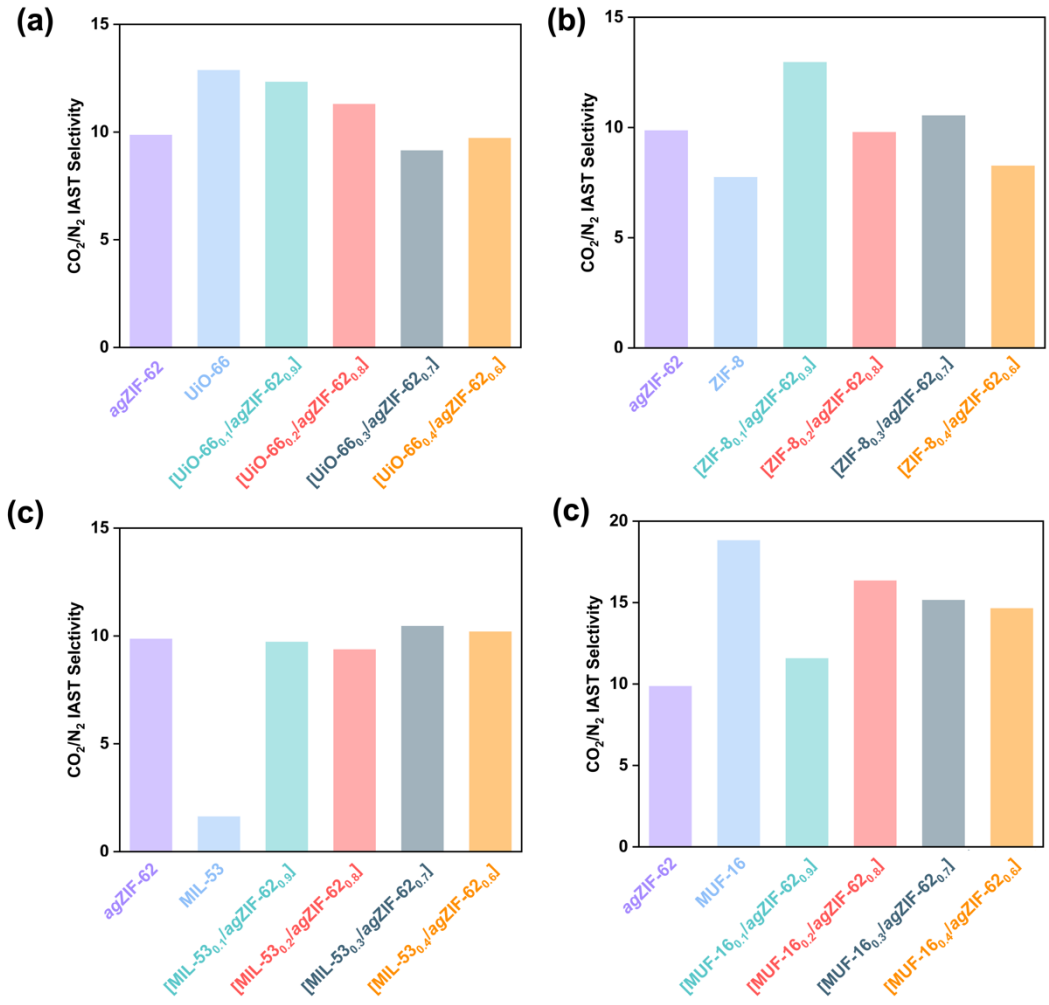


**Figure 2.15** $CO_2/N_2$ (50/50) IAST selectivity of (a) [UiO-66$_x$/*ag*ZIF-62$_{1-x}$], (b) [ZIF-8$_x$/*ag*ZIF-62$_{1-x}$], (c) [MIL-53$_x$/*ag*ZIF-62$_{1-x}$] and (d) [MUF-16$_x$/*ag*ZIF-62$_{1-x}$] CGCMs at 293 K under 1 bar.

### 2.2.6 Pore volume and pore size distribution analysis

To characterize the micropores and their corresponding pore size distribution, adsorption isotherm curves of CGCMs were carried out. These curves were derived from the analysis of $CO_2$ adsorption isotherms at 273 K using the utilization of the Non-local Density Functional Theory (NLDFT) method. As the UiO-66 loading within the CGCMs increased,

a notable enhancement in both $CO_2$ uptake (Fig. 2.16a) and total micropore volume (Fig. 2.16b, Table A. 9 in Electronic Appendix) was observed. The increased pore volume demonstrates the porous nature of UiO-66 CGCMs and have the potential for efficient separation. Notably, all UiO-66 CGCMs showed the main micropore of approximately 5.2 Å in diameter, the constancy of this pore size across the various CGCMs suggests the robustness of membranes amidst the evolving UiO-66 content. In addition, when compared to pure *ag*ZIF-62 membrane, the pore volume around 3.8 Å and 9.4 Å remained relatively consistent, further indicating the stability of pore structure of UiO-66 CGCMs

In addition, ZIF-8, MIL-53, and MUF-16 CGCMs display a similar trend of increased pore volume and a consistent pore width of 5.3 Å (Fig. A. 34, Table A. 10 in Electronic Appendix), 5.7 Å (Fig. A. 35, Table A. 11 in Electronic Appendix), and 3.6 Å (Fig. A. 36, Table A. 12 in Electronic Appendix), respectively. These results indicate that the embedded MOF crystals within the glass matrix could form the continuous porosity and thus improving the improve the gas storage capability.

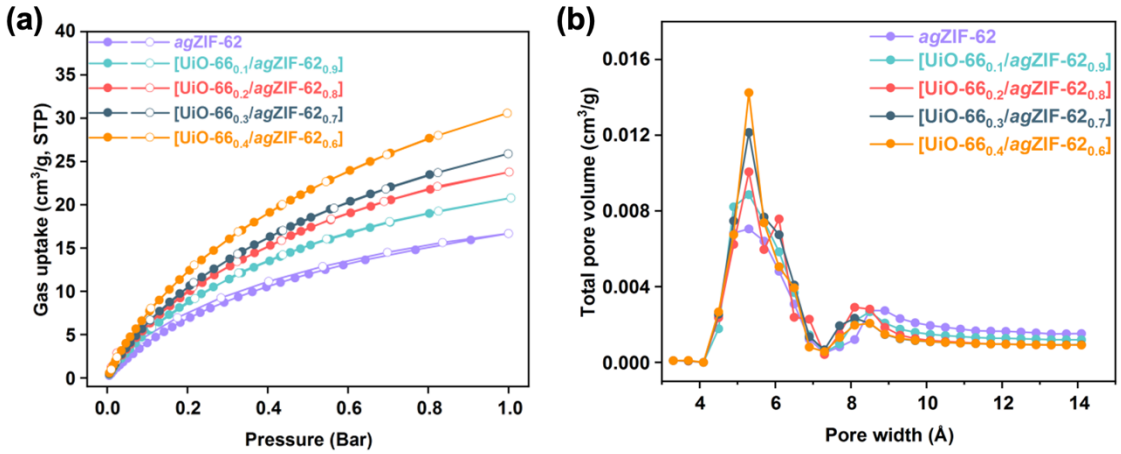


**Figure 2.16** (a) $CO_2$ adsorption–desorption isothermal curves of *ag*ZIF-62 and UiO-66 CGCMs at 273 K. (b) Micropore size distribution of *ag*ZIF-62 and UiO-66 CGCMs calculated by the NLDFT method using $CO_2$ adsorption isotherm curves.

### 2.2.7 Gas permeation tests

The gas permeation properties of as-fabricated CGCMs were evaluated using the Wicke–Kallenbach method.[115] For the single gas permeation test, all UiO-66 CGCMs displayed the ultrahigh gas permeance (Fig. 2.17a, Table A. 13 in Electronic Appendix). With the increase of UiO-66 loading in membrane, the corresponding $CO_2$ permeance increased, which is mainly caused by the increased pore volume of the membranes. In this way, the gas transport

and diffusion could be enhanced. In addition to the adsorption differences between $CO_2$ and $N_2$, the enhancement in ideal selectivity of $CO_2/N_2$ could be observed. When the loading of UiO-66 is 40 wt.%, the ideal selectivity value of $CO_2/N_2$ is 4.7, exceeding their corresponding Knudsen selectivity value (0.80), which are determined by the inverse of the square root of the molecular masses. This result suggests the UiO-66 CGCMs have the potential for $CO_2$ separation. And the mixed gas permeation test (50/50) of [UiO-$66_{0.4}$/ZIF-$62_{0.6}$] CGCM shows the slightly lower gas permeance than pure gas permeance (Fig. 2.17b, Table A. 17 in Electronic Appendix), which is mainly due to the competitive adsorption of mixed gases.

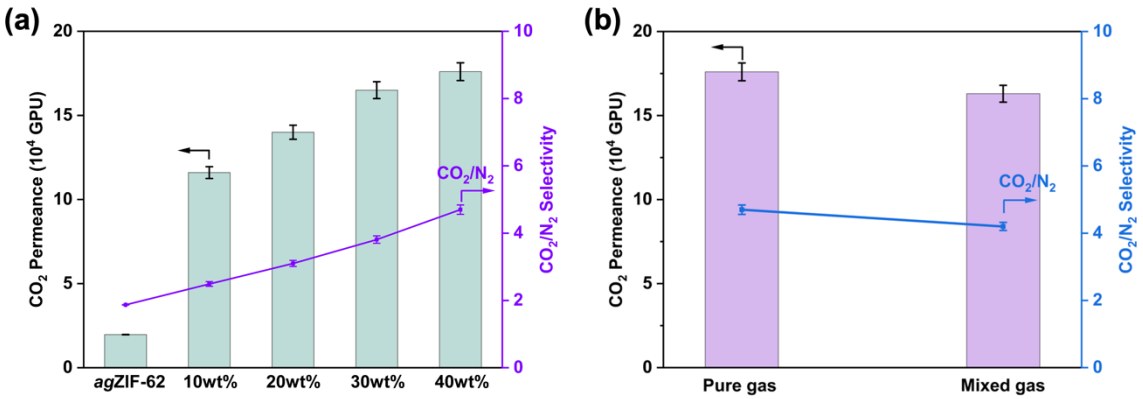


**Figure 2.17** Gas permeance and selectivity results of (a) [UiO-$66_x$/*ag*ZIF-$62_{1-x}$] CGCMs and (b) comparison of single gas and mixed gas test of [UiO-$66_{0.4}$/*ag*ZIF-$62_{0.6}$] CGCMs (1 bar, room temperature).

For ZIF-8 CGCMs, the main pore width is close to that of UiO-66 CGCMs, the separation results of ZIF-8 CGCMs demonstrates the similar trend of increased gas permeance and selectivity values as UiO-66 CGCMs (Fig. 2.18a, Table A. 14, Electronic Appendix). ZIF-8 crystals in membrane could provide gas transport channels, when its loading reaches 40 wt.%, the corresponding membrane displayed the ideal selectivity of $CO_2/N_2$ is 5.4. This is probably due to the aperture size of ZIF-8 (3.4 Å), which plays a certain role in sieving effect for $N_2$.[181]

It should be noted that MIL-53 is present in the membranes with large pores, the resulting membranes show the consistent pore width (5.7 Å) and increased pore volume with the increased MIL-53 loading. The pore size in MIL-53 CGCMs is larger than that of UiO-66 (5.2 Å) and ZIF-8 CGCMs (5.3 Å). Therefore, MIL-53 CGCMs show the increased $CO_2$ permeance, while the corresponding ideal $CO_2/N_2$ selectivities are lower than those of UiO-66 and ZIF-8 CGCMs (Fig. 2.18b, Table A. 15 in Electronic Appendix). In addition, the

mixed gas permeance and $CO_2/N_2$ selectivity of all CGCM with 40 wt.% MOF loading are shown in Table A. 17 (Electronic Appendix).

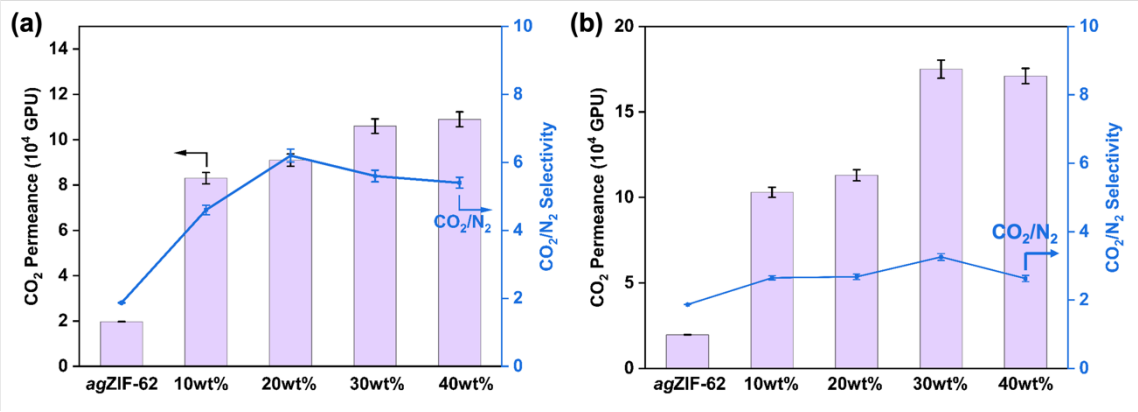


**Figure 2.18** Gas permeance and selectivity results of (a) [ZIF-$8_x$/*ag*ZIF-$62_{1-x}$] CGCMs and (b) [MIL-$53_x$/*ag*ZIF-$62_{1-x}$] CGCMs (1 bar, room temperature).

MUF-16, known for its exceptional $CO_2$ separation capabilities, presenting an exciting opportunity to engineer membranes with enhanced $CO_2/N_2$ and $CO_2/CH_4$ selectivities. As anticipated, MUF-16 CGCMs have demonstrated the higher selectivity than the previously reported counterparts. With increasing MUF-16 loading in the membrane increased, a corresponding rise in the pore volume of the membranes could be observed (Fig. A. 36a, Electronic Appendix). It is notable that the pore volume at the width of 3.6 Å also increased and exhibits greater values than the pore of around 5.2 Å (Fig. A. 36b, Electronic Appendix). This distinctive 3.6 Å pore, attributed to MUF-16, has the potential to facilitate $CO_2$ transport due to its strong adsorption capability for $CO_2$.[180] At the same time, MUF-16 barely absorbs either $N_2$ and $CH_4$. Consequently, a clear cut-off effect for $CO_2$ versus $N_2$ and $CH_4$ molecules becomes evident in [MUF-$16_x$/*ag*ZIF-$62_{1-x}$] CGCMs. As a result, the $CO_2/N_2$ selectivity of MUF-16 CGCMs increased with the increasing MUF-16 loading. When the loading of MUF-16 is 40 wt.%, the corresponding ideal selectivities reached 5.7 for $CO_2/N_2$ (Fig. 2.19, Table A. 16 in Electronic Appendix). Overall, all CGCMs in this work display enhanced $CO_2$ permeance compared to the pure *ag*ZIF-62 membrane ($CO_2$ permeance: 19700 GPU).

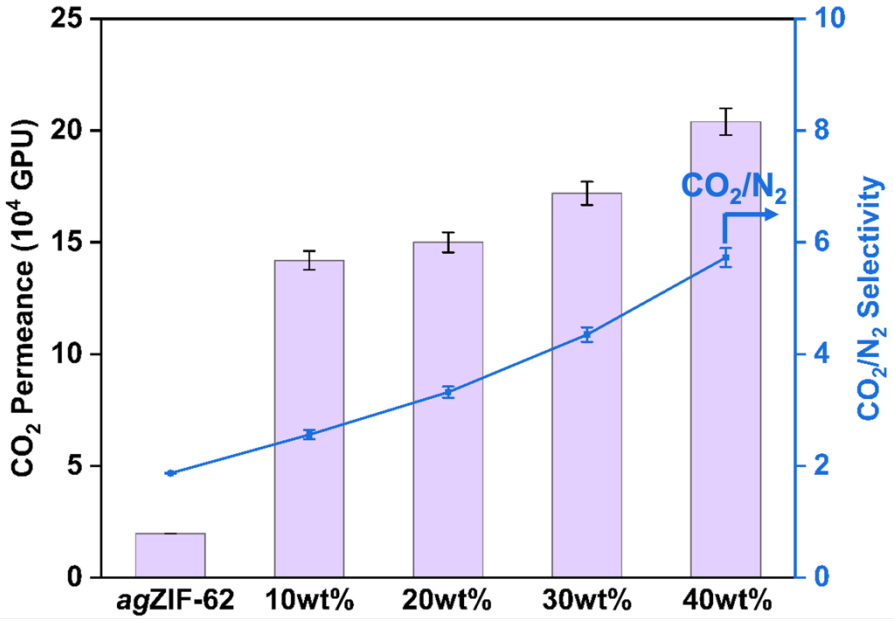


**Figure 2.19** Gas permeance and ideal selectivity results of [MUF-16$_x$/*ag*ZIF-62$_{1-x}$] CGCM (1 bar, room temperature).

## 2.3 Conclusion

In this study, we have successfully fabricated a series of CGCMs with different loadings of crystalline MOF derived from diverse metal precursors integrated into the *ag*ZIF-62 matrix through the glass transition treatment. And these MOF crystals with different crystal size in the membranes show the excellent interfacial combability, which retain their crystalline porosities and ensure efficient gas transport. [ZIF-8$_{0.4}$/ZIF-62$_{0.6}$] CGCM display a high $CO_2$ permeance of 109000 GPU, and selectivity of $CO_2/N_2$ (5.4). In addition, we also developed the remelting process at a lower temperature to fabricate CGCM, which could preserve MUF-16, which is not stable at high temperatures. Here, the resulting [MUF-16$_{0.4}$/*ag*ZIF-62$_{0.6}$] CGCM displays the high $CO_2$ permeance of 204000 GPU, and good selectivity of $CO_2/N_2$ (5.7). This work provides a practical approach for the preparation of high-performance membranes and broadens the application of glassy materials for the development of multifunctional CGCMs.

# Chapter 3 MUF-16/Pebax Mixed Matrix Membranes for $CO_2$ Separation

## 3.1 Introduction

As the primary greenhouse gas, the escalating emissions of $CO_2$ are giving rise to significant environmental challenges.[182-184] Nowadays, growing concerns about global warming and the demand for clean energy have driven researchers to seek effective ways to capture $CO_2$ from other gases such as $N_2$ and $CH_4$.[185-186] Membrane separation technology, with its low capital cost and energy consumption compared to traditional separation approaches, has potential for economic and environmentally friendly $CO_2$ capture.[187-188] Notably, polymeric materials dominate the commercial membrane market due to their comparatively low cost, ease of scale-up, and their applicability to complex gas-pair separations.[189-190] However, polymeric gas separation membranes face a trade-off between permeability and selectivity, i.e. high gas permeability correlates with low selectivity and vice versa.[71-72] To overcome this limitation, the development of MMMs is considered the most promising method and has emerged as the research hotspot for gas separation membranes.[49, 191] By combining the processability and mechanical properties of the polymer matrix with the high separation performance of the filler particles, MMMs offer a synergistic effect of enhanced permeability, while maintaining excellent separation selectivity. MMMs can overcome the trade-off barrier by creating nanochannels with improved separation properties that transcend the Robeson upper bound.

To date, various filler particles, primarily MOFs,[162, 192] zeolites,[193-194] COFs,[195-196] and other 2D materials [197-198] have been used in the preparation of MMMs. Among the numerous filler particles, MOFs are the most promising due to their exceptional porosity, high modularity, and diverse functionalities.[74] The MOF-incorporated MMMs have attracted considerable attentions in recent research due to their potential for the separation of important gas pairs. For example, Jin and co-workers used polyimide-based MMMs incorporating M-gallate MOF particles (where M represents Ni, Co, or Mg) to achieve highly efficient separation of $C_2H_4/C_2H_6$ gas pairs, exceeding the upper bound limit of pure polymer membranes.[199] Jiang et al. prepared MMMs by adding amino-functionalized ZIF-7 to a matrix of polymers with intrinsic microporosity (PIM-1). The nano-sized ZIF-7-$NH_2$ exhibited strong interfacial affinity to the polymers,[200] and the $CO_2/CH_4$ selectivity of the fabricated MMMs was significantly improved.

However, the challenge is to fully exploit the advantages and realize the full potential of MMMs. Despite the potential of MMMs to provide exceptional gas separation performance,

poor compatibility between the polymer matrix and the MOF fillers can lead to the formation of non-selective defects or voids at their interface, which significantly reduce the separation selectivity. To address this problem, efforts have been made to improve MOF-polymer compatibility via crystal engineering or polymer modification. Zhu et al. reported a fabrication strategy for UiO-66-CN@sPIM-1 MMMs to enhance $CO_2$ capture efficiency. To achieve this, they converted -$NH_2$ to -CN groups in the UiO-66 backbone, resulting in improved compatibility between the polymer and MOF components. The experimental results revealed an exceptionally high $CO_2$ permeability (22665 Barrer) and favourable $CO_2/N_2$ selectivity (29.6) compared to a pure PIM-1 membrane ($CO_2$ permeability = 15433.4 Barrer and $CO_2/N_2$ = 24.6).[201] Smith et al. developed a method to construct defect-free MMMs with uniform particle dispersion by functionalizing the surface of UiO-66-$NH_2$ filler with a polyimide chain,[202] which increased $CO_2$ permeability and $CO_2/CH_4$ selectivity by 48 % and 15 %, respectively.

In addition to improving the interface affinity between filler and polymer, the incorporation of novel MOFs with a high affinity for $CO_2$ represents a promising approach to enhance the $CO_2$ selectivity of MMMs. MUF-15 (MUF = Massey University Framework), [$Co_3(\mu_3\text{-}OH)(ipa)_{2.5}(H_2O)$]), exhibited exceptional performance in discriminating $CO_2$ from $N_2$. It had been incorporated into PIM-1 for $CO_2$ separation.[115] The layered crystalline structure of MUF-15 promoted $CO_2$ transport in MMMs while maintaining a remarkable selectivity. This research breakthrough set a valuable precedent for the MMM community, encouraging the exploration and use of new MOFs as fillers, expanding the options beyond the conventional choices such as ZIF-8 and UiO-66. However, the low stability and limited dispersibility in polymeric materials may prevent MUF-15 from being widely used in practical separations.

MUF-16 is another MOF developed previously by our group as a standalone material. Constructed from 5-aminoisophthalic acid ($H_2$aip) and cobalt acetate, MUF-16 is a very stable filler that can absorb a large amount of $CO_2$ while barely adsorbing other gas molecules, resulting in high selectivity for $CO_2$ over $N_2$ and $CH_4$ and other light hydrocarbons.[180, 203] Importantly, MUF-16 is a low-cost, durable, recyclable adsorbent with a high affinity for $CO_2$, making it an ideal candidate for the preparation of MMMs for $CO_2$ separation. The choice of polymer to be combined with MUF-16 is critical, as it should have inherent selectivity for $CO_2$ over other gases and offer favorable interfacial compatibility with the filler. Among the various polymer materials available, Pebax-1657, a commercially available polymer, was selected as the continuous phase in our study. Pebax-1657 is a well-

known rubbery copolymer consisting of a hard segment of polyamide (PA) and a soft segment of polyethylene oxide (PEO). This combination gives the material excellent mechanical strength and good $CO_2$ selectivity ($CO_2/N_2$ = 34 and $CO_2/CH_4$ = 14).[204]

In this chapter, a MMM was prepared from Pebax-1657 and MUF-16 and tested for $CO_2$ separation from $N_2$ and $CH_4$ (Fig. 3.1). The effect of the incorporation of MUF-16 into the MMMs was investigated in terms of morphologies, $CO_2$ permeability, and selectivities ($CO_2/N_2$ and $CO_2/CH_4$). The thermal properties and stability of the prepared MMMs were also investigated.

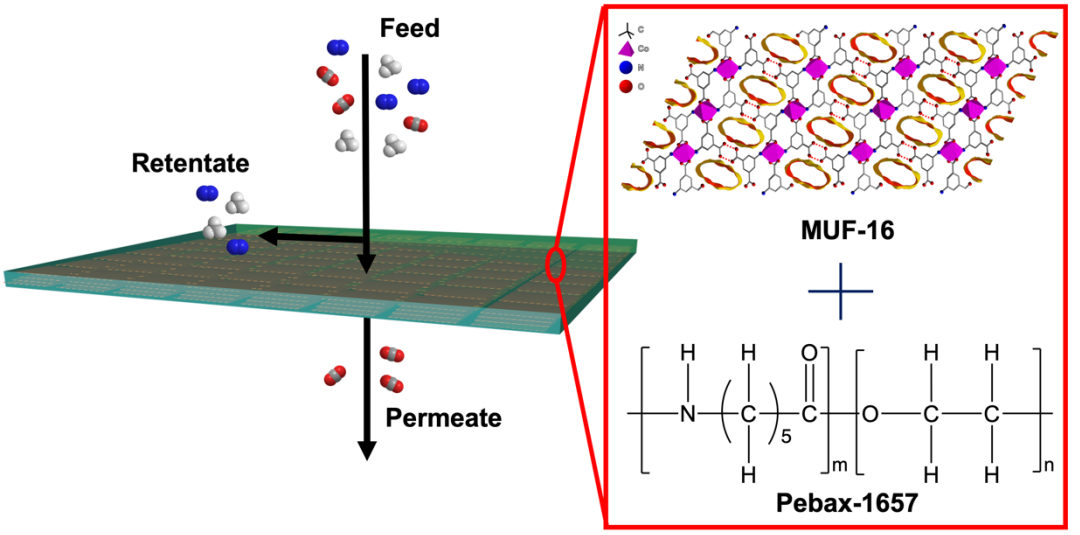


**Figure 3.1** Schematic diagram of gas transport in Pebax/MUF-16 mixed matrix membrane.

## 3.2 Results and discussion

### 3.2.1 Characterization of the MUF-16 filler

Small particle fillers are preferred for MMM fabrication because they effectively reduce the chance of undesired non-selective gas permeation pathways forming at the filler-polymer interface.[205] Using the conventional solvothermal synthesis protocol, the MUF-16 crystals have a bulky flower-like structure with a large cluster size of ~100 µm (Fig. 3.2a). These bulky crystals are likely to lead to aggregation and poor dispersion in the Pebax-1657 matrix. In this context, it is important to manage the size of MUF-16 fillers for a good dispersion. Accordingly, a simple and scalable ball-mill method was developed for producing nano-sized MUF-16 crystals. After two hours of grinding MUF-16 in a ball mill, well-ordered and uniform nano-sized MUF-16 (*ns*MUF-16) was produced (Fig. 3.2b). The matching PXRD patterns revealed that the structure of MUF-16 was maintained (Fig. 3.2c). Overall, this simple and cost-effective method is suitable for industrial and commercial applications.

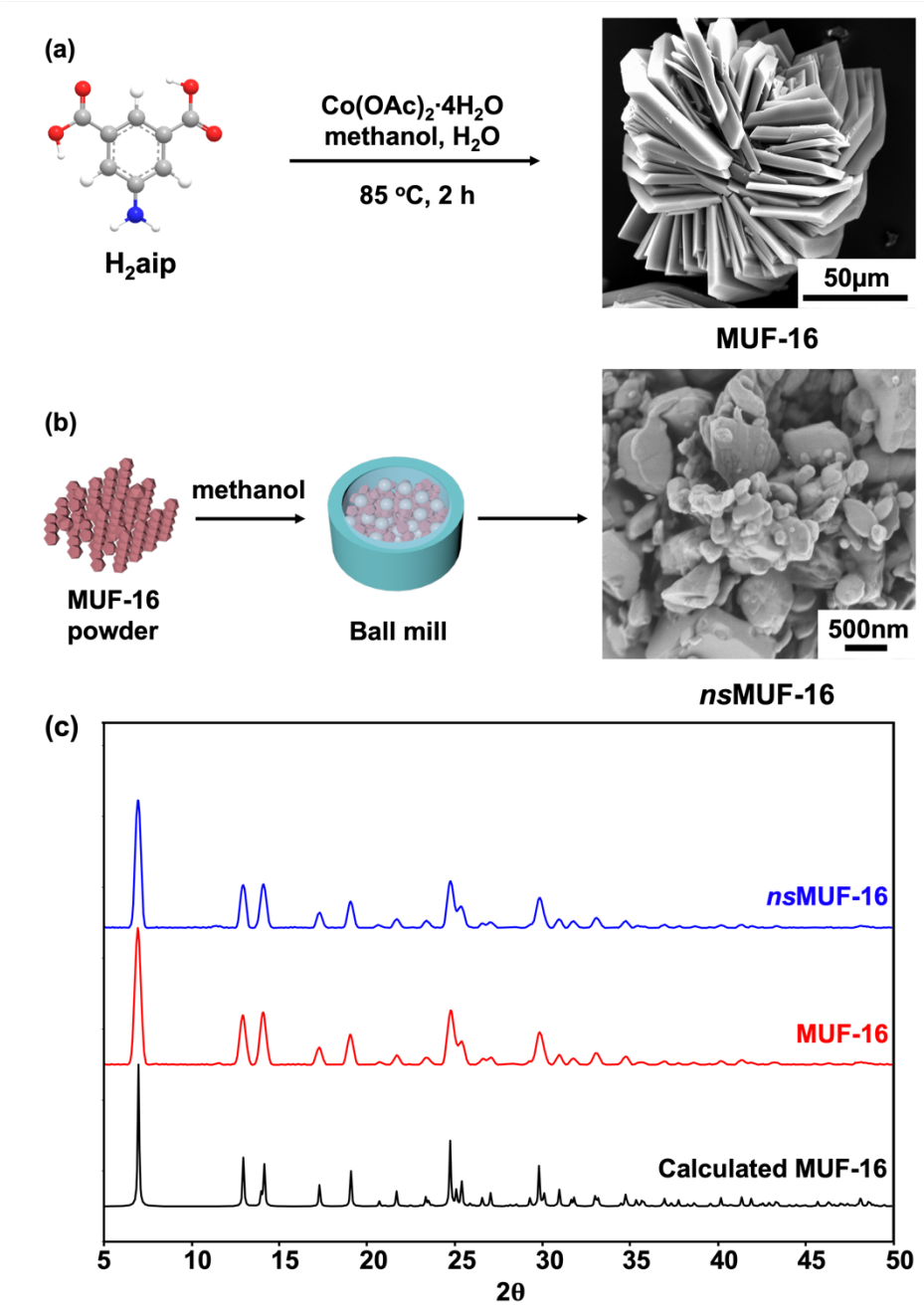


**Figure 3.2** SEM morphologies of (a) solvothermal-synthesized MUF-16, (b) *ns*MUF-16 (ball mill treatment), and (c) PXRD patterns of MUF-16, *ns*MUF-16, and calculated MUF-16.

**FTIR of MUF-16 and *ns*MUF-16.**

The FTIR spectra of *ns*MUF-16 and solvothermally synthesized MUF-16 are identical, indicating that the chemical structure has not changed during the ball mill process (Fig. 3.3).

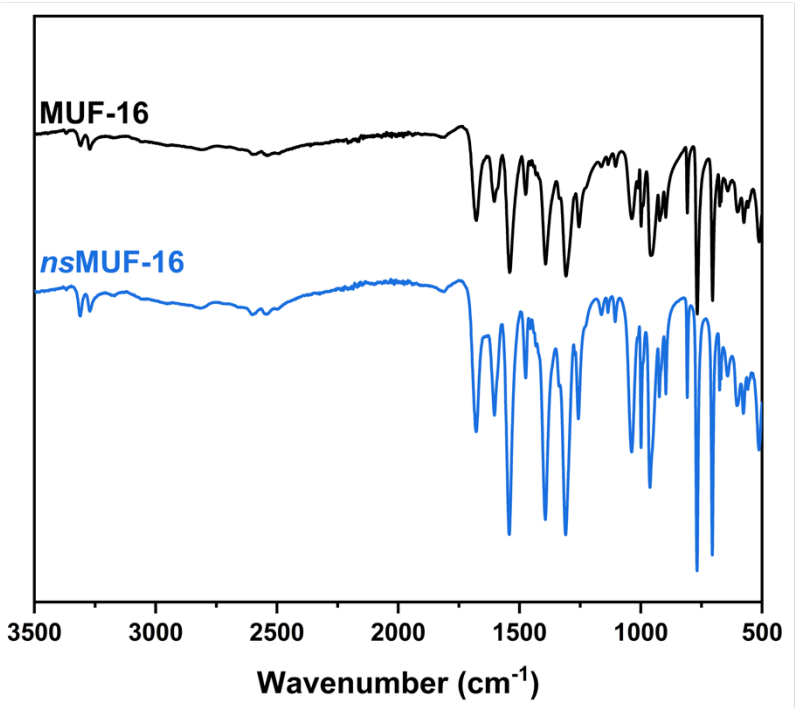


**Figure 3.3** FTIR spectra of MUF-16 (solvothermal-synthesized) and *ns*MUF-16.

**Stability test of MUF-16**

To evaluate the durability of MUF-16 (*solvothermal-synthesized*) in different solvents, it was stored at room temperature for two years in ethanol (EtOH), methanol (MeOH), dimethylformamide (DMF), chloroform ($CHCl_3$), dichloromethane (DCM) and acetone. The PXRD of MUF-16 in various solvents retains the same patterns as the original MUF-16, indicating the excellent stability (Fig. 3.4a). In addition, MUF-16 was also dispersed in water and DMF under boiling conditions for two hours. The PXRD shows the same pattern as pristine MUF-16 (Fig. 3.4b). Overall, the stability tests reveal that MUF-16 is a highly stable MOF. Moreover, the *ns*MUF-16 crystals seem to share the good stability exhibited by the larger crystals.

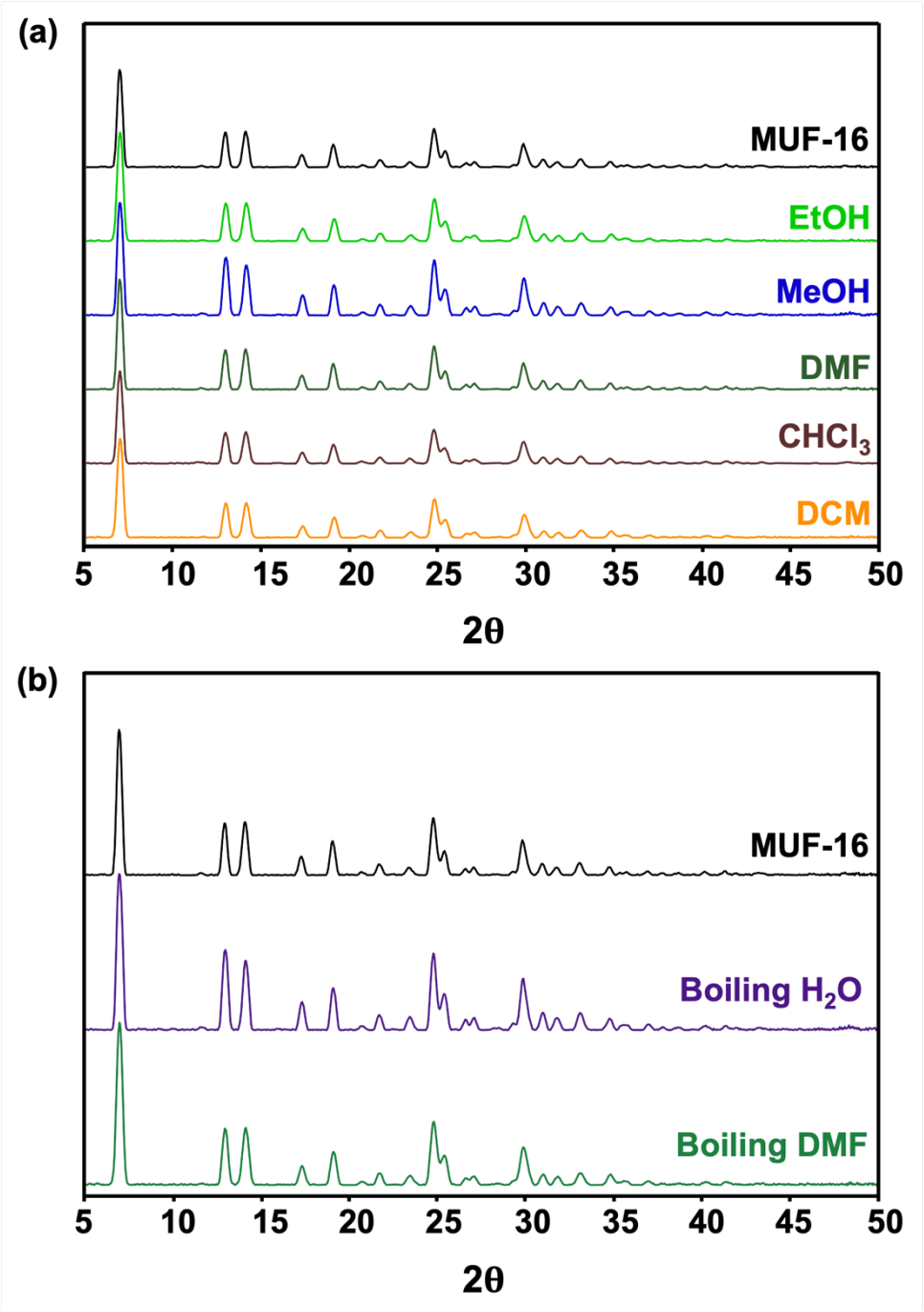


**Figure 3.4** PXRD patterns of MUF-16 and MUF-16 soaking in various solvents over a two-year period. (b) PXRD patterns of MUF-16 after in boiling $H_2O$ and DMF for 2 h.

**Gas adsorption of MUF-16 and *ns*MUF-16.**

The $CO_2$ adsorption capacity of MUF-16 was examined before and after ball milling to produce *ns*MUF-16. The isotherms are almost identical (Fig. 3.5). This finding confirms that the ball milling process did not affect the structural integrity of MUF-16, which is consistent with the PXRD and FTIR results.

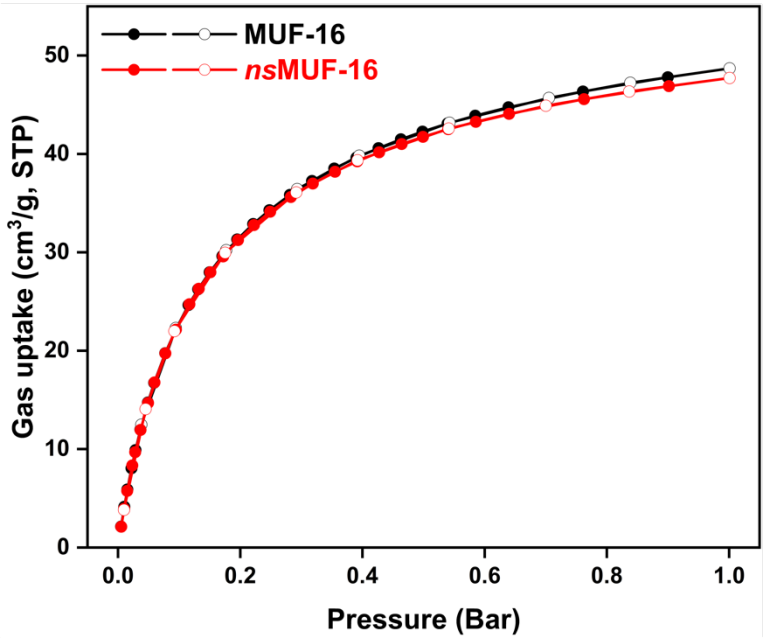


**Figure 3.5** $CO_2$ adsorption (filled cycles) and desorption (open cycles) isotherms of MUF-16 and *ns*MUF-16 at 293 K.

### 3.2.2 Fabrications of MMMs

*ns*MUF-16 crystals were dispersed in ethanol/$H_2O$ (70/30 wt.%) and sonicated for 30 minutes. Pebax-1657 pellets (3.0 g) were then dissolved in this solution under reflux (80 °C) over 2 hours. The MMMs were fabricated by solution casting (Fig. 3.6). Prior to casting, the solution was sonicated for 30 minutes at room temperature to remove air bubbles. The casting solutions with different contents of MUF-16 were then poured into PTFE Petri dishes. The film was dried at ambient temperature for 24 hours and then kept in a vacuum oven at 80 °C for another 24 hours. The obtained MMMs were designated as Pebax/MUF-16(x) (x = 25 wt.%, 33.3 wt.%, 37.5 wt.%, and 43.4 wt.%), where x represents the proportion of MUF-16 in the total weight (MUF-16 + Pebax). Notably, the thickness of the MMMs was controlled to around 70 μm by using a constant total weight (MUF-16 + Pebax).

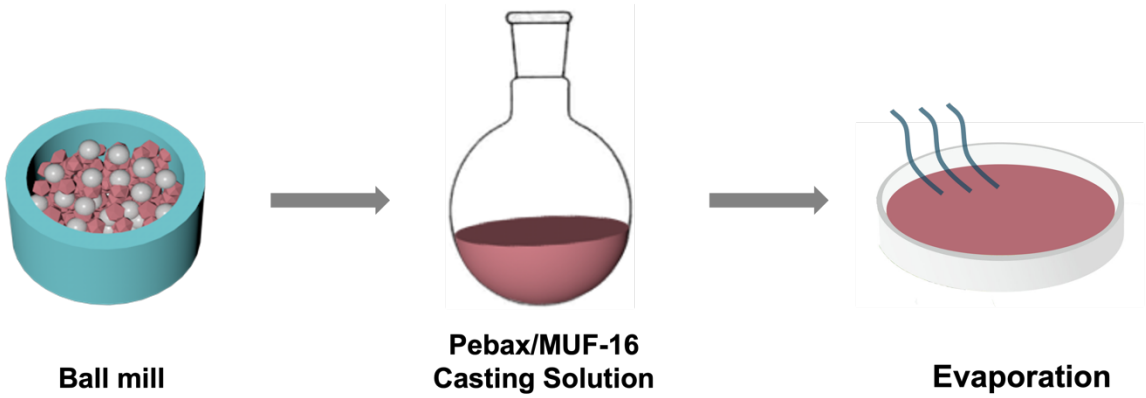


**Figure 3.6** Schematic illustration of the fabrication process of Pebax/MUF-16 MMMs.

### 3.2.3 Characterization of MMMs

#### SEM morphology

SEM was used to determine the morphologies of MUF-16/Pebax MMMs. The pure Pebax membrane had a comparatively smooth surface (Figs. 3.7a and 3.7b). After incorporating *ns*MUF-16 into the Pebax matrix, a similar continuous morphology was obtained, indicating excellent compatibility between the *ns*MUF-16 crystal and the Pebax phase and good dispersion of the filler particles (Figs. 3.7c and 3.7d). The MMMs still maintained a well-integrated appearance and defect-free appearance when the loading of *ns*MUF-16 was varied from 25.0 wt.% to 43.4 wt.% (Figs. B. 1 to Fig B. 4, Electronic Appendix B). EDS mapping of the MMMs revealed that *ns*MUF-16 was uniformly distributed throughout the MMMs with 40 wt. % of *ns*MUF-16 (Fig. 3.20). Notably, high magnification of the membrane cross section with 40 wt.% *ns*MUF-16 loading highlights the excellent dispersion of the crystals in the polymer matrix and an absence of defects or voids (Fig. 3.7e). A photo of Pebax/*ns*MUF-16 membrane with 40 wt.% loading is shown in Fig. 3.7f.

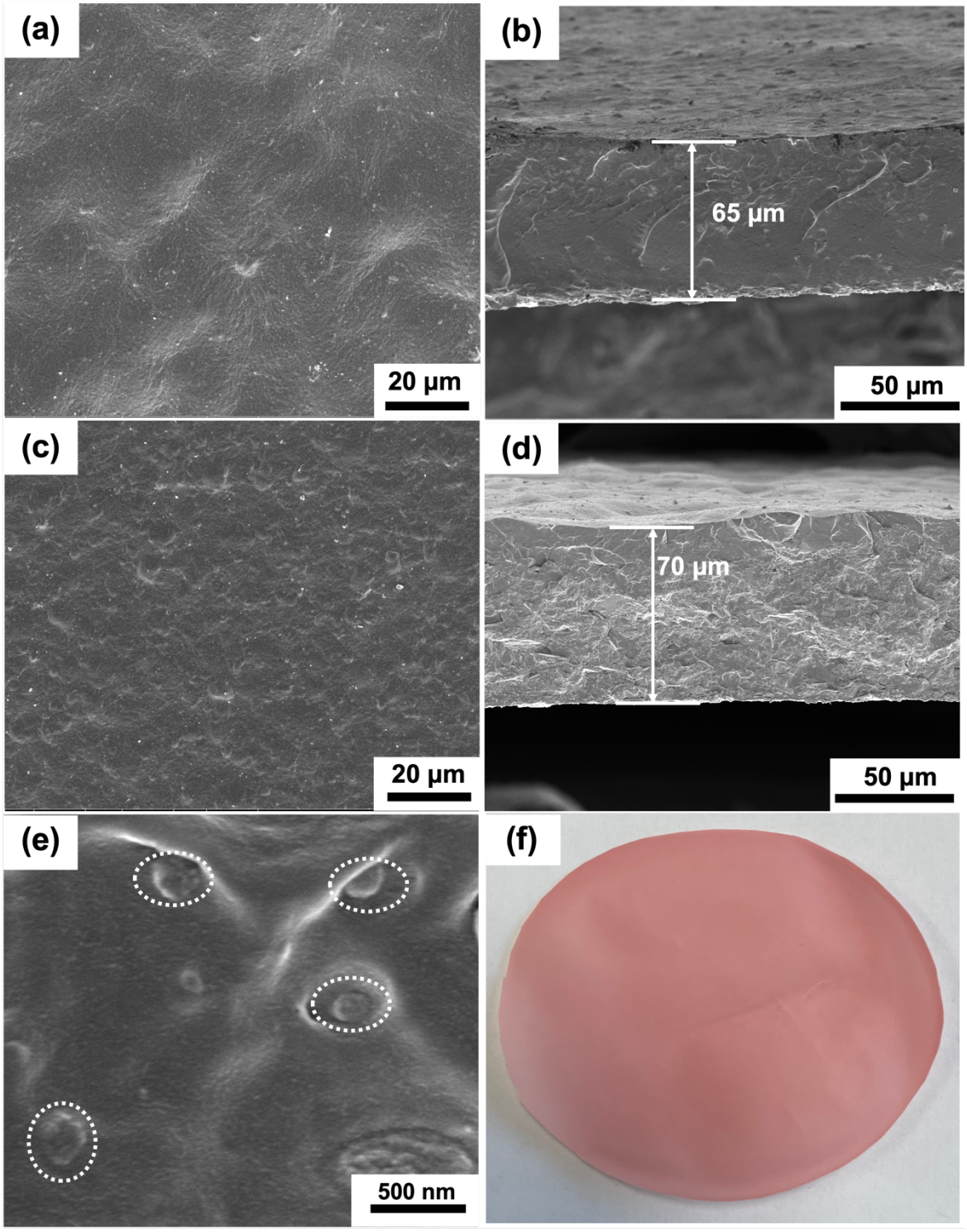


**Figure 3.7** SEM morphologies of (a) surface and (b) cross-section of pure Pebax membrane, (c) surface and (d) cross section of MMM with 40 wt.% *ns*MUF-16 loading, and (e) high magnification of cross-section of Pebax/*ns*MUF-16 membrane with 40 wt.% loading (*ns*MUF-16 particles are shown as white dashed circles). (f) Photograph of Pebax/*ns*MUF-16 membrane with 40 wt.% loading.

### XRD patterns

All MMMs showed prominent peaks corresponding to the MUF-16 in the XRD patterns. This indicates the preservation of MUF-16 crystal structure without the formation of any new phases during the MMM preparation (Fig. 3.8).

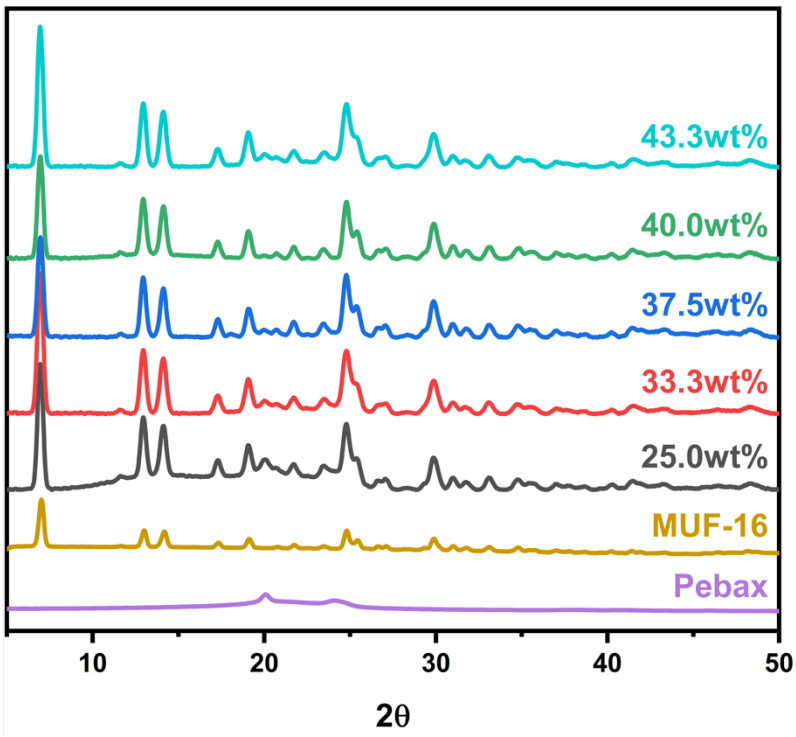


**Figure 3.8** XRD patterns of Pebax, MUF-16 and corresponding MMMs with different *ns*MUF-16 loading.

### FTIR spectra

Fourier transform infrared (FTIR) spectroscopy was performed to investigate any changes in chemical bonding of the fabricated MMMs. As shown in Fig. 3.9a, no new peaks appeared in the FTIR spectra upon incorporation of *ns*MUF-16 into the Pebax matrix. However, some minor peak shifts were observed (Figs. 3.9b and 3.9c). Specifically, the peak at around 3300 $cm^{-1}$, which is attributed to stretching of the N-H groups in the Pebax matrix, shifts to higher frequencies. Similarly, the peak at around 1642 $cm^{-1}$, which can be attributed to C=O stretching in the Pebax matrix, shifts to higher frequencies with increasing *ns*MUF-16 loading in the membranes. These shifts are a result of interactions between the glassy polyamide segment of Pebax and the *ns*MUF-16 filler. Hydrogen-bonding could occur at the interface between *ns*MUF-16 and Pebax matrix. The amino groups on the *ns*MUF-16 surface and the (C=O) of polymer chains can form hydrogen bonds, leading to improved adhesion and interfacial interactions (Fig 3.9d).[206-209] As a result, the formation of hydrogen bonds in

membranes enhanced their mechanical stability compared with the pure Pebax membrane, as measured by tensile tests (Fig 3.9e).

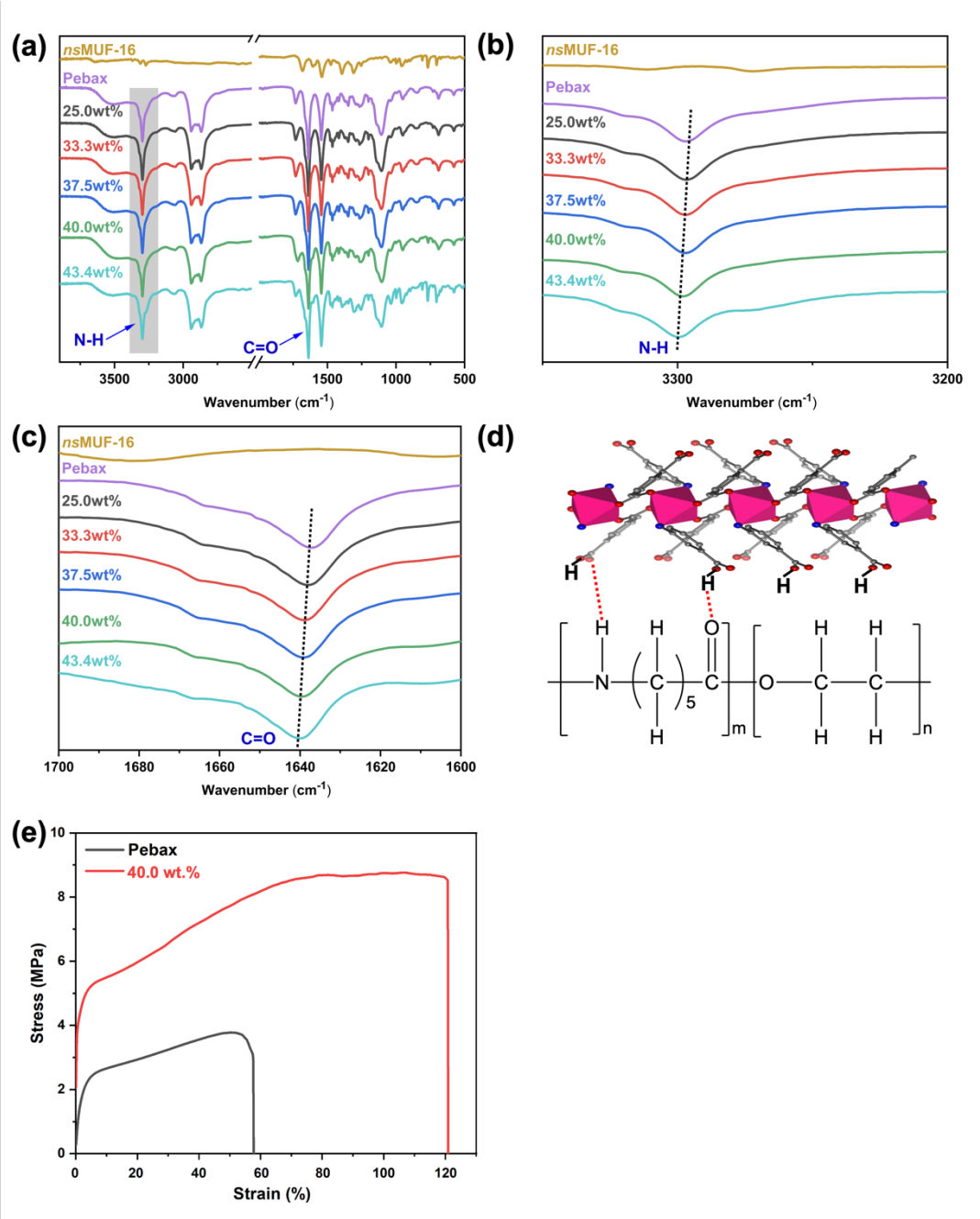


**Figure 3.9** (a - c) FTIR spectra of *ns*MUF-16 and corresponding MMMs with different *ns*MUF-16 loadings. (d) Hydrogen bond between Pebax and MUF-16. (e) Comparison of tensile tests of pristine Pebax and MMMs with 40 wt.% *ns*MUF-16 loadings.

### TGA analysis

Thermogravimetric analysis (TGA) of neat Pebax-1657, MUF-16 and MMM with 40 wt.% *ns*MUF-16 loading recorded under $N_2$ is shown in Fig. 3.10. Residual water and solvent loss can be observed up to 100 °C. When the temperature is increased to around 350

°C, none of the samples show any weight loss, indicating the stability of both the MUF-16 and the polymer. Further increases in temperature cause the MUF-16 to decompose.

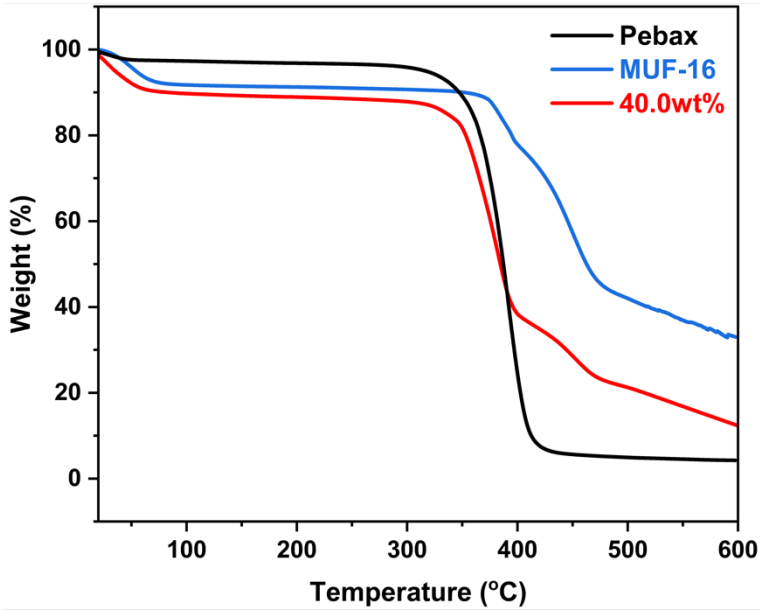


**Figure 3.10** TGA curves of Pebax membrane, *ns*MUF-16 power and MMM with 40wt% *ns*MUF-16 loading.

### 3.2.4 Gas separation performance of MMMs

#### 3.2.4.1 Single gas permeability tests

The permeability of the *ns*MUF-16/Pebax MMMs to single gases was measured (Figs. 3.11a to 3.11c). Several clear trends were observed.

- $CO_2$ permeability increased with increasing *ns*MUF-16 loading up to 40 wt.%.
- $CH_4$ permeability decreased with filler loading.
- $N_2$ permeability was largely unaffected by the MOF loading, however the presence of the filler decreased the permeability relative to pure Pebax.
- The permeability of all gases increased with increasing feed pressure.
- The absolute values of the permeability decrease in the order $CO_2 >> CH_4 > N_2$.

A series of significant conclusions may be drawn from these results:

i. The filler particles do not introduce non-selective voids at the filler-polymer interface, indicating good interfacial compatibility.

ii. MUF-16 promotes $CO_2$ transport in MMMs while inhibiting the passage of $N_2$ and $CH_4$ molecules.

iii. The gas separation selectivities that can be predicted from these single gas experiments are high (Figs. 3.11d and 3.11e).

Assessing the results in more detail, as the *ns*MUF-16 loading in MMMs increases, the $CO_2$ permeability increased first, reaching a peak of 231 Barrer when the *ns*MUF-16 loading is 40.0 wt.% at a feed pressure of 5 bar at 293K (Fig. 3.11a). At this pressure, the $CO_2/N_2$ and $CO_2/CH_4$ selectivities reached 243 and 211, respectively. For single gas tests, the $CO_2$ permeability increased from 75.6 of the pure Pebax membrane to 231 (3.1-fold increase) of the MMM with 40 wt.% filler loading at 5 bar. The corresponding ideal $CO_2/N_2$ and $CO_2/CH_4$ selectivities increased from 35.2 to 243 (6.9-fold increase) and from 27.2 to 211 (7.8 times higher), respectively (Figs. 3.11d and 3.11e).

Interestingly, increasing the *ns*MUF-16 filler loading to 43.4 wt.% caused a *decrease* in $CO_2$ and $CH_4$ permeabilities and a slight increase in $N_2$ permeability. As the *ns*MUF-16 loading increases, the increased gas transport resistance can lead to the formation of pathways that were less permeable to gas molecules. In addition, the tortuosity of the gas transport path may also increase due to the formation of agglomerates. This could increase the length of gas diffusion pathways, resulting in reduced gas permeability. A concomitant decrease in calculated $CO_2/N_2$ and $CO_2/CH_4$ selectivity is observed at the 43.4 wt.% MOF loading.

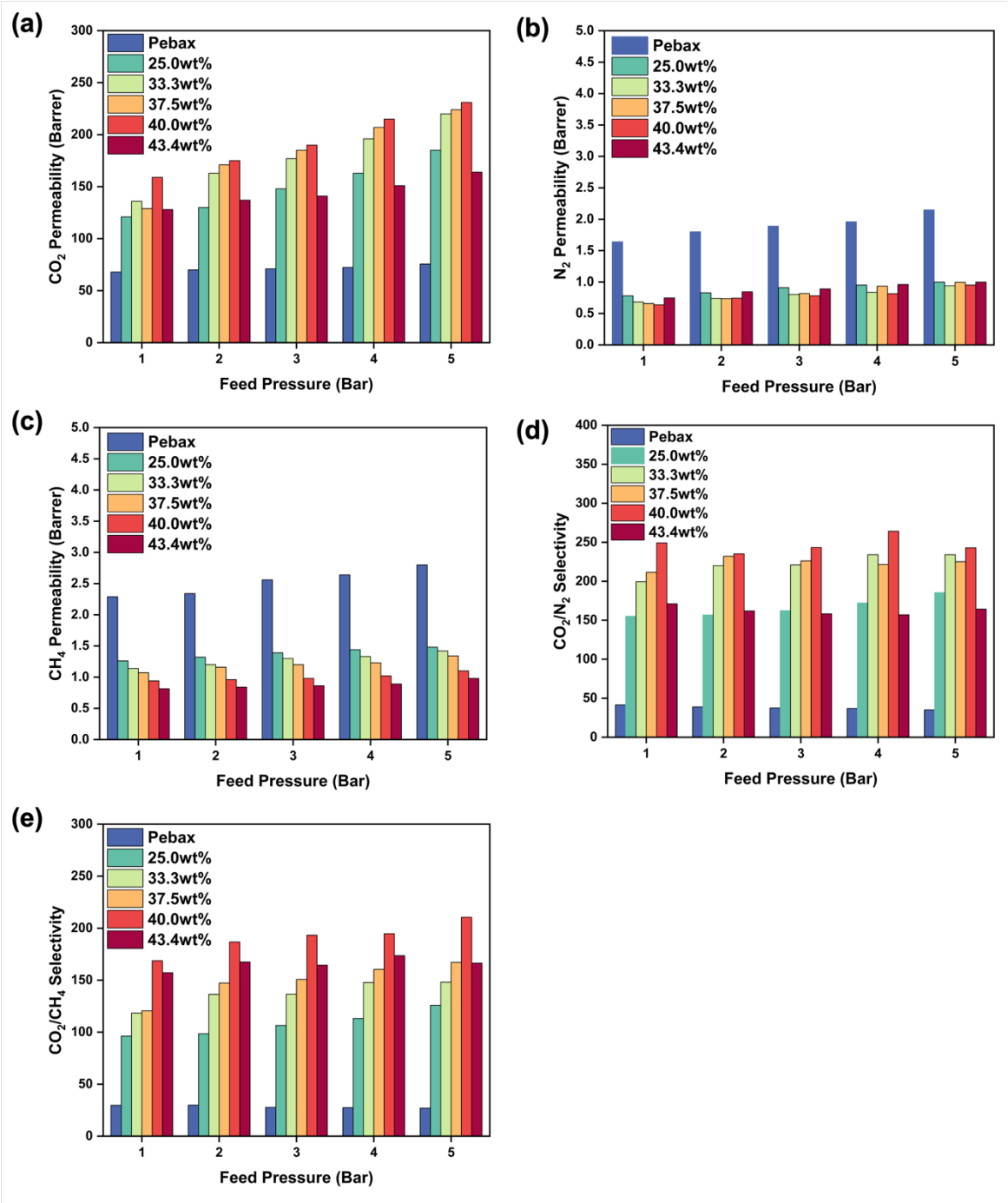


**Figure 3.11** Gas permeability of (a) $CO_2$, (b) $N_2$, (c) $CH_4$ using pure gases and calculated (d) $CO_2/N_2$ and (e) $CO_2/CH_4$ selectivities (1-5 bar, 293 K).

Using the selectivities calculated from these single gas permeation experiments, the MMMs with different *ns*MUF-16 loading almost all surpass the 2008 and 2019 Robeson upper bound limits (Fig. 3.12a and 3.12b). Moreover, compared to the other Pebax-based MMMs with different fillers, our membranes show exceptional performance (high selectivity and moderate permeability) for the separation of $CO_2$ from both $CO_2/N_2$ and $CO_2/CH_4$ mixtures.

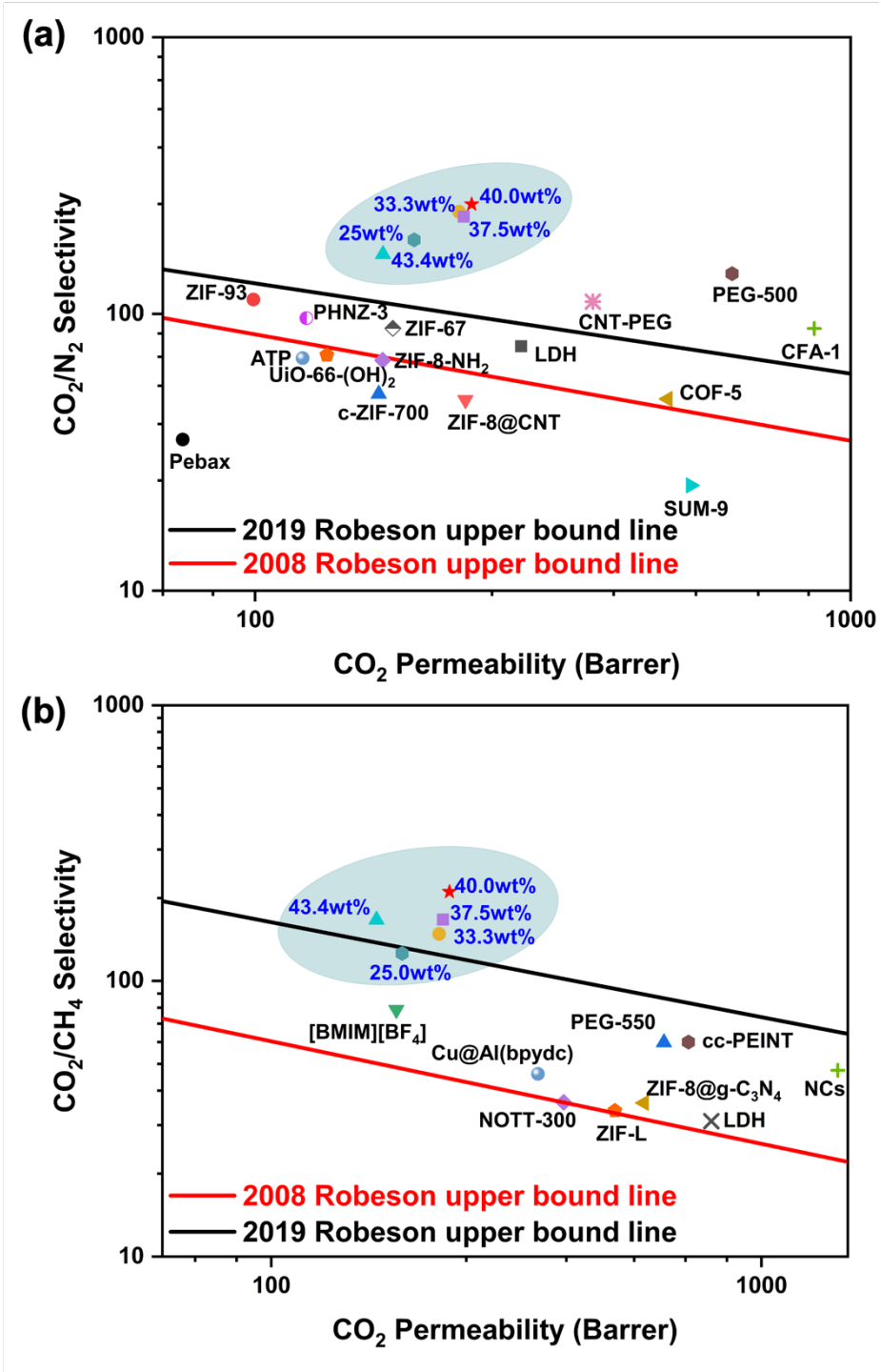


**Figure 3.12** Ideal selectivity versus $CO_2$ permeability including out Pebax/*ns*MUF-16 MMMs and some other Pebax based MMMs with different fillers for (a) $CO_2/N_2$ separation (ZIF-93[118], PHNZ-3[210], ZIF-67[211], ZIF-8-$NH_2$[212], LDH[198], PEG-500[213], CAF-1[214], COF-5[215], SUM-9[216]) and (b) $CO_2/CH_4$ separation ([BMM][$BF_4$][217], Cu@Al(bpydc)[218], NOTT-300[219], PEG-550[213], ZIF-L[220], cc-PEINT[221], ZIF-8@g-$C_3N_4$[222], LDH[223], NCs[224]).

### 3.2.4.2 Mixed gas permeability tests

To evaluate the actual separation performance of the Pebax/MUF-16 membranes, the MMM containing 40 wt.% *ns*MUF-16 was tested with gas *mixtures*. Volume ratios of $CO_2/N_2$ = 20/80 and $CO_2/CH_4$ = 20/80 were used as the feed gas at a pressure of 5 bar at room temperature (Fig. 3.13). A reduction in $CO_2$ permeability and $CO_2/N_2$ and $CO_2/CH_4$ selectivities were observed compared to the single gas experiments This is ascribed to a combination of adsorption solubility and diffusivity.[225] In the mixed gas tests, competitive adsorption might occur, which could result in partial blocking of certain gas molecules from passing through the membrane due to competition for adsorption sites, leading to reduced overall gas permeability.[226] In terms of adsorption solubility in the membrane, there is a solubility difference between $CO_2$ and $N_2$ (or $CH_4$) as the gas adsorption sites in MUF-16 are preferential to $CO_2$. In this case, $CO_2$ could be adsorbed more easily. This could create a concentration gradient in the membrane, reducing the driving force for mixed gases to permeate across the membrane. In addition, the presence of $N_2$ (or $CH_4$) affected the rate of $CO_2$ diffusion. As a result, the $CO_2$ permeability decreased under mixed gas conditions.[227-228]

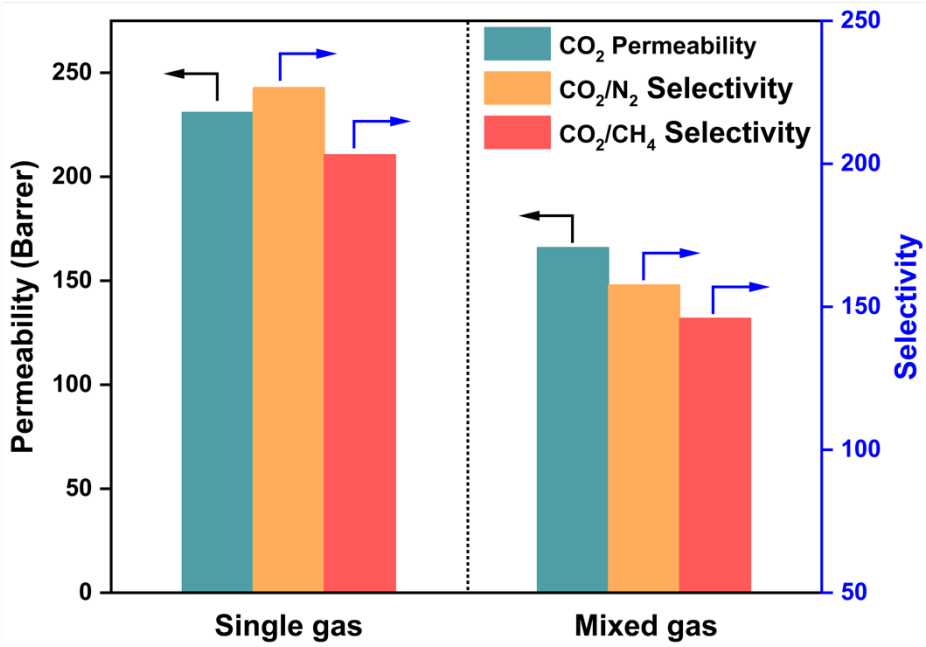


**Figure 3.13** Results for MMMs containing 40 wt.% *ns*MUF-16 in Pebax (5 bar, 293 K). The left panel shows the permeability measured for $CO_2$ and selectivities estimated from single gas experiments. The right panel shows selectivities obtained from mixed gas experiments.

### 3.2.4.3 Long-term permeability tests

Long-term separation stability is an important index for evaluating membrane performance for practical applications. We evaluated the ability of the membrane with 40 wt.% *ns*MUF-16 to separate gas mixtures at a feed pressure of 5 bar over a period of months. After 48 h of continuous testing at room temperature, the membrane maintained an average $CO_2$ permeability of 160 Barrer (Fig. 3.14a). In addition, the $CO_2/N_2$ selectivity was maintained at around 145. The membrane also showed a consistent trend for $CO_2/CH_4$ separation over a 48-hour period (Fig. 3.14b). To investigate long-term anti-aging properties, we examined the membrane performance over five months. Over this period the maintained a consistently high $CO_2$ permeability and good $CO_2/N_2$ and $CO_2/CH_4$ selectivities (Fig. 3.14c). Overall, the long-term test demonstrated that Pebax/*ns*MUF-16 membrane has exceptional stability.

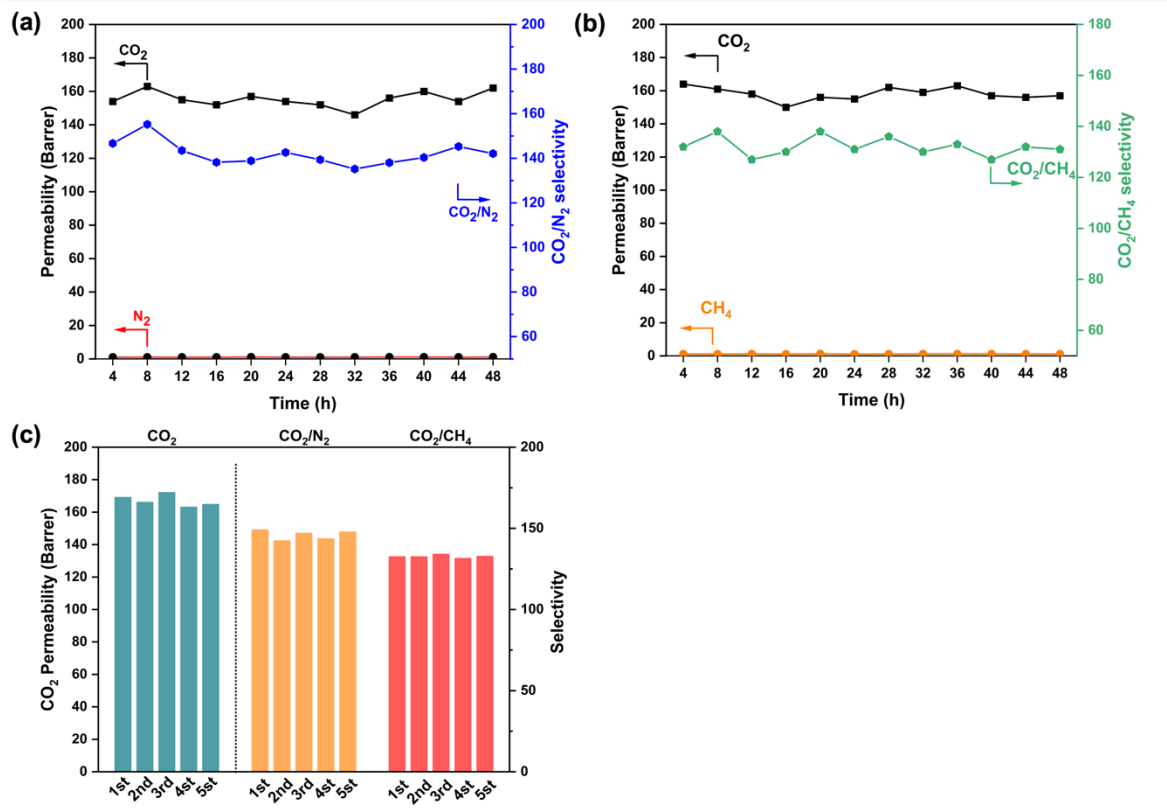


**Figure 3.14** Long-term stability for mixed gas tests of (a) $CO_2/N_2$ and (b) $CO_2/CH_4$ of MMMs with 40 wt.% *ns*MUF-16 for 48 h (volume ratios of $CO_2/N_2$ = 20/80 and $CO_2/CH_4$ =20/80, room temperature). (c) Anti-aging property of mixed gas tests of MMMs with 40 wt.% *ns*MUF-16 for 5 months.

### 3.2.4.4 Gas solubilities and diffusion in the MMMs

To investigate the gas transport mechanism, we selected pure Pebax and MMM with 40 wt% *ns*MUF-16 loading and analyzed the solubility coefficients (*S*) and diffusion coefficients (*D*) for $CO_2$, $N_2$ and $CH_4$. MUF-16 has an inherently high affinity for $CO_2$, and a much lower affinity for $N_2$ and $CH_4$.[180, 203] In this study, the solubility coefficients were calculated from high-pressure adsorption isotherms, as detailed in the Supporting Information. The $CO_2$ solubility ($S_{(CO2)}$) in the MMM is much higher than the pure Pebax. On the other hand, $S(N_2)$ and $S(CH_4)$ are significant lower in the MMM than in PEBAX (Fig. 3.15a).

The determination of *S* allows us to calculate *D* (Gas permeabilities were tested under 5 bar). In the MMM, $D_{(CO2)}$ is almost twice as large as in the pure membrane. On the other hand, $D_{(N2)}$ increases slightly in the MMM while and $D_{(CH4)}$ is close to the value obtained for pure Pebax (Fig. 3.15b).

These observations can be attributed to the following factors:

(1) The addition of *ns*MUF-16 to the membrane facilitates $CO_2$ transport due to its high affinity for $CO_2$.

(2) The presence of *ns*MUF-16 hinders the solubility of $N_2$ and $CH_4$ in the membrane.

(3) The *ns*MUF-16 increases the diffusivity of $CO_2$ and $N_2$.

(4) Both the increased $S_{(CO2)}$ and $D_{(CO2)}$ of MMMs increases $CO_2$ permeability through the membrane, resulting in a better separation performance than a pure Pebax membrane.

(5) The enhanced sorption and diffusion brought about by the *ns*MUF-16 filler combine to elevate the $CO_2/N_2$ and $CO_2/CH_4$ selectivities, with the sorption selectivity being the most dominant factor.[227]

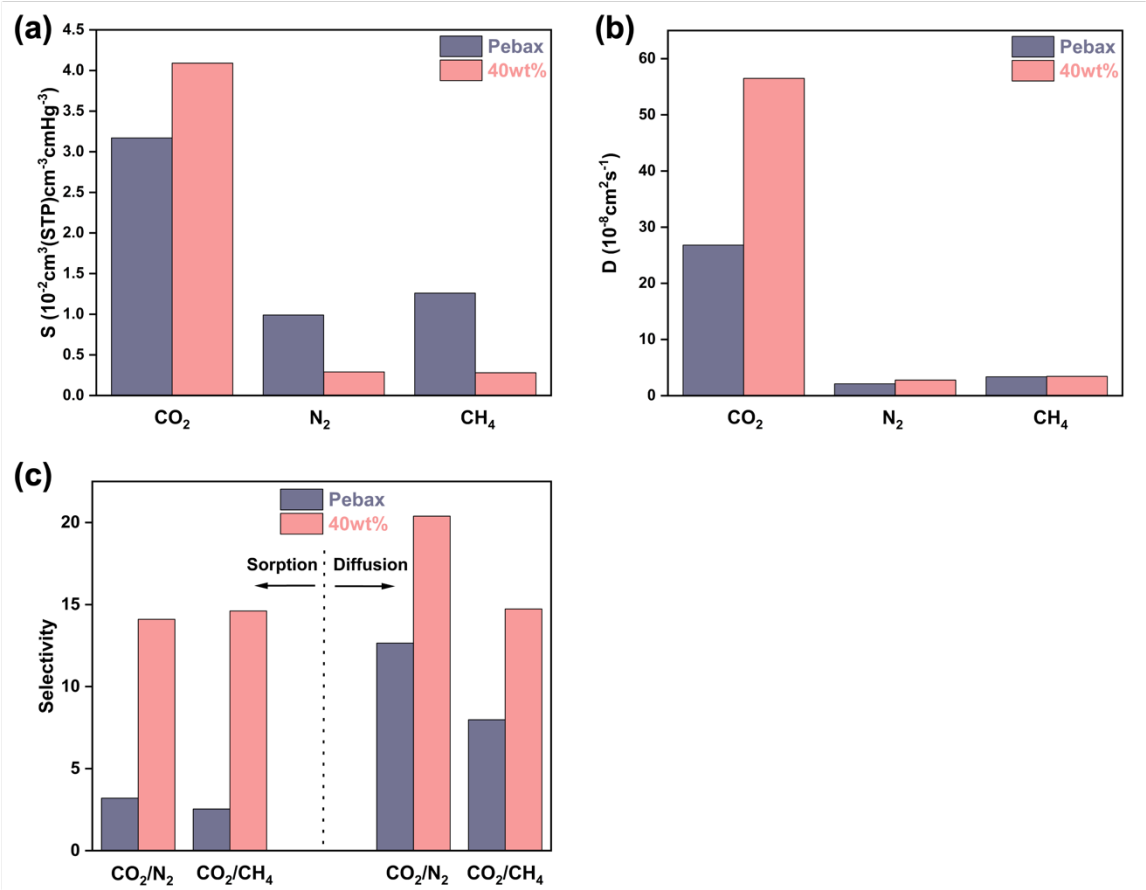


**Figure 3.15** (a) Solubility coefficient (b) diffusivity coefficient of $CO_2$, $N_2$ and $CH_4$ and sorption, diffusion selectivity of $CO_2/N_2$, $CO_2/CH_4$ in MMMs with 40 wt.% *ns*MUF-16 loadings.

### 3.3 Conclusion

In summary, MUF-16, a MOF with a high affinity for $CO_2$, has been used in this work to fabricate MMMs with Pebax for $CO_2$ separation. MUF-16 is a robust and recyclable adsorbent that can maintain its crystal structure in a variety of solvents for extended periods of time. After ball milling, MUF-16 achieves excellent dispersion in Pebax phase, minimizing the interfacial voids in MMMs. These advantages make MUF-16 a suitable filler for MMMs fabrication. Due to the synergistic effect of MUF-16 and Pebax, the as-prepared MMMs achieved significant improvement in $CO_2$ permeability as well as $CO_2/N_2$ and $CO_2/CH_4$ selectivity. Compared with the pristine Pebax membrane, separation results of the MMMs with 40.0 wt.% MUF-16 loading displayed optimized performance, $CO_2$ permeability increased threefold from 75.6 Barrer to 231 Barrer, and $CO_2/N_2$ and $CO_2/CH_4$ selectivity increased 7 (from 35.2 to 243) and 7.8 (from 27.2 to 211) fold, respectively. In addition, the gas separation results surpass the Robeson upper bound limit (2008 and 2019).

Notably, the produced MMMs demonstrated the hydrogen bonding between MUF-16 and Pebax, which improved their stiffness. Long-term operating tests showed stable gas permeability and selectivity, indicating the potential for industrial use. Overall, this work presents a strategy for using novel MOFs to design high-performance MMMs with acceptable interfacial morphologies.

In the context of related literature, this work represents a significant advancement in separation performance. The results of this study showcase remarkable performance improvements, surpassing those of existing membranes in several crucial aspects. Notably, the reported membrane demonstrates superior selectivity while maintaining exceptional $CO_2$ permeability, a combination that has often posed challenges in membrane design. This work not only underscores the substantial progress achieved in membrane technology but also highlight the potential for this newly-developed membrane to outperform in industrial applications. Further comparative studies against other state-of-the-art membranes will provide deeper insights into the extent of its superiority and potential real-world impact.

# Chapter 4 MUF-16/Polyamide (PI) Mixed Matrix Membranes for $CO_2$ Separation

## 4.1 Introduction

Gas separations hold pivotal significance in the energy and chemical sectors because they allow the separation of individual gases from mixtures. For example, the carbon capture and separation (CCS) process can reduce greenhouse gas emissions from industrial processes and power generation, making it an essential tool in the fight against climate change.[229-230] Compared to traditional separation approaches, such as cryogenic distillation and adsorptive separation, membrane separation technology has been identified as the most promising candidate due to its distinct advantages of low investment cost, high separation efficiency, and low energy consumption.[231-232] However, the inescapable trade-off between gas permeability and selectivity that pervades most membranes steers the development of MST towards achieving a harmonious balance between these two attributes.[72-73] Recently, MMMs, which combine the advantages of a processable polymer with the excellent gas separation performance of filler particles, have been identified as the next generation of gas separation membranes.[191, 233] However, due to the interfacial incompatibility between polymer and filler particles, as well as the aggregation or sedimentation of filler particles within the polymer matrix, it is challenging to translate the properties of fillers into MMMs.[234-235] This makes it difficult to evaluate advanced gas separation performance. Consequently, the pursuit of improved gas separation performance requires a meticulous arrangement in fine-tuning the transport properties and interfacial compatibility between filler particles and the polymer matrix, which is the key to creating MMMs with enticing gas separation performance.

Among the numerous porous materials used for membrane separation, such as graphene,[236-237] zeolites,[238-239] COFs,[240-241] MOFs possess unique advantages for membrane separation applications due to their tunable pore aperture size and pore environment.[242-243] Moreover, a variety of pure MOF membranes or MOF-based MMMs have been developed for $H_2$ purification,[156, 244] $CO_2$ separation,[245-246] and $C_3H_6/C_3H_8$ separations.[247-249] Currently, some of the MOF adsorbents known for strong $CO_2$ affinity have demonstrated remarkable $CO_2/N_2$ ($CH_4$) separation performance via an equilibrium-based adsorption mechanism, suggesting their potential application in the development of enhanced $CO_2$ separation MMMs.[194, 250] However, crystalline MOFs are inherently incompatible to amorphous polymers, which could influence the effective filler loading and lead to inevitable interfacial defects in the polymer

matrix, especially within glassy polymers featuring rigid backbones.[251] In this case, most MOF-based MMMs exhibit limited improvement on gas permeability or selectivity. To address the interfacial issues for MMMs, extensive research has been conducted to investigate the impact of MOF filler particle size,[252] morphology,[135, 253] surface modification or functionality[163, 254] on gas separation performance. For example, MOF nanosheets with a relatively large external surface area can provide the enhanced MOF nanosheet-polymer interfacial capability required for high MOF loading in MMMs.[154] Furthermore, the different gas transport pathways in MMMs can lead to a simultaneous significant increase in gas permeability and selectivity. The in-situ or post-modification approach has been demonstrated to bridge the MOFs with polymer matrix through a hydrogen bonding and π-π interaction, which significantly improves the MOFs-polymer compatibility, resulting in exceptional separation performance of the MMMs.[255]

Optimizing the crystal size of the MOF filler is a simple and direct approach to enhance the interfacial combability. As not all the MOFs have a unique nanoscale crystal size, and only a small number of MOFs have been investigated in MMMs for attractive gas separation performance. Some MOFs adsorbents have excellent gas separation performance but large crystal size, which is the fundamental obstacle to the fabricate ideal MMMs. To date, several approaches have been attempted to reduce the crystal size of MOFs. Typically, a reduced MOF crystal can be produced by controlling the crystal growth period or by modifying the synthesis conditions (concentration, temperature, solvent, and pH).[256-257] However, this takes a long time and occasionally the crystalline MOF structures cannot be maintained. In addition, various physical treatments can lower the size of MOF crystals without affecting their structures. For example, cryogenic grinding has been used to produce smaller MOFs crystals. This simple strategy preserved the MOFs structure and rendered MOFs brittle enough to allow the disassembly of aggregates of large crystals.[258] Although smaller MOFs crystals can be obtained, the repeated treatments involving liquid nitrogen and redispersing MOFs in solvent are not scalable. Recently, mechanochemical synthesis or mechanical treatment has gained popularity in the construction of MOFs.[259-260] To promote chemical reactivity and coordination, mechanical force is applied to solid-state reagents by milling, shearing, or grinding with minimal quantities or no solvents. Mechanical force can also be used to post-treat MOFs. Compared to typical hydrothermal synthesis, this green and friendly approach can produce reduced MOFs crystals with a small amount of hazardous solvent and a faster reaction time. As a result, it can be a viable approach for MOFs synthesis or treatment.

Here we report a new MMMs incorporated with an emerging MOF material, MUF-16 (Massey University Framework-16, $Co(H_2aip)_2$, $H_2aip$ = 5-aminoisophthalic acid) (Fig. 4.1a). As a low-cost, robust, recyclable $CO_2$ adsorbent, MUF-16 has excellent $CO_2/N_2$ and $CO_2/CH_4$ separation properties, which can be implemented into the MMMs for advanced $CO_2$ separation.[180] However, the original solvothermal synthesized results with a huge crystal size of MUF-16 with hundreds of micrometers, which leads to interfacial voids in the membranes. As a result, smaller MUF-16 crystals are essential for membrane construction to achieve the exceptional $CO_2$ separation performance. A mechanochemistry-based ball mill was used in this study to produce MUF-16 of reduced crystal size. Two ball mill-assisted synthesis approaches were employed in this study. One method is direct synthesis in a ball mill jar to produce MUF-16 (*bm*MUF-16) of smaller size, while another method is post-treatment of synthesized MUF-16 bulk crystals using a ball mill to produce nano-sized MUF-16 (*ns*MUF-16). In this case, both *ns*MUF-16 and *bm*MUF-16 could show improved dispersion properties in the polymer matrix. These prepared MUF-16 with different crystal sizes were used to construct MMMs with polyimides. Not surprisingly, MUF-16 with smaller crystal size (*bm*MUF-16 and *ns*MUF-16) exhibited excellent interfacial compatibility with two representative polyimide matrices (6FDA-DAM and 6FDA-Durene) (Fig. 4.1b). The MMMs fabricated with *ns*MUF-16 show the superior $CO_2$ separation performance compared to those fabricated with large crystals (MUF-16 and *bm*MUF-16).

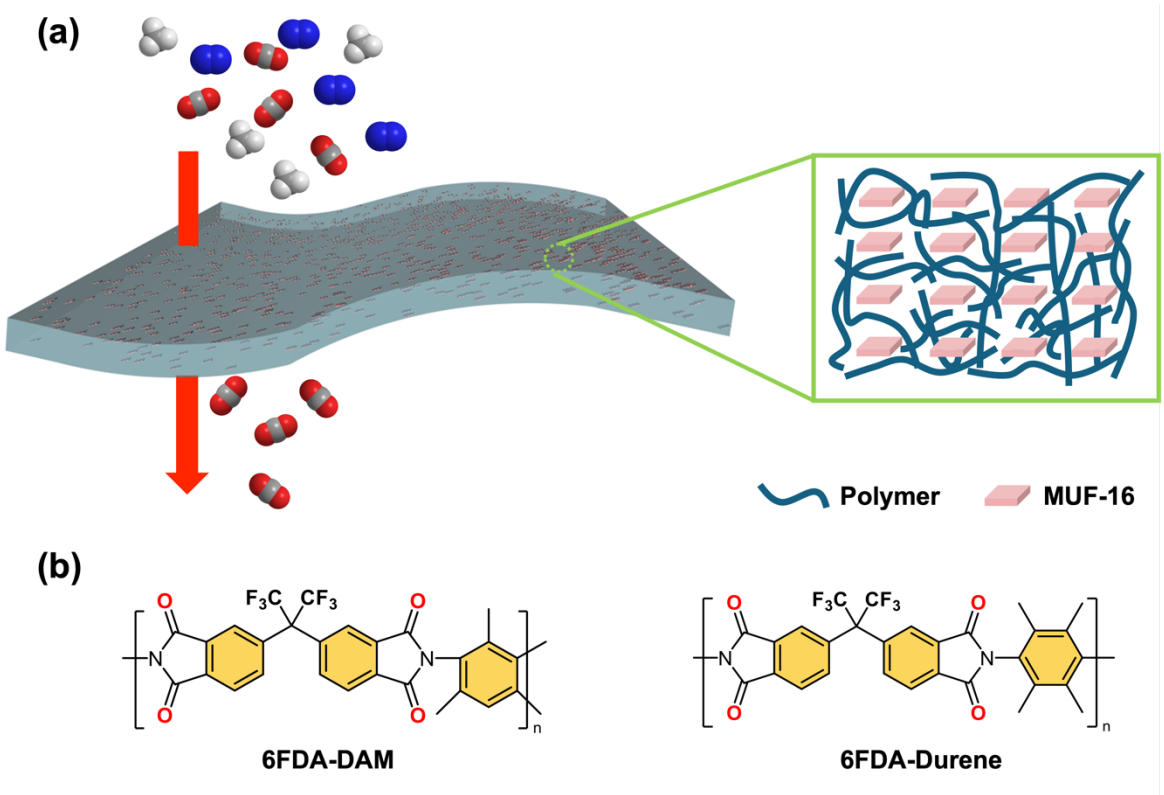


**Figure 4.1** (a) Schematic illustration of highly efficient $CO_2$ capture by the MUF-16 based MMMs and arrangement between nsMUF-16 and polymer matrix. (b) Chemical structures of two representative polyimide polymers: 6FDA-DAM and 6FDA-Durene.

## 4.2 Results and discussion

### 4.2.1 Synthesis of MUF-16 using different approaches

Submicron MOF filler particles are well known for their favorable interfacial compatibility with the polymer matrix in the construction of MMMs. Previous attempts of direct synthesis consistently yielded large MUF-16 crystals up to hundreds of microns in size (Figs. 4.2a and 4.2b). These large crystals can induce interfacial voids in the MMMs, leading to a poor selectivity. To address this issue, we propose two strategies to synthesize smaller MUF-16 crystals and thus minimize the interfacial voids between the MOF fillers and the polymer matrix.

Accordingly, a green and facile ball mill-assisted synthetic method was used to create MUF-16 (*bm*MUF-16) with a crystal size of approximately 1 μm (Figs. 4.1c and 4.1d). In addition, the ball mill post-treatment was employed to produce nano-sized MUF-16 (*ns*MUF-16) with a crystal size of approximately 300 - 400 nm (Figs. 4.1e and 4.1f). These two

approaches preserve the structure of MUF-16 and produce the smaller crystal sizes than hydrothermal synthesis. Notably, the facile and inexpensive ball mill process can be easily scaled up, indicating that it has potential for commercial MOF synthesis as well as laboratory-scale fabrication of MOF-based MMMs.

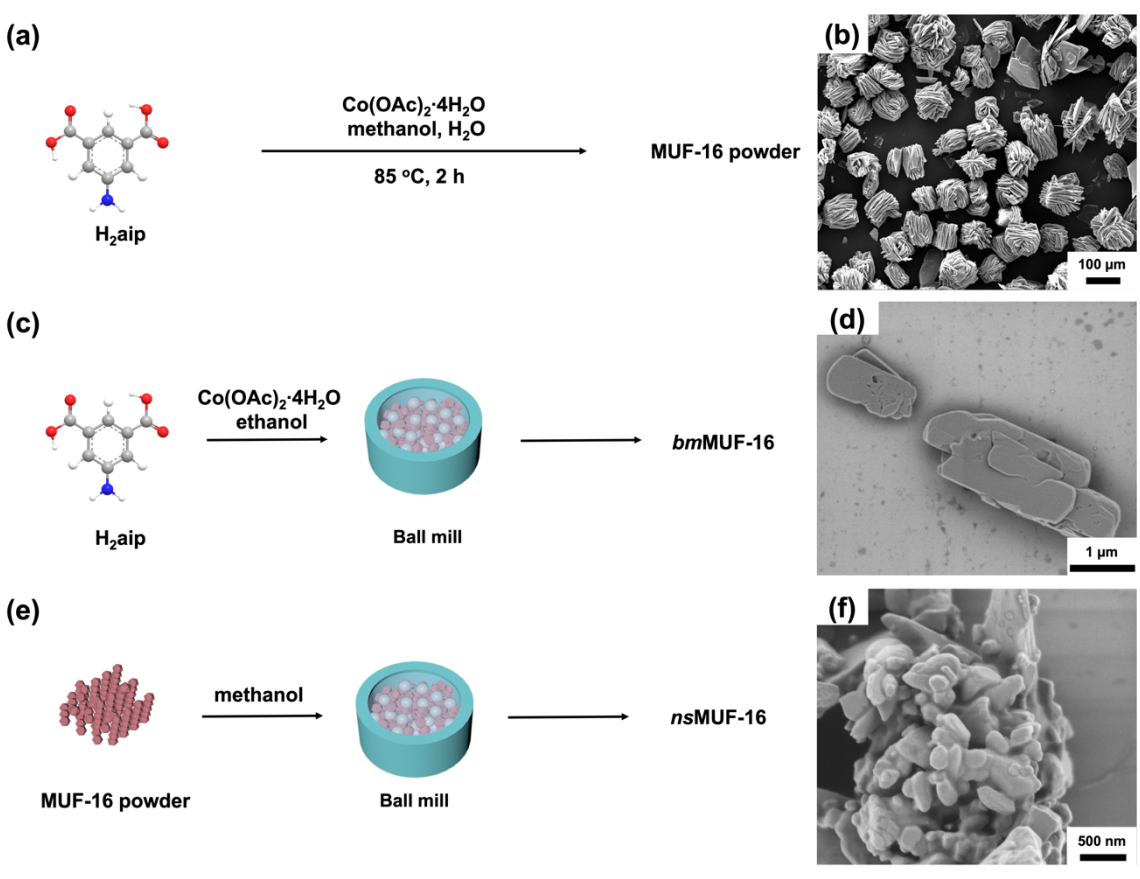


**Figure 4.2** (a) Solvothermal synthesis of MUF-16, (b) SEM morphology of MUF-16. (c) Ball mill synthesis of MUF-16 (*bm*MUF-16). (d) SEM morphology of *bm*MUF-16, (e) preparation of nano-sized MUF-16 (*ns*MUF-16) by wet ball milling, (f) SEM morphology of *ns*MUF-16.

### 4.2.2 Characterization of MUF-16 fillers

Power X-ray diffraction (PXRD) was carried out to verify the crystalline structures of these refined MUF-16 crystals. The patterns of all the MUF-16 samples of different crystal sizes matched with the calculated MUF-16, indicating the crystalline structure of MUF-16 was well preserved (Fig. 4.3a). In addition, the patterns of infrared (IR) spectra remain unchanged between the MUF-16 samples of different crystal sizes (Fig. 4.3b). Furthermore, MUF-16 and *ns*MUF-16 showed comparable $CO_2$ adsorption uptake at 1 bar (293 K), indicating that the size reduction does not affect the adsorption capacity. Moreover, *bm*MUF-16 also displayed a high

$CO_2$ adsorption uptake at 1 bar (Fig. 4.3c). Benefiting from the MUF-16, the MMMs are expected to possess high $CO_2$ uptake regardless of the filler size. Owning to a hindering effect on $N_2$ or $CH_4$ permeation, the resulting MUF-16-based MMMs could show a high $CO_2$ separation performance. Prior to membrane fabrication, MUF-16 with different crystal sizes was dispersed in $CHCl_3$ and an improved dispersity was observed (Fig. 4.3d). Therefore, *ns*MUF-16 can be used to fabricate membranes with excellent interfacial compatibility in a polymer matrix.

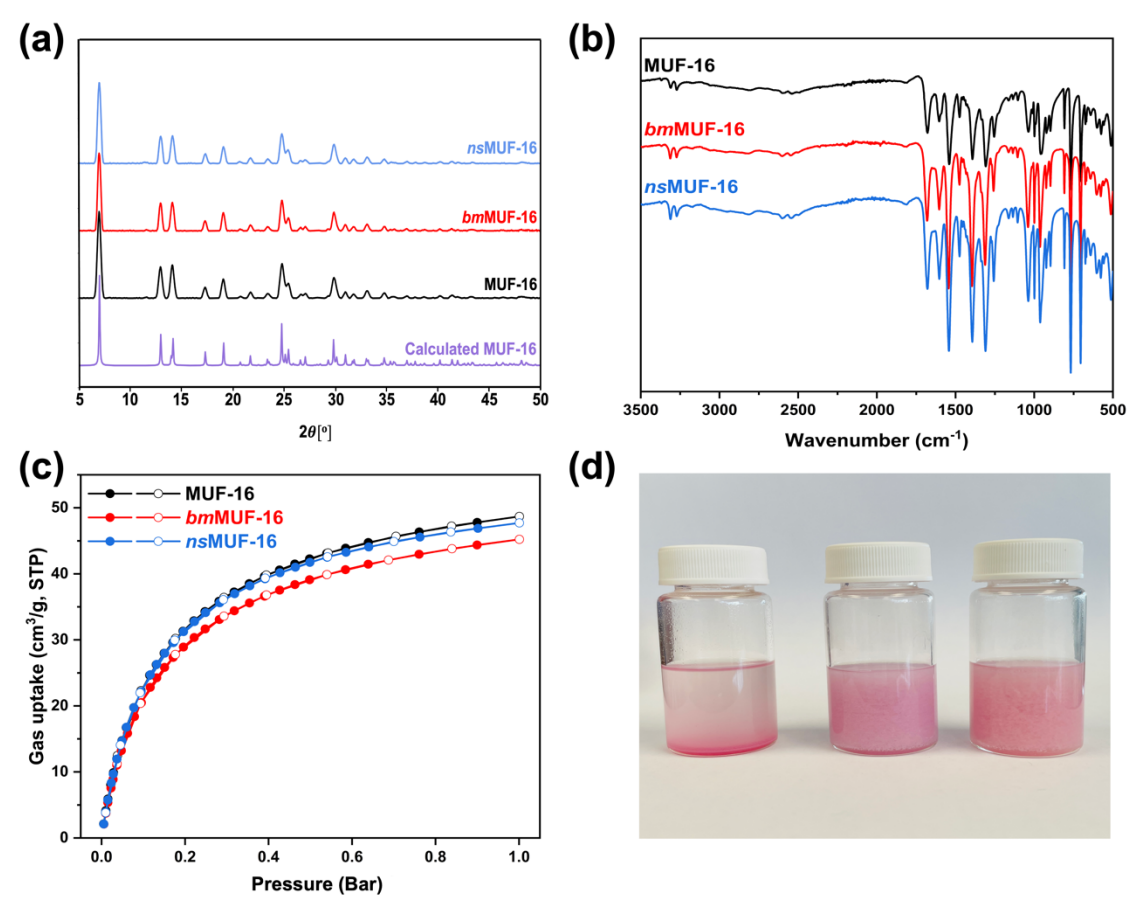


**Figure 4.3** (a) PXRD patterns of calculated MUF-16, as-synthesized MUF-16, *bm*MUF-16, and *ns*MUF-16, (b) FTIR spectra of MUF-16, *bm*MUF-16, and *ns*MUF-16, (c) $CO_2$ adsorption (filled cycles) and desorption (open cycles) isotherms of MUF-16, *bm*MUF-16, and *ns*MUF-16 at 293 K, (d) dispersity of MUF-16, *bm*MUF-16, and *ns*MUF-16 (from left to right) in $CHCl_3$ solution.

### 4.2.3 Characterization of membranes

#### XRD of membranes

First, MMMs were fabricated using an identical MUF-16 loading (40 wt.%) but varying crystal sizes. The matching PXRD patterns of MUF-16/6FDA-DAM and MUF-16/6FDA-Durene MMMs show that the crystalline structures of MUF-16 with different crystal sizes are all retained (Figs. 4.4a and 4.4c) during the membrane fabrication process. For membranes with different *ns*MUF-16 loadings, the crystalline nature of *ns*MUF-16 was retained in both 6FDA-DAM (Fig. 4.4b) and 6FDA-Durene (Fig. 4.4d) based membranes. These results demonstrate that the MUF-16 is stable in the polymer matrix.

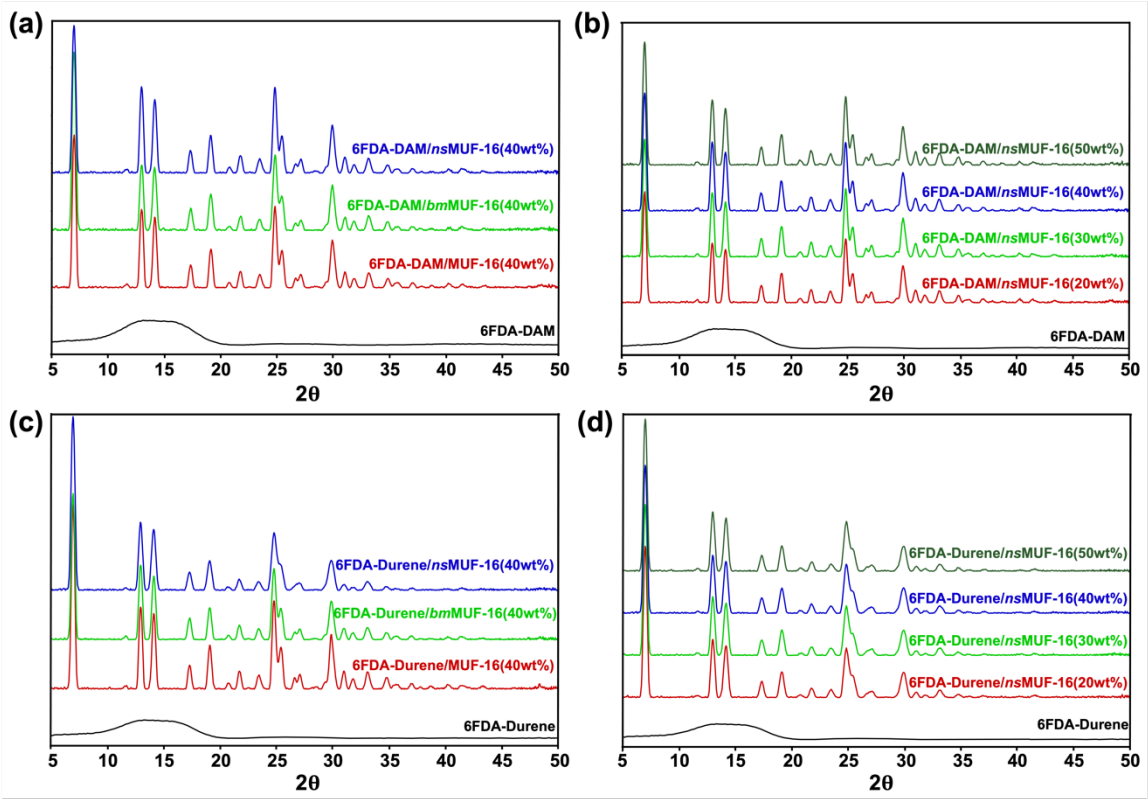


**Figure 4.4** PXRD patterns of (a) 6FDA-DAM based membranes with different MUF-16 crystal size (40 wt.% loading) and (b) 6FDA-DAM based membranes with different nsMUF-16 loading (20 wt.% to 50 wt.%). (c) 6FDA-Durene based membranes with different MUF-16 crystal size (40 wt.% loading) and (b) 6FDA-Durene based membranes with different nsMUF-16 loading (20 wt.% to 50 wt.%).

In addition, the in-plane XRD measurement was carried out to further investigate the orientation of MUF-16 crystal in the MMMs. The XRD patterns of associated membrane (Fig. 4.5a) show only two major Bragg diffractions indexed as the (2,0,0), (400) crystallographic planes of MUF-16 structure, demonstrating the strong preferential in-plane alignment of (200)

nanosheets and the attainment of the desired uniform [001]-oriented continuous MMM. These results demonstrate that the successful translation of *ns*MUF-16 into a [001]-oriented macroscopic membrane, where 1D channels of nanosheets are all parallel, an ideal scenario for distinct molecular separation (Fig. 4.5b).

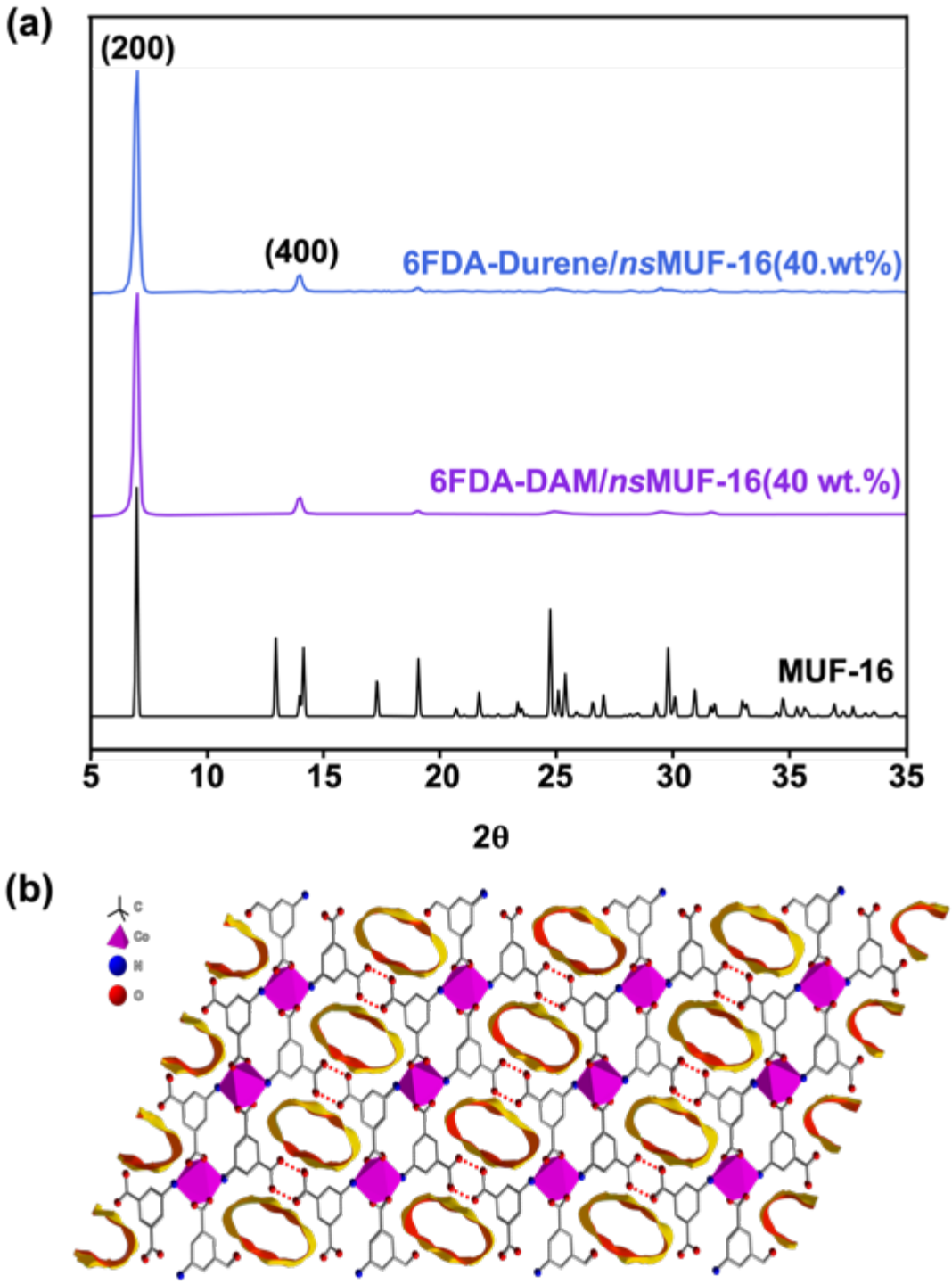


**Figure 4.5** (a) XRD patterns of 40 wt.% *ns*MUF-16 in 6FDA-DAM and 6FDA-Durene matrix. (b) Structure view along the [001] direction of MUF-16.

**Morphologies of membranes**

Subsequently, the as-synthesized MUF-16 with different crystal sizes were incorporated into glassy PI (6FDA-DAM and 6FDA-Durene) matrix to fabricate MMMs. And the interfacial properties of the polymer/MUF-16 in MMMs were investigated using SEM. Here, 6FDA-Durene based MMMs are taken as an example. As shown in Figs. 4.6a and 4.6b, the pure 6FDA-Durene membrane has a smooth morphology with a thickness of 70 μm. In addition, the *ns*MUF-16 crystals were uniformly distributed throughout the polymer matrix (Figs. 4.6c and 4.6d). In particular, the membrane showed an excellent MOF/polymer interface with no voids was observed, which can provide the good separation performance (Fig. 4.6g). This good MOF/polymer interface was due to the small crystal size that allows for good dispersion of *ns*MUF-16 in the membrane without any sedimentation; and the formation of hydrogen bonds between *ns*MUF-16 and 6FDA-Durene polymer chains, ensuring a dense morphology. This is supported by the FTIR results (Fig. 4.7). Similarly, *ns*MUF-16/6FDA-DAM MMMs exhibits a uniform and dense membrane structure (Figs. 4.6e, 4.6f and 4.6g). As a result, *bm*MUF-16 can display the similar morphology in membrane (see Electronic Appendix C). MUF-16 (solvothermally synthesized), on the other hand, does not adhere to polymer matrices as well as *ns*MUF-16 due to its enormous crystal size (Figs. 4.6i and 4.6j). Some cracks can be seen on the membrane surface (Fig. 4.6i), and filler sedimentation occurred during the membrane fabrication (Fig. 4.6j). Therefore, it is challenging to use the large MUF-16 crystals of solvothermal synthesis to fabricate MMMs for advanced separation properties due to the visible interfacial defects in the membranes.

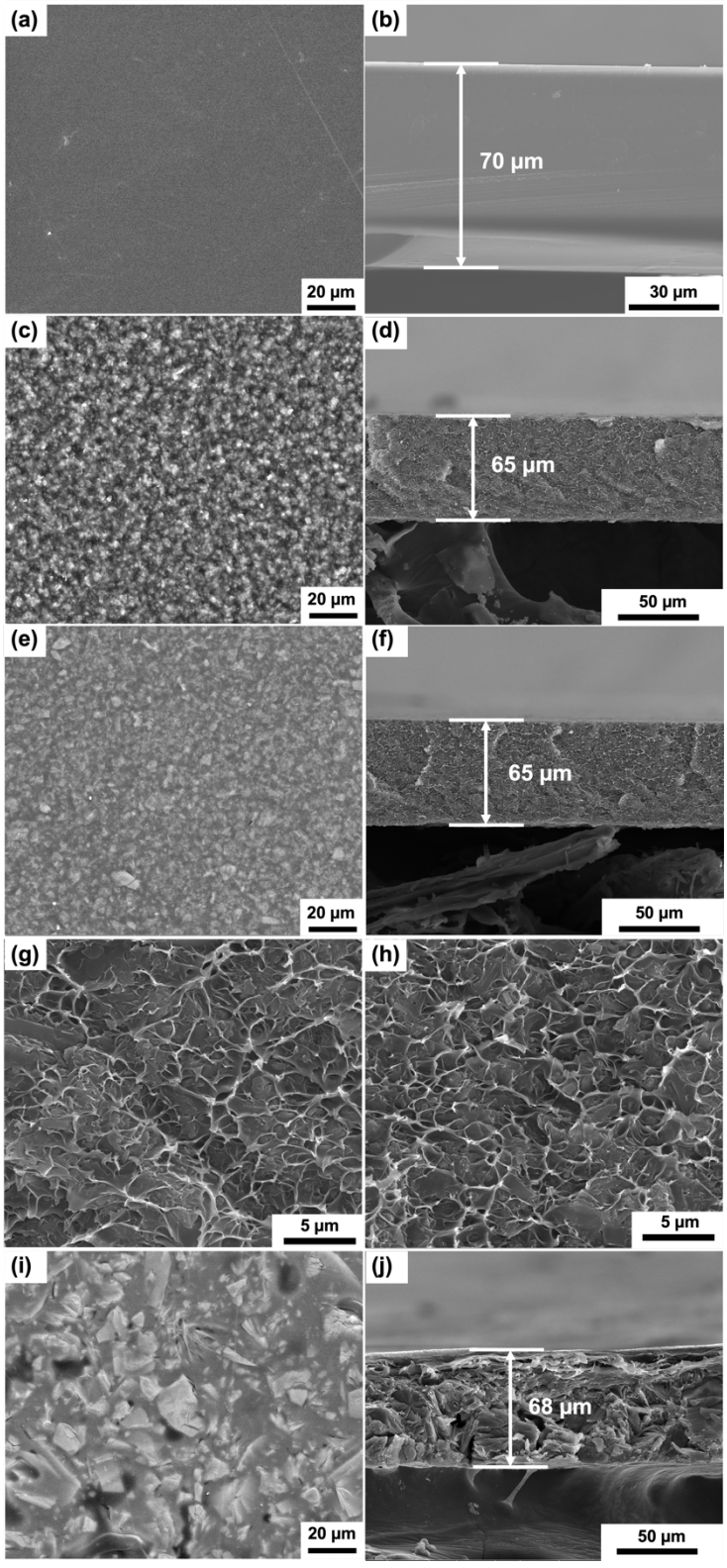


**Figure 4.6** SEM morphologies of (a) surface and (b) cross section of pure 6FDA-Durene membrane, (c) surface and (b) cross section of 6FDA-Durene membrane with 40 wt.% *ns*MUF-16, and (e) surface and (f) cross section of 6FDA-Durene membrane with 40 wt.% *bm*MUF-16. High resolution cross section of (g) 6FDA-Durene membrane with 40 wt.%

*ns*MUF-16 and (h) 6FDA-Durene membrane with 40 wt.% *bm*MUF-16. SEM morphologies of (i) surface and (j) cross section of 6FDA-Durene membrane with 40 wt.% MUF-16.

**FTIR spectra of the membranes**

The FTIR spectra of the fabricated MMMs are shown in Fig. 4.7. The symmetric –C=O stretching at around 1725 $cm^{-1}$ was found to be shifted in *ns*MUF-16 incorporated 6FDA-DAM matrix (Figs. 4.7a and 4.7b), suggesting a hydrogen bonding interaction (Fig. 4.7c).[261-262] In addition, the as-prepared *ns*MUF-16(40 wt.%)/6FDA-Durene MMMs shows a similar trend (Figs. 4.7d and 4.7e), indicating the formation of hydrogen bonding in the *ns*MUF-16 based 6FDA-Durene membranes (Fig. 4.7f).

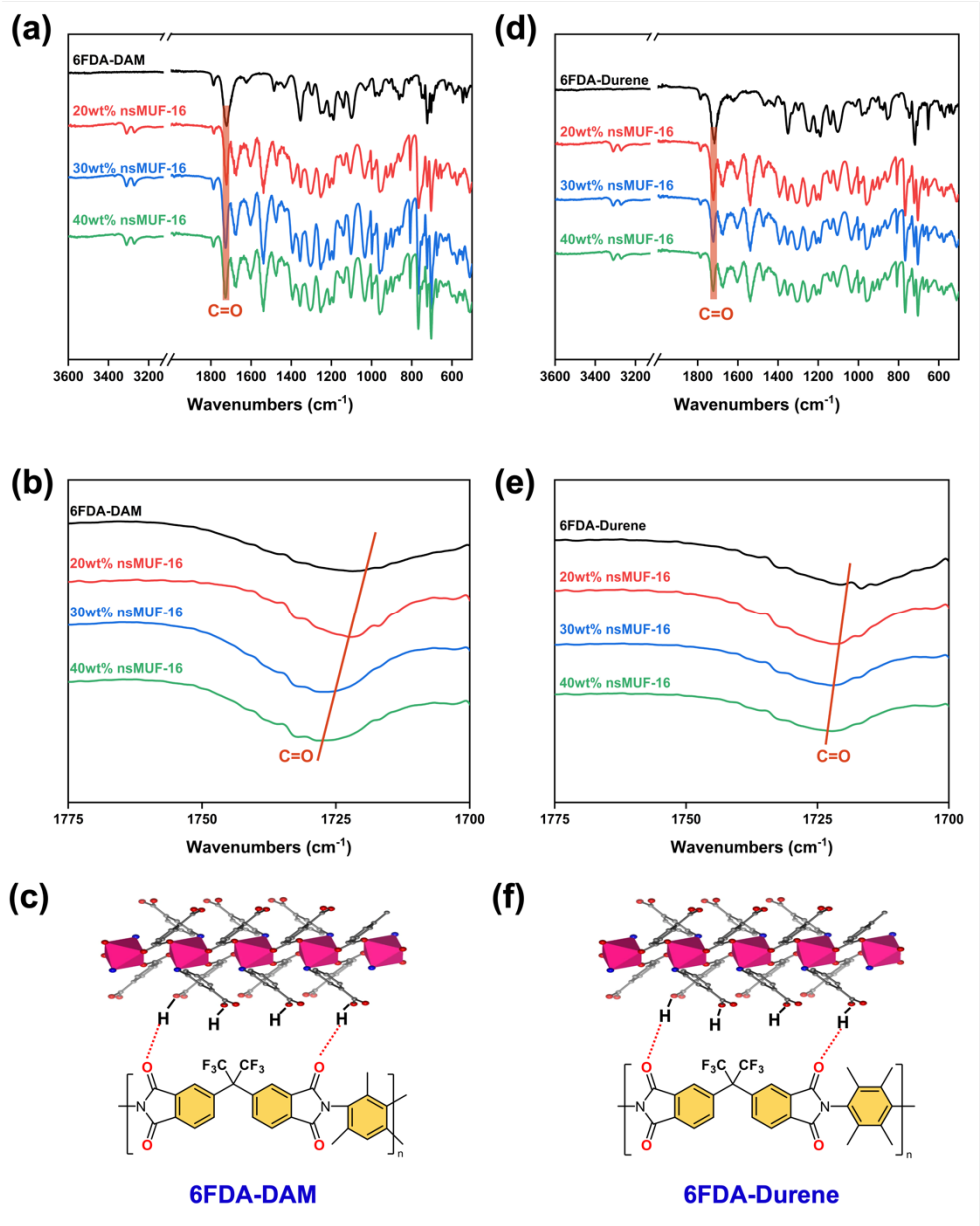


**Figure 4.7** FTIR spectra of 6FDA-DAM (a, b) and 6FDA-Durene (d, e) based MMMs with different *ns*MUF-16 loadings. Schematic diagram of hydrogen bonding between *ns*MUF-16 and (c) 6FDA-DAM and (f) 6FDA-Durene.

### TGA analysis

Thermogravimetric analysis (TGA) under $N_2$ atmosphere of the neat 6FDA-DAM membrane and the MMM samples incorporated with 40 wt.% MUF-16 fillers of different crystal sizes (MUF-16, *ns*MUF-16, and *bm*MUF-16) are shown in Fig. 4.8a. Residual water and solvents loss can be observed up to 100 °C. Upon reaching temperatures of approximately 400°C, all the samples exhibited a consistent and stable state, displaying no noticeable weight

loss. This observation underscores the robust stability of both MUF-16 and the polymers (6FDA-DAM and 6FDA-Durene). In addition, all the MMMs with different filler loadings exhibited the similar trend (Fig. 4.8b). Overall, both MUF-16 and its MMMs exhibited robust thermal stability, underscoring their favorable operational stability throughout the separation process.

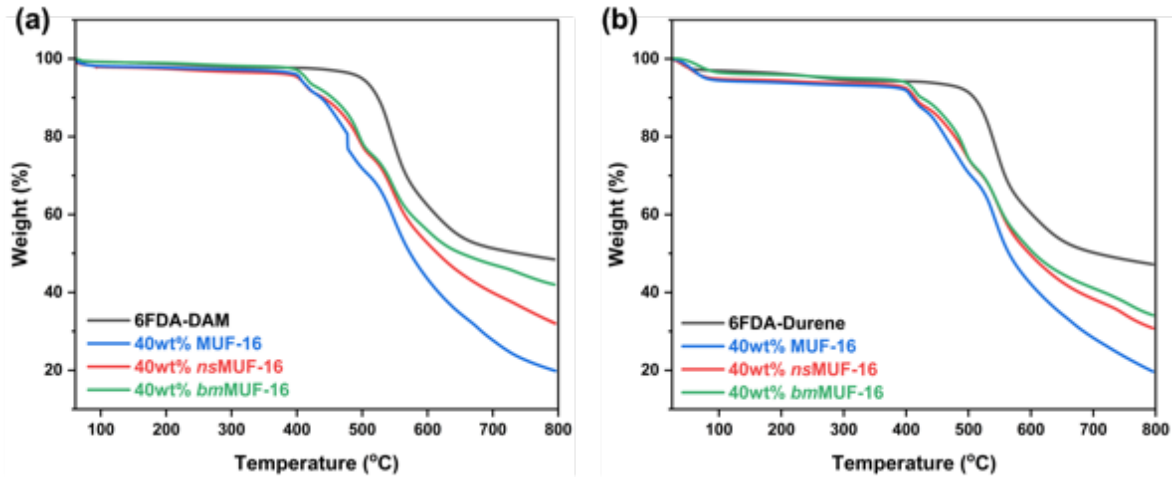


**Figure 4.8** TGA curves of (a) 6FDA-DAM membrane, 6FDA-DAM membrane with 40 wt.% MUF-16, *ns*MUF-16, and *bm*MUF-16, (b) 6FDA-Durene membrane, 6FDA-Durene membrane with 40 wt.% MUF-16, *ns*MUF-16, and *bm*MUF-16.

**Tensile test**

To further investigate the effect of crystal size on the physical properties of the membranes, Young's modulus, and elongation strain tests of membranes with different crystal sizes were evaluated (Figs. 4.9a and 4.9b). It was found that the incorporation of *bm*MUF-16 and *ns*MUF-16 can increase the Young's modulus of the MMMs. In particular, the membrane loaded with *ns*MUF-16 shows a significant increase in Young's modulus, which can be attributed to the improved interfacial compatibility between the crystal and the polymer matrix. Moreover, the membrane fabricated with 40 wt.% of *ns*MUF-16 still maintained excellent flexibility (Fig. 4.9c).

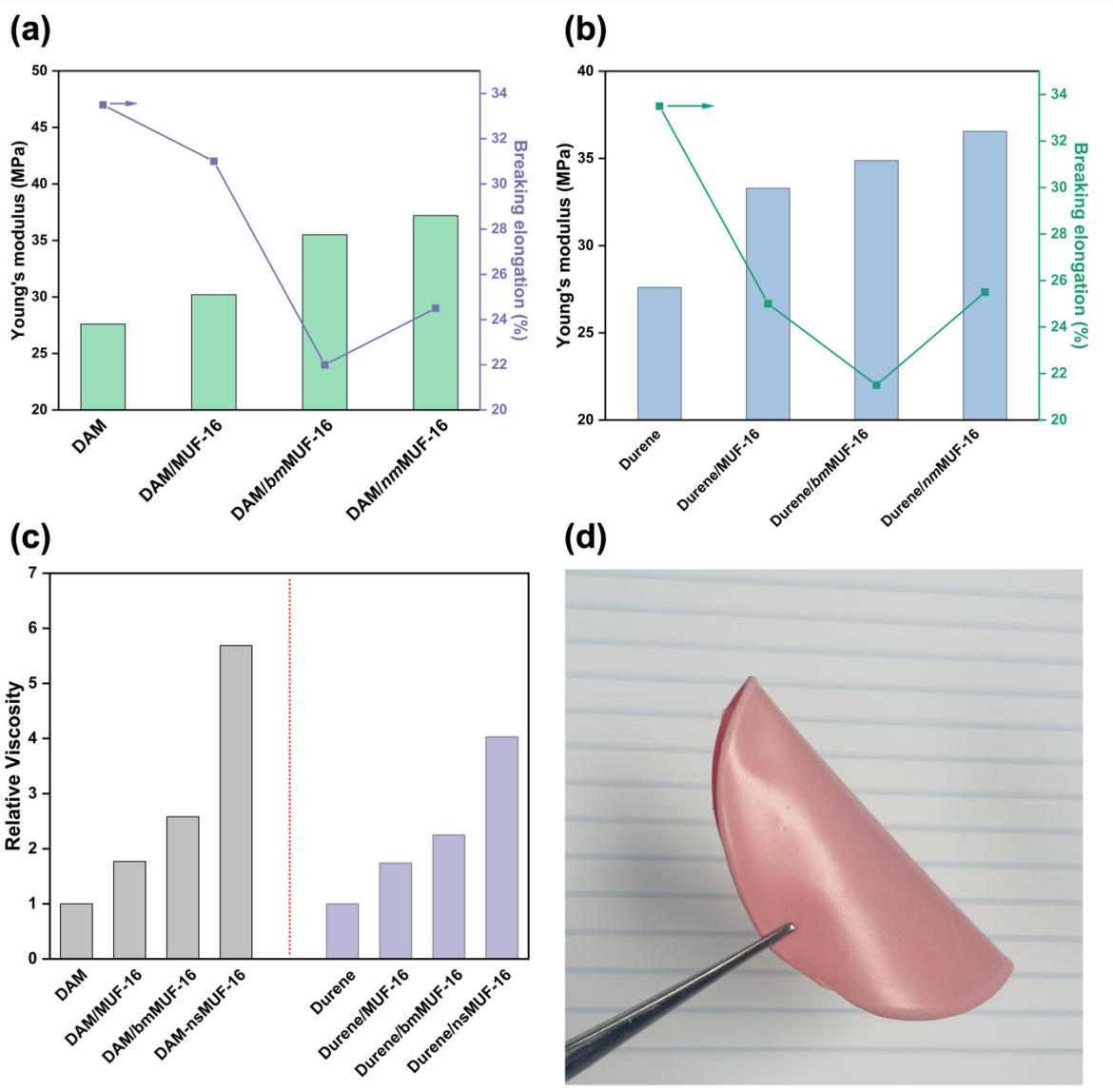


**Figure 4.9** Mechanical studies of the (a) 6FDA-DAM based MMMs and (b) 6FDA-Durene based MMMs. (c) Optical image of *ns*MUF-16 (40 wt.%)/6FDA-Durene membrane.

### Viscosity test

The viscosity of the MOF/polymer casting solution was tested to elucidate the interaction between MOF and polymer. The MOF-polymer suspensions were fabricated first using the same amount of polymer and MOFs (different crystal size but same loading of 40 wt.%) and stirring at room temperature overnight. All the MOF-polymer suspensions became more viscous than the polymer. For easier comparison, a relative viscosity was used to compare with the pure polymer suspension. The relative viscosity of the solution doped with *ns*MUF-16 was apparently higher than that of the other MOF-polymer suspensions (Fig. 4.10). This high

viscosity indicates a strong interaction between the MOF and polymer materials, which could be attributed to the formation of hydrogen bonding between *ns*MUF-16 and the polymer. This also explains the better MOF-polymer interfacial compatibility in the MMMs when the nanoscale MUF-16 crystallites are employed.

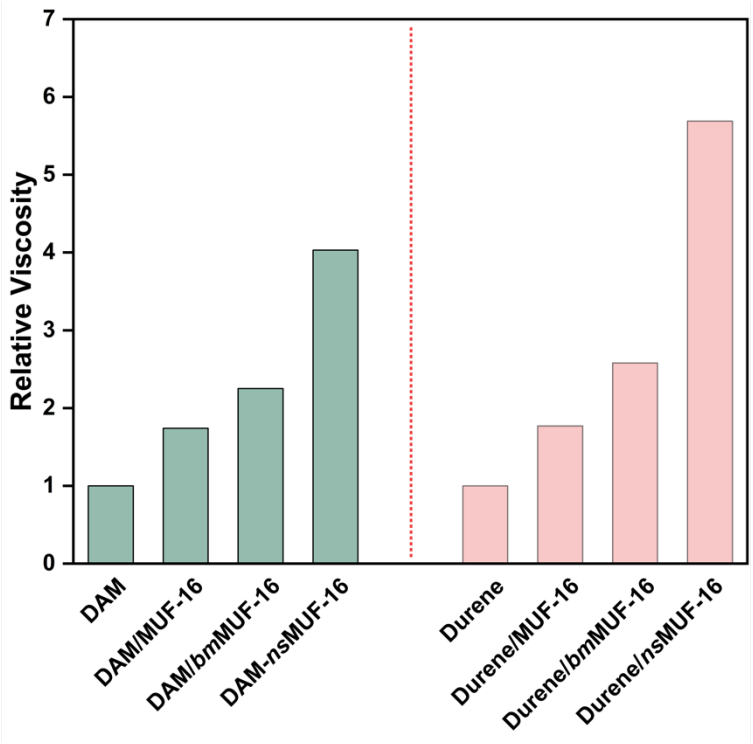


**Figure 4.10** Relative viscosity comparison of MOF/polymer and polymer suspension (40 wt.% loading).

### 4.2.4 Gas separation performance of MMMs

#### 4.2.4.1 Impact of crystal size on gas separation performance

To assess the impact of filler crystal size, single gas permeation experiments were conducted on 6FDA-Durene-based MMMs containing 40 wt.% MUF-16 fillers of varying sizes (MUF-16, *bm*MUF-16, and *ns*MUF-16). Notably, a predictable trend emerged wherein gas separation performance was enhanced as crystal size diminished (Fig. 4.11a). This is because the smaller particles could minimize or prevent the formation of interfacial voids within the membrane structure. This hypothesis can be supported by the SEM images of the membranes (Fig. 4.6 and Figs. C1 to C2, Electronic Appendix C).

The *ns*MUF-16 loaded membrane exhibited the optimal separation performance in contrast to membranes loaded with MUF-16 or *bm*MUF-16. This is mainly attributed to the smaller size

of *ns*MUF-16 fillers, which could eliminate interfacial voids while promoting better interfacial compatibility between the polymer phase and *ns*MUF-16. In contrast, membranes containing MUF-16 or *bm*MUF-16 exhibited a lower gas selectivity, presumably due to the presence of interfacial voids. These findings are consistent with the results obtained from SEM analysis, tensile tests, and viscosity assessments. Similar trends were also observed in the 6FDA-DAM based membranes (Fig. 4.11b).

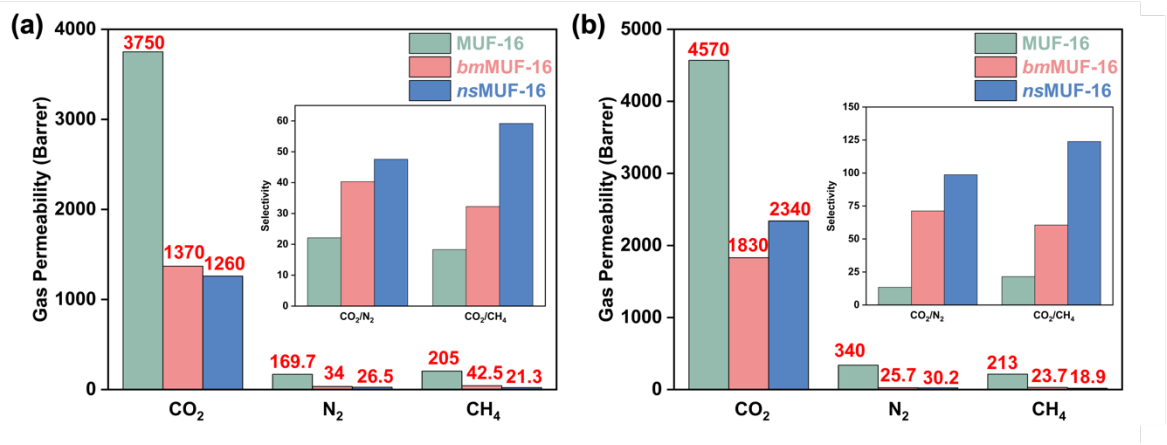


**Figure 4.11** Gas permeability of (a) 6FDA-DAM and (b) 6FDA-Durene based membranes with different crystal size (MUF-16, *bm*MUF-16, and *ns*MUF-16).

### 4.2.4.2 MMMs loaded with 40 wt.% *ns*MUF-16

The remarkable separation performance of *ns*MUF-16 based MMMs was confirmed by conducting further single and mixed gas permeation tests. During the single gas tests, we carefully investigated the influence of varying *ns*MUF-16 loadings on the separation performance. The *ns*MUF-16 within MMMs could lead to a substantial enhancement of $CO_2$ permeability and the $CO_2/N_2$ and $CO_2/CH_4$ selectivities. Taking *ns*MUF-16/6FDA-DAM membrane as an example, the $CO_2$ permeability exhibited an upward trend as increasing the *ns*MUF-16 loadings, whereas the $N_2$ and $CH_4$ permeabilities declined (Fig. 4.12a). This behavior can be attributed to the pronounced affinity of *ns*MUF-16 for $CO_2$, coupled with the constraining effect on the transport of $N_2$ and $CH_4$. Notably, when the loading reached 40 wt.%, the corresponding membrane achieved the best separation performance ($CO_2$ permeability: 1250 Barrer, $CO_2/N_2$ selectivity: 47.5 and $CO_2/CH_4$ selectivity: 59.2) (Fig. 4.12b). However, a subsequent increase in loading to 50 wt.% led to a decrease in both $CO_2$ permeability and selectivity. This reduction in performance could be attributed to particle aggregation caused by the high *ns*MUF-16 loading. This aggregation might hinder $CO_2$ selectivity of the membrane,

resulting in decreased gas separation performance. It is worth highlighting that both 6FDA-DAM and -Durene exhibited a similar trend in responses to the *ns*MUF-16 loading (Figs. 4.12c and 4.12d). Understanding the loading effect could offers a potential to customize and optimize the design of *ns*MUF-16-based MMMs for a wide range of separation applications.

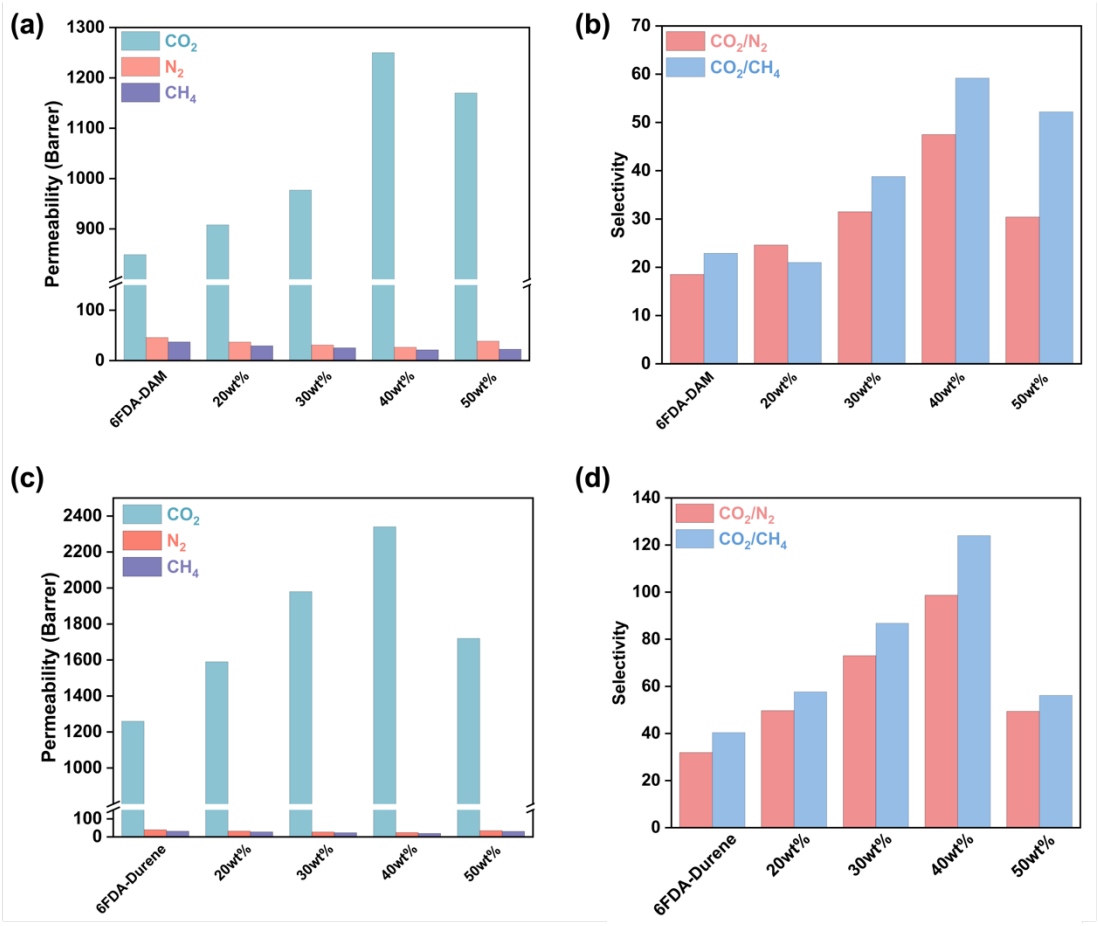


**Figure 4.12** $CO_2$, $N_2$ and $CH_4$ gas permeabilities of (a) 6FDA-DAM and (c) 6FDA-Durene based MMMs with different *ns*MUF-16 loading. Corresponding $CO_2/N_2$ and $CO_2/CH_4$ selectivity of (b) 6FDA-DAM and (d) 6FDA-DAM based MMMs with different *ns*MUF-16 loading.

Furthermore, the performance of the membrane containing 40wt% *ns*MUF-16 was evaluated with mixed gas compositions using different varying $CO_2$ concentrations ($CO_2/N_2(CH_4)$: 10/90; 20/80 and 50/50) under a constant feed pressure of two bar and at room temperature (20 °C). Compared to the single-gas tests, the mixed-gas tests displayed reduced separation performance due to a competing transport behavior as the mixed gases pass through the membrane.[264-265] Notably, the $CO_2$ permeability gradually increased at higher $CO_2$

concentration in the feed stream ($CO_2/N_2$ from 10/90 to 50/50), and the $CO_2/N_2$ selectivity was also improved accordingly (Figs. 4.13a and 4.13c). This observed trend underlines the pronounced effect of the preferential adsorption of $CO_2$ by *ns*MUF-16 within the membrane, which significantly limits the passage of $N_2$. As a result, this phenomenon contributes to both enhanced $CO_2$ permeability and $CO_2/N_2$ selectivity. And when the $CO_2$ concentration was equal to $N_2$, the resulting separation was close to the single gas test. Furthermore, this behavior was consistently observed for all MMMs fabricated for $CO_2/CH_4$ separation (Figs. 4.13b and 4.13d), indicating the significant role played by the homogeneous integration of *ns*MUF-16 and the polymer matrix in our study. This synergy effect between *ns*MUF-16 and polymers underscores the crucial role of meticulous material selection and formulation in dictating the performance of the mixed matrix membranes.

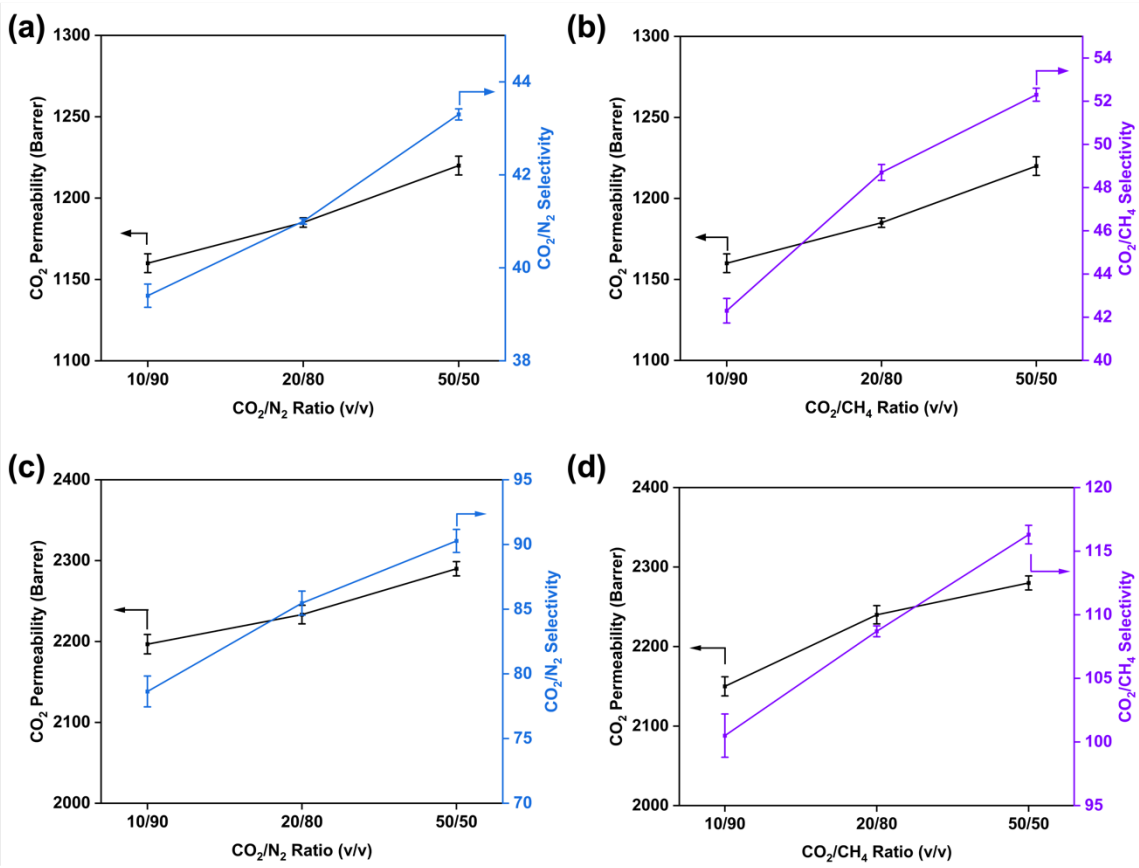


**Figure 4.13** Effects of feed $CO_2$ concentration on $CO_2$ permeability and (a) (c) $CO_2/N_2$ and (b) (d) $CO_2/CH_4$ selectivity for *ns*MUF-16 (40 wt.%) based 6FDA-DAM (a) (b) and 6FDA-Durene (c) (d) mixed-gas permeability ($CO_2/N_2(CH_4)$: 50/50, 20/80 and 10/90 at 2 bar, 20°C). (Error bar: standard deviation).

#### 4.2.4.4 Long-term gas permeability

To evaluate the long-term stability of the membranes, the time-dependent $CO_2/N_2$ and $CO_2/CH_4$ separations was performed for the MMMs loaded with 40 wt.% *ns*MUF-16. Taking *ns*MUF-16/6FDA-DAM membrane as an example, pure gas test displayed a relatively stable separation performance over a span of 12 hours in the initial stage (Fig. 4.14a). Subsequently, the membrane was tested with mixed gas involving varying $CO_2$ concentration (10/90, 20/80 and 50/50) for 18 hours. During this stage, a gradual increase in $CO_2$ permeability was observed as the $CO_2$ feed concentration increased from $CO_2/N_2$ ($CH_4$) ration of 10/90 to 50/50. This rise in $CO_2$ permeability was accompanied by an improvement in the corresponding selectivities. When $CO_2$ concentration reached the same level as $N_2$ ($CH_4$), the resulting separation performance became comparable to the initial pure gas test. And the whole mixed gas test process displayed the reduced gas separation performance because of the competing transport behavior.[264-265] After cycling the mixed gas test with varying $CO_2$ concentrations, a subsequent pure gas test was performed to access the ongoing separation performance. This subsequent test showed a consistent $CO_2$ permeability of 1270 Barrer, and $CO_2/N_2$ selectivity of 47 and $CO_2/CH_4$ selectivity of 56, which were close to that during the initial pure gas tests (Fig. 4.14a). A similar trend could also be observed in the *ns*MUF-16/6FDA-Durene membrane, further demonstrating the excellent operational stability of our MUF-16 in polymer matrix (Fig. 4.14b). And these outcomes underscore the robustness and durability of our membranes under different conditions, affirming its reliability for sustained separation applications.

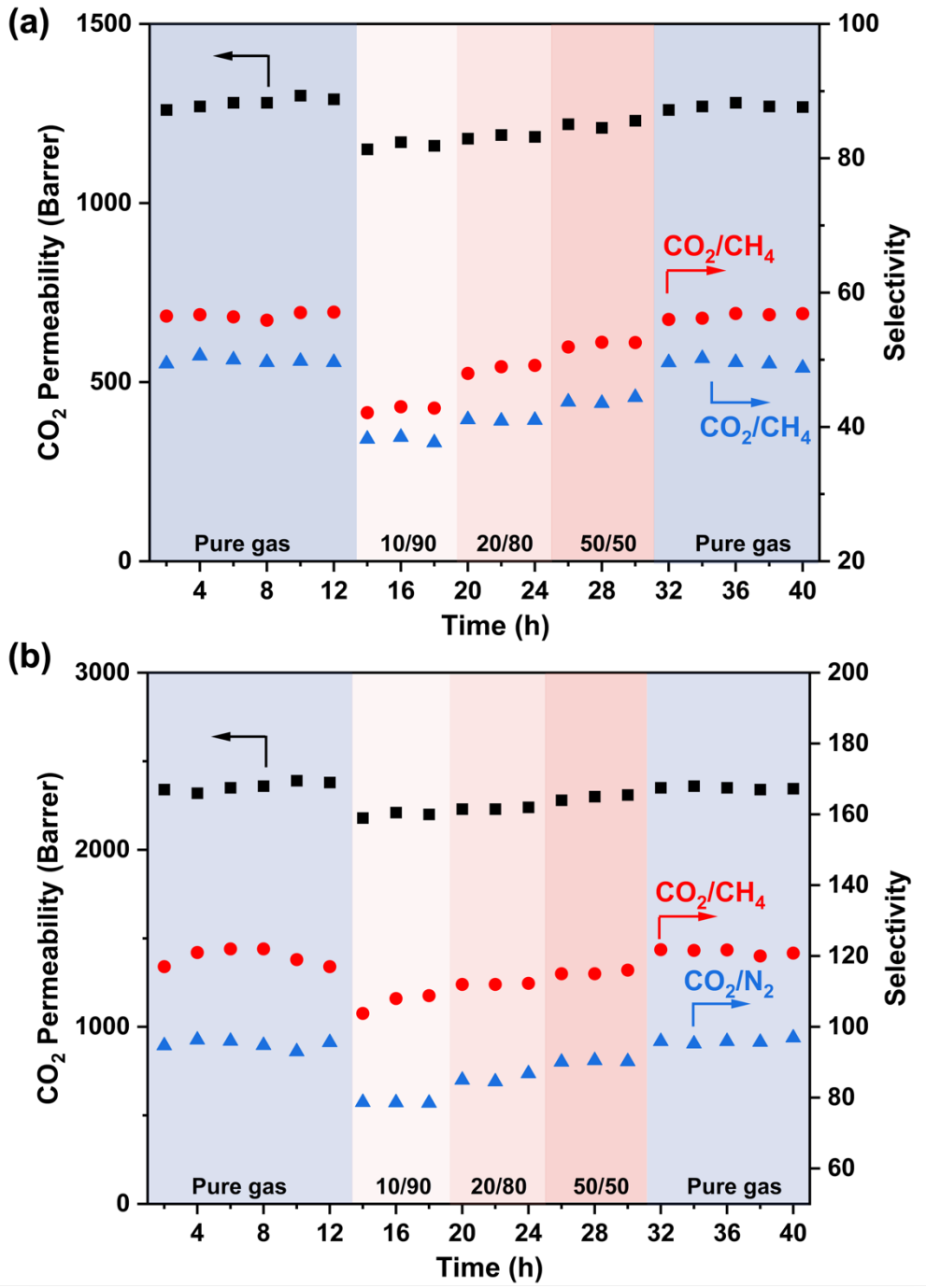


**Figure 4.14** Long-term stability test of (a) 6FDA-DAM and (b) 6FDA-Durene with 40 wt.% *ns*MUF-16.

#### 4.2.4.5 Comparison with other MMMs.

A visual representation of the comparison between the $CO_2/N_2$ and $CO_2/CH_4$ separation performance of *ns*MUF-16 based MMMs and other reported MMMs are shown in Fig. 4.15. Notably, our *ns*MUF-16 based both 6FDA-DAM or 6FDA-Durene membranes for $CO_2/N_2$

separation have surpassed the 2008 upper bound limit. Impressively, the incorporation of *ns*MUF-16 in 6FDA-Durene matrix has yielded even more remarkable separation performance, surpassing the 2019 $CO_2/CH_4$ upper bound limit. A key highlight of our membranes is the superior $CO_2/N_2$ and $CO_2/CH_4$ selectivities, consistently outperforming those reported in existing literature. At the same time, these membranes have maintained a relatively high $CO_2$ permeability. This selectivity and permeability balance underscores the unique advantages of our membrane design. The exceptional separation properties of our membranes can be attributed to two crucial factors: the strong affinity of MUF-16 for $CO_2$ and the excellent interfacial compatibility of *ns*MUF-16 within the polymeric matrix. This combination has enabled our membranes to not only achieve enhanced $CO_2$ permeability but also realize elevated $CO_2/N_2$ and $CO_2/CH_4$ selectivities, indicating our membranes as promising candidates for advanced separation applications.

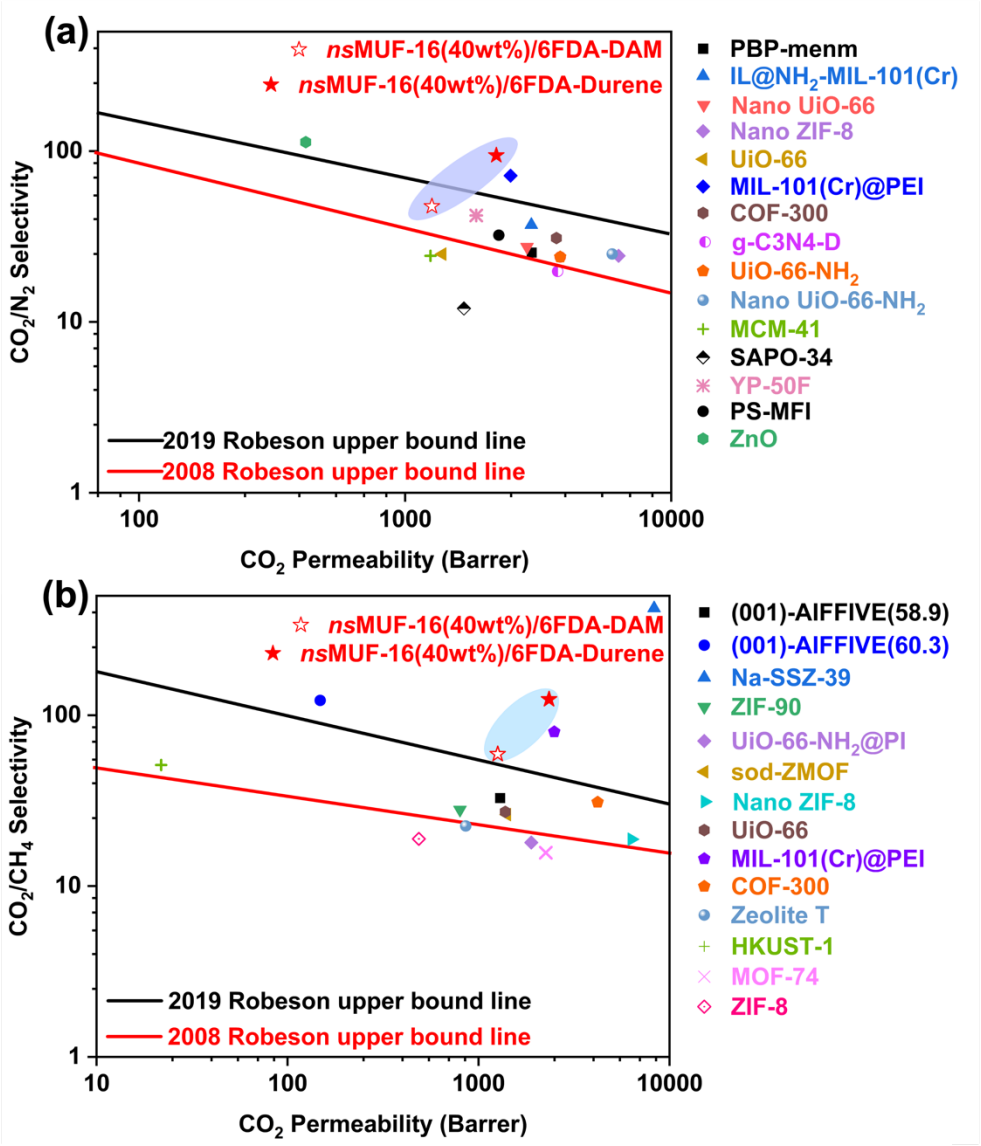


**Figure 4.15** Plots of (a) $CO_2/N_2$ and (b) $CO_2/CH_4$ selectivities versus $CO_2$ permeability from a recent literature review of MMMs. (PBP-menm,[266] IL@$NH_2$-MIL-101(Cr),[267] nano UiO-66,[122] nano ZIF-8,[117] UiO-66,[268] MIL-101(Cr)@PEI,[269] COF-300,[270] g-$C_3N_4$-D,[271] UiO-66-$NH_2$,[272] nano UiO-66-$NH_2$,[272] MCM-41,[273] SAPO-34,[274] YP-50F,[275] PS-MFI,[276] ZnO,[277] (001)-AIFFIVE (58.9) and (001)-AIFFIVE (60.3),[154] Na-SSZ-39,[59] ZIF-90,[278] UiO-66-$NH_2$@PI,[122] sod-ZMOF,[279] UiO-66/AO-PIM-1,[268] zeolite T,[280] HKAUST,[281] MOF-74,[282] ZIF-8.[283])

#### 4.2.4.6 Maxwell Model predication

Through fitting the predicted separation preformation (back-calculated using Maxwell model) of MMMs with different MOF loading, we obtained the theoretical $CO_2$ permeability, $CO_2/N_2$ and $CO_2/CH_4$ selectivity of pure MUF-16, which are 5649 Barrer, 3922 and 2556,

respectively. This indicates that the pure MUF-16 membrane has better $CO_2$ separation performance than most of MOFs (Table C. 1, Electronic Appendix). In addition, the experimentally obtained $CO_2$ permeability and $CO_2/N_2$, $CO_2/CH_4$ selectivities of membranes at different MOF loading are shown in Figs. 4.16a and 4.16b. The good agreement between the experimental and theoretical predictions indicates that the excellent interfacial compatibility between *ns*MUF-16 and polymer matrices.

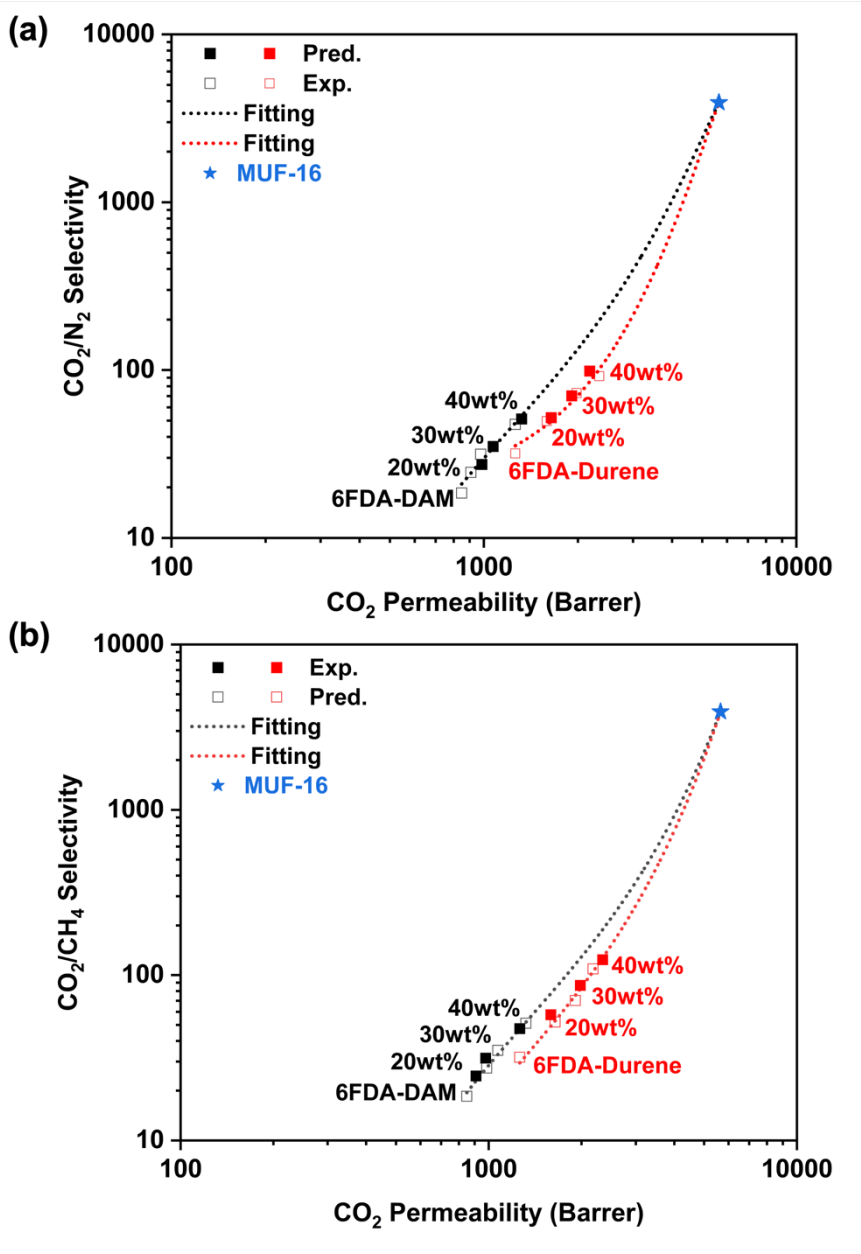


**Figure 4.16** $CO_2$ permeability (x-axis), and (a) $CO_2/N_2$ or (b) $CO_2/CH_4$ selectivity (y-axis) of *ns*MUF-16/polymer mixed matrix membranes (*ns*MUF-16 loading in 6FDA-DAM of 20, 30 and 40 wt.%; in 6FDA-Durene of 20, 30, 40 wt.% respectively). The permeability properties of the pure MUF-16 and *ns*MUF-16/polymer mixed matrix membranes are predicted by using

the measured permeability and selectivity of the 6FDA-DAM membranes, 6FDA-Durene membranes, and *ns*MUF-16/6FDA-DAM, *ns*MUF-16/6FDA-Durene mixed matrix membranes according to the theoretical model for mixed matrix membranes (see Electronic Appendix C).

## 4.3 Conclusion

Tuning the crystallite sizes of added MOFs is a viable way to improve the mixed matrix membrane properties beyond the current performance limits of polymeric membrane materials. The ultra-high performance MUF-16-filled MMMs for $CO_2$ separations were obtained by regulating the crystal size, which showed unprecedented $CO_2$ separation performance, surpassing that of most MOF-based MMMs. Importantly, the achievement of in-plane alignment and extremely high loading of (001) *ns*MUF-16 is significantly responsible for the achieved separation performance. We developed a scalable method to tailor MOF crystal morphology and fabricate defect-free MOF-filled membranes with a commercially available glassy polymer, thus expanding the range of high-performance MOF-filled MMMs for advanced gas separations, especially those MOFs that are difficult to engineer into defect-free membranes.

# Chapter 5 Investigation of MUF-15 and its analogues as fillers for 6FDA-DAM-based membranes

## 5.1 Introduction

Natural gas is an important energy source worldwide.[284] However, raw natural gas often contains high levels of $CO_2$ that must be removed.[285] The separation of $CO_2$ and $CH_4$ can be achieved using membranes. Membranes can offer advantages of a small footprint and high separation efficiency.[286-287] Despite dominating the membrane market, polymer membranes encounter an intrinsic trade-off between gas permeability and selectivity.[72] To address this challenge, mixed matrix membranes (MMMs), consisting of a polymer matrix and porous fillers, have been investigated. MMMs combine the processibility of polymers with the gas separation performance of the fillers. The Ultimate goal is to produce membranes that combine high permeabilities with high selectivities. Metal-organic framework (MOF) fillers are prominent.[74, 154, 162, 288]

MOFs are porous crystalline materials that that are composed of metal nodes and organic linkers. The well-defined pore sizes, high gas uptake capacity, excellent thermal and chemical stability make them as hot materials in MMMs preparation.[74] Notably, based on the advantage of their tunable pore architectures, MOFs with different pore environments could be tailored for improved gas transport properties via post-modification or functionalization approaches, which could also solve interfacial problems in MMMs.[289] The most common strategy is the direct synthesis MOFs using modified organic ligands.[290-291] For example, a representative zirconium MOF, UiO-66 (UiO: University of Oslo), $Zr_6(\mu_3\text{-}O)_4(\mu_3OH)_4(O_2C{-}C_6H_4{-}CO_2)_{12}$ is formed by connecting octahedral $Zr_6O_4(OH)_4$ with organic linker 1,4-benzene-dicarboxylate (BDC). The BDC can be functionalized with different functional groups (-COOH, $-NH_2$). In this manner, UiO-66 and its two derivatives (UiO-66-$NH_2$ and UiO-66-COOH) were incorporated in 6FDA-DAM matrix. in this way, the interfacial boundaries in the membrane could be alleviated. Therefore, the resulting MMMs demonstrated improved $CO_2$ permeability and excellent $CO_2/CH_4$ selectivity.[124] Similarly, two other traditional MOFs, MIL-53 and ZIF-8, were functionalized with different amine groups were synthesized and used for MMMs fabrication and improved MOF-polymer interfacial interaction.[292-294]

MUF-15 (Massey University Framework-15) $[Co_6(\mu_3OH)_2(ipa)_5(H_2O)_2]$ could be constructed by coordinating hexanuclear cobalt(II) clusters with isophthalate (ipa) linkers.[295]

Then it was used for MMMs fabrication based PIM-1 for gas separation.[115] Although the fabricated MMMs showed improved gas separation performance, the interfacial issues between PIM-1 chains and MUF-15 cannot be completely avoided during the MMMs fabrication due to the weak interface affinity and limited gas solubility, thus hindering its further application. Therefore, how to improve the interfacial compatibility is important for the ideal MMMs with both high gas permeability and selectivity.

Due to the unique structure of MUF-15, the phenyl rings of the ipa ligands are directed towards the void space, suggesting that ipa ligand can be substituted with different functional groups (orange spheres in Fig. 5.1a).[296] Therefore, the analogues of MUF-15 can be obtained. The functionalized MUF-15 with different groups can be denoted as MUF-15-X $[Co_6(\mu_3OH)_2(ipa\text{-}X)_5(H_2O)_2]$ (X = F, Br, $CH_3$ and $NO_2$). Therefore, these ligand functional groups could endow MUF-15 with different gas sorption properties, which motivates us to investigate its structural properties and gas separation performance by using different functional groups. In this chapter, we presented a study of 6FDA-DAM based MMMs with MUF-15 and its analogues for $CO_2$ separation over $CH_4$ (Fig. 5.1b).

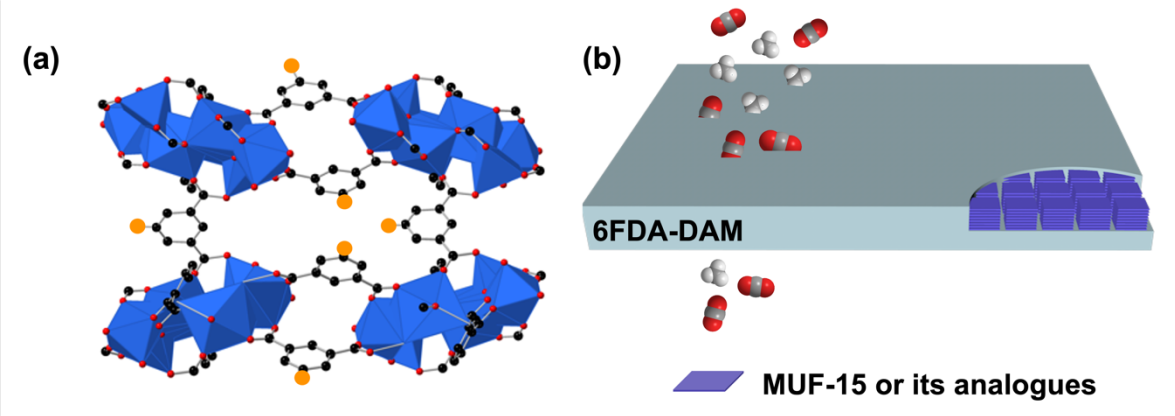


**Figure 5.1** (a) Schematic of the MUF-15 pore structure with the pink spheres highlighting the position of the functional groups. (b) Scheme of 6FDA-DAM based MUF-15 or its analogues MMMs for $CO_2$ separation.

## 5.2 Results and discussion

### 5.2.1 Characterization of MUF-15 and its analogues

PXRD of MUF-15 and its analogues

Crystalline MUF-15 and its analogues (MUF-15-F, MUF-15-Br, and MUF-15-$CH_3$, MUF-15-$NO_2$) were synthesized simply by heating a mixture of cobalt acetate and the 5-

functionalised isophthalic acids (Table D. 1 in Appendix). Their PXRD patterns confirm the isoreticular nature of these MOFs (Figs. 5.2a to Fig. 5.2f).

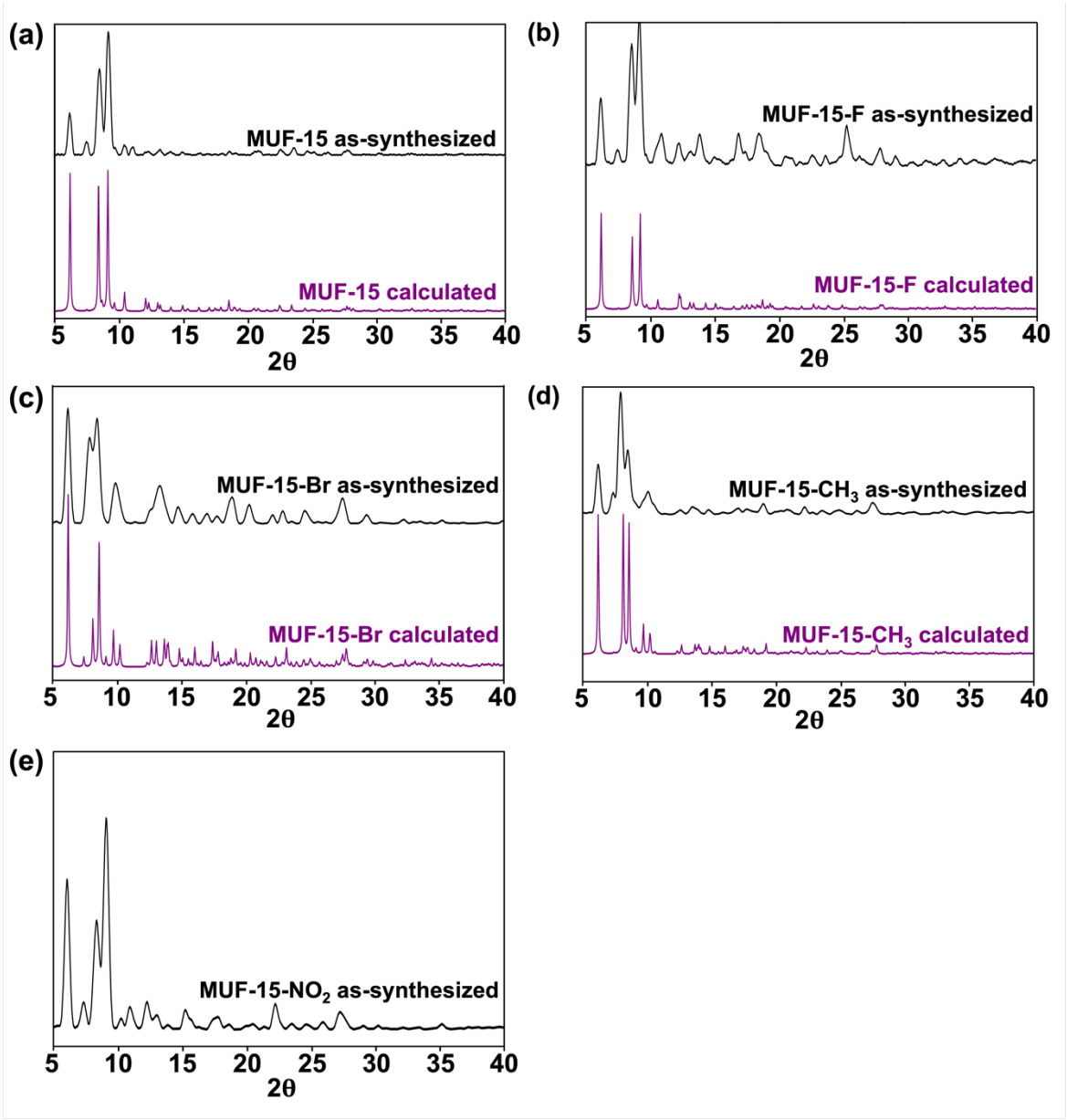


**Figure 5.2** PXRD patterns of (a) MUF-15, (b) MUF-15-F, (c) MUF-15-Br, (d) MUF-15-$CH_3$ and (e) MUF-15-$NO_2$.

### 5.2.2 Characterization of MMMs

#### XRD of MMMs

The MMS were fabricated by blending the MUF-15-X crystallites with 6FDA-DAM in chloroform followed by casting and slow evaporation. In this work, 6FDA-DAM based MMMs were fabricated by incorporating with different MUF-15 loadings (10 to 30 wt.%). And the

resulting membranes showed the maintained structural integrity of MUF-15 fillers (Fig. 5.3a). For the MMMs with the MUF-15 analogues, 30 wt.% loading was used. And their structural integrities were maintained in the corresponding MMMs, indicating an excellent structural stability of these fillers throughout the membrane fabrication process (Figs. 5.3b to 3e).

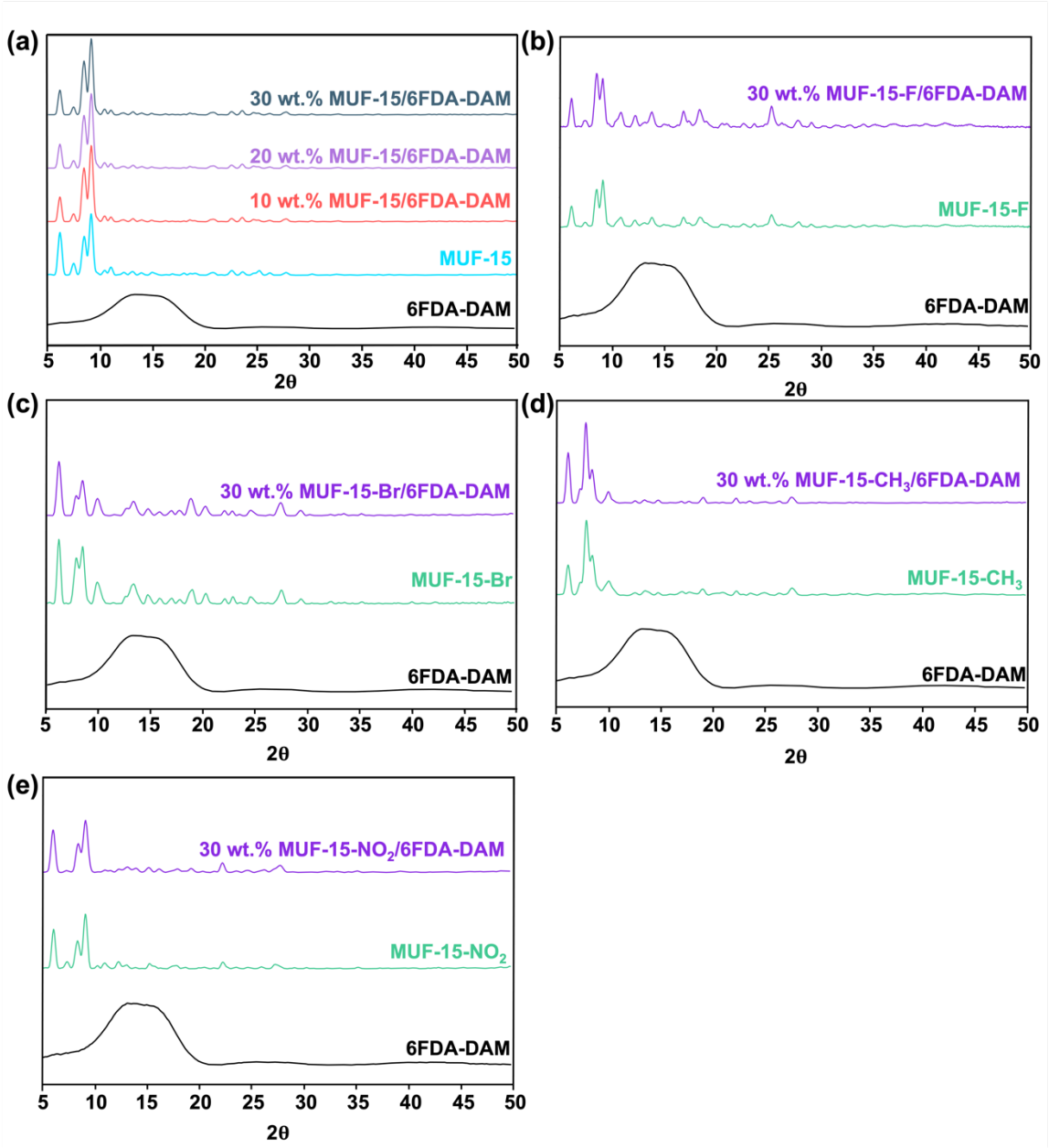


**Figure 5.3** XRD patterns of 6FDA-DAM membranes with (a) MUF-15 (10 to 30 wt.%) and 30 wt.% loading of (b) MUF-15-F, (c) MUF-15-Br, (d) MUF-15-$CH_3$ and (e) MUF-15-$NO_2$.

**SEM morphology of MMMs with MUF-15**

Scanning electron microscopy (SEM) images show that the membranes have a smooth top surface without agglomeration of the fillers from 10 to 20 wt.% (Figs. 5.4a to Fig. 5.4d). When the loading of MUF-15 is further increased to 30 wt.%, a degree of surface roughness becomes

apparent (Fig. 5.4e). However, while the corresponding cross-sectional morphology was still dense and uniform (Fig. 5.4f), which could guarantee the exceptional separation performance.

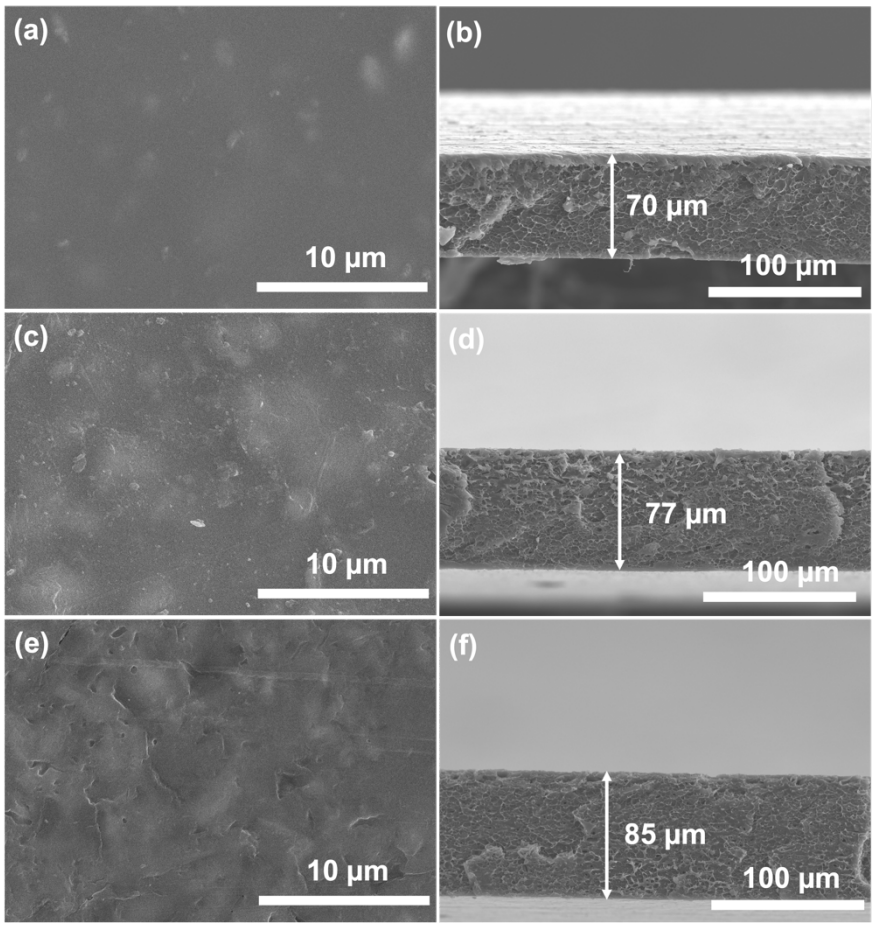


**Figure 5.4** Surface and cross-sectional SEM images of 6FDA-DAM membrane with (a) (b) 10 wt.%, (c) (d) 20 wt.% and (e) (f) 30 wt.% MUF-15.

**SEM morphology of MMMs with MUF-15 analogues**

Cross-sectional images show that no void-space defects are present in the dense MMMs composed of MUF-15-F, which appear as a particularly dense and well-integrated morphology with a uniform distribution of filler particles (Figs. 5.5a and 5.5b). This indicates good interfacial compatibility between the MUF-15-F fillers and the 6FDA-DAM polymer matrix. In contrast, the cross-section images of the MMMs with 30 wt.% MUF-15-Br (Figs. 5.5c and 5.5d), MUF-15-$CH_3$ (Figs. 5.5e and 5.5f) and MUF-15-$NO_2$ (Figs. 5.5g and 5.5h), are noticeably less uniform and more textured. This may indicate filler agglomeration and the potential voids between the filler particles and the polymer and/or the fillers themselves. As detailed in the next section, defect compromised the gas separation performance of the MMMs with MUF-15-Br and MUF-15-$CH_3$, however the performance of the MMM with MUF-15-$NO_2$ was very good.

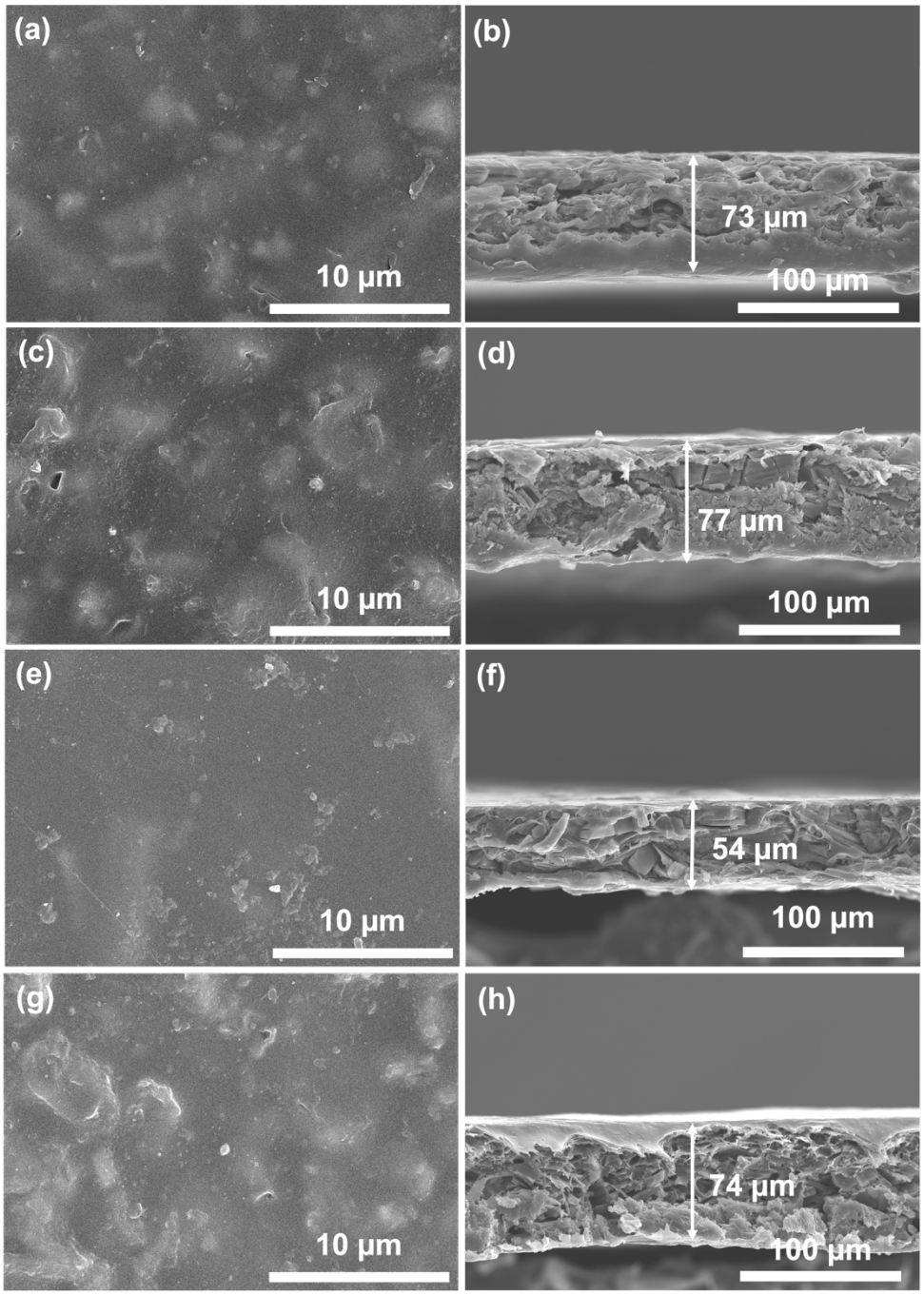


**Figure 5.5** Surface and cross-sectional SEM images of 6FDA-DAM membrane with 30 wt.% loading of (a) (b) MUF-15-F, (c) (d) MUF-15-Br, (e) (f) MUF-15-$CH_3$ and (g) (h) MUF-15-$NO_2$.

**FTIR spectra**

FTIR spectra were measured to confirm the unchanged nature of the MUF-15-X fillers when blended into the 6FDA-DAM matrix (Fig. 5.6). The results reveal that MMMs with different MUF-15 loadings exhibit a broad peak at 1605 $cm^{-1}$ attributed to the C=O vibrations of MUF-15 fillers (Fig. 5.6a). Bands also arise from C-F (1258 $cm^{-1}$) (Fig. 5.6b), C-Br (572

$cm^{-1}$) (Fig. 5.6c), C-H (1258 $cm^{-1}$ and 1301 $cm^{-1}$) (Fig. 5.6d), and N-O (1535 and 1558 $cm^{-1}$) (Fig. 5.6e) vibrational modes where relevant.

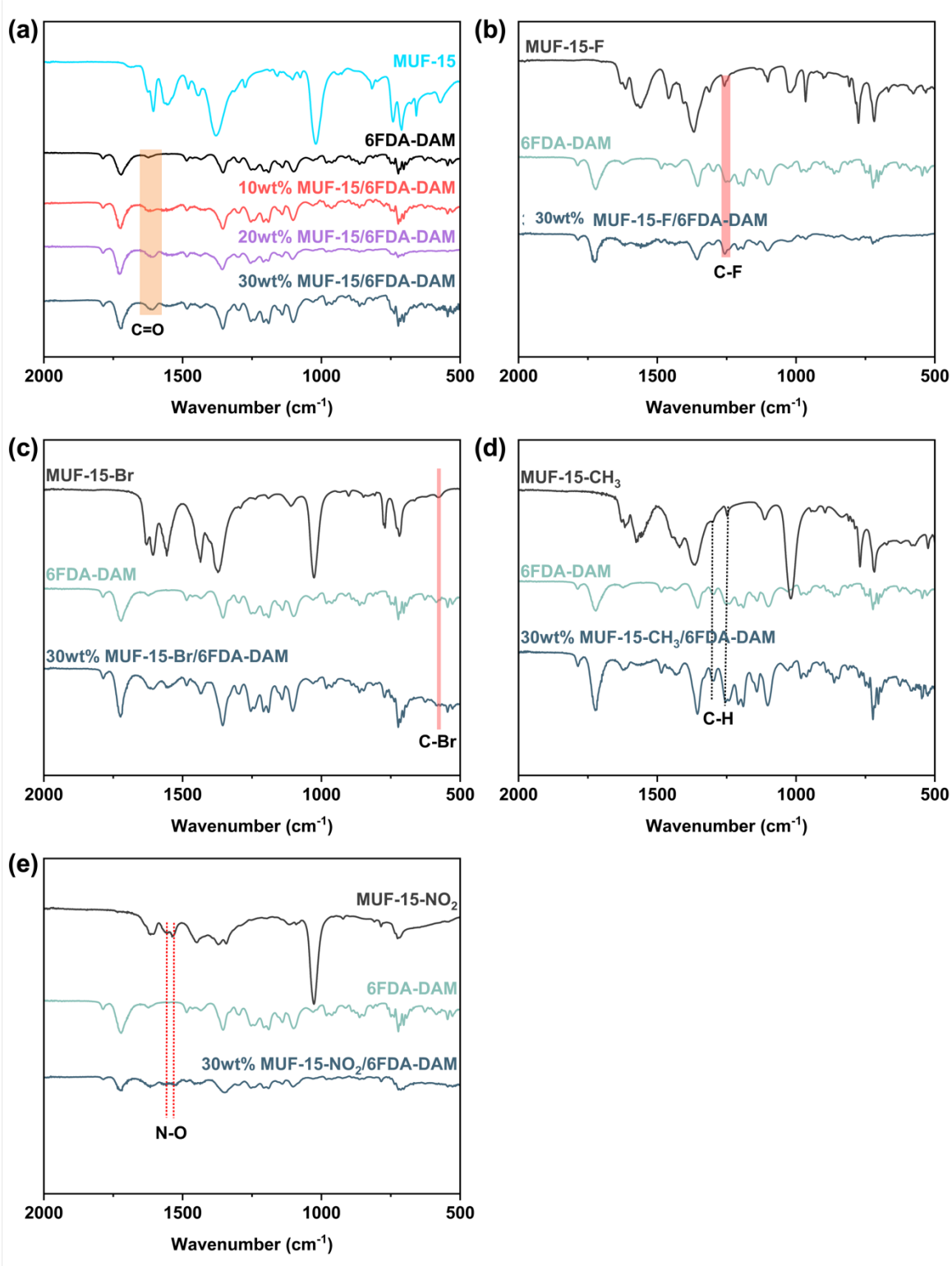


**Figure 5.6** FTIR spectra of 6FDA-DAM membranes with (a) MUF-15 (10 to 30 wt.%) and 30 wt.% loading of (b) MUF-15-F, (c) MUF-15-Br, (d) MUF-15-$CH_3$ and (e) MUF-15-$NO_2$.

**TGA**

Thermogravimetric traces of the MMMs show progressive weight loss (Fig. 5.7 a). Up to 120 °C, the membranes lose residual solvent. In the range 420 - 500 °C decomposition of the MOF fillers begins. This continues at nigher temperatures with concomitant decomposition of the 6FDA-DAM polymer.

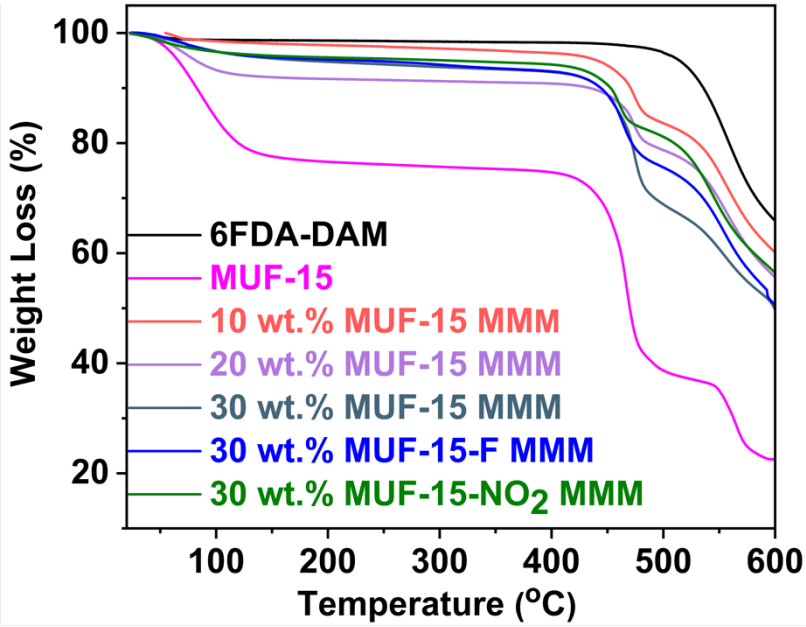


**Figure 5.7** TGA curves of 6FDA-DAM membrane, MUF-15 powder and membrane with MUF-15 (10 to 30 wt.%) and 30 wt.% loading of MUF-15-F, MUF-15-Br, MUF-15-$CH_3$, and MUF-15-$NO_2$.

### 5.2.4 Gas permeability test

#### 5.2.4.1 Single gas test and comparison with state-of-art membranes

The inclusion of MUF-15 as a filler significant enhances the $CO_2$ permeability of MMMs with a loading in the range 10 - 30 wt.% (Fig. 5.8a and Table 5.1). Specifically, the 30 wt.% MUF-15 MM displayed a $CO_2$ permeability of 1540 Barrer, marking an 84% increase over the pristine 6FDA-DAM membrane. Since this increase was accompanied by an increase in $CH_4$ permeability, the ideal $CO_2/CH_4$ selectivity drops upon the inclusion of MUF-15 (Fig. 5.8a and Table 5.1). However, an improvement in both $CO_2$ permeability and $CO_2/CH_4$ selectivity could be achieved by functionalising the MUF-15 with fluoro or nitro groups. At a loading of 30 wt.%, the MMM with MUF-15-F exhibited a $CO_2$ permeability of 1300 Barrer and $CO_2/CH_4$ selectivity of 37.1. For the MUF-15-$NO_2$ MMM the $CO_2$ permeability is 1430 Barrer and the $CO_2/CH_4$ selectivity is 33.7. These values surpass the 2008 Robeson upper bond (Fig. 5.8b). In the case of MUF-15-Br and MUF-15-$CH_3$ functionalisation leads to very high gas

permeability and low $CO_2/CH_4$ selectivity (Table 5.1). This can be ascribed to membrane defects which allow the gases to bypass the MOF fillers.

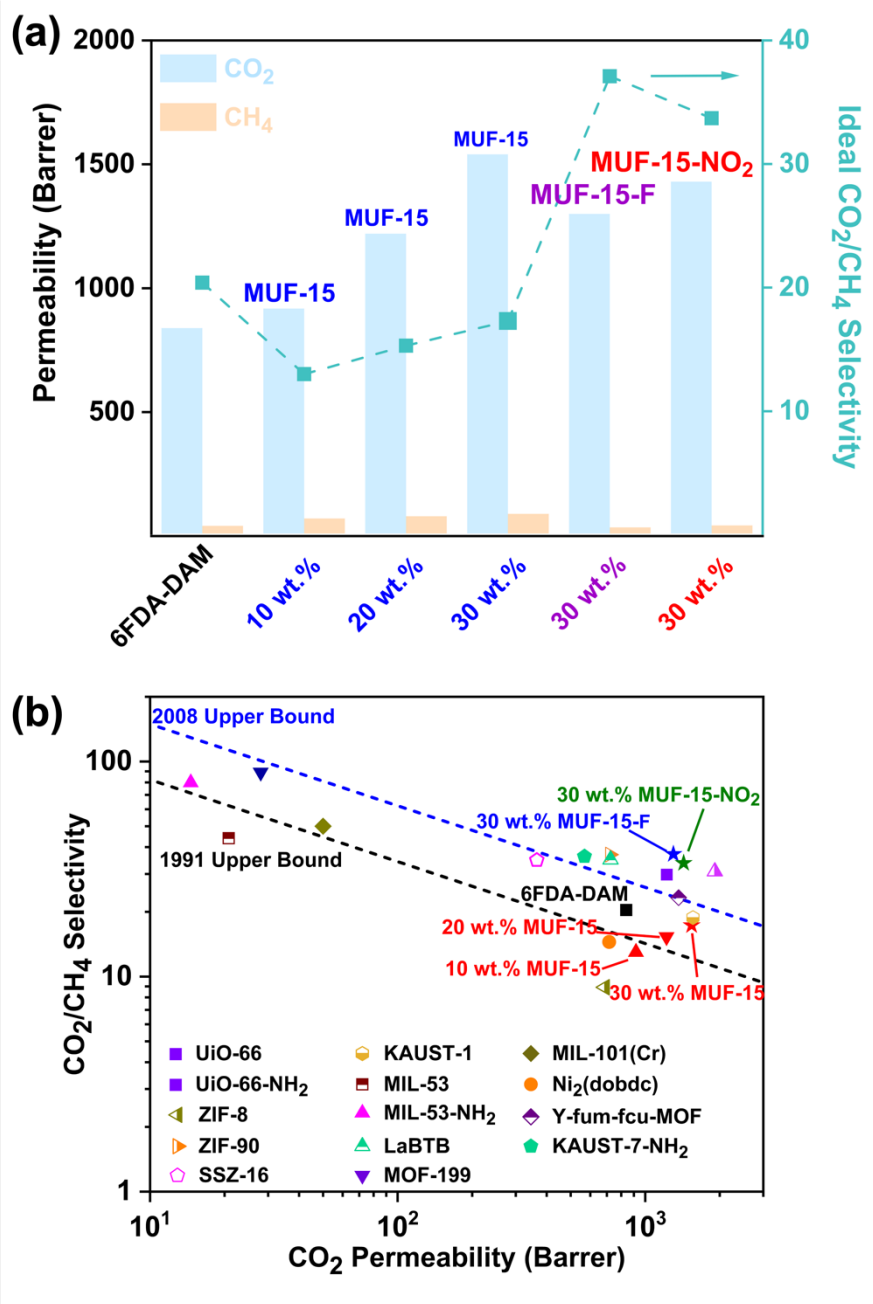


**Figure 5.8** (a) Gas permeabilities and $CO_2/CH_4$ selectivity for pristine 6FDA-DAM membrane and the MMMs incorporated with MUF-15, MUF-15-F and MUF-15-$NO_2$, and (b) $CO_2/N_2$ separation performance of the membranes as compared to literature data and the 1991/2008 Robeson upper bound. (UiO-66,[124] UiO-66-$NH_2$,[124] ZIF-8,[297] ZIF-90,[278] SSZ-16,[298] KAUST-1,[299] MIL-53,[300] MIL-53-$NH_2$,[300] LaBTB,[301] MOF-199,[302] MIL-101(Cr),[302] $Ni_2$(dobdc),[282] Y-fum-fcu-MOF,[258] KAUST-7-$NH_2$.[303]

**Table 5.1** Pure gas separation performance of the MMMs.

| Membrane | Permeability (Barrer) | | Selectivity |
|---|---|---|---|
| | $CO_2$ | $CH_4$ | $CO_2/CH_4$ |
| 6FDA-DAM | 839 | 41.2 | 20.4 |
| 10 wt.% MUF-15 MMM | 918 | 70.8 | 13.0 |
| 20 wt.% MUF-15 MMM | 1220 | 79.9 | 15.3 |
| 30 wt.% MUF-15 MMM | 1540 | 89.2 | 17.3 |
| 30 wt.% MUF-15-$NO_2$ MMM | 1430 | 42.4 | 33.7 |
| 30 wt.% MUF-15-F MMM | 1300 | 35.0 | 37.1 |
| 30 wt.% MUF-15-Br MMM | 8090 | 1600 | 5.1 |
| 30 wt.% MUF-15-$CH_3$ MMM | 11400 | 1440 | 7.9 |

#### 5.2.4.2 Gas solubility and diffusion in MMM

For a deeper analysis of these results using single, pure gases, we focussed on the MMMs comprising MUF-15 and MUF-15-F. Gas adsorption isotherms (Fig. 5.9a) reveal that MMMs incorporated with these fillers possesses superior gas update capabilities as compared to pristine 6FDA-DAM. The isotherms could be well fitted by a Langmuir adsorption model (Table D. 1). This enabled calculation of the gas solubilities and diffusivities using the solution-diffusion model (Fig. 5.9b and 5.9c, Table 5. 2). $CO_2$ solubility increases from 4240 mol/$m^3$·bar for the pristine 6FDA-DAM membrane to 4390 and 6070 mol/$m^3$·bar for MMMs with 30 wt.% MUF-15 and MUF-15-F fillers, respectively. Similarly, the CH4 solubility increases when the MOFs are added to the membrane. In terms of overall $CO_2/CH_4$ solubility selectivity, this declines when MUF-15 fillers are added and increases with the addition of MUF-15-F fillers. This highlights the way that MMM performance can be tuned by preferential gas adsorption by way of adding functional groups to the MOF linkers. Both the MUF-15 and MUF-15-F fillers enhance the $CO_2$ diffusivity. Incorporating MUF-15 also increases $CH_4$ diffusivity, therefore the enhancement in $CO_2/CH_4$ diffusivity selectivity of the MUF-15 MMM is only minor. In contrast, the incorporation of MUF-15-F significantly lowers the $CH_4$ diffusivity, and this enhances the $CO_2/CH_4$ diffusivity selectivity of the membrane.

**Table 5.2** Gas solubilities and diffusivities in pristine 6FDA-DAM, 30 wt.% MUF-15 MMM, and 30 wt.% MUF-15-F MMM.

| Membrane | Solubility ($10^3$ mol/m$^3$·bar) | | Diffusivity ($\times10^{-12}$ m$^2$/s) | | $CO_2/CH_4$ | |
|---|---|---|---|---|---|---|
| | $CO_2$ | $CH_4$ | $CO_2$ | $CH_4$ | Solubility selectivity | Diffusivity selectivity |
| 6FDA-DAM | 4.24 | 0.46 | 6.63 | 2.97 | 9.13 | 2.23 |
| 30 wt.% MUF-15 MMM | 4.39 | 0.59 | 11.73 | 5.05 | 7.43 | 2.33 |
| 30 wt.% MUF-15-F MMM | 6.07 | 0.61 | 7.18 | 1.94 | 10.02 | 3.71 |

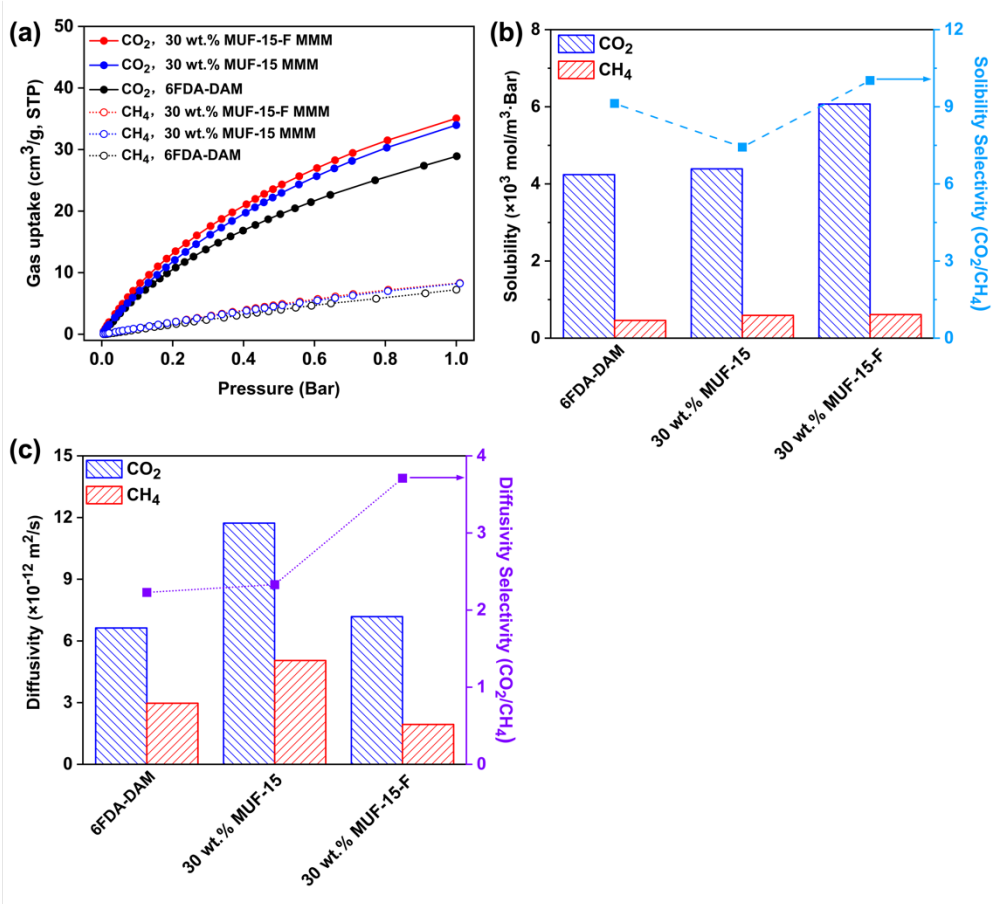


**Figure 5.9** (a) $CO_2$ and $CH_4$ adsorption isotherms at 293 K of a pristine 6FDA-DAM membrane and the MMMs incorporated with 30 wt.% MUF-15 and MUF-15-F. Comparison of gas (b) solubilities and (c) diffusivities in pristine 6FDA-DAM membrane and MMMs incorporated with 30 wt.% MUF-15 and MUF-15-F.

### 5.2.4.3 Mixed gas test

Binary gas separation was measured for the MMMs embedded with 30 wt.% of MUF-15 and MUF-15-F fillers. The results show a reduced $CO_2$ permeability and lower $CO_2/CH_4$ selectivity (Fig. 5.10) than their pure gas separation for all the membranes. This could be due to the competitive transport of gas molecules as they pass through the membranes.

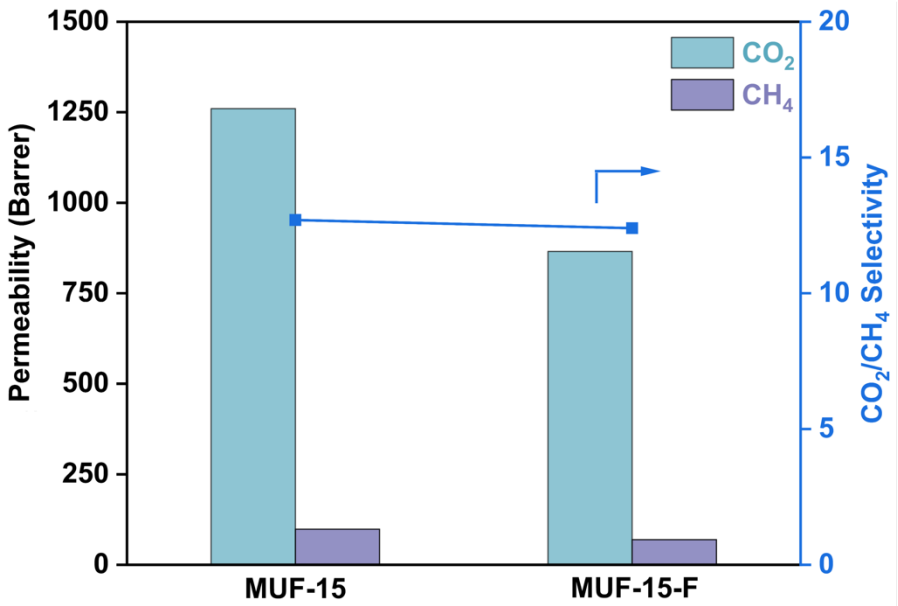


**Figure 5.10** Binary gas permeation results for the MMMs incorporated with 30 wt.% MUF-15, MUF-15-F.

## 5.3 Conclusion

In summary, we prepared novel MMMs by incorporating 6FDA-DAM with MUF-15 and its analogues. The MMM embedded with MUF-15-F and MUF-15-$NO_2$ exhibited uniform filler distribution and excellent interfacial compatibility even at a loading up to 30 wt.%, resulting in enhancement in $CO_2$ permeability and $CO_2/CH_4$ selectivity. This marks the first utilization of MUF-15 analogues as fillers in MMMs for $CO_2/CH_4$ separation. The study introduces a range of emerging MUF-15 derivatives as filler material for MMM development and underscores the effectiveness of pore structure functionalization in enhancing the separation performance of MMMs.

However, membranes with MUF-15-$CH_3$ and MUF-15-Br do not demonstrate improved separation performance. To address this issue, reducing the MOF loading in membrane and adjusting the particle size to a smaller scale may achieve a better interfacial compatibility in the membranes and deliver membranes with better separation performance.

# Chapter 6 Summary

## 6.1 Thesis summary

The study presented in this thesis involves the design, preparation, and evaluation of metal-organic frameworks for gas separation applications with a focus on the development of mixed-matrix membranes with both high gas permeability and good selectivity. Two types of membranes, including crystal glass composite membranes (CGCMs) and mixed matrix membranes (MMMs), were prepared, and characterized followed by a comprehensive evaluation of their performance for $CO_2/N_2$ and $CO_2/CH_4$ separation.

In Chapter 2, a series of CGCMs were prepared by combining crystalline MOF crystals, including UiO-66, ZIF-8, and MIL-53, with the glass-forming material ZIF-62 via the melt quenching treatment. The crystalline nature of these MOF crystals was retained during the glass transformation, which could increase the pore volume and gas transport in the resulting membranes. Notably, these MOF crystals, which are derived from different metal precursors and have different crystal sizes, all show good interfacial compatibility with the *ag*ZIF-62 phase in membrane. This could provide the resulting free-standing CGCMs with a continuous structure, which is beneficial for good separation performance. This type of CGCMs displayed superior high $CO_2$ permeance and not bad $CO_2/N_2$ and $CO_2/CH_4$ selectivities. In addition, MUF-16 with low decomposition temperature was also used to produce CGCMs with *ag*ZIF-62 by using a low temperature to remelt *ag*ZIF-62. In this way, crystalline MUF-16 with high $CO_2$ adsorption property could be retained, which makes it possible to pursue better separation performance. As expected, the prepared MUF-16 CGCMs showed high $CO_2$ permeance and better $CO_2/N_2$ and $CO_2/CH_4$ selectivities. This work provides a practical approach for the preparation of high-performance membranes and broadens the application of glassy materials for the development of multifunctional CGCMs.

In Chapter 3, MUF-16 was used to fabricate MMMs with a rubbery polymer Pebax for $CO_2$ separation. Prior to the membrane fabrication, the crystal size of MUF-16 was first regulated using a ball mill. This also reduced the crystal size and maintained the crystalline structure. Therefore, MUF-16 achieved excellent dispersion in the Pebax phase, minimizing the interfacial voids in MMMs. Due to the synergistic effect of MUF-16 and Pebax, the as-prepared MMMs achieved significant improvement in $CO_2$ permeability as well as superior $CO_2/N_2$ and $CO_2/CH_4$ selectivity. In addition, the gas separation results surpass the Robeson upper bound

limit (2008 and 2019). Notably, the produced MMMs demonstrated the hydrogen bonding between MUF-16 and Pebax, which improved their stiffness. Long-term operational tests showed stable gas permeability and selectivity, indicating the potential for industrial use. In the context of the relevant literature, this work represents a significant advance in separation performance. The results of this study show the remarkable performance improvements, surpassing those of existing membranes in several crucial aspects. Notably, the reported membrane demonstrates superior selectivity while maintaining exceptional $CO_2$ permeability, a combination that has often posed challenges in membrane design. This work not only underscores the significant advances that have been made in membrane technology, but also highlights the potential for this newly developed membrane to outperform in industrial applications. Further comparative studies with other state-of-the-art membranes will provide deeper insights into the extent of its superiority and potential real-world impact.

Tuning the crystal sizes of added MOFs is a viable way to improve the mixed matrix membrane properties beyond the current performance limits of polymeric membrane materials. In Chapter 4, to extend the application of MUF-16 in membrane separation, MUF-16 was combined with the glassy polymer 6FDA-DAM and 6FDA-Durene to prepare MMMs for $CO_2$ separation. Similar to chapter 3, nanosized MUF-16 (*ns*MUF-16) was produced using a ball mill. And the ultra-high performance *ns*MUF-16-filled MMMs for $CO_2$ separations were obtained, which showed unprecedented $CO_2$ separation performance, surpassing that of most MOF-based MMMs. Importantly, the achievement of in-plane alignment and extremely high loading of (001) *ns*MUF-16 is significantly responsible for the achieved separation performance. This work demonstrated a scalable method to tailor MOF crystal morphology and fabricate defect-free MOF-filled membranes with a commercially available glassy polymer, greatly expanding the range of high-performance MOF-filled MMMs for advanced gas separations, especially those MOFs that are difficult to engineer into defect-free membranes.

The pore aperture of MUF-15 can be modified by substituting it with different functional groups. These tunable pore characteristics of MUF-15 could motivate us to investigate its structural properties and gas separation performance by using different functional groups. In Chapter 5, MUF-15 and its analogues were synthesized by using different functional groups (-F, -Br, $-CH_3$ and $-NO_2$), which could provide MUF-15 with different gas sorption properties. Then these MOFs were used to prepare MMMs with 6FDA-DAM, and the corresponding separation performance was briefly investigated. By combining with 6FDA-DAM, the membranes with MUF-15-F and MUF-15-Br showed enhanced $CO_2$ permeability as well as

improved $CO_2/CH_4$ selectivity. These two MOFs can be the promising candidates for the construction of MMMs for $CO_2/CH_4$ separation. However, the membranes with MUF-15-$CH_3$ and MUF-15-$NO_2$ cannot show improved separation performance due to the defects and the poor interfacial compatibility in the membrane. To address this issue, it is possible to reduce the MOF loading in membrane or adjust the particle size to a smaller scale are possible to achieve a better interfacial compatibility in membrane, which may enable the resulting membrane with better separation performance. In addition, ultrasonication and ball milling treatment are feasible approaches to regulate the smaller MOF crystal size. In the future work, ultrasonic or ball milling treatment will be used to adjust the crystal size of MUF-15 and its analogues.

# Chapter 7 Future work

## 7.1 MUF-16 membrane growth on an alumina support

The Maxwell model prediction results demonstrate that pure MUF-16 membrane has outstanding $CO_2$ permeability and high $CO_2/N_2$ and $CO_2/CH_4$ selectivity. Therefore, by developing pure MUF-16 membrane it may be possible to achieve superior separation performance. In preliminary experiments, a seed growth method was used to construct the MUF-16 layer on the alumina support (Fig. 7.1).

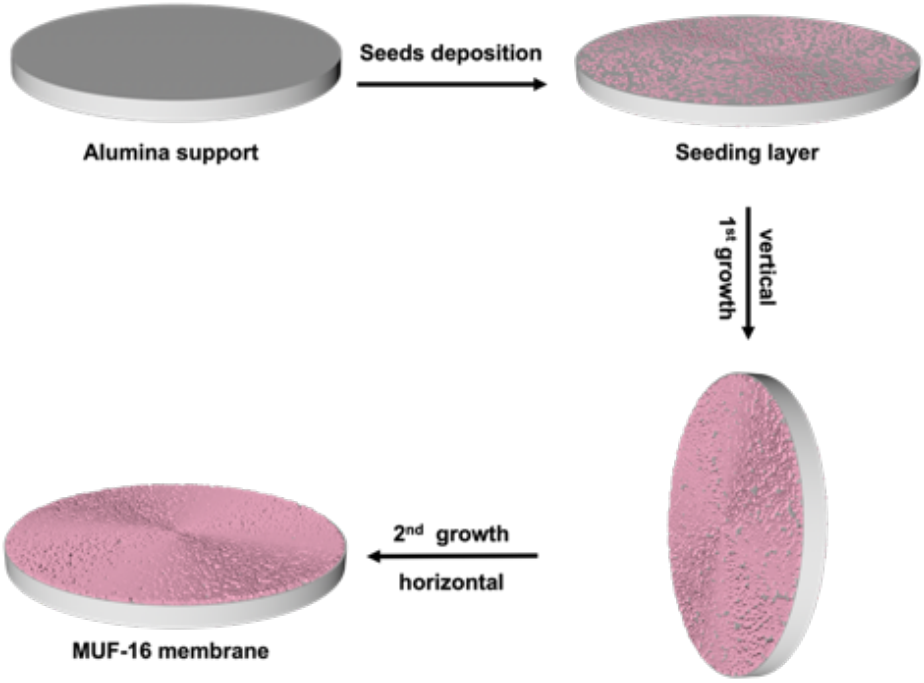


**Figure 7.1** Schematic fabrication process of MUF-16 membrane on alumina support.

### 7.1.1 The key to defect-free MUF-16 membrane

To ensure that the seed layer can completely cover the alumina support, spin coating or spray coating could be good candidates to produce a thin and uniform seed layer.[304] These methods have been successfully used in the development of MOF membranes. In this way, a thin and uniform MOF seed layer could be obtained, which could guarantee the further crystal growth on the entire surface of alumina. Therefore, the defect-free MUF-16 with expected separation performance can be obtained.

## 7.2 Development of large-scale MUF-16 membrane

MUF-16 membranes have the potential to address critical global challenges such as clean energy production and the greenhouse effect. MUF-16 membranes can be used for the $CO_2$ separation and purification of gases, including carbon capture from industrial emissions. Large-scale production of MUF-16 membranes enables their widespread use, contributing to mitigating climate change and promoting sustainable development. Moreover, large-scale production of MUF-16 membranes enables their integration into industrial processes, leading to improved efficiency, reduced energy consumption, and enhanced product quality.

The large-scale development of MUF-16 membranes involves several steps, including synthesis, membrane fabrication, and scale-up considerations. Here is a generalized process for the large-scale development of MUF-16 membranes:

(a) Synthesis of MUF-16 crystals

Developing a scalable synthesis route for the preparation of MUF-16 crystals. Ball mill synthesis is a convenient and effective approach to produce MUF-16 with small crystal size (around 1 μm).

(b) Preparation of substrates

Select appropriate substrates on which to grow MUF-16 crystals to form membranes. Common substrate materials include porous supports such as ceramic membranes or polymeric materials.

Prepare the substrates by cleaning, activation, and functionalization processes to promote adhesion and uniform growth of MUF-16 crystals.

(c) Membrane Fabrication

Develop a scalable deposition method to coat the substrate with MUF-16 crystals to form membranes. Techniques such as in situ growth, or interfacial synthesis may be employed.

Optimize deposition parameters such as precursor concentration, immersion time, temperature, and post-synthesis treatments to control membrane thickness, morphology, and crystal orientation.

Implement quality control measures to ensure the uniformity and integrity of MUF-16 membranes across large areas.

(d) Scale-up considerations

Address scale-up challenges by optimizing process parameters and equipment to accommodate larger volumes or areas while maintaining product quality and consistency.

Importantly, reactor design, mixing strategies, and solvent handling need to be considered to ensure efficient and cost-effective production of MUF-16 membranes on a large scale.

(e) Characterization and Testing

Thoroughly characterize the fabricated MUF-16 membranes using techniques such as scanning electron microscopy (SEM), X-ray diffraction (XRD), gas permeation testing, surface area analysis, and Fourier-transform infrared spectroscopy (FTIR).

Evaluate the structural integrity, morphology, porosity, and performance of MUF-16 membranes under relevant operating conditions.

Conduct long-term stability and durability tests to assess the reliability of the membranes for practical applications.

### 7.3 Size regulation of MUF-15 and its analogues

The direct use of solvothermally synthesized MUF-15 and its analogues to produce MMMs is not conducive to achieving good separation performance due to their large crystal size, which could easily cause the interfacial defects in the membranes. Therefore, it is necessary to control the size of MOF crystals prior to the membrane fabrication.

To obtain smaller crystals of MUF-15 and its analogues, two approaches are possible in future work: ultrasonication and ball milling treatment.

#### 7.3.1 Ultrasonication

Ultrasonication is a powerful technique for regulating the size of MOF crystals. By adjusting the sonication parameters, such as time, frequency, and intensity, the size of MOF crystals can be precisely controlled. And smaller MOF crystals are less prone to agglomeration in membranes, which can achieve good interfacial compatibility with the polymer matrix. In addition, smaller MOF crystals can pack more densely in membranes, which can increase their loading capacity for gas transport. Therefore, using ultrasonication may be a good approach to regulate the crystal size of MUF-15 and its analogues.

#### 7.3.2 Ball milling treatment

Ball milling has become a popular technique in the fields of MOF synthesis.[305] It provides precise control over the size reduction of MOF crystals and may be used to produce smaller size of MUF-15 and analogues. Similar to the ultrasonication treatment, an appropriate operating condition is necessary to both control the size and preserve the stability of MOF crystals during ball milling treatment.

### 7.3.3 Improvement of the stability of MMMs based on MUF-15 and its analogues

Improving the stability of MMMs-based MUF-15 and its analogues is essential for their practical applications. Some problems are prone to occur, especially the detachment of MOF particle and membrane degradation over time. Here are some strategies to improve the stability of MMMs-based MUF-15 and its analogues.

1) Improve the compatibility between MUF particles and the polymer matrix by modifying the MUF surface or linker properties to enhance MUF-linker interaction, which can reduce the risk of MUF particle detachment.

2) A suitable polymer matrix that is compatible with MUF-15 and its analogues and can provide good adhesion, which can improve the mechanical stability and chemical resistance of the MMMs.

3). A controlled and uniform MUF particle size can also improve their dispersion in polymer matrix. And the optimal MUF loading in MMMs needs to be determined to achieve the desired separation performance with good stability.

By combining these strategies, it is possible to improve the operational stability and longevity of the MMMs with MUF-15 and its analogues.

## References

1. Dong, K.; Dong, X.; Jiang, Q.; Zhao, J., Assessing energy resilience and its greenhouse effect: A global perspective. *Energy Econ.* **2021**, *104*, 105659.

2. Alivand, M. S.; Mazaheri, O.; Wu, Y.; Stevens, G. W.; Scholes, C. A.; Mumford, K. A., Development of aqueous-based phase change amino acid solvents for energy-efficient $CO_2$ capture: The role of antisolvent. *Appl. Energy.* **2019**, *256*, 113911.

3. Qiao, H.; Zheng, F.; Jiang, H.; Dong, K., The greenhouse effect of the agriculture-economic growth-renewable energy nexus: Evidence from G20 countries. *Sci. Total Environ.* **2019**, *671*, 722-731.

4. Haszeldine, R. S., Carbon Capture and Storage: How Green Can Black Be? *Science.* **2009**, *325* (5948), 1647-1652.

5. Morales-Flórez, V.; Santos, A.; Lemus, A.; Esquivias, L., Artificial weathering pools of calcium-rich industrial waste for $CO_2$ sequestration. *Chem. Eng. J.* **2011**, *166* (1), 132-137.

6. Arens, M.; Åhman, M.; Vogl, V., Which countries are prepared to green their coal-based steel industry with electricity? - Reviewing climate and energy policy as well as the implementation of renewable electricity. *Renew. Sustain. Energy Rev.* **2021**, *143*, 110938.

7. Farghali, M.; Osman, A. I.; Mohamed, I. M. A.; Chen, Z.; Chen, L.; Ihara, I.; Yap, P.-S.; Rooney, D. W., Strategies to save energy in the context of the energy crisis: a review. *Environ. Chem. Lett.* **2023**.

8. Zhang, X.; Duan, Y.; Zhang, R.; Wei, H.; Chen, L., Optical study of oxygen enrichment on methane combustion characteristics under high compression-ratio conditions. *Fuel.* **2022**, *328*, 125251.

9. Shin, H.-C.; Park, J.-W.; Park, K.; Song, H.-C., Removal characteristics of trace compounds of landfill gas by activated carbon adsorption. *Environ. Pollut.* **2002**, *119* (2), 227-236.

10. Chaemchuen, S.; Kabir, N. A.; Zhou, K.; Verpoort, F., Metal–organic frameworks for upgrading biogas via $CO_2$ adsorption to biogas green energy. *Chem Soc Rev.* **2013**, *42* (24), 9304-9332.

11. Leung, D. Y. C.; Caramanna, G.; Maroto-Valer, M. M., An overview of current status of carbon dioxide capture and storage technologies. *Renew. Sustain. Energy Rev.* **2014**, *39*, 426-443.

12. Khan, M. U.; Lee, J. T. E.; Bashir, M. A.; Dissanayake, P. D.; Ok, Y. S.; Tong, Y. W.; Shariati, M. A.; Wu, S.; Ahring, B. K., Current status of biogas upgrading for direct biomethane use: A review. *Renew. Sustain. Energy Rev.* **2021**, *149*, 111343.

13. Olabi, A. G.; Wilberforce, T.; Elsaid, K.; Sayed, E. T.; Maghrabie, H. M.; Abdelkareem, M. A., Large scale application of carbon capture to process industries – A review. *J. Clean. Prod.* **2022**, *362*, 132300.

14. Danaci, D.; Bui, M.; Petit, C.; Mac Dowell, N., En Route to Zero Emissions for Power and Industry with Amine-Based Post-combustion Capture. *Environ. Sci. Technol.* **2021**, *55* (15), 10619-10632.

15. Subraveti, S. G.; Roussanaly, S.; Anantharaman, R.; Riboldi, L.; Rajendran, A., Techno-economic assessment of optimised vacuum swing adsorption for post-combustion $CO_2$ capture from steam-methane reformer flue gas. *Sep. Purif. Technol.* **2021**, *256*, 117832.

16. Hussin, F.; Aroua, M. K., Recent trends in the development of adsorption technologies for carbon dioxide capture: A brief literature and patent reviews (2014–2018). *J. Clean. Prod.* **2020**, *253*, 119707.

17. Song, C.; Liu, Q.; Deng, S.; Li, H.; Kitamura, Y., Cryogenic-based $CO_2$ capture technologies: State-of-the-art developments and current challenges. *Renew. Sustain. Energy Rev.* **2019**, *101*, 265-278.

18. Asif, M.; Suleman, M.; Haq, I.; Jamal, S. A., Post-combustion $CO_2$ capture with chemical absorption and hybrid system: current status and challenges. *Greenh. Gases: Sci. Technol.* **2018**, *8* (6), 998-1031.

19. Ochedi, F. O.; Yu, J.; Yu, H.; Liu, Y.; Hussain, A., Carbon dioxide capture using liquid absorption methods: a review. *Environ. Chem. Lett.* **2021**, *19* (1), 77-109.

20. Kim, S.; Scholes, C. A.; Heath, D. E.; Kentish, S. E., Gas-liquid membrane contactors for carbon dioxide separation: A review. *Chem. Eng. J.* **2021**, *411*, 128468.

21. Iliuta, I.; Hasib-ur-Rahman, M.; Larachi, F., $CO_2$ absorption in diethanolamine/ionic liquid emulsions – Chemical kinetics and mass transfer study. *Chem. Eng. J.* **2014**, *240*, 16-23.

22. Ghalib, L.; Abdulkareem, A.; Ali, B. S.; Mazari, S. A., Modeling the rate of corrosion of carbon steel using activated diethanolamine solutions for $CO_2$ absorption. *Chin. J. Chem. Eng.* **2020**, *28* (8), 2099-2110.

23. Choi, B.-K.; Kim, S.-M.; Kim, K.-M.; Lee, U.; Choi, J. H.; Lee, J.-S.; Baek, I. H.; Nam, S. C.; Moon, J.-H., Amine blending optimization for maximizing $CO_2$ absorption capacity in a diisopropanolamine – methyldiethanolamine – $H_2O$ system using the electrolyte UNIQUAC model. *Chem. Eng. J.* **2021**, *419*, 129517.

24. Shahid, M. Z.; Maulud, A. S.; Bustam, M. A.; Suleman, H.; Abdul Halim, H. N.; Shariff, A. M., Packed column modelling and experimental evaluation for $CO_2$ absorption using MDEA solution at high pressure and high $CO_2$ concentrations. *J. Nat. Gas Eng.* **2021**, *88*, 103829.

25. Zhang, W.; Ma, Z.; Liu, X.; Liu, Y.; Hou, Z.; Qi, J.; Ma, Y.; Wang, L.; Wang, Y., Molecular Mechanism and Absorption Performance Evaluation of $CO_2$ Capture from the PCC Process by Monoethanolamine-Based Deep Eutectic Solvents. *Ind. Eng. Chem. Res.* **2021**, *60* (3), 1483-1493.

26. Li, X.; Zhou, X.; Wei, J.; Fan, Y.; Liao, L.; Wang, H., Reducing the energy penalty and corrosion of carbon dioxide capture using a novel nonaqueous monoethanolamine-based biphasic solvent. *Sep. Purif. Technol.* **2021**, *265*, 118481.

27. Cavaignac, R. S.; Ferreira, N. L.; Guardani, R., Techno-economic and environmental process evaluation of biogas upgrading via amine scrubbing. *Renew. Energy.* **2021**, *171*, 868-880.

28. Kazemi, A.; Moreno, J.; Iribarren, D., Techno-economic comparison of optimized natural gas combined cycle power plants with $CO_2$ capture. *Energy.* **2022**, *255*, 124617.

29. Ji, L.; Zheng, X.; Zhang, L.; Feng, L.; Li, K.; Yu, H.; Yan, S., Feasibility and mechanism of an amine-looping process for efficient $CO_2$ mineralization using alkaline ashes. *Chem. Eng. J.* **2022**, *430*, 133118.

30. Zheng, X.; Zhang, L.; Feng, L.; He, Q.; Ji, L.; Yan, S., Insights into dual functions of amino acid salts as $CO_2$ carriers and $CaCO_3$ regulators for integrated $CO_2$ absorption and mineralisation. *J. CO2 Util.* **2021**, *48*, 101531.

31. Esmaeili, A.; Tamuzi, A.; Borhani, T. N.; Xiang, Y.; Shao, L., Modeling of carbon dioxide absorption by solution of piperazine and methyldiethanolamine in a rotating packed bed. *Chem. Eng. Sci.* **2022**, *248*, 117118.

32. Xu, Y.; Chen, X.; Zhao, Y.; Jin, B., Modeling and analysis of $CO_2$ capture by aqueous ammonia + piperazine blended solution in a spray column. *Sep. Purif. Technol.* **2021**, *267*, 118655.

33. Hampe, E. M.; Rudkevich, D. M., Exploring reversible reactions between $CO_2$ and amines. *Tetrahedron.* **2003**, *59* (48), 9619-9625.

34. Chao, C.; Deng, Y.; Dewil, R.; Baeyens, J.; Fan, X., Post-combustion carbon capture. *Renew. Sustain. Energy Rev.* **2021**, *138*, 110490.

35. Wang, Y.; Dong, Y.; Zhang, L.; Chu, G.; Zou, H.; Sun, B.; Zeng, X., Carbon dioxide capture by non-aqueous blend in rotating packed bed reactor: Absorption and desorption investigation. *Sep. Purif. Technol.* **2021**, *269*, 118714.

36. Yang, Y.; Burke, N.; Ali, S.; Huang, S.; Lim, S.; Zhu, Y., Experimental studies of hydrocarbon separation on zeolites, activated carbons and MOFs for applications in natural gas processing. *RSC Adv.* **2017**, *7* (21), 12629-12638.

37. Wilkes, M. D.; Brown, S., Flexible $CO_2$ capture for open-cycle gas turbines via vacuum-pressure swing adsorption: A model-based assessment. *Energy.* **2022**, *250*, 123805.

38. Park, K.-H.; Lee, J. W.; Lim, Y.; Seo, Y., Life cycle cost analysis of $CO_2$ compression processes coupled with a cryogenic distillation unit for purifying high-$CO_2$ natural gas. *J. CO2 Util.* **2022**, *60*, 102002.

39. Bi, Y.; Ju, Y., Review on cryogenic technologies for $CO_2$ removal from natural gas. *Front. Energy Res.* **2022**, *16* (5), 793-811.

40. Campos, A. C. C.; dos Reis, R. A.; Ortiz, A.; Gorri, D.; Ortiz, I., A Perspective of Solutions for Membrane Instabilities in Olefin/Paraffin Separations: A Review. *Ind. Eng. Chem. Res.* **2018**, *57* (31), 10071-10085.

41. Park, J.; Kim, S.-J.; Lee, I.; Shin, J.-W.; Park, Y.-I.; Kim, K.; Park, Y.-K., Techno-economics and sensitivity analysis of hybrid process combining carbon molecular sieve membrane and distillation column for propylene/propane separation. *Chem Eng Res Des.* **2021**, *172*, 204-214.

42. Xu, Y.; Tang, Y.; He, C.; Shu, Y.; Chen, Q. L.; Zhang, B. J., Internal coupling process of membrane/distillation column hybrid configuration for ethylene/ethane separation. *Chem. Eng. Process.* **2022**, *177*, 108982.

43. Koros, W. J.; Zhang, C., Materials for next-generation molecularly selective synthetic membranes. *Nat. Mater.* **2017**, *16* (3), 289-297.

44. Chen, T.; Wei, X.; Chen, Z.; Morin, D.; Alvarez, S. V.; Yoon, Y.; Huang, Y., Designing energy-efficient separation membranes: Knowledge from nature for a sustainable future. *Adv. Membr.* **2022**, *2*, 100031.

45. Wang, Z.; Luo, X.; Song, Z.; Lu, K.; Zhu, S.; Yang, Y.; Zhang, Y.; Fang, W.; Jin, J., Microporous polymer adsorptive membranes with high processing capacity for molecular separation. *Nat Commun.* **2022**, *13* (1), 4169.

46. Knebel, A.; Caro, J., Metal–organic frameworks and covalent organic frameworks as disruptive membrane materials for energy-efficient gas separation. *Nat. Nanotechnol.* **2022**, *17* (9), 911-923.

47. Torres, D.; Pérez-Rodríguez, S.; Cesari, L.; Castel, C.; Favre, E.; Fierro, V.; Celzard, A., Review on the preparation of carbon membranes derived from phenolic resins for gas separation: From petrochemical precursors to bioresources. *Carbon.* **2021**, *183*, 12-33.

48. Iulianelli, A.; Drioli, E., Membrane engineering: Latest advancements in gas separation and pre-treatment processes, petrochemical industry and refinery, and future perspectives in emerging applications. *Fuel Process. Technol.* **2020**, *206*, 106464.

49. Huang, X.; Chen, L.; Chen, S.; Su, P.; Li, W., Reconstruction of mixed matrix membranes by in situ vapor aminolysis for $CO_2/N_2$ and $CH_4/N_2$ separations. *J. Membr. Sci.* **2023**, *685*, 121984.

50. Olabi, A. G.; Alami, A. H.; Ayoub, M.; Aljaghoub, H.; Alasad, S.; Inayat, A.; Abdelkareem, M. A.; Chae, K.-J.; Sayed, E. T., Membrane-based carbon capture: Recent progress, challenges, and their role in achieving the sustainable development goals. *Chemosphere.* **2023**, *320*, 137996.

51. George, G.; Bhoria, N.; AlHallaq, S.; Abdala, A.; Mittal, V., Polymer membranes for acid gas removal from natural gas. *Sep. Purif. Technol.* **2016**, *158*, 333-356.

52. Han, Y.; Ho, W. S. W., Polymeric membranes for $CO_2$ separation and capture. *J. Membr. Sci.* **2021**, *628*, 119244.

53. Lei, L.; Pan, F.; Lindbråthen, A.; Zhang, X.; Hillestad, M.; Nie, Y.; Bai, L.; He, X.; Guiver, M. D., Carbon hollow fiber membranes for a molecular sieve with precise-cutoff ultramicropores for superior hydrogen separation. *Nat Commun.* **2021**, *12* (1), 268.

54. Ullah, S.; Assiri, M. A.; Al-Sehemi, A. G.; Bustam, M. A.; Abdul Mannan, H.; Abdulkareem, F. A.; Irfan, A.; Saqib, S., High-temperature $CO_2$ removal from $CH_4$ using silica membrane: experimental and neural network modeling. *Greenh. Gases: Sci. Technol.* **2019**, *9* (5), 1010-1026.

55. Kosinov, N.; Gascon, J.; Kapteijn, F.; Hensen, E. J. M., Recent developments in zeolite membranes for gas separation. *J. Membr. Sci.* **2016**, *499*, 65-79.

56. Zhang, H.; Xue, K.; Cheng, C.; Gao, D.; Chen, H., Study on the performance of $CO_2$ capture from flue gas with ceramic membrane contactor. *Sep. Purif. Technol.* **2021**, *265*, 118521.

57. Nian, M.; Ge, K.; Zhao, J.; Shen, Y.; Duan, Y.; Wu, Y.; Duan, J., Orienting of metal-organic framework nanosheets into continuous membranes for fast hydrogen permeation. *J. Membr. Sci.* **2023**, *672*, 121447.

58. Dechnik, J.; Gascon, J.; Doonan, C. J.; Janiak, C.; Sumby, C. J., Mixed-matrix membranes. *Angew. Chem. Int. Ed.* **2017**, *56* (32), 9292-9310.

59. Tan, X.; Robijns, S.; Thür, R.; Ke, Q.; De Witte, N.; Lamaire, A.; Li, Y.; Aslam, I.; Van Havere, D.; Donckels, T.; Van Assche, T.; Van Speybroeck, V.; Dusselier, M.; Vankelecom, I., Truly combining the advantages of polymeric and zeolite membranes for gas separations. *Science.* **2022**, *378* (6625), 1189-1194.

60. Kukobat, R.; Sakai, M.; Tanaka, H.; Otsuka, H.; Vallejos-Burgos, F.; Lastoskie, C.; Matsukata, M.; Sasaki, Y.; Yoshida, K.; Hayashi, T.; Kaneko, K., Ultrapermeable 2D-channeled graphene-wrapped zeolite molecular sieving membranes for hydrogen separation. *Sci. Adv. 8* (20), eabl3521.

61. Li, S.; Sun, Y.-J.; Wang, Z.-X.; Jin, C.-G.; Yin, M.-J.; An, Q.-F., Rapid Fabrication of High-Permeability Mixed Matrix Membranes at Mild Condition for $CO_2$ Capture. *Small.* **2023**, *19* (19), 2208177.

62. Zhu, B.; He, S.; Yang, Y.; Li, S.; Lau, C. H.; Liu, S.; Shao, L., Boosting membrane carbon capture via multifaceted polyphenol-mediated soldering. *Nat Commun.* **2023**, *14* (1), 1697.

63. Wang, S.; Wei, X.; Li, Z.; Liu, Y.; Wang, H.; Zou, L.; Lu, D.; Hassan Akhtar, F.; Wang, X.; Wu, C.; Luo, S., Recent advances in developing mixed matrix membranes based on covalent organic frameworks. *Sep. Purif. Technol.* **2022**, *301*, 122004.

64. Dai, G.; Zhang, Q.; Xiong, S.; Deng, L.; Gao, Z.; Chen, A.; Li, X.; Pan, C.; Tang, J.; Yu, G., Building interfacial compatible PIM-1-based mixed-matrix membranes with β-ketoenamine-linked COF fillers for effective $CO_2/N_2$ separation. *J. Membr. Sci.* **2023**, *676*, 121561.

65. Lee, C. S.; Moon, J.; Park, J. T.; Kim, J. H., Engineering $CO_2$-philic pathway via grafting poly(ethylene glycol) on graphene oxide for mixed matrix membranes with high $CO_2$ permeance. *Chem. Eng. J.* **2023**, *453*, 139818.

66. Regmi, C.; Ashtiani, S.; Průša, F.; Friess, K., Synergistic effect of hybridized TNT@GO fillers in CTA-based mixed matrix membranes for selective $CO_2/CH_4$ separation. *Sep. Purif. Technol.* **2022**, *282*, 120128.

67. Nejad, M. N.; Asghari, M.; Afsari, M., Investigation of Carbon Nanotubes in Mixed Matrix Membranes for Gas Separation: A Review. *ChemBioEng Rev.* **2016**, *3* (6), 276-298.

68. Wang, H.; Zheng, W.; Yang, X.; Ning, M.; Li, X.; Xi, Y.; Yan, X.; Zhang, X.; Dai, Y.; Liu, H.; He, G., Pebax-based mixed matrix membranes derived from microporous carbon nanospheres for permeable and selective $CO_2$ separation. *Sep. Purif. Technol.* **2021**, *274*, 119015.

69. Zhu, W.; Liu, F.; Gou, M.; Guo, R.; Li, X., Mixed matrix membrane containing metal oxide nanosheets for efficient $CO_2$ separation. *Green Chem. Eng.* **2021**, *2* (1), 132-143.

70. Li, E.; Chen, Z.; Duan, C.; Yuan, B.; Yan, S.; Luo, X.; Pan, F.; Jiang, Z., Enhanced $CO_2$-capture performance of polyimide-based mixed matrix membranes by incorporating ZnO@MOF nanocomposites. *Sep. Purif. Technol.* **2022**, *289*, 120714.

71. Robeson, L. M., Correlation of separation factor versus permeability for polymeric membranes. *J. Membr. Sci.* **1991**, *62* (2), 165-185.

72. Robeson, L. M., The upper bound revisited. *J. Membr. Sci.* **2008**, *320* (1), 390-400.

73. Park, H. B.; Kamcev, J.; Robeson, L. M.; Elimelech, M.; Freeman, B. D., Maximizing the right stuff: The trade-off between membrane permeability and selectivity. *Science.* **2017**, *356* (6343), eaab0530.

74. Cheng, Y.; Datta, S. J.; Zhou, S.; Jia, J.; Shekhah, O.; Eddaoudi, M., Advances in metal–organic framework-based membranes. *Chem Soc Rev.* **2022**, *51* (19), 8300-8350.

75. Fan, W.; Ying, Y.; Peh, S. B.; Yuan, H.; Yang, Z.; Yuan, Y. D.; Shi, D.; Yu, X.; Kang, C.; Zhao, D., Multivariate Polycrystalline Metal–Organic Framework Membranes for $CO_2/CH_4$ Separation. *J. Am. Chem. Soc.* **2021**, *143* (42), 17716-17723.

76. Rong, R.; Sun, Y.; Ji, T.; Liu, Y., Fabrication of highly $CO_2/N_2$ selective polycrystalline UiO-66 membrane with two-dimensional transition metal dichalcogenides as zirconium source via tertiary solvothermal growth. *J. Membr. Sci.* **2020**, *610*, 118275.

77. Babu, D. J.; He, G.; Hao, J.; Vahdat, M. T.; Schouwink, P. A.; Mensi, M.; Agrawal, K. V., Restricting Lattice Flexibility in Polycrystalline Metal–Organic Framework Membranes for Carbon Capture. *Adv Mater.* **2019**, *31* (28), 1900855.

78. Yan, J.; Sun, Y.; Ji, T.; Zhang, C.; Liu, L.; Liu, Y., Room-temperature synthesis of defect-engineered Zirconium-MOF membrane enabling superior $CO_2/N_2$ selectivity with zirconium-oxo cluster source. *J. Membr. Sci.* **2022**, *653*, 120496.

79. Gallucci, F.; Fernandez, E.; Corengia, P.; van Sint Annaland, M., Recent advances on membranes and membrane reactors for hydrogen production. *Chem. Eng. Sci.* **2013**, *92*, 40-66.

80. Liu, Y.; Pan, J. H.; Wang, N.; Steinbach, F.; Liu, X.; Caro, J., Remarkably Enhanced Gas Separation by Partial Self-Conversion of a Laminated Membrane to Metal–Organic Frameworks. *Angew. Chem. Int. Ed.* **2015**, *54* (10), 3028-3032.

81. Wang, N.; Liu, Y.; Qiao, Z.; Diestel, L.; Zhou, J.; Huang, A.; Caro, J., Polydopamine-based synthesis of a zeolite imidazolate framework ZIF-100 membrane with high $H_2/CO_2$ selectivity. *J. Mater. Chem. A.* **2015**, *3* (8), 4722-4728.

82. Jiang, X.; Li, S.; Bai, Y.; Shao, L., Ultra-facile aqueous synthesis of nanoporous zeolitic imidazolate framework membranes for hydrogen purification and olefin/paraffin separation. *J. Mater. Chem. A.* **2019**, *7* (18), 10898-10904.

83. Zhou, S.; Shekhah, O.; Jia, J.; Czaban-Jóźwiak, J.; Bhatt, P. M.; Ramírez, A.; Gascon, J.; Eddaoudi, M., Electrochemical synthesis of continuous metal–organic framework membranes for separation of hydrocarbons. *Nat. Energy.* **2021**, *6* (9), 882-891.

84. Cao, H.; Xia, Y.; Lu, Y.; Wu, Y.; Xia, Y.; Hou, X.; Wang, Y.; Liu, G.; Huang, K.; Xu, Z., MOF-801 polycrystalline membrane with sub-10 nm polymeric assembly layer for ion sieving and flow battery storage. *AIChE J.* **2022**, *68* (6), e17657.

85. Hou, J.; Zhang, H.; Thornton, A. W.; Hill, A. J.; Wang, H.; Konstas, K., Lithium Extraction by Emerging Metal–Organic Framework-Based Membranes. *Adv. Funct. Mater.* **2021**, *31* (46), 2105991.

86. Fan, J.; Wu, W.; Lu, Z.; Wei, Y., Rapid synthesis strategy of ultrathin UiO-66 separation membranes: Ultrasonic-assisted nucleation followed with microwave-assisted growth. *J. Membr. Sci.* **2022**, *664*, 121085.

87. Hou, J.; Zhang, H.; Simon, G. P.; Wang, H., Polycrystalline Advanced Microporous Framework Membranes for Efficient Separation of Small Molecules and Ions. *Adv Mater.* **2020**, *32* (18), 1902009.

88. Lu, Y.; Zhang, H.; Zhu, Y.; Marriott, P. J.; Wang, H., Emerging Homochiral Porous Materials for Enantiomer Separation. *Adv. Funct. Mater.* **2021**, *31* (25), 2101335.

89. Chan, J. Y.; Zhang, H.; Nolvachai, Y.; Hu, Y.; Zhu, H.; Forsyth, M.; Gu, Q.; Hoke, D. E.; Zhang, X.; Marriot, P. J.; Wang, H., Incorporation of Homochirality into a Zeolitic Imidazolate Framework Membrane for Efficient Chiral Separation. *Angew. Chem. Int. Ed.* **2018**, *57* (52), 17130-17134.

90. Liu, Y.; Ng, Z.; Khan, E. A.; Jeong, H.-K.; Ching, C.-b.; Lai, Z., Synthesis of continuous MOF-5 membranes on porous α-alumina substrates. *Microporous Mesoporous Mater.* **2009**, *118* (1), 296-301.

91. Zhang, C.; Yan, J.; Ji, T.; Du, D.; Sun, Y.; Liu, L.; Zhang, X.; Liu, Y., Fabrication of highly (110)-Oriented ZIF-8 membrane at low temperature using nanosheet seed layer. *J. Membr. Sci.* **2022**, *641*, 119915.

92. Chen, D.-H.; Gliemann, H.; Wöll, C., Layer-by-layer assembly of metal-organic framework thin films: Fabrication and advanced applications. *Chem. Phys. Rev.* **2023**, *4* (1), 011305.

93. Shekhah, O.; Swaidan, R.; Belmabkhout, Y.; du Plessis, M.; Jacobs, T.; Barbour, L. J.; Pinnau, I.; Eddaoudi, M., The liquid phase epitaxy approach for the successful construction of ultra-thin and defect-free ZIF-8 membranes: pure and mixed gas transport study. *ChemComm.* **2014**, *50* (17), 2089-2092.

94. Hurrle, S.; Friebe, S.; Wohlgemuth, J.; Wöll, C.; Caro, J.; Heinke, L., Sprayable, Large-Area Metal–Organic Framework Films and Membranes of Varying Thickness. *Chem. Eur. J.* **2017**, *23* (10), 2294-2298.

95. Zhou, S.; Wei, Y.; Li, L.; Duan, Y.; Hou, Q.; Zhang, L.; Ding, L.-X.; Xue, J.; Wang, H.; Caro, J., Paralyzed membrane: Current-driven synthesis of a metal-organic framework with sharpened propene/propane separation. *Sci. Adv. 4* (10), eaau1393.

96. Zhao, Y.; Wei, Y.; Lyu, L.; Hou, Q.; Caro, J.; Wang, H., Flexible Polypropylene-Supported ZIF-8 Membranes for Highly Efficient Propene/Propane Separation. *J. Am. Chem. Soc.* **2020**, *142* (50), 20915-20919.

97. Wei, R.; Chi, H.-Y.; Li, X.; Lu, D.; Wan, Y.; Yang, C.-W.; Lai, Z., Aqueously Cathodic Deposition of ZIF-8 Membranes for Superior Propylene/Propane Separation. *Adv. Funct. Mater.* **2020**, *30* (7), 1907089.

98. Zhang, X.; Wan, K.; Subramanian, P.; Xu, M.; Luo, J.; Fransaer, J., Electrochemical deposition of metal–organic framework films and their applications. *J. Mater. Chem. A.* **2020**, *8* (16), 7569-7587.

99. Lee, M. J.; Kwon, H. T.; Jeong, H.-K., High-Flux Zeolitic Imidazolate Framework Membranes for Propylene/Propane Separation by Postsynthetic Linker Exchange. *Angew. Chem. Int. Ed.* **2018**, *57* (1), 156-161.

100. Cacho-Bailo, F.; Etxeberría-Benavides, M.; Karvan, O.; Téllez, C.; Coronas, J., Sequential amine functionalization inducing structural transition in an aldehyde-containing zeolitic imidazolate framework: application to gas separation membranes. *CrystEngComm.* **2017**, *19* (11), 1545-1554.

101. Wisanrakkit, G.; Gillham, J. K., The glass transition temperature (Tg) as an index of chemical conversion for a high-Tg amine/epoxy system: Chemical and diffusion-controlled reaction kinetics. *J. Appl. Polym. Sci.* **1990**, *41* (11-12), 2885-2929.

102. Zhang, J.; Longley, L.; Liu, H.; Ashling, C. W.; Chater, P. A.; Beyer, K. A.; Chapman, K. W.; Tao, H.; Keen, D. A.; Bennett, T. D.; Yue, Y., Structural evolution in a melt-quenched zeolitic imidazolate framework glass during heat-treatment. *ChemComm.* **2019**, *55* (17), 2521-2524.

103. Qiao, A.; Bennett, T. D.; Tao, H.; Krajnc, A.; Mali, G.; Doherty, C. M.; Thornton, A. W.; Mauro, J. C.; Greaves, G. N.; Yue, Y., A metal-organic framework with ultrahigh glass-forming ability. *Sci. Adv. 4* (3), eaao6827.

104. Zhou, C.; Longley, L.; Krajnc, A.; Smales, G. J.; Qiao, A.; Erucar, I.; Doherty, C. M.; Thornton, A. W.; Hill, A. J.; Ashling, C. W.; Qazvini, O. T.; Lee, S. J.; Chater, P. A.; Terrill, N. J.; Smith, A. J.; Yue, Y.; Mali, G.; Keen, D. A.; Telfer, S. G.; Bennett, T. D., Metal-organic framework glasses with permanent accessible porosity. *Nat Commun.* **2018**, *9* (1), 5042.

105. Bennett, T. D.; Yue, Y.; Li, P.; Qiao, A.; Tao, H.; Greaves, N. G.; Richards, T.; Lampronti, G. I.; Redfern, S. A. T.; Blanc, F.; Farha, O. K.; Hupp, J. T.; Cheetham, A. K.; Keen, D. A., Melt-Quenched Glasses of Metal–Organic Frameworks. *J. Am. Chem. Soc.* **2016**, *138* (10), 3484-3492.

106. Wang, Y.; Jin, H.; Ma, Q.; Mo, K.; Mao, H.; Feldhoff, A.; Cao, X.; Li, Y.; Pan, F.; Jiang, Z., A MOF Glass Membrane for Gas Separation. *Angew. Chem. Int. Ed.* **2020**, *59* (11), 4365-4369.

107. Xia, H.; Jin, H.; Zhang, Y.; Song, H.; Hu, J.; Huang, Y.; Li, Y., A long-lasting TIF-4 MOF glass membrane for selective $CO_2$ separation. *J. Membr. Sci.* **2022**, *655*, 120611.

108. Tuffnell, J. M.; Ashling, C. W.; Hou, J.; Li, S.; Longley, L.; Ríos Gómez, M. L.; Bennett, T. D., Novel metal–organic framework materials: blends, liquids, glasses and crystal–glass composites. *ChemComm.* **2019**, *55* (60), 8705-8715.

109. Longley, L.; Calahoo, C.; Limbach, R.; Xia, Y.; Tuffnell, J. M.; Sapnik, A. F.; Thorne, M. F.; Keeble, D. S.; Keen, D. A.; Wondraczek, L.; Bennett, T. D., Metal-organic framework and inorganic glass composites. *Nat Commun.* **2020**, *11* (1), 5800.

110. Ashling, C. W.; Macreadie, L. K.; Southern, T. J. F.; Zhang, Y.; McHugh, L. N.; Evans, R. C.; Kaskel, S.; Telfer, S. G.; Bennett, T. D., Guest size limitation in metal–organic framework crystal–glass composites. *J. Mater. Chem. A.* **2021**, *9* (13), 8386-8393.

111. Abdollahzadeh, M.; Chai, M.; Hosseini, E.; Zakertabrizi, M.; Mohammad, M.; Ahmadi, H.; Hou, J.; Lim, S.; Habibnejad Korayem, A.; Chen, V.; Asadnia, M.; Razmjou, A., Designing Angstrom-Scale Asymmetric MOF-on-MOF Cavities for High Monovalent Ion Selectivity. *Adv Mater.* **2022**, *34* (9), 2107878.

112. Zulkifli, M. Y. B.; Su, K.; Chen, R.; Hou, J.; Chen, V., Future perspective on MOF glass composite thin films as selective and functional membranes for molecular separation. *Adv. Membr.* **2022**, *2*, 100036.

113. Paul, D. R.; Kemp, D. R., The diffusion time lag in polymer membranes containing adsorptive fillers. *J. polym. sci., Polym. symp.* **1973**, *41* (1), 79-93.

114. Li, C.; Qi, A.; Ling, Y.; Tao, Y.; Zhang, Y.-B.; Li, T., Establishing gas transport highways in MOF-based mixed matrix membranes. *Sci. Adv. 9* (13), eadf5087.

115. Yin, H.; Alkaş, A.; Zhang, Y.; Zhang, Y.; Telfer, S. G., Mixed matrix membranes (MMMs) using an emerging metal-organic framework (MUF-15) for $CO_2$ separation. *J. Membr. Sci.* **2020**, *609*, 118245.

116. Setiawan, W. K.; Chiang, K.-Y., Silica applied as mixed matrix membrane inorganic filler for gas separation: a review. *Sustain. Environ. Res.* **2019**, *29* (1), 32.

117. He, S.; Zhu, B.; Jiang, X.; Han, G.; Li, S.; Lau, C. H.; Wu, Y.; Zhang, Y.; Shao, L., Symbiosis-inspired de novo synthesis of ultrahigh MOF growth mixed matrix membranes for sustainable carbon capture. *PNAS.* **2022**, *119* (1), e2114964119.

118. Ding, Y.; Wang, H.; Yu, M.; Zheng, W.; Ruan, X.; Li, X.; Xi, Y.; Dai, Y.; Liu, H.; He, G., Amine group graft ZIF-93 to create gas storage space to improve the gas separation performance of Pebax-1657 MMMs. *Sep. Purif. Technol.* **2023**, *309*, 122949.

119. Song, S.; Zhao, M.; Guo, Z.; Ren, Y.; Wang, J.; Liang, X.; Pu, Y.; Wang, S.; Ma, H.; Wang, X.; He, G.; Jiang, Z., Mixed matrix composite membranes with MOF-protruding structure for efficient $CO_2$ separation. *J. Membr. Sci.* **2023**, *669*, 121340.

120. Lei, L.; Cheng, Y.; Chen, C.; Kosari, M.; Jiang, Z.; He, C., Taming structure and modulating carbon dioxide ($CO_2$) adsorption isosteric heat of nickel-based metal organic framework (MOF-74(Ni)) for remarkable $CO_2$ capture. *J Colloid Interface Sci.* **2022**, *612*, 132-145.

121. Jun, H. J.; Yoo, D. K.; Jhung, S. H., Metal-organic framework (MOF-808) functionalized with ethyleneamines: Selective adsorbent to capture $CO_2$ under low pressure. *J. CO2 Util.* **2022**, *58*, 101932.

122. Ghalei, B.; Sakurai, K.; Kinoshita, Y.; Wakimoto, K.; Isfahani, Ali P.; Song, Q.; Doitomi, K.; Furukawa, S.; Hirao, H.; Kusuda, H.; Kitagawa, S.; Sivaniah, E., Enhanced selectivity in mixed matrix membranes for $CO_2$ capture through efficient dispersion of amine-functionalized MOF nanoparticles. *Nat. Energy.* **2017**, *2* (7), 17086.

123. Chuah, C. Y.; Li, W.; Samarasinghe, S. A. S. C.; Sethunga, G. S. M. D. P.; Bae, T.-H., Enhancing the $CO_2$ separation performance of polymer membranes via the incorporation of amine-functionalized HKUST-1 nanocrystals. *Microporous Mesoporous Mater.* **2019**, *290*, 109680.

124. Ahmad, M. Z.; Navarro, M.; Lhotka, M.; Zornoza, B.; Téllez, C.; de Vos, W. M.; Benes, N. E.; Konnertz, N. M.; Visser, T.; Semino, R.; Maurin, G.; Fila, V.; Coronas, J., Enhanced

gas separation performance of 6FDA-DAM based mixed matrix membranes by incorporating MOF UiO-66 and its derivatives. *J. Membr. Sci.* **2018**, *558*, 64-77.

125. Molavi, H.; Shojaei, A.; Mousavi, S. A., Improving mixed-matrix membrane performance via PMMA grafting from functionalized $NH_2$–UiO-66. *J. Mater. Chem. A.* **2018**, *6* (6), 2775-2791.

126. Zhao, Q.; Lian, S.; Li, R.; Yu, Z.; Liu, Q.; Zang, G.-L.; Song, C., Architecting MOFs-based mixed matrix membrane for efficient $CO_2$ separation: Ameliorating strategies toward non-ideal interface. *Chem. Eng. J.* **2022**, *443*, 136290.

127. Deng, J.; Dai, Z.; Deng, L., Effects of the Morphology of the ZIF on the $CO_2$ Separation Performance of MMMs. *Ind. Eng. Chem. Res.* **2020**, *59* (32), 14458-14466.

128. Winarta, J.; Meshram, A.; Zhu, F.; Li, R.; Jafar, H.; Parmar, K.; Liu, J.; Mu, B., Metal–organic framework-based mixed-matrix membranes for gas separation: An overview. *J. Polym. Sci.* **2020**, *58* (18), 2518-2546.

129. Jeon, M. Y.; Kim, D.; Kumar, P.; Lee, P. S.; Rangnekar, N.; Bai, P.; Shete, M.; Elyassi, B.; Lee, H. S.; Narasimharao, K.; Basahel, S. N.; Al-Thabaiti, S.; Xu, W.; Cho, H. J.; Fetisov, E. O.; Thyagarajan, R.; DeJaco, R. F.; Fan, W.; Mkhoyan, K. A.; Siepmann, J. I.; Tsapatsis, M., Ultra-selective high-flux membranes from directly synthesized zeolite nanosheets. *Nature.* **2017**, *543* (7647), 690-694.

130. Peng, Y.; Li, Y.; Ban, Y.; Jin, H.; Jiao, W.; Liu, X.; Yang, W., Metal-organic framework nanosheets as building blocks for molecular sieving membranes. *Science.* **2014**, *346* (6215), 1356-1359.

131. Liu, Q.; Li, X.; Wen, Y.; Xu, Q.; Wu, X.-T.; Zhu, Q.-L., Twofold Interpenetrated 2D MOF Nanosheets Generated by an Instant In Situ Exfoliation Method: Morphology Control and Fluorescent Sensing. *Adv. Mater. Interfaces.* **2020**, *7* (16), 2000813.

132. Li, J.-M.; Lin, Q.-C.; Li, N.; Li, Z.-H.; Tan, G.; Liu, S.-J.; Chung, L.-H.; Liao, W.-M.; Yu, L.; He, J., Symbiotically Reinforced Bimetallic Photocatalysis in Conjugated Metal−Organic Framework Nanosheets. *Adv. Funct. Mater.* **2023**, *33* (5), 2210717.

133. Shi, Y.; Wang, Z.; Shi, Y.; Zhu, S.; Lu, K.; Zhang, Y.; Jin, J., Micrometer-sized MOF particles incorporated mixed-matrix membranes driven by π-π interfacial interactions for improved gas separation. *Sep. Purif. Technol.* **2022**, *295*, 121258.

134. Goh, S. H.; Lau, H. S.; Yong, W. F., Metal–Organic Frameworks (MOFs)-Based Mixed Matrix Membranes (MMMs) for Gas Separation: A Review on Advanced Materials in Harsh Environmental Applications. *Small.* **2022**, *18* (20), 2107536.

135. Feng, S.; Bu, M.; Pang, J.; Fan, W.; Fan, L.; Zhao, H.; Yang, G.; Guo, H.; Kong, G.; Sun, H.; Kang, Z.; Sun, D., Hydrothermal stable ZIF-67 nanosheets via morphology regulation strategy to construct mixed-matrix membrane for gas separation. *J. Membr. Sci.* **2020**, *593*, 117404.

136. Huang, D.; Xin, Q.; Ni, Y.; Shuai, Y.; Wang, S.; Li, Y.; Ye, H.; Lin, L.; Ding, X.; Zhang, Y., Synergistic effects of zeolite imidazole framework@graphene oxide composites in humidified mixed matrix membranes on $CO_2$ separation. *RSC Adv.* **2018**, *8* (11), 6099-6109.

137. Dong, L.; Chen, M.; Li, J.; Shi, D.; Dong, W.; Li, X.; Bai, Y., Metal-organic framework-graphene oxide composites: A facile method to highly improve the $CO_2$ separation performance of mixed matrix membranes. *J. Membr. Sci.* **2016**, *520*, 801-811.

138. Wu, X.; Zhang, H.; Yin, Z.; Yang, Y.; Wang, Z., ZIF-8/GO sandwich composite membranes through a precursor conversion strategy for $H_2/CO_2$ separation. *J. Membr. Sci.* **2022**, *647*, 120291.

139. Li, X.; Yu, S.; Li, K.; Ma, C.; Zhang, J.; Li, H.; Chang, X.; Zhu, L.; Xue, Q., Enhanced gas separation performance of Pebax mixed matrix membranes by incorporating ZIF-8 in situ inserted by multiwalled carbon nanotubes. *Sep. Purif. Technol.* **2020**, *248*, 117080.

140. Bondi, A. A., *Physical properties of molecular crystals, liquids, and glasses*. Wiley: 1968.

141. Farnam, M.; bin Mukhtar, H.; bin Mohd Shariff, A., A Review on Glassy and Rubbery Polymeric Membranes for Natural Gas Purification. *ChemBioEng Rev.* **2021**, *8* (2), 90-109.

142. Liu, Z.; Liu, Y.; Qiu, W.; Koros, W. J., Molecularly Engineered 6FDA-Based Polyimide Membranes for Sour Natural Gas Separation. *Angew. Chem. Int. Ed.* **2020**, *59* (35), 14877-14883.

143. Jusoh, N.; Yeong, Y. F.; Lau, K. K.; M. Shariff, A., Enhanced gas separation performance using mixed matrix membranes containing zeolite T and 6FDA-durene polyimide. *J. Membr. Sci.* **2017**, *525*, 175-186.

144. Checchetto, R.; Scarpa, M.; De Angelis, M. G.; Minelli, M., Mixed gas diffusion and permeation of ternary and quaternary $CO_2/CO/N_2/O_2$ gas mixtures in Matrimid®, polyetherimide and poly(lactic acid) membranes for $CO_2/CO$ separation. *J. Membr. Sci.* **2022**, *659*, 120768.

145. Yin, H.; Yang, B.; Chua, Y. Z.; Szymoniak, P.; Carta, M.; Malpass-Evans, R.; McKeown, N. B.; Harrison, W. J.; Budd, P. M.; Schick, C.; Böhning, M.; Schönhals, A., Effect of Backbone Rigidity on the Glass Transition of Polymers of Intrinsic Microporosity Probed by Fast Scanning Calorimetry. *ACS Macro Lett.* **2019**, *8* (8), 1022-1028.

146. Zhang, Y.; Wang, W.; Zhang, J.; Ni, Y., Dielectric relaxation processes in PVDF composite. *Polym. Test.* **2020**, *91*, 106801.

147. Aslam, M.; Raza, Z. A.; Siddique, A., Fabrication and chemo-physical characterization of CuO/chitosan nanocomposite-mediated tricomponent PVA films. *Polym. Bull.* **2021**, *78* (4), 1955-1965.

148. Nadeali, A.; Zamani Pedram, M.; Omidkhah, M.; Yarmohammadi, M., Promising Performance for Efficient $CO_2$ Separation with the p-tert-Butylcalix[4]arene/Pebax-1657 Mixed Matrix Membrane. *ACS Sustain. Chem. Eng.* **2019**, *7* (23), 19015-19026.

149. Vinh-Thang, H.; Kaliaguine, S., Predictive Models for Mixed-Matrix Membrane Performance: A Review. *Chem. Rev.* **2013**, *113* (7), 4980-5028.

150. Hashemifard, S. A.; Ismail, A. F.; Matsuura, T., Prediction of gas permeability in mixed matrix membranes using theoretical models. *J. Membr. Sci.* **2010**, *347* (1), 53-61.

151. Nobakht, D.; Abedini, R., Improved gas separation performance of Pebax®1657 membrane modified by poly-alcoholic compounds. *J. Environ. Chem. Eng.* **2022**, *10* (3), 107568.

152. Beuscher, U.; Kappert, E. J.; Wijmans, J. G., Membrane research beyond materials science. *J. Membr. Sci.* **2022**, *643*, 119902.

153. Yong, W. F.; Zhang, H., Recent advances in polymer blend membranes for gas separation and pervaporation. *Prog. Mater. Sci.* **2021**, *116*, 100713.

154. Datta, S. J.; Mayoral, A.; Murthy Srivatsa Bettahalli, N.; Bhatt, P. M.; Karunakaran, M.; Carja, I. D.; Fan, D.; Graziane M. Mileo, P.; Semino, R.; Maurin, G.; Terasaki, O.; Eddaoudi, M., Rational design of mixed-matrix metal-organic framework membranes for molecular separations. *Science.* **2022**, *376* (6597), 1080-1087.

155. Zhou, S.; Shekhah, O.; Ramírez, A.; Lyu, P.; Abou-Hamad, E.; Jia, J.; Li, J.; Bhatt, P. M.; Huang, Z.; Jiang, H.; Jin, T.; Maurin, G.; Gascon, J.; Eddaoudi, M., Asymmetric pore windows in MOF membranes for natural gas valorization. *Nature.* **2022**, *606* (7915), 706-712.

156. Shu, L.; Peng, Y.; Yao, R.; Song, H.; Zhu, C.; Yang, W., Flexible Soft-Solid Metal–Organic Framework Composite Membranes for $H_2/CO_2$ Separation. *Angew. Chem. Int. Ed.* **2022**, *61* (14), e202117577.

157. Liu, J.; Wang, S.; Huang, T.; Manchanda, P.; Abou-Hamad, E.; Nunes, S. P., Smart covalent organic networks (CONs) with “on-off-on” light-switchable pores for molecular separation. *Sci. Adv. 6* (34), eabb3188.

158. Yuan, S.; Li, X.; Zhu, J.; Zhang, G.; Van Puyvelde, P.; Van der Bruggen, B., Covalent organic frameworks for membrane separation. *Chem Soc Rev.* **2019**, *48* (10), 2665-2681.

159. Liu, J.; Han, G.; Zhao, D.; Lu, K.; Gao, J.; Chung, T.-S., Self-standing and flexible covalent organic framework (COF) membranes for molecular separation. *Sci. Adv. 6* (41), eabb1110.

160. Kim, D.; Ghosh, S.; Akter, N.; Kraetz, A.; Duan, X.; Gwak, G.; Rangnekar, N.; Johnson, J. R.; Narasimharao, K.; Malik, M. A.; Al-Thabaiti, S.; McCool, B.; Boscoboinik, J. A.; Mkhoyan, K. A.; Tsapatsis, M., Twin-free, directly synthesized MFI nanosheets with improved thickness uniformity and their use in membrane fabrication. *Sci. Adv. 8* (14), eabm8162.

161. Xia, Y.; Cao, H.; Xu, F.; Chen, Y.; Xia, Y.; Zhang, D.; Dai, L.; Qu, K.; Lian, C.; Huang, K.; Xing, W.; Jin, W.; Xu, Z., Polymeric membranes with aligned zeolite nanosheets for sustainable energy storage. *Nat. Sustain.* **2022**, *5* (12), 1080-1091.

162. Qian, Q.; Asinger, P. A.; Lee, M. J.; Han, G.; Mizrahi Rodriguez, K.; Lin, S.; Benedetti, F. M.; Wu, A. X.; Chi, W. S.; Smith, Z. P., MOF-based membranes for gas separations. *Chem. Rev.* **2020**, *120* (16), 8161-8266.

163. Kalaj, M.; Bentz, K. C.; Ayala, S., Jr.; Palomba, J. M.; Barcus, K. S.; Katayama, Y.; Cohen, S. M., MOF-polymer hybrid materials: from simple composites to tailored architectures. *Chem. Rev.* **2020**, *120* (16), 8267-8302.

164. Frentzel-Beyme, L.; Kloß, M.; Kolodzeiski, P.; Pallach, R.; Henke, S., Meltable mixed-linker zeolitic imidazolate frameworks and their microporous glasses: From melting point engineering to selective hydrocarbon sorption. *J. Am. Chem. Soc.* **2019**, *141* (31), 12362-12371.

165. Hou, J.; Chen, P.; Shukla, A.; Krajnc, A.; Wang, T.; Li, X.; Doasa, R.; Tizei, L. H. G.; Chan, B.; Johnstone, D. N.; Lin, R.; Schülli, T. U.; Martens, I.; Appadoo, D.; Ari, M. S.; Wang, Z.; Wei, T.; Lo, S.-C.; Lu, M.; Li, S.; Namdas, E. B.; Mali, G.; Cheetham, A. K.; Collins, S. M.; Chen, V.; Wang, L.; Bennett, T. D., Liquid-phase sintering of lead halide perovskites and metal-organic framework glasses. *Science.* **2021**, *374* (6567), 621-625.

166. Zhou, B.; Qi, Z.; Yan, D., Highly efficient and direct ultralong all-phosphorescence from metal–organic framework photonic glasses. *Angew. Chem. Int. Ed.* **2022**, *61* (39), e202208735.

167. Chai, M.; Chen, R.; Xu, K.; Chen, Y.; Ma, S.; Lin, R.; Chen, V.; Hou, J., Ion transport and conduction in metal-organic framework glasses. *J. Mater. Chem. A.* **2023**.

168. Tao, H.; Bennett, T. D.; Yue, Y., Melt-quenched hybrid glasses from metal–organic frameworks. *Adv Mater.* **2017**, *29* (20), 1601705.

169. Song, J.; Frentzel-Beyme, L.; Pallach, R.; Kolodzeiski, P.; Koutsianos, A.; Xue, W.-L.; Schmid, R.; Henke, S., Modulating Liquid–Liquid Transitions and Glass Formation in Zeolitic

Imidazolate Frameworks by Decoration with Electron-Withdrawing Cyano Groups. *J. Am. Chem. Soc.* **2023**, *145* (16), 9273-9284.

170. Li, S.; Limbach, R.; Longley, L.; Shirzadi, A. A.; Walmsley, J. C.; Johnstone, D. N.; Midgley, P. A.; Wondraczek, L.; Bennett, T. D., Mechanical properties and processing techniques of bulk metal–organic framework glasses. *J. Am. Chem. Soc.* **2019**, *141* (2), 1027-1034.

171. Zhang, Y.; Wang, Y.; Xia, H.; Gao, P.; Cao, Y.; Jin, H.; Li, Y., A hybrid ZIF-8/ZIF-62 glass membrane for gas separation. *ChemComm.* **2022**, *58* (68), 9548-9551.

172. Yang, Z.; Belmabkhout, Y.; McHugh, L. N.; Ao, D.; Sun, Y.; Li, S.; Qiao, Z.; Bennett, T. D.; Guiver, M. D.; Zhong, C., ZIF-62 glass foam self-supported membranes to address $CH_4/N_2$ separations. *Nat. Mater.* **2023**.

173. Ao, D.; Yang, Z.; Qiao, Z.; Sun, Y.; Zhang, Z.; Guiver, M. D.; Zhong, C., Metal–Organic Framework Crystal–Glass Composite Membranes with Preferential Permeation of Ethane. *Angew. Chem. Int. Ed.* **2023**, *62* (28), e202304535.

174. Lin, R.; Chai, M.; Zhou, Y.; Chen, V.; Bennett, T. D.; Hou, J., Metal–organic framework glass composites. *Chem Soc Rev.* **2023**, *52* (13), 4149-4172.

175. Thorne, M. F.; Gómez, M. L. R.; Bumstead, A. M.; Li, S.; Bennett, T. D., Mechanochemical synthesis of mixed metal, mixed linker, glass-forming metal–organic frameworks. *Green Chem.* **2020**, *22* (8), 2505-2512.

176. Shigematsu, A.; Yamada, T.; Kitagawa, H., Wide Control of Proton Conductivity in Porous Coordination Polymers. *J. Am. Chem. Soc.* **2011**, *133* (7), 2034-2036.

177. Kim, J. Y.; Zhang, L.; Balderas-Xicohténcatl, R.; Park, J.; Hirscher, M.; Moon, H. R.; Oh, H., Selective Hydrogen Isotope Separation via Breathing Transition in MIL-53(Al). *J. Am. Chem. Soc.* **2017**, *139* (49), 17743-17746.

178. Liu, J.; Zhang, F.; Zou, X.; Yu, G.; Zhao, N.; Fan, S.; Zhu, G., Environmentally friendly synthesis of highly hydrophobic and stable MIL-53 MOF nanomaterials. *ChemComm.* **2013**, *49* (67), 7430-7432.

179. García-Ben, J.; López-Beceiro, J.; Artiaga, R.; Salgado-Beceiro, J.; Delgado-Ferreiro, I.; Kolen'ko, Y. V.; Castro-García, S.; Señarís-Rodríguez, M. A.; Sánchez-Andújar, M.; Bermúdez-García, J. M., Discovery of Colossal Breathing-Caloric Effect under Low Applied Pressure in the Hybrid Organic–Inorganic MIL-53(Al) Material. *Chem. Mater.* **2022**, *34* (7), 3323-3332.

180. Qazvini, O. T.; Babarao, R.; Telfer, S. G., Selective capture of carbon dioxide from hydrocarbons using a metal-organic framework. *Nat Commun.* **2021**, *12* (1), 197.

181. An, H.; Jung, W.; Shin, J. H.; Shin, M. C.; Park, J. H.; Lee, J.; Lee, J. S., Highly concentrated multivariate ZIF-8 mixed-matrix hollow fiber membranes for $CO_2$ separation: Scalable fabrication and process analysis. *J. Membr. Sci.* **2023**, *684*, 121875.

182. Burney, J.; Persad, G.; Proctor, J.; Bendavid, E.; Burke, M.; Heft-Neal, S., Geographically resolved social cost of anthropogenic emissions accounting for both direct and climate-mediated effects. *Sci. Adv. 8* (38), eabn7307.

183. Zheng, X.; Lu, Y.; Ma, C.; Yuan, J.; Stenseth, N. C.; Hessen, D. O.; Tian, H.; Chen, D.; Chen, Y.; Zhang, S., Greenhouse gas emissions from extractive industries in a globalized era. *J. Environ. Manage.* **2023**, *343*, 118172.

184. Ansari, S. A.; Shakeel, A.; Sawarkar, R.; Maddalwar, S.; Khan, D.; Singh, L., Additive facilitated co-composting of lignocellulosic biomass waste, approach towards minimizing greenhouse gas emissions: An up to date review. *Environ. Res.* **2023**, *224*, 115529.

185. Wilberforce, T.; Baroutaji, A.; Soudan, B.; Al-Alami, A. H.; Olabi, A. G., Outlook of carbon capture technology and challenges. *Sci. Total Environ.* **2019**, *657*, 56-72.

186. Wilson, I.; Saini, S.; Sreenivasan, H.; Sahu, C.; Krishna, S.; Gupta, P., Review and Perspectives of Energy-Efficient Methane Production from Natural Gas Hydrate Reservoirs Using Carbon Dioxide Exchange Technology. *Energy & Fuels.* **2023**, *37* (14), 9841-9872.

187. Lee, S.; Kim, J.-K., Sub-ambient membrane process for $CO_2$ removal in the industrial sector: Iron and steel, cement, and refinery. *J. Membr. Sci.* **2023**, 122018.

188. Chen, G.; Wang, T.; Zhang, G.; Liu, G.; Jin, W., Membrane materials targeting carbon capture and utilization. *Adv. Membr.* **2022**, *2*, 100025.

189. Sidhikku Kandath Valappil, R.; Ghasem, N.; Al-Marzouqi, M., Current and future trends in polymer membrane-based gas separation technology: A comprehensive review. *J. Ind. Eng. Chem.* **2021**, *98*, 103-129.

190. Bozorg, M.; Addis, B.; Piccialli, V.; Ramírez-Santos, Á. A.; Castel, C.; Pinnau, I.; Favre, E., Polymeric membrane materials for nitrogen production from air: A process synthesis study. *Chem. Eng. Sci.* **2019**, *207*, 1196-1213.

191. Kamble, A. R.; Patel, C. M.; Murthy, Z. V. P., A review on the recent advances in mixed matrix membranes for gas separation processes. *Renew. Sustain. Energy Rev.* **2021**, *145*, 111062.

192. Feng, Y.; Yan, W.; Kang, Z.; Zou, X.; Fan, W.; Jiang, Y.; Fan, L.; Wang, R.; Sun, D., Thermal treatment optimization of porous MOF glass and polymer for improving gas permeability and selectivity of mixed matrix membranes. *Chem. Eng. J.* **2023**, *465*, 142873.

193. Dunn, C. A.; Denning, S.; Crawford, J. M.; Zhou, R.; Dwulet, G. E.; Carreon, M. A.; Gin, D. L.; Noble, R. D., $CO_2/CH_4$ separation characteristics of poly(RTIL)-RTIL-zeolite mixed-matrix membranes evaluated under binary feeds up to 40 bar and 50°C. *J. Membr. Sci.* **2021**, *621*, 118979.

194. Chen, G.; Liu, G.; Pan, Y.; Liu, G.; Gu, X.; Jin, W.; Xu, N., Zeolites and metal–organic frameworks for gas separation: the possibility of translating adsorbents into membranes. *Chem Soc Rev.* **2023**, *52* (14), 4586-4602.

195. Li, H.; Dilipkumar, A.; Abubakar, S.; Zhao, D., Covalent organic frameworks for $CO_2$ capture: from laboratory curiosity to industry implementation. *Chem Soc Rev.* **2023**.

196. Chen, B.; Xie, H.; Shen, L.; Xu, Y.; Zhang, M.; Zhou, M.; Li, B.; Li, R.; Lin, H., Covalent Organic Frameworks: The Rising-Star Platforms for the Design of $CO_2$ Separation Membranes. *Small.* **2023**, *19* (17), 2207313.

197. Huang, M.; Wang, Z.; Jin, J., Two-dimensional microporous material-based mixed matrix membranes for gas separation. *Chem. Asian J.* **2020**, *15* (15), 2303-2315.

198. Yang, H.; Liang, S.; Zhang, P.; Zhang, X.; Lu, P.; Liu, Y.; Cao, X.; Li, Y.; Wang, Q., Improved $CO_2$ separation performance of mixed matrix membranes via expanded layer double hydroxides and methanol post-treatment. *J. Membr. Sci.* **2023**, *670*, 121345.

199. Chen, G.; Chen, X.; Pan, Y.; Ji, Y.; Liu, G.; Jin, W., M-gallate MOF/6FDA-polyimide mixed-matrix membranes for $C_2H_4/C_2H_6$ separation. *J. Membr. Sci.* **2021**, *620*, 118852.

200. Wang, Y.; Ren, Y.; Wu, H.; Wu, X.; Yang, H.; Yang, L.; Wang, X.; Wu, Y.; Liu, Y.; Jiang, Z., Amino-functionalized ZIF-7 embedded polymers of intrinsic microporosity membrane with enhanced selectivity for biogas upgrading. *J. Membr. Sci.* **2020**, *602*, 117970.

201. Yu, G.; Zou, X.; Sun, L.; Liu, B.; Wang, Z.; Zhang, P.; Zhu, G., Constructing Connected Paths between UiO-66 and PIM-1 to Improve Membrane $CO_2$ Separation with Crystal-Like Gas Selectivity. *Adv Mater.* **2019**, *31* (15), 1806853.

202. Qian, Q.; Wu, A. X.; Chi, W. S.; Asinger, P. A.; Lin, S.; Hypsher, A.; Smith, Z. P., Mixed-Matrix Membranes Formed from Imide-Functionalized UiO-66-$NH_2$ for Improved Interfacial Compatibility. *ACS Appl. Mater. Interfaces.* **2019**, *11* (34), 31257-31269.

203. Qazvini, O. T.; Telfer, S. G., MUF-16: A robust metal–organic framework for pre- and post-combustion carbon dioxide capture. *ACS Appl. Mater. Interfaces.* **2021**, *13* (10), 12141-12148.

204. Li, T.; Pan, Y.; Peinemann, K.-V.; Lai, Z., Carbon dioxide selective mixed matrix composite membrane containing ZIF-7 nano-fillers. *J. Membr. Sci.* **2013**, *425-426*, 235-242.

205. Hu, Z.; Miu, J.; Zhang, X.-F.; Jia, M.; Yao, J., UiO-66-$NH_2$ particle size effects on gas separation performance of cellulose acetate composite membranes. *J. Appl. Polym. Sci.* **2022**, *139* (33), e52810.

206. Asim, M.; Khan, A.; Helal, A.; Alshitari, W.; Akbar, U. A.; Khan, M. Y., A 2D Graphitic-Polytriaminopyrimidine (g-PTAP)/Poly(ether-block-amide) Mixed Matrix Membrane for $CO_2$ Separation. *Chem. Asian J.* **2021**, *16* (13), 1839-1848.

207. Sutrisna, P. D.; Hou, J.; Li, H.; Zhang, Y.; Chen, V., Improved operational stability of Pebax-based gas separation membranes with ZIF-8: A comparative study of flat sheet and composite hollow fibre membranes. *J. Membr. Sci.* **2017**, *524*, 266-279.

208. Sutrisna, P. D.; Hou, J.; Zulkifli, M. Y.; Li, H.; Zhang, Y.; Liang, W.; D'Alessandro, Deanna M.; Chen, V., Surface functionalized UiO-66/Pebax-based ultrathin composite hollow fiber gas separation membranes. *J. Mater. Chem. A.* **2018**, *6* (3), 918-931.

209. Qian, J.; Wu, T.; Shi, J.; Chang, H.; Liu, D.; Pan, Y., Improved $CO_2/CH_4$ separation performance of mixed-matrix membrane by adding ZIF-7-$NH_2$ nanocrystals. *J. Appl. Polym. Sci.* **2021**, *138* (20), 5042

210. Ding, R.; Li, Z.; Dai, Y.; Li, X.; Ruan, X.; Gao, J.; Zheng, W.; He, G., Boosting the $CO_2/N_2$ selectivity of MMMs by vesicle shaped ZIF-8 with high amino content. *Sep. Purif. Technol.* **2022**, *298*, 121594.

211. Meshkat, S.; Kaliaguine, S.; Rodrigue, D., Comparison between ZIF-67 and ZIF-8 in Pebax® MH-1657 mixed matrix membranes for $CO_2$ separation. *Sep. Purif. Technol.* **2020**, *235*, 116150.

212. Ding, R.; Zheng, W.; Yang, K.; Dai, Y.; Ruan, X.; Yan, X.; He, G., Amino-functional ZIF-8 nanocrystals by microemulsion based mixed linker strategy and the enhanced $CO_2/N_2$ separation. *Sep. Purif. Technol.* **2020**, *236*, 116209.

213. Nadeali, A.; Kalantari, S.; Yarmohammadi, M.; Omidkhah, M.; Ebadi Amooghin, A.; Zamani Pedram, M., $CO_2$ Separation Properties of a Ternary Mixed-Matrix Membrane Using Ultraselective Synthesized Macrocyclic Organic Compounds. *ACS Sustain. Chem. Eng.* **2020**, *8* (34), 12775-12787.

214. Zheng, W.; Tian, Z.; Wang, Z.; Peng, D.; Zhang, Y.; Wang, J.; Zhang, Y., Dual-function biomimetic carrier based facilitated transport mixed matrix membranes with high stability for efficient $CO_2/N_2$ separation. *Sep. Purif. Technol.* **2022**, *285*, 120371.

215. Duan, K.; Wang, J.; Zhang, Y.; Liu, J., Covalent organic frameworks (COFs) functionalized mixed matrix membrane for effective $CO_2/N_2$ separation. *J. Membr. Sci.* **2019**, *572*, 588-595.

216. Feng, X.; Qin, Z.; Lai, Q.; Zhang, Z.; Shao, Z.-W.; Tang, W.; Wu, W.; Dai, Z.; Liu, C., Mixed-matrix membranes based on novel hydroxamate metal–organic frameworks with two-dimensional layers for $CO_2/N_2$ separation. *Sep. Purif. Technol.* **2023**, *305*, 122476.

217. Ghasemi Estahbanati, E.; Omidkhah, M.; Ebadi Amooghin, A., Interfacial Design of Ternary Mixed Matrix Membranes Containing Pebax 1657/Silver-Nanopowder/[BMIM][$BF_4$] for Improved $CO_2$ Separation Performance. *ACS Appl. Mater. Interfaces.* **2017**, *9* (11), 10094-10105.

218. Gou, M.; Guo, R.; Cao, H.; Zhu, W.; Liu, F.; Wei, Z., An MOF-tailored hierarchical porous microenvironment for $CO_2$ as an efficient filler for mixed matrix membranes. *Chem. Eng. J.* **2022**, *438*, 135651.

219. Habib, N.; Shamair, Z.; Tara, N.; Nizami, A.-S.; Akhtar, F. H.; Ahmad, N. M.; Gilani, M. A.; Bilad, M. R.; Khan, A. L., Development of highly permeable and selective mixed matrix membranes based on Pebax®1657 and NOTT-300 for $CO_2$ capture. *Sep. Purif. Technol.* **2020**, *234*, 116101.

220. Zhu, W.; Li, X.; Sun, Y.; Guo, R.; Ding, S., Introducing hydrophilic ultra-thin ZIF-L into mixed matrix membranes for $CO_2/CH_4$ separation. *RSC Adv.* **2019**, *9* (40), 23390-23399.

221. Sun, Y.; Gou, M., Highly efficient of $CO_2/CH_4$ separation performance via the pebax membranes with multi-functional polymer nanotubes. *Microporous Mesoporous Mater.* **2022**, *342*, 112120.

222. Li, X.; Lv, X.; Ding, S.; Huang, L.; Wei, Z., Mixed matrix membranes containing composite nanosheets with three-dimensional nanopores for efficient $CO_2$ separation. *Int. J. Greenh. Gas Control.* **2022**, *117*, 103658.

223. Wang, Y.; Zhang, N.; Wu, H.; Ren, Y.; Yang, L.; Wang, X.; Wu, Y.; Liu, Y.; Zhao, R.; Jiang, Z., Exfoliation-free layered double hydroxides laminates intercalated with amino acids for enhanced $CO_2$ separation of mixed matrix membrane. *J. Membr. Sci.* **2021**, *618*, 118691.

224. Zhang, H.; Guo, R.; Zhang, J.; Li, X., Facilitating $CO_2$ Transport Across Mixed Matrix Membranes Containing Multifunctional Nanocapsules. *ACS Appl. Mater. Interfaces.* **2018**, *10* (49), 43031-43039.

225. Cheng, J.; Yang, C.; Hou, W.; Liu, N.; Xia, R.; Chen, Z.; Zhang, H.; Liu, J., Carbon nanotubes grown on ZIF-L(Zn@Co) surface improved $CO_2$ permeability of mixed matrix membranes. *J. Membr. Sci.* **2023**, *670*, 121356.

226. Ribeiro, C. P.; Freeman, B. D.; Paul, D. R., Pure- and mixed-gas carbon dioxide/ethane permeability and diffusivity in a cross-linked poly(ethylene oxide) copolymer. *J. Membr. Sci.* **2011**, *377* (1), 110-123.

227. Shen, Q.; Cong, S.; Zhu, J.; Zhang, Y.; He, R.; Yi, S.; Zhang, Y., Novel pyrazole-based MOF synergistic polymer of intrinsic microporosity membranes for high-efficient $CO_2$ capture. *J. Membr. Sci.* **2022**, *664*, 121107.

228. Yu, G.; Li, Y.; Wang, Z.; Liu, T. X.; Zhu, G.; Zou, X., Mixed matrix membranes derived from nanoscale porous organic frameworks for permeable and selective $CO_2$ separation. *J. Membr. Sci.* **2019**, *591*, 117343.

229. Kim, E. J.; Siegelman, R. L.; Jiang, H. Z. H.; Forse, A. C.; Lee, J.-H.; Martell, J. D.; Milner, P. J.; Falkowski, J. M.; Neaton, J. B.; Reimer, J. A.; Weston, S. C.; Long, J. R., Cooperative carbon capture and steam regeneration with tetraamine-appended metal–organic frameworks. *Science.* **2020**, *369* (6502), 392-396.

230. Prasetya, N.; Himma, N. F.; Sutrisna, P. D.; Wenten, I. G.; Ladewig, B. P., A review on emerging organic-containing microporous material membranes for carbon capture and separation. *Chem. Eng. J.* **2020**, *391*, 123575.

231. Lai, H. W. H.; Benedetti, F. M.; Ahn, J. M.; Robinson, A. M.; Wang, Y.; Pinnau, I.; Smith, Z. P.; Xia, Y., Hydrocarbon ladder polymers with ultrahigh permselectivity for membrane gas separations. *Science.* **2022**, *375* (6587), 1390-1392.

232. Zhu, Q.; Cai, Z.; Zhou, P.; Sun, X.; Xu, J., Recent progress of membrane technology for chiral separation: A comprehensive review. *Sep. Purif. Technol.* **2023**, *309*, 123077.

233. Wang, B.; Sheng, M.; Xu, J.; Zhao, S.; Wang, J.; Wang, Z., Recent advances of gas transport channels constructed with different dimensional nanomaterials in mixed-matrix membranes for $CO_2$ separation. *Small Methods.* **2020**, *4* (3), 1900749.

234. Chen, Z.; Yan, D.; Ma, L.; Zhang, Y.; Zhang, J.; Li, H.; Khoo, R.; Zhang, J.; Svec, F.; Lv, Y.; Tan, T., Polymerizable metal-organic frameworks for the preparation of mixed matrix membranes with enhanced interfacial compatibility. *iScience.* **2021**, *24* (6), 102560.

235. Wu, C.; Zhang, K.; Wang, H.; Fan, Y.; Zhang, S.; He, S.; Wang, F.; Tao, Y.; Zhao, X.; Zhang, Y.-B.; Ma, Y.; Lee, Y.; Li, T., Enhancing the gas separation selectivity of mixed-matrix membranes using a dual-Interfacial engineering approach. *J. Am. Chem. Soc.* **2020**, *142* (43), 18503-18512.

236. Zhao, J.; He, G.; Huang, S.; Villalobos, L. F.; Dakhchoune, M.; Bassas, H.; Agrawal, K. V., Etching gas-sieving nanopores in single-layer graphene with an angstrom precision for high-performance gas mixture separation. *Sci. Adv. 5* (1), eaav1851.

237. Choi, K.; Droudian, A.; Wyss, R. M.; Schlichting, K.-P.; Park, H. G., Multifunctional wafer-scale graphene membranes for fast ultrafiltration and high permeation gas separation. *Sci. Adv. 4* (11), eaau0476.

238. Du, P.; Zhang, Y.; Wang, X.; Canossa, S.; Hong, Z.; Nénert, G.; Jin, W.; Gu, X., Control of zeolite framework flexibility for ultra-selective carbon dioxide separation. *Nat Commun.* **2022**, *13* (1), 1427.

239. Dakhchoune, M.; Villalobos, L. F.; Semino, R.; Liu, L.; Rezaei, M.; Schouwink, P.; Avalos, C. E.; Baade, P.; Wood, V.; Han, Y.; Ceriotti, M.; Agrawal, K. V., Gas-sieving zeolitic membranes fabricated by condensation of precursor nanosheets. *Nat. Mater.* **2021**, *20* (3), 362-369.

240. Fan, H.; Peng, M.; Strauss, I.; Mundstock, A.; Meng, H.; Caro, J., MOF-in-COF molecular sieving membrane for selective hydrogen separation. *Nat Commun.* **2021**, *12* (1), 38.

241. Chang, X.; Guo, H.; Chang, Q.; Tian, Z.; Zhang, Y.; Li, D.; Wang, J.; Zhang, Y., Mixed-matrix membranes composed of dopamine modified covalent organic framework and PIM-1 for efficient $CO_2/N_2$ separation. *J. Membr. Sci.* **2023**, *686*, 122017.

242. Wei, R.; Liu, X.; Zhou, Z.; Chen, C.; Yuan, Y.; Li, Z.; Li, X.; Dong, X.; Lu, D.; Han, Y.; Lai, Z., Carbon nanotube supported oriented metal organic framework membrane for effective ethylene/ethane separation. *Sci. Adv. 8* (7), eabm6741.

243. Lin, R.-B.; Xiang, S.; Zhou, W.; Chen, B., Microporous metal-organic framework materials for gas separation. *Chem.* **2020**, *6* (2), 337-363.

244. Hu, L.; Chen, K.; Lee, W.-I.; Kisslinger, K.; Rumsey, C.; Fan, S.; Bui, V. T.; Esmaeili, N.; Tran, T.; Ding, Y.; Trebbin, M.; Nam, C.-Y.; Swihart, M. T.; Lin, H., Palladium-Percolated Networks Enabled by Low Loadings of Branched Nanorods for Enhanced $H_2$ Separations. *Adv Mater.* **2023**, *35* (26), 2301007.

245. Ying, Y.; Zhang, Z.; Peh, S. B.; Karmakar, A.; Cheng, Y.; Zhang, J.; Xi, L.; Boothroyd, C.; Lam, Y. M.; Zhong, C.; Zhao, D., Pressure-responsive two-dimensional metal–organic framework composite membranes for $CO_2$ separation. *Angew. Chem. Int. Ed.* **2021**, *60* (20), 11318-11325.

246. Zhao, Q.; Niu, K.; Wang, R.; Lian, S.; Li, R.; Zang, G.; Song, C., Pre-anchoring matrix onto zeolitic imidazolate frameworks towards defect-free mixed matrix membranes for efficient $CO_2$ separation. *J. Membr. Sci.* **2023**, *683*, 121869.

247. Wang, J.; Wang, Y.; Liu, Y.; Wu, H.; Zhao, M.; Ren, Y.; Pu, Y.; Li, W.; Wang, S.; Song, S.; Liang, X.; He, G.; Han, Y.; Jiang, Z., Ultrathin ZIF-8 membrane through inhibited ostwald ripening for high-flux $C_3H_6/C_3H_8$ separation. *Adv. Funct. Mater.* **2022**, *32* (47), 2208064.

248. Lee, T. H.; Jung, J. G.; Kim, Y. J.; Roh, J. S.; Yoon, H. W.; Ghanem, B. S.; Kim, H. W.; Cho, Y. H.; Pinnau, I.; Park, H. B., Defect engineering in metal–organic frameworks

towards advanced mixed matrix membranes for efficient propylene/propane separation. *Angew. Chem. Int. Ed.* **2021**, *60* (23), 13081-13088.

249. He, R.; Cong, S.; Peng, D.; Zhang, Y.; Shan, M.; Zhu, J.; Wang, J.; Gascon, J., Enhanced compatibility and selectivity in mixed matrix membranes for propylene/propane separation. *AIChE J.* **2023**, *69* (3), e17948.

250. He, C.; Zhang, P.; Wang, Y.; Zhang, Y.; Hu, T.; Li, L.; Li, J., Thermodynamic and kinetic synergetic separation of $CO_2$/C2$H_2$ in an ultramicroporous metal-organic framework. *Sep. Purif. Technol.* **2023**, *304*, 122318.

251. Hu, L.; Clark, K.; Alebrahim, T.; Lin, H., Mixed matrix membranes for post-combustion carbon capture: From materials design to membrane engineering. *J. Membr. Sci.* **2022**, *644*, 120140.

252. Ma, C.; Yang, Z.; Guo, X.; Qiao, Z.; Zhong, C., Size-reduced low-crystallinity ZIF-62 for the preparation of mixed-matrix membranes for $CH_4$/$N_2$ separation. *J. Membr. Sci.* **2022**, *663*, 121069.

253. Hwang, J.; Ejsmont, A.; Freund, R.; Goscianska, J.; Schmidt, B. V. K. J.; Wuttke, S., Controlling the morphology of metal–organic frameworks and porous carbon materials: metal oxides as primary architecture-directing agents. *Chem Soc Rev.* **2020**, *49* (11), 3348-3422.

254. Wang, Z.; Wang, D.; Zhang, S.; Hu, L.; Jin, J., Interfacial design of mixed matrix membranes for improved gas separation performance. *Adv Mater.* **2016**, *28* (17), 3399-3405.

255. Nishijima, A.; Kametani, Y.; Uemura, T., Reciprocal regulation between MOFs and polymers. *Coord. Chem. Rev.* **2022**, *466*, 214601.

256. Huelsenbeck, L.; Luo, H.; Verma, P.; Dane, J.; Ho, R.; Beyer, E.; Hall, H.; Geise, G. M.; Giri, G., Generalized approach for rapid aqueous MOF synthesis by controlling solution pH. *Cryst. Growth Des.* **2020**, *20* (10), 6787-6795.

257. Freund, R.; Lanza, A. E.; Canossa, S.; Gemmi, M.; Goscianska, J.; Cauda, V.; Oschatz, M.; Wuttke, S., Understanding the Chemistry of Metal Oxide to Metal–Organic Framework Reactions for Morphology Control. *Chem. Mater.* **2023**, *35* (5), 1891-1900.

258. Liu, G.; Chernikova, V.; Liu, Y.; Zhang, K.; Belmabkhout, Y.; Shekhah, O.; Zhang, C.; Yi, S.; Eddaoudi, M.; Koros, W. J., Mixed matrix formulations with MOF molecular sieving for key energy-intensive separations. *Nat. Mater.* **2018**, *17* (3), 283-289.

259. Lee, H. K.; Lee, J. H.; Moon, H. R., Mechanochemistry as a reconstruction tool of decomposed metal–organic frameworks. *Inorg. Chem.* **2021**, *60* (16), 11825-11829.

260. Martinez, V.; Stolar, T.; Karadeniz, B.; Brekalo, I.; Užarević, K., Advancing mechanochemical synthesis by combining milling with different energy sources. *Nat. Rev. Chem.* **2023**, *7* (1), 51-65.

261. Li, G.; Si, Z.; Yang, S.; Zhuang, Y.; Pang, S.; Cui, Y.; Baeyens, J.; Qin, P., A defects-free ZIF-90/6FDA-Durene membrane based on the hydrogen bonding/covalent bonding interaction for gas separation. *J. Membr. Sci.* **2022**, *661*, 120910.

262. Lee, T. H.; Lee, B. K.; Youn, C.; Kang, J. H.; Kim, Y. J.; Kim, K. I.; Ha, Y. R.; Han, Y.; Park, H. B., Interface engineering in MOF/crosslinked polyimide mixed matrix membranes for enhanced propylene/propane separation performance and plasticization resistance. *J. Membr. Sci.* **2023**, *667*, 121182.

263. Liu, T.; Zhang, R.; Si, G.-R.; Liu, B.; Xie, Y.; Xie, L.-H.; Li, J.-R., Molecularly Homogenized Composite Membranes Containing Solvent-Soluble Metallocavitands for $CO_2/CH_4$ Separation. *ACS Sustain. Chem. Eng.* **2022**, *10* (40), 13534-13544.

264. Chen, K.; Ni, L.; Zhang, H.; Xiao, C.; Li, L.; Guo, X.; Qi, J.; Wang, C.; Sun, X.; Li, J., Incorporating KAUST-7 into PIM-1 towards mixed matrix membranes with long-term stable $CO_2/CH_4$ separation performance. *J. Membr. Sci.* **2022**, *661*, 120848.

265. Chen, Z.; Meng, X.; Fan, Y.; Li, N.; Wu, L.; Luo, S.; Xie, W.; Wang, C., Two morphology distinct fillers with chemical similarity incorporated into Tröger' base polymers towards enhanced gas separation. *J. Membr. Sci.* **2023**, *685*, 121964.

266. Lee, Y.; Chuah, C. Y.; Lee, J.; Bae, T.-H., Effective functionalization of porous polymer fillers to enhance $CO_2/N_2$ separation performance of mixed-matrix membranes. *J. Membr. Sci.* **2022**, *647*, 120309.

267. Ma, J.; Ying, Y.; Guo, X.; Huang, H.; Liu, D.; Zhong, C., Fabrication of mixed-matrix membrane containing metal–organic framework composite with task-specific ionic liquid for efficient $CO_2$ separation. *J. Mater. Chem. A.* **2016**, *4* (19), 7281-7288.

268. Carja, I.-D.; Tavares, S. R.; Shekhah, O.; Ozcan, A.; Semino, R.; Kale, V. S.; Eddaoudi, M.; Maurin, G., Insights into the Enhancement of MOF/Polymer Adhesion in Mixed-Matrix Membranes via Polymer Functionalization. *ACS Appl. Mater. Interfaces.* **2021**, *13* (24), 29041-29047.

269. Xin, Q.; Ouyang, J.; Liu, T.; Li, Z.; Li, Z.; Liu, Y.; Wang, S.; Wu, H.; Jiang, Z.; Cao, X., Enhanced Interfacial Interaction and $CO_2$ Separation Performance of Mixed Matrix Membrane by Incorporating Polyethylenimine-Decorated Metal–Organic Frameworks. *ACS Appl. Mater. Interfaces.* **2015**, *7* (2), 1065-1077.

270. Cheng, Y.; Zhai, L.; Ying, Y.; Wang, Y.; Liu, G.; Dong, J.; Ng, D. Z. L.; Khan, S. A.; Zhao, D., Highly efficient $CO_2$ capture by mixed matrix membranes containing three-dimensional covalent organic framework fillers. *J. Mater. Chem. A.* **2019**, *7* (9), 4549-4560.

271. Voon, B. K.; Shen Lau, H.; Liang, C. Z.; Yong, W. F., Functionalized two-dimensional g-$C_3N_4$ nanosheets in PIM-1 mixed matrix membranes for gas separation. *Sep. Purif. Technol.* **2022**, *296*, 121354.

272. Husna, A.; Hossain, I.; Choi, O.; Lee, S. M.; Kim, T.-H., Efficient $CO_2$ Separation Using a PIM-PI-Functionalized UiO-66 MOF Incorporated Mixed Matrix Membrane in a PIM-PI-1 Polymer. *Macromol. Mater. Eng.* **2021**, *306* (10), 2100298.

273. Zornoza, B.; Téllez, C.; Coronas, J.; Esekhile, O.; Koros, W. J., Mixed matrix membranes based on 6FDA polyimide with silica and zeolite microsphere dispersed phases. *AIChE J.* **2015**, *61* (12), 4481-4490.

274. Wu, T.; Shi, Y.; Liu, Y.; Kumakiri, I.; Tanaka, K.; Chen, X.; Kita, H., Improved Gas Permeation Properties of 6FDA-TrMPD Mixed-Matrix Membrane with SAPO-34 Crystals Toward $CO_2$ Separation. *Energy & Fuels.* **2021**, *35* (13), 10680-10688.

275. Chuah, C. Y.; Lee, J.; Song, J.; Bae, T.-H. Carbon Molecular Sieve Membranes Comprising Graphene Oxides and Porous Carbon for $CO_2/N_2$ Separation *Membr.* [Online], 2021.

276. Chuah, C. Y.; Lee, J.; Bao, Y.; Song, J.; Bae, T.-H., High-performance porous carbon-zeolite mixed-matrix membranes for $CO_2/N_2$ separation. *J. Membr. Sci.* **2021**, *622*, 119031.

277. Dilshad, M. R.; Islam, A.; Sabir, A.; Shafiq, M.; Butt, M. T. Z.; Ijaz, A.; Jamil, T., Fabrication and performance characterization of novel zinc oxide filled cross-linked PVA/PEG 600 blended membranes for $CO_2/N_2$ separation. *J. Ind. Eng. Chem.* **2017**, *55*, 65-73.

278. Bae, T.-H.; Lee, J. S.; Qiu, W.; Koros, W. J.; Jones, C. W.; Nair, S., A High-Performance Gas-Separation Membrane Containing Submicrometer-Sized Metal–Organic Framework Crystals. *Angew. Chem. Int. Ed.* **2010**, *49* (51), 9863-9866.

279. Liu, G.; Labreche, Y.; Chernikova, V.; Shekhah, O.; Zhang, C.; Belmabkhout, Y.; Eddaoudi, M.; Koros, W. J., Zeolite-like MOF nanocrystals incorporated 6FDA-polyimide mixed-matrix membranes for $CO_2/CH_4$ separation. *J. Membr. Sci.* **2018**, *565*, 186-193.

280. Jusoh, N.; Yeong, Y. F.; Lau, K. K.; M. Shariff, A., Fabrication of silanated zeolite T/6FDA-durene composite membranes for $CO_2/CH_4$ separation. *J. Clean. Prod.* **2017**, *166*, 1043-1058.

281. Nik, O. G.; Chen, X. Y.; Kaliaguine, S., Functionalized metal organic framework-polyimide mixed matrix membranes for $CO_2/CH_4$ separation. *J. Membr. Sci.* **2012**, *413-414*, 48-61.

282. Bachman, J. E.; Long, J. R., Plasticization-resistant $Ni_2$(dobdc)/polyimide composite membranes for the removal of $CO_2$ from natural gas. *Energy Environ. Sci.* **2016**, *9* (6), 2031-2036.

283. Chen, K.; Ni, L.; Zhang, H.; Li, L.; Guo, X.; Qi, J.; Zhou, Y.; Zhu, Z.; Sun, X.; Li, J., Phenolic resin regulated interface of ZIF-8 based mixed matrix membrane for enhanced gas separation. *J. Membr. Sci.* **2023**, *666*, 121117.

284. Gajanan, K.; Ranjith, P. G.; Yang, S. Q.; Xu, T., Advances in research and developments on natural gas hydrate extraction with gas exchange. *Renew. Sustain. Energy Rev.* **2024**, *190*, 114045.

285. Liao, R.; Guo, Y.; Yang, L.; Zhou, H.; Jin, W., Solvent-induced microstructure of polyimide membrane to enhance $CO_2/CH_4$ separation. *J. Membr. Sci.* **2023**, *666*, 121199.

286. Pasichnyk, M.; Stanovsky, P.; Polezhaev, P.; Zach, B.; Šyc, M.; Bobák, M.; Jansen, J. C.; Přibyl, M.; Bara, J. E.; Friess, K.; Havlica, J.; Gin, D. L.; Noble, R. D.; Izák, P., Membrane technology for challenging separations: Removal of $CO_2$, $SO_2$ and $NO_x$ from flue and waste gases. *Sep. Purif. Technol.* **2023**, *323*, 124436.

287. Zhang, Y.; Zhu, J.; Hou, J.; Yi, S.; Van der Bruggen, B.; Zhang, Y., Carbonic anhydrase membranes for carbon capture and storage. *J. Mater. Sci. Lett.* **2022**, *2* (2), 100031.

288. Winarta, J.; Meshram, A.; Zhu, F.; Li, R.; Jafar, H.; Parmar, K.; Liu, J.; Mu, B., Metal–organic framework-based mixed-matrix membranes for gas separation: An overview. *Journal of Polymer Science* **2020**, *58* (18), 2518-2546.

289. Kang, Z.; Fan, L.; Sun, D., Recent advances and challenges of metal–organic framework membranes for gas separation. *J. Mater. Chem. A.* **2017**, *5* (21), 10073-10091.

290. Ali Akbar Razavi, S.; Morsali, A., Linker functionalized metal-organic frameworks. *Coord. Chem. Rev.* **2019**, *399*, 213023.

291. Vahabi, A. H.; Norouzi, F.; Sheibani, E.; Rahimi-Nasrabadi, M., Functionalized Zr-UiO-67 metal-organic frameworks: Structural landscape and application. *Coord. Chem. Rev.* **2021**, *445*, 214050.

292. Loloei, M.; Kaliaguine, S.; Rodrigue, D., Mixed matrix membranes based on $NH_2$-MIL-53 (Al) and 6FDA-ODA polyimide for $CO_2$ separation: Effect of the processing route on improving MOF-polymer interfacial interaction. *Sep. Purif. Technol.* **2021**, *270*, 118786.

293. Suhaimi, N. H.; Yeong, Y. F.; Ch'ng, C. W.; Jusoh, N., Tailoring $CO_2/CH_4$ Separation Performance of Mixed Matrix Membranes by Using ZIF-8 Particles Functionalized with Different Amine Groups. *Polymers.* **2019**, *11* (12).

294. Fan, Y.; Li, C.; Zhang, X.; Yang, X.; Su, X.; Ye, H.; Li, N., Tröger 's base mixed matrix membranes for gas separation incorporating $NH_2$-MIL-53(Al) nanocrystals. *J. Membr. Sci.* **2019**, *573*, 359-369.

295. Qazvini, O. T.; Babarao, R.; Shi, Z.-L.; Zhang, Y.-B.; Telfer, S. G., A Robust Ethane-Trapping Metal–Organic Framework with a High Capacity for Ethylene Purification. *J. Am. Chem. Soc.* **2019**, *141* (12), 5014-5020.

296. Qazvini, O. T.; Macreadie, L. K.; Telfer, S. G., Effect of Ligand Functionalization on the Separation of Small Hydrocarbons and $CO_2$ by a Series of MUF-15 Analogues. *Chem. Mater.* **2020**, *32* (15), 6744-6752.

297. Jusoh, N.; Yeong, Y. F.; Lau, K. K.; M. Shariff, A., Transport properties of mixed matrix membranes encompassing zeolitic imidazolate framework 8 (ZIF-8) nanofiller and 6FDA-durene polymer: Optimization of process variables for the separation of $CO_2$ from $CH_4$. *J. Clean. Prod.* **2017**, *149*, 80-95.

298. Ahmad, M. Z.; Martin-Gil, V.; Supinkova, T.; Lambert, P.; Castro-Muñoz, R.; Hrabanek, P.; Kocirik, M.; Fila, V., Novel MMM using $CO_2$ selective SSZ-16 and high-performance 6FDA-polyimide for $CO_2/CH_4$ separation. *Sep. Purif. Technol.* **2021**, *254*, 117582.

299. Duan, C.; Jie, X.; Zhu, H.; Liu, D.; Peng, W.; Cao, Y., Gas-permeation performance of metal organic framework/polyimide mixed-matrix membranes and additional explanation from the particle size angle. *J. Appl. Polym. Sci.* **2018**, *135* (10), 45728.

300. Chen, X. Y.; Vinh-Thang, H.; Rodrigue, D.; Kaliaguine, S., Amine-Functionalized MIL-53 Metal–Organic Framework in Polyimide Mixed Matrix Membranes for $CO_2/CH_4$ Separation. *Ind. Eng. Chem. Res.* **2012**, *51* (19), 6895-6906.

301. Hua, Y.; Wang, H.; Li, Q.; Chen, G.; Liu, G.; Duan, J.; Jin, W., Highly efficient $CH_4$ purification by LaBTB PCP-based mixed matrix membranes. *J. Mater. Chem. A.* **2018**, *6* (2), 599-606.

302. Nuhnen, A.; Klopotowski, M.; Tanh Jeazet, H. B.; Sorribas, S.; Zornoza, B.; Téllez, C.; Coronas, J.; Janiak, C., High performance MIL-101(Cr)@6FDA-mPD and MOF-199@6FDA-mPD mixed-matrix membranes for $CO_2/CH_4$ separation. *Dalton Trans.* **2020**, *49* (6), 1822-1829.

303. Wang, L.; Bai, X.; Gu, Y.; Shi, X.; Wang, S.; Hua, J.; Hou, R.; Wang, C.; Pan, Y., Aligned Metal–Organic Framework Nanoplates in Mixed-Matrix Membranes for Highly Selective $CO_2/CH_4$ Separation. *Adv. Mater. Interfaces.* **2023**, *10* (12), 2202524.

304. Wang, C.; Park, M. J.; Yu, H.; Matsuyama, H.; Drioli, E.; Shon, H. K., Recent advances of nanocomposite membranes using layer-by-layer assembly. *J. Membr. Sci.* **2022**, *661*, 120926.

305. Głowniak, S.; Szczęśniak, B.; Choma, J.; Jaroniec, M., Mechanochemistry: Toward green synthesis of metal–organic frameworks. *Mater. Today.* **2021**, *46*, 109-124.

306. Song, Q.; Nataraj, S. K.; Roussenova, M. V.; Tan, J. C.; Hughes, D. J.; Li, W.; Bourgoin, P.; Alam, M. A.; Cheetham, A. K.; Al-Muhtaseb, S. A.; Sivaniah, E., Zeolitic imidazolate framework (ZIF-8) based polymer nanocomposite membranes for gas separation. *Energy Environ. Sci.* **2012**, *5* (8), 8359-8369.

307. Chen, X. Y.; Hoang, V.-T.; Rodrigue, D.; Kaliaguine, S., Optimization of continuous phase in amino-functionalized metal–organic framework (MIL-53) based co-polyimide mixed matrix membranes for $CO_2/CH_4$ separation. *RSC Adv.* **2013**, *3* (46), 24266-24279.

# Electronic Appendices

## Table of Contents

# Appendix A for Chapter 2

## 1. Experimental section

### Materials

All the reagents and solvents were analytical grade and were used without further purification. $Zn(NO_3)_2 \cdot 6H_2O$ (99.99 %, Sigma-Aldrich), zinc oxide (ZnO, 99 %, Sigma-Aldrich), $ZrOCl_2 \cdot 8H_2O$ (99.9 %, Sigma-Aldrich), aluminium nitrate nonahydrate ($Al(NO_3)_3 \cdot 9H_2O$, 99.99 %), imidazole (Im, 99.5 %, Sigma-Aldrich), benzimidazole (bIm, 99.9 %, Sigma-Aldrich), 2-Methylimidazole (2-mIm, 99.9 %, Sigma-Aldrich), terephthalic acid ($H_2BDC$, 98 %, Sigma-Aldrich), Cobalt(II) acetate (99.99%, Sigma-Aldrich), 5-amino isophthalic acid ($H_2aip$, 99 %, Sigma-Aldrich), N,N-dimethylformamide (DMF, 99.5 %, VWR Chemicals), methanol (MeOH, 99.5 %, Fisher Scientific), acetone (≥99.5 %, Milton Adams Ltd), sodium hydroxide (NaOH, 98 %, Sigma-Aldrich), Triton X-100 (laboratory grade, BDH Chemicals Ltd), cyclohexane anhydrous (99.5 %, Fisher Scientific) and hexanol (analytical standard, BDH Chemicals Ltd). Press apparatus (home-made from hard steel, 18 mm in diameter). Deionized (DI) water was produced from a lab-based reverse osmosis water treatment.

### Synthesis of ZIF-62 powder

An environmentally friendly mechanochemical method was used to synthesize ZIF-62. In detail, to a 50 mL zirconium grinding jar, all reagents including ZnO (402.83 mg, 4.95 mmol), zinc acetate dihydrate (9.174 mg, 0.05 mmol), Im (596 mg, 8.75 mmol), Bim (148 mg, 1.25 mmol) and DMF (3mL) required for the synthesis were added, and 2 of 10 mm grinding balls were added. The grinding jar was sealed and shaken at 30 Hz in our ball mill. 40 min later, the jars were opened. After washing with DCM (20 mL) and DMF (20 mL) 2 times, respectively, the powder was dried in an oven at 120 $^oC$ overnight for further use.

### Synthesis of ZIF-8 powder

$Zn(NO_3)_2 \cdot 6H_2O$ (1.68 g, 6 mmol) was dissolved in of MeOH (20 mL), and 2-mIm (4.0 g, 48 mmol) was dissolved in 60 mL of MeOH, respectively. The metal source solution was quickly poured into the linker solution and kept stirring at room temperature for 1 h. Afterward, the milky suspension was centrifuged at the obtained solid, washed with MeOH three times, and then dried at 80 $^oC$ under vacuum overnight.

### Synthesis of UiO-66 powder

The aqueous phase of solution A was prepared by dissolving $ZrOCl_2 \cdot 8H_2O$ (3.22 g, 10 mmol) in water (85 mL) and acetic acid (15 mL). The resulting mixture was heated to 70 °C under flux for 2 h before cooling to room temperature. For solution B, the aqueous phase was prepared by adding $H_2BDC$ (1.66 g, 10 mmol) to aqueous NaOH (100 mL, 0.2 M) and heating at 85 °C until the solid was fully dissolved. The mixture was cooled to room temperature for further use. Subsequently, Zr stock was made by adding the mixture of Triton X-100 (12.46 g), cyclohexane (40 mL) and hexanol (4.8 mL) and solution A (6 mL). For $H_2BDC$ stock, Triton X-100 (12.46 g), cyclohexane (40 mL) and hexanol (4.8 mL) and solution B (6 mL). After stirring overnight, UiO-66 was synthesized using standard microemulsion synthesis procedures through inject $H_2BDC$ stock (40 mL) to Zr stock (40 mL) at a rate of 20 mL/h, then the mixture solution stirred overnight. Finally, the UiO-66 crystal could be obtained by washing with acetone, hexanol, and methanol each 2 times.

**Synthesis of MIL-53 powder**

$Al(NO_3)_3 \cdot 9H_2O$ (26.00 g, 69.3 mmol) and $H_2BDC$ (5.76 g, 49.6 mmol) were dissolved in water (100 mL) and placed into a Teflon-lined autoclave and placed in an oven at 220 °C for 72 h. The resulting powder was washed with deionized water (3 × 30 mL) and dried in a vacuum oven at 150 °C for 24 h.

**Synthesis of MUF-16 powder and post-treatment of MUF-16**

A mixture of $Co(OAc)_2 \cdot 4H_2O$ (0.625 g, 2.5 mmol), $H_2aip$ (1.8 g, 10 mmol), methanol (80 mL), and DI water (5 mL) was sonicated for 20 min in a sealed 1000 mL Schott bottle, which was then heated in a pre-heated oven at 85 °C for 2 h. After cooing to room temperature, the resulting pink crystals were isolated by decanting off the mother liquor, washed with methanol for several times, then dried under vacuum at 130 °C for 20 h. Ball mill was then used to the MUF-16 treatment. To 50 mL zirconium grinding jars, the as-fabricated MUF-16 (2.0 g) was added, then 10 × 4 mm (zirconium grinding balls) were added. The grinding jars were sealed and span at 30 HZ for 2 h in a ball mill. The nanosized MUF-16 powder was collected for further use.

**Fabrication of pure *ag*ZIF-62 membrane**

The ZIF-62 powders were mixed by grinding in a zirconium mortar for 10 min. Subsequently, 200 mg of ZIF-62 powders were compacted within the home-made press under 5 tons pressure for 30 s to obtain the ZIF-62 tablet. The tablet was first purged with Ar for 30 min in the tube furnace and then heated under Ar to 409 °C at a ramping rate of 10 °C/min and held at target

temperature for 10 min, followed by naturally cooling to room temperature. In this way, the pure *ag*ZIF-62 membranes were obtained.

**Fabrication of CGCMs**

Similar to the pure *ag*ZIF-62 membrane fabrication, a series of MOF CGCs with ZIF-8, UiO-66 and MIL-53 were prepared (40 wt.%). The MOF crystals (ZIF-8, UiO-66, and MIL-53) and ZIF-62 powders were mixed by grinding in a mortar at 30 Hz for 10 min. Subsequently, MOF compositing tablet could be obtained after pressing with a 5 tons pressure for 30 s. The fabricated tablet was transferred to a tube furnace and purged with Ar for 30 min, then heated to 409 ºC at a ramping rate of 10 ºC/min and held at target temperature 10 min, followed by naturally cooling to room temperature. In this manner, all the CGCMs were obtained.

In addition, two re-melting CGCMs were fabricated under a lower temperature. MUF-16 were grinded with *ag*ZIF-62 at 30 Hz for 10 min to obtain the homogeneous composites in the ball mill, respectively. After undergoing the similar processes (high pressure pressing and heating in a furnace), the corresponding CGCM could be fabricated. Notably, the temperature was set at 330 ºC for re-melting of *ag*ZIF-62.

**Table A. 1** Compositions of [UiO-66$_x$/*ag*ZIF-62$_{1-x}$] CGCMs.

| Membrane | Crystal phase (mg) | ZIF-62 (mg) |
|---|---|---|
| [UiO-66$_{0.1}$/*ag*ZIF-62$_{0.9}$] CGCM | 20 | 180 |
| [UiO-66$_{0.2}$/*ag*ZIF-62$_{0.8}$] CGCM | 40 | 160 |
| [UiO-66$_{0.3}$/*ag*ZIF-62$_{0.7}$] CGCM | 60 | 140 |
| [UiO-66$_{0.4}$/*ag*ZIF-62$_{0.6}$] CGCM | 80 | 120 |

**Table A.2** Compositions of [ZIF-8$_x$/*ag*ZIF-62$_{1-x}$] CGCMs.

| Membrane | Crystal phase (mg) | ZIF-62 (mg) |
|---|---|---|
| [(ZIF-8$_{0.1}$/*ag*ZIF-62$_{0.9}$] CGCM | 20 | 180 |
| [(ZIF-8$_{0.2}$/*ag*ZIF-62$_{0.8}$] CGCM | 40 | 160 |
| [(ZIF-8$_{0.3}$/*ag*ZIF-62$_{0.7}$] CGCM | 60 | 140 |
| [(ZIF-8$_{0.4}$/*ag*ZIF-62$_{0.6}$] CGCM | 80 | 120 |

**Table A.3** Compositions of [MIL-$53_x$/*ag*ZIF-$62_{1-x}$] CGCMs.

| Membrane | Crystal phase (mg) | ZIF-62 (mg) |
|---|---|---|
| [MIL-$53_{0.1}$/*ag*ZIF-$62_{0.9}$] CGCM | 20 | 180 |
| [MIL-$53_{0.2}$/*ag*ZIF-$62_{0.8}$] CGCM | 40 | 160 |
| [MIL-$53_{0.3}$/*ag*ZIF-$62_{0.7}$] CGCM | 60 | 140 |
| [MIL-$53_{0.4}$/*ag*ZIF-$62_{0.6}$] CGCM | 80 | 120 |

**Table A.4** Compositions of [MUF-$16_x$/*ag*ZIF-$62_{1-x}$] CGCMs.

| Membrane | Crystal phase (mg) | *ag*ZIF-62 (mg) |
|---|---|---|
| [MUF-$16_{0.1}$/*ag*ZIF-$62_{0.9}$] CGCM | 20 | 180 |
| [MUF-$16_{0.2}$/*ag*ZIF-$62_{0.8}$] CGCM | 40 | 160 |
| [MUF-$16_{0.3}$/*ag*ZIF-$62_{0.7}$] CGCM | 60 | 140 |
| [MUF-$16_{0.4}$/*ag*ZIF-$62_{0.6}$] CGCM | 80 | 120 |

**2. Characterization of MOF crystals and CGCMs**

The X-ray powder diffraction (XRD) patterns were recorded on a Bruker D8 Venture Diffractometer with $Cu_\alpha$ radiation (wavelength = 1.54018 Å), with a diamond microfocus X-ray source and a Photon III 28 detector. The collection 1D diffractograms were processed using APEX3. Scanning Electron Microscope (SEM) images were taken on a FEI Quanta 200 Environmental with EDAX module. Transmission Electron Microscope (TEM) images were taken on a FEI Tecnai G2 Biotwin with a tomography unit. Thermogravimetric analysis (TGA) data were collected using the TA Q50 instrument at a heating rate of 10 °C/min from 20 to 500 °C with the $N_2$ flow rate of 60 mL/min. Attenuated total reflection flourier transformed infrared spectroscopy (ATR-FTIR) measurements were performed on Nicolet iS5 IR with iD7 ATR Accessory, and the spectra were collected in the range of wavenumbers from 1600 to 600 $cm^{-1}$ with a scan per sample (except the re-melting CGCMs). Proton NMR (1H-NMR) spectra were collected at room temperature using a Bruker Advance 500 MHz spectrometer, using of the solvent proton as an internal standard. The sample was dissolved using DCl/$D_2O$ as solvent. The gas sorption isotherms for $CO_2$, $N_2$, $CH_4$ were measured using a Quantachrome Autosorb iQ2 instrument at 293 K. All adsorption measurements used ultra-high purity gases. Melting-quenching treatments of CGCM were carried out using a SKGL-1200C vacuum tube-type

furnace. All the samples were put into the furnace and purged with Ar for 30 min, then heated to 409 ºC and held at the target temperature for 10 min before being allowed to cool to room temperature. For re-melting CGCMs, the furnace was heated to 330 ºC and other procedures were all same with direct melting CGCMs. Moreover, all the samples were ground with a Vertical Planetary Ball Mill (Semi-circle Type) at a frequency of 30 Hz for 1 h.

**3. IAST adsorption selectivity calculation**

The experimental isotherm data for $CO_2$, $N_2$ and $CH_4$ (measured at 293 K) were fitted using a Langmuir model:

$$q = q_m \frac{bp^{1/n}}{1 + bp^{1/n}}$$

$$S_{ads} = \frac{q_1/p_1}{q_2/p_2}$$

Where q is the adsorbed amount per mass of adsorbent (mol/kg), p is the pressure of the bulk gas at equilibrium (kPa), $q_m$ is the saturation capacities of sites (mol/kg), b is the affinity coefficients of the sites (1/kPa), n is the measure of the deviations from an ideal homogeneous surface.

**4. Gas permeation measurement of CGCMs**

Gas permeation tests were carried out with a Wicke-Kallenbach apparatus, and the as-prepared CGCMs were fixed in a module sealed with O-rings. Gas flow rate was monitored using Alicat mass flow controllers (MFC). Helium (He) (20 sccm) was used as the carried gas in each test. The permeated gas through CGCMs was analyzed via a mass spectrometer (MS, UGA-200, SRS). For single gas permeation measurement, a volumetric flow rate of 20 sccm was applied to the feed side of the membrane, and Helium (He) (20 sccm) was used as sweep gas on the permeated side. For the mixed gas permeation test, the total volume flow rate was 20 sccm ($CO_2/N_2$ = 1:1 and $CO_2/CH_4$ = 1:1). A RGA was employed to measure the concentration of single gas or mixed gases on the permeate side. The feeding pressure fixed at 1 bar, and all the gas permeation tests were carried out under room temperature (20 ºC)

The gas permeability was calculated from the following equation:

$$P=Q/(\Delta P \times A)$$

Where P is the gas permeance; Q is the volume flow rate of permeated gas; ΔP is the transmembrane pressure (1 bar) and A is the membrane effective area in gas permeation test (d = 6 mm).

## 5. Appendix Figures and Tables

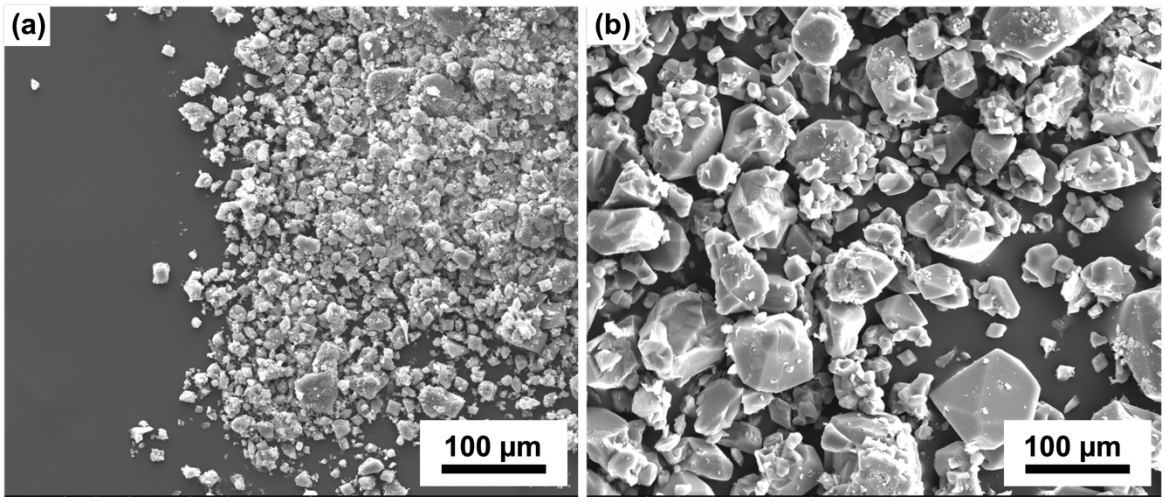


**Figure A. 1** SEM images of (a) ZIF-62 and (b) *ag*ZIF-62.

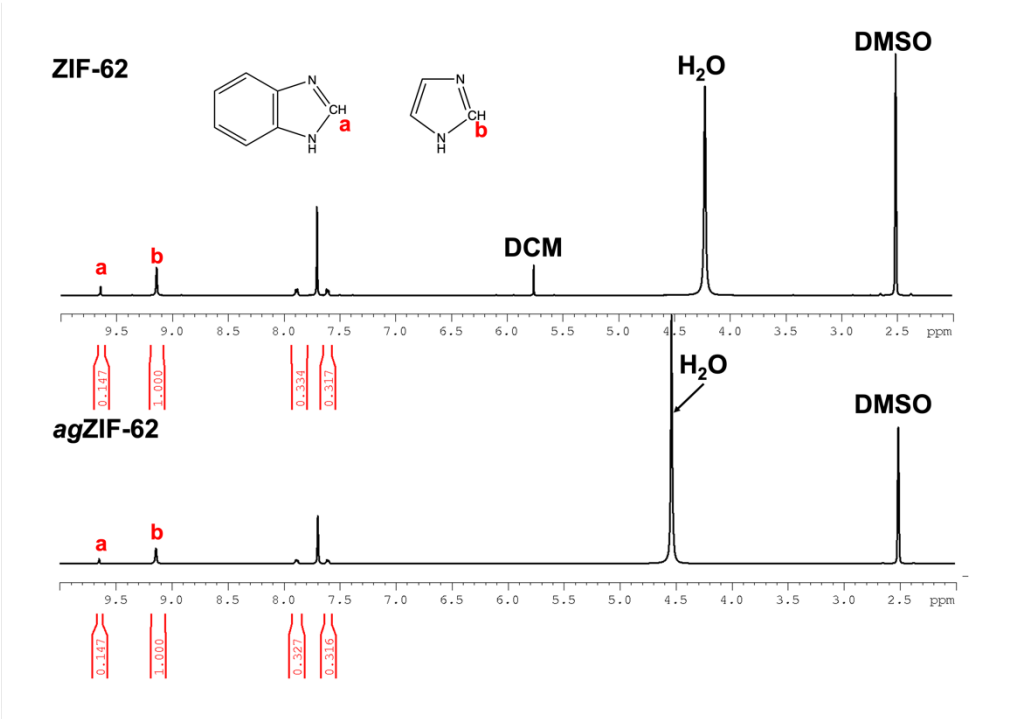


**Figure. A. 2** The $^{1}$H NMR spectra of digested (a) ZIF-62 and (b) *ag*ZIF-62 in DCl/$D_2O$.

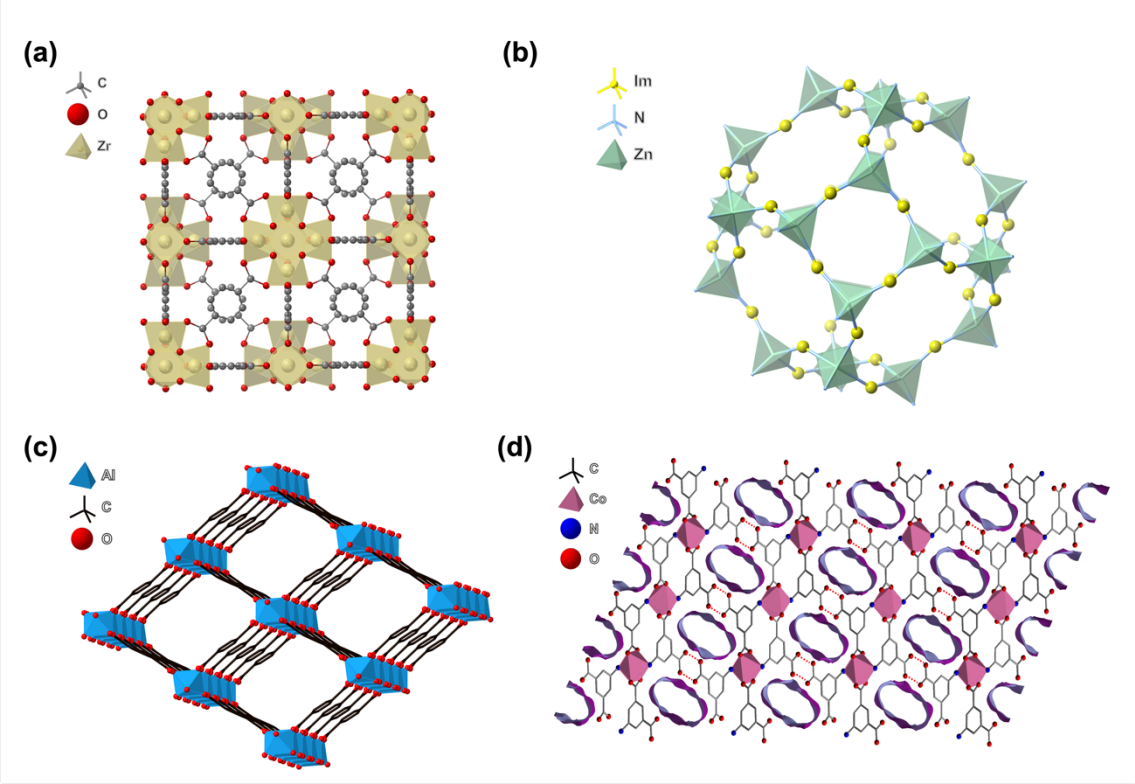


**Figure. A. 3** Molecular structures of (a) UiO-66, (b) ZIF-8 and (c) MIL-53 and (d) MUF-16.

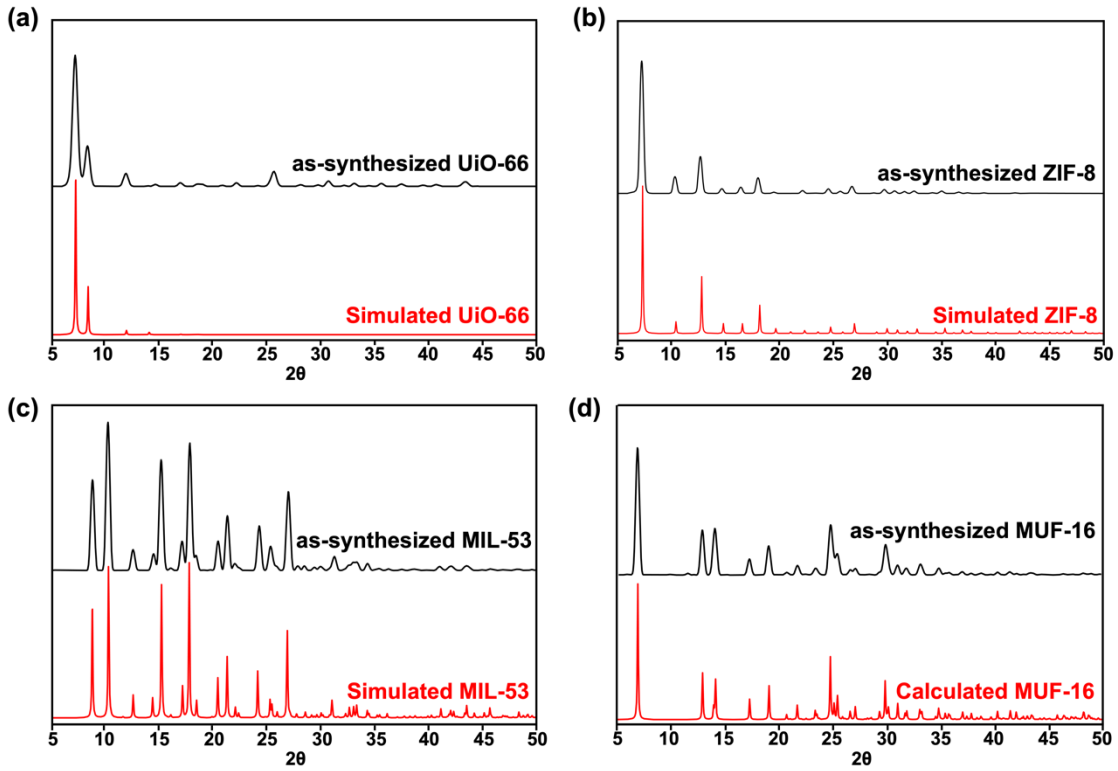


**Figure A. 4** PXRD pattern of simulated and as-synthesized (a) UiO-66, (b) ZIF-8, (c) MIL-53, and (d) MUF-16.

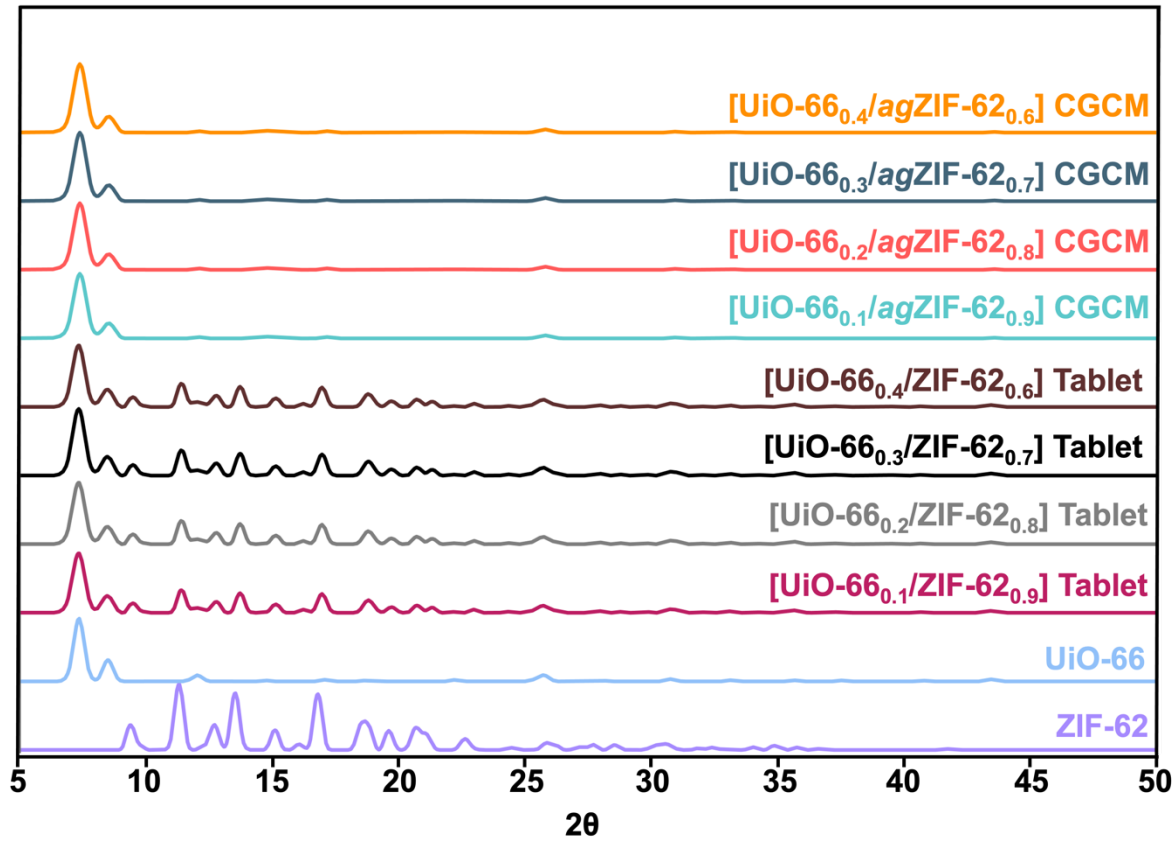


**Figure A. 5** PXRD patterns of ZIF-62, UiO-66, [UiO-66$_x$/ZIF-62$_{1-x}$] tablets and corresponding [UiO-66$_x$/*ag*ZIF-62$_{1-x}$] CGCMs.

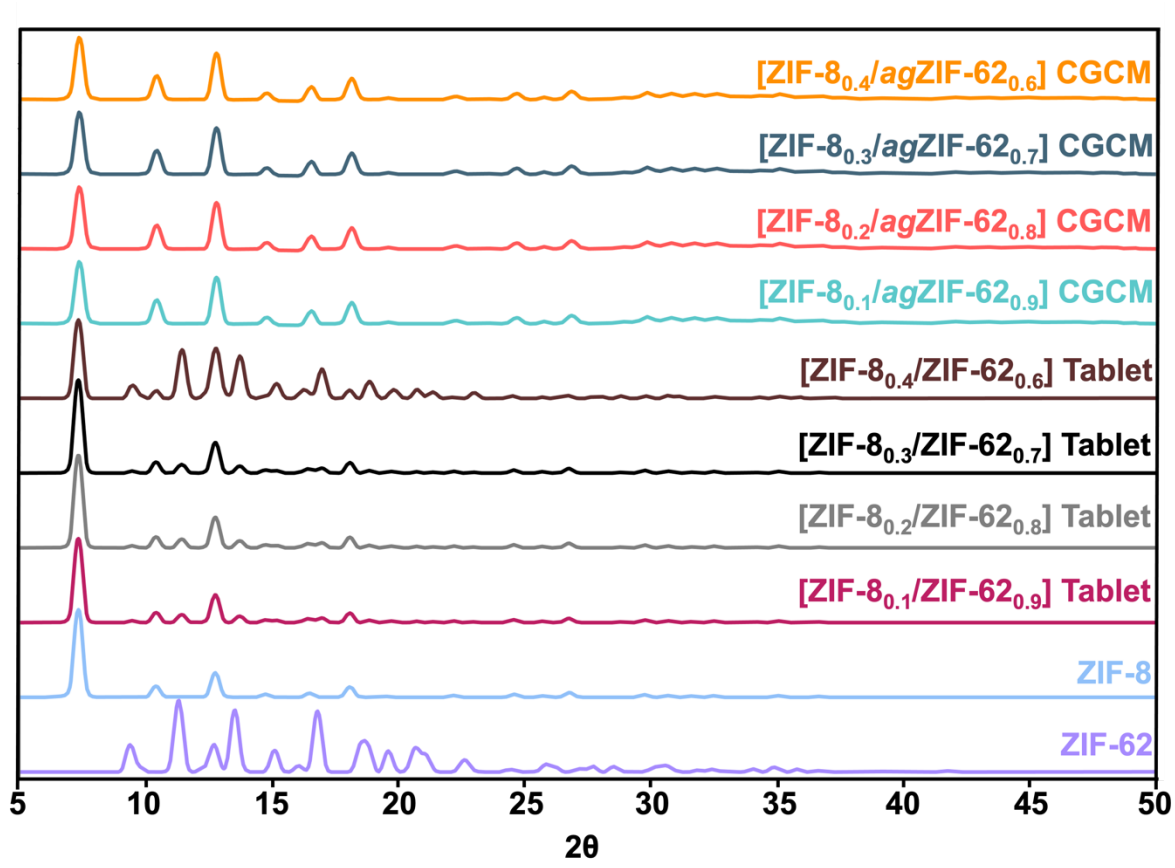


**Figure A. 6** PXRD patterns of ZIF-62, ZIF-8, [ZIF-8$_x$/ZIF-62$_{1-x}$] CGC tablets and corresponding [ZIF-8$_x$/*ag*ZIF-62$_{1-x}$] CGCMs.

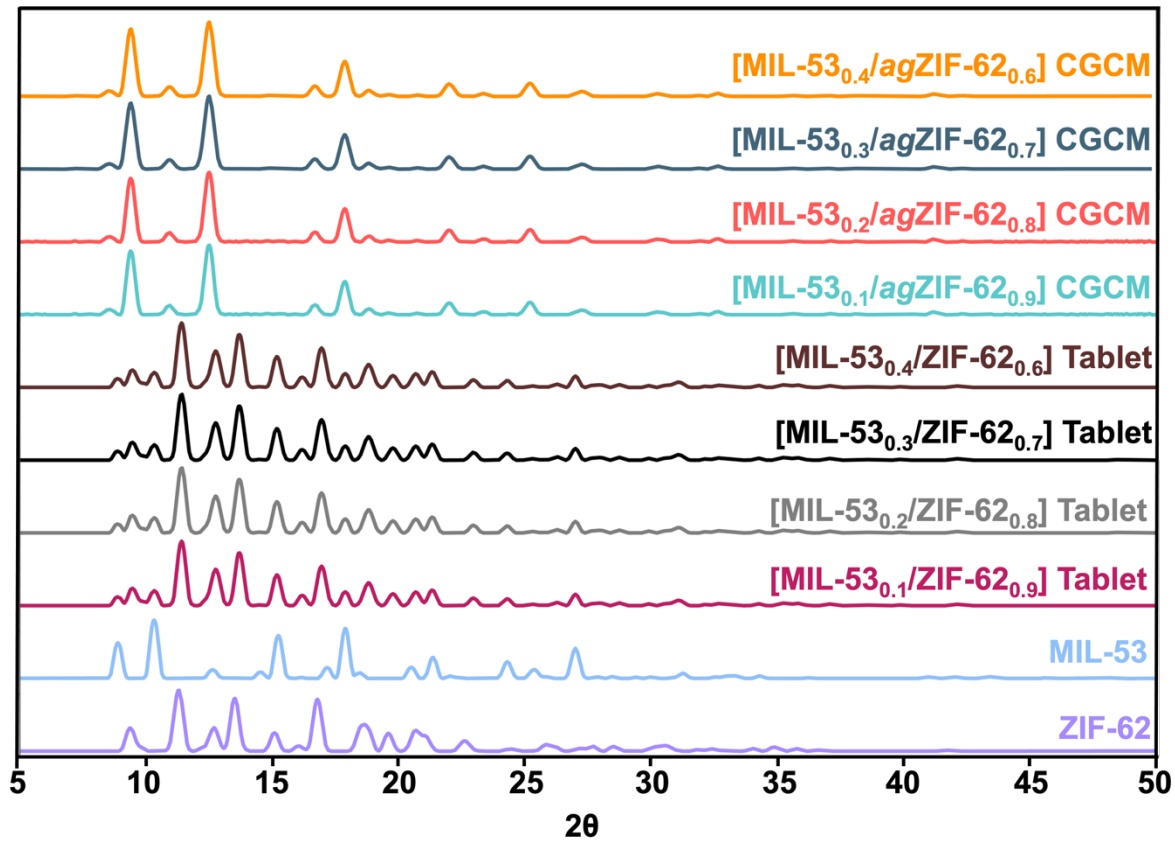


**Figure A. 7** PXRD patterns of ZIF-62, MIL-53, [MIL-53$_x$/ZIF-62$_{1-x}$] tablets and corresponding [MIL-53$_x$/*ag*ZIF-62$_{1-x}$] CGCMs.

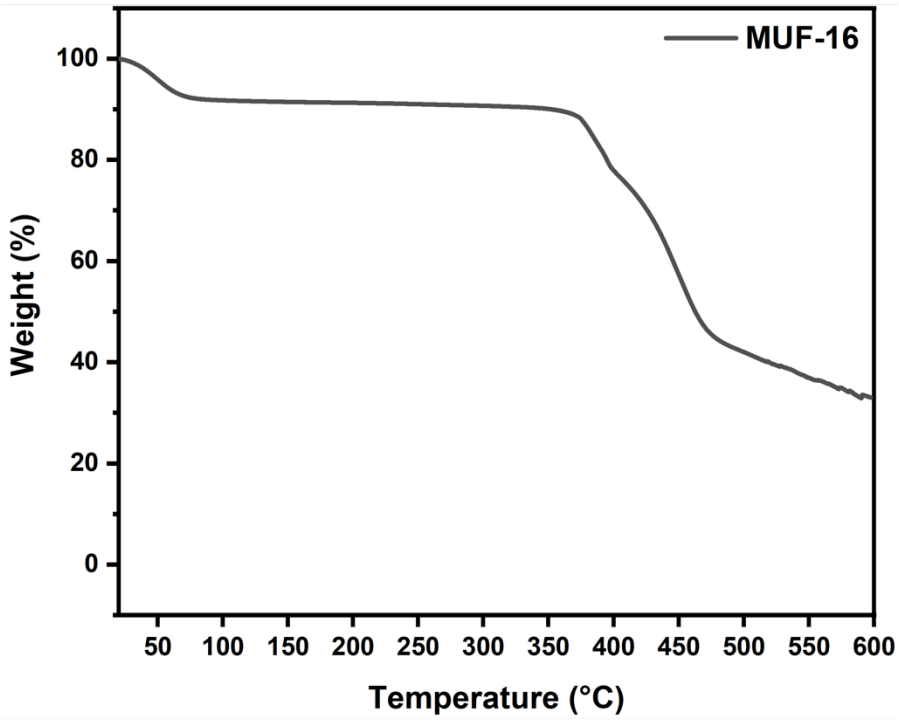


**Figure A. 8** TGA curve of MUF-16.

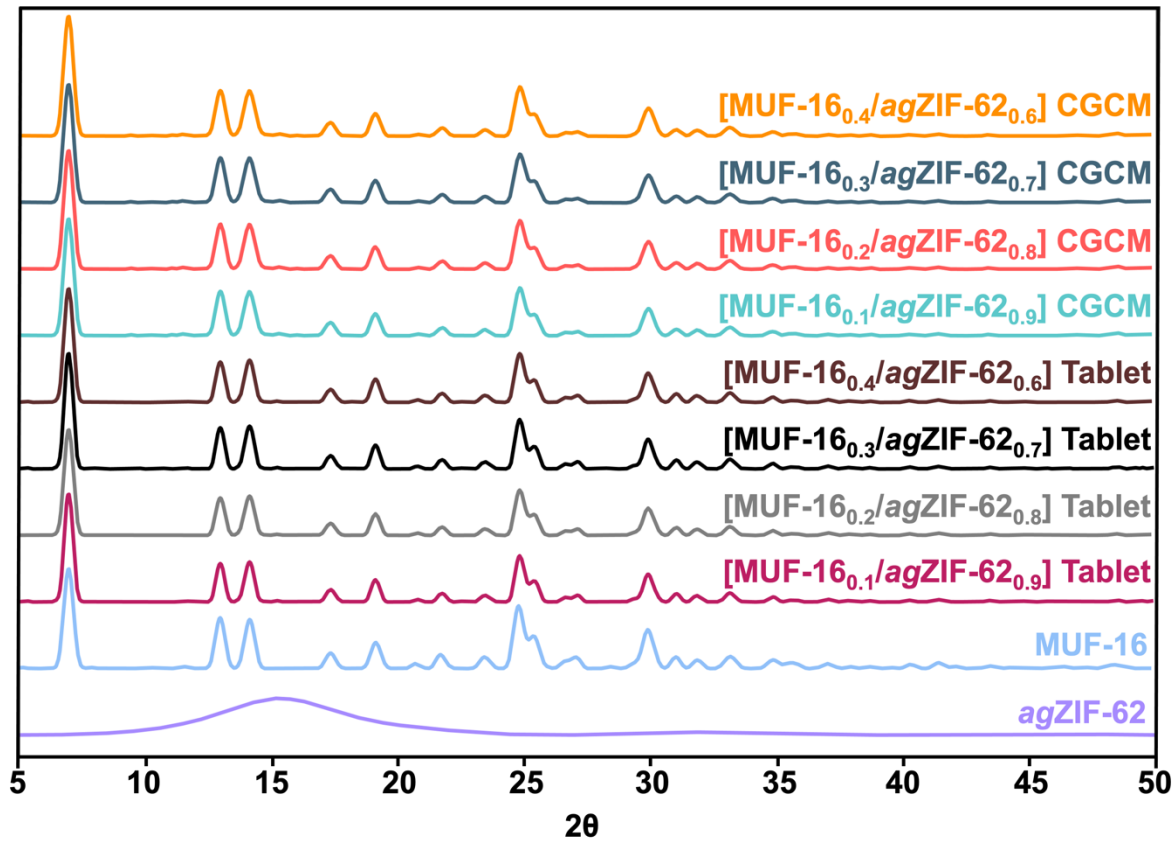


**Figure A. 9** PXRD patterns of *ag*ZIF-62, MUF-16, [MUF-16$_x$/*ag*ZIF-62$_{1-x}$] tablets and corresponding [MUF-16$_x$/*ag*ZIF-62$_{1-x}$] CGCMs.

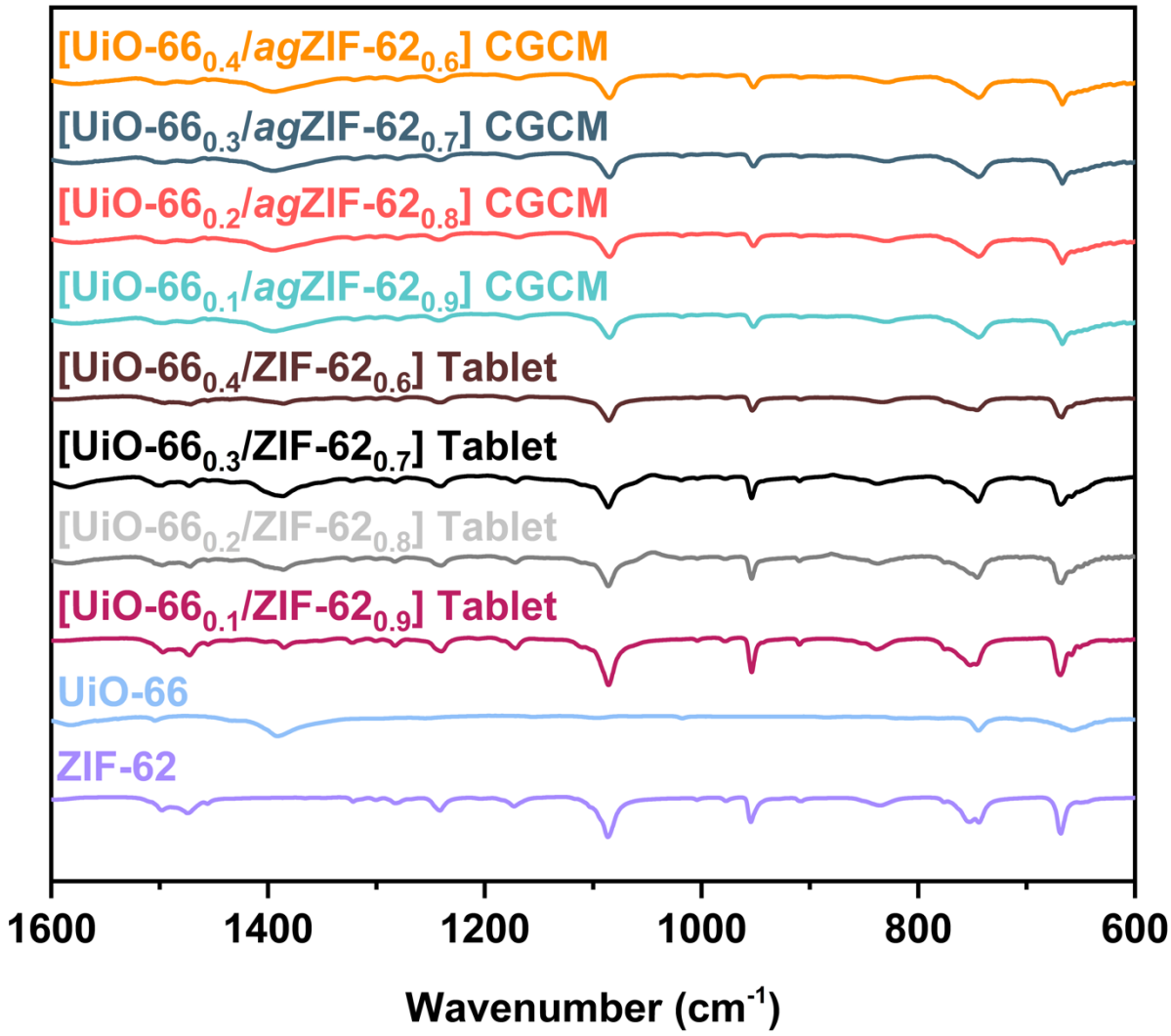


**Figure A. 10** FTIR spectra of ZIF-62, UiO-66, [UiO-66$_x$/ZIF-62$_{1-x}$] tablets and [UiO-66$_x$/*ag*ZIF-62$_{1-x}$] CGCMs.

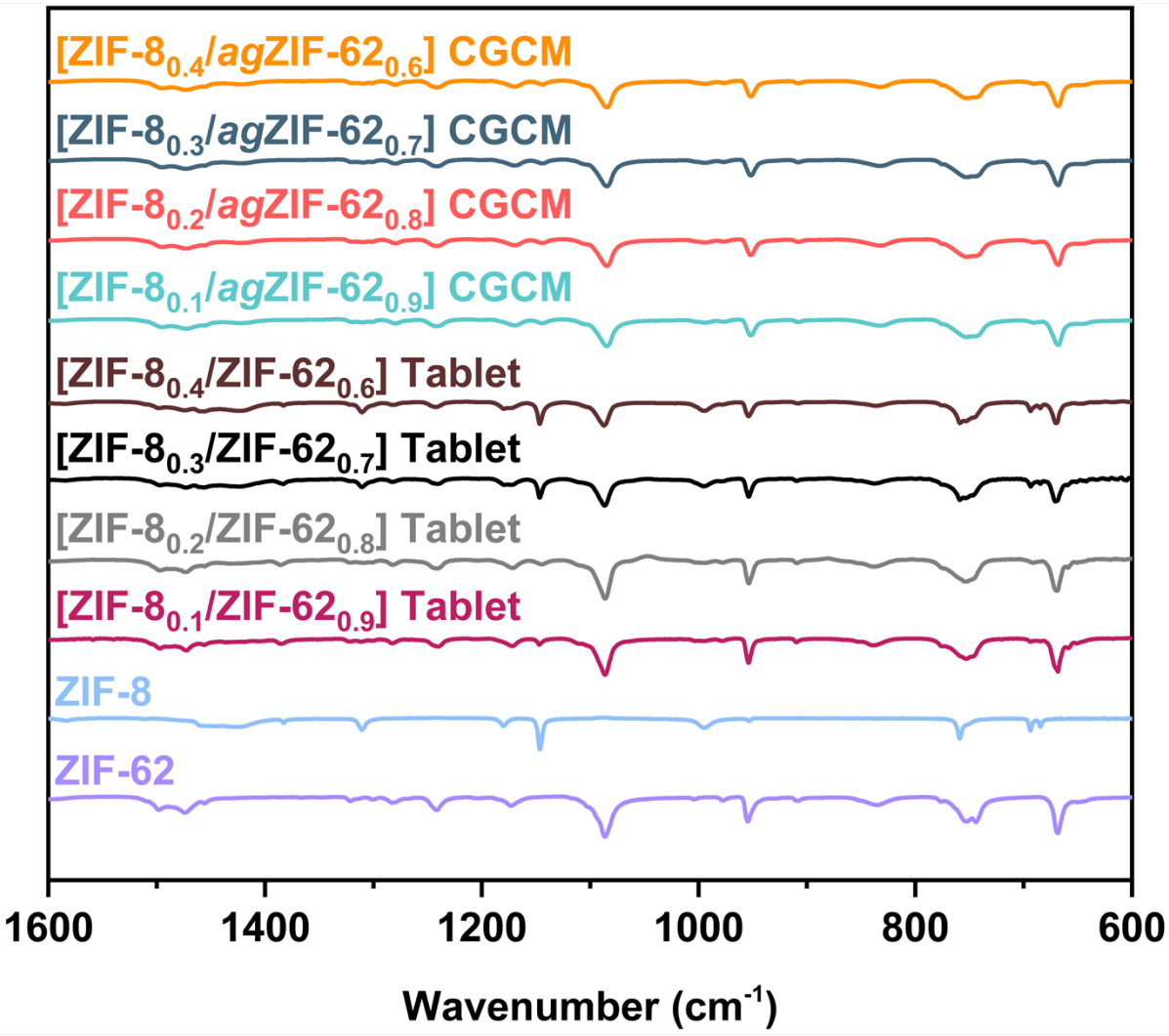


**Figure A. 11** FTIR spectra of ZIF-62, ZIF-8, [ZIF-8$_x$/ZIF-62$_{1-x}$] tablets and [ZIF-8$_x$/*ag*ZIF-62$_{1-x}$] CGCMs.

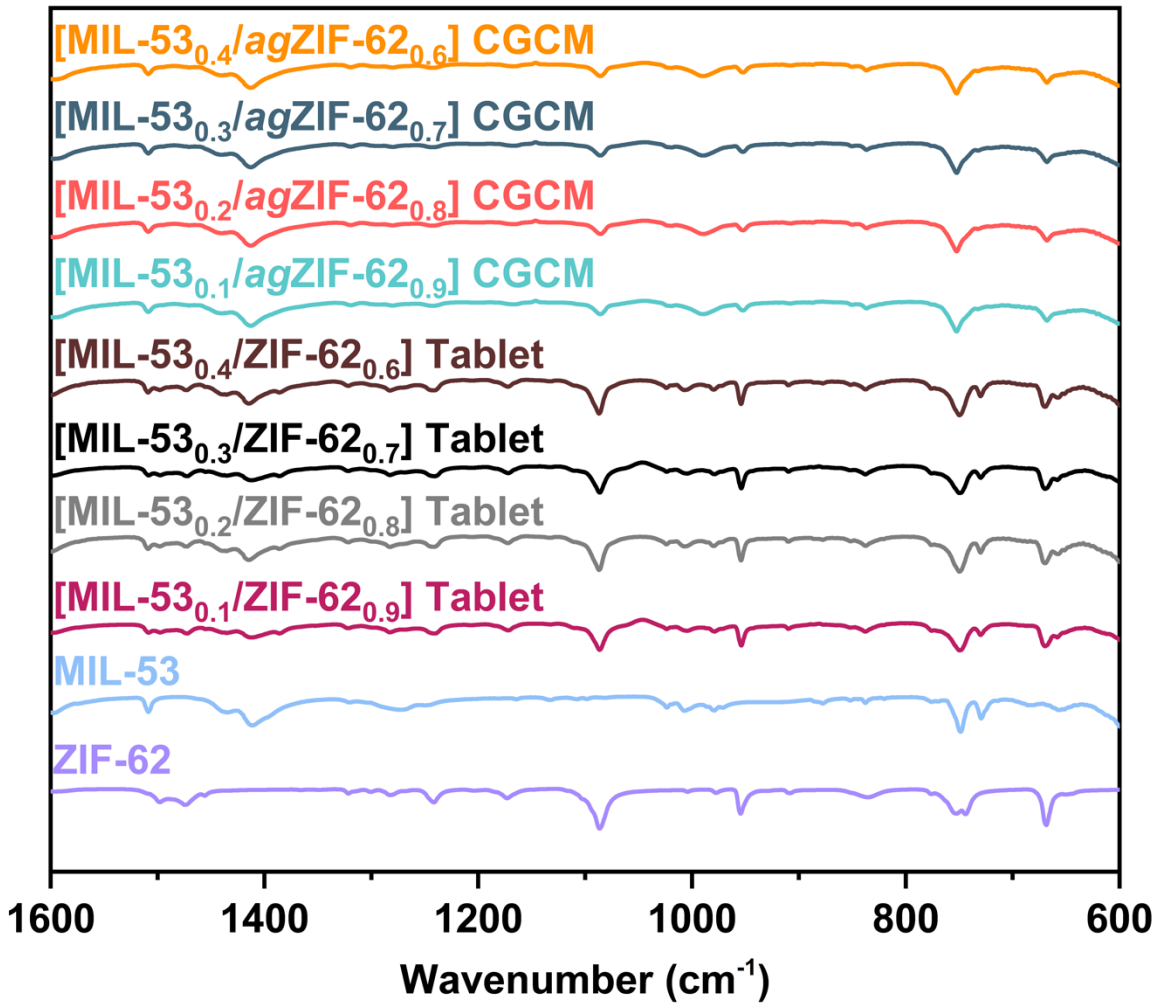


**Figure A. 12** FTIR spectra of ZIF-62, MIL-53, [MIL-53$_x$/*ag*ZIF-62$_{1-x}$] tablets and [MIL-53$_x$/*ag*ZIF-62$_{1-x}$] CGCMs.

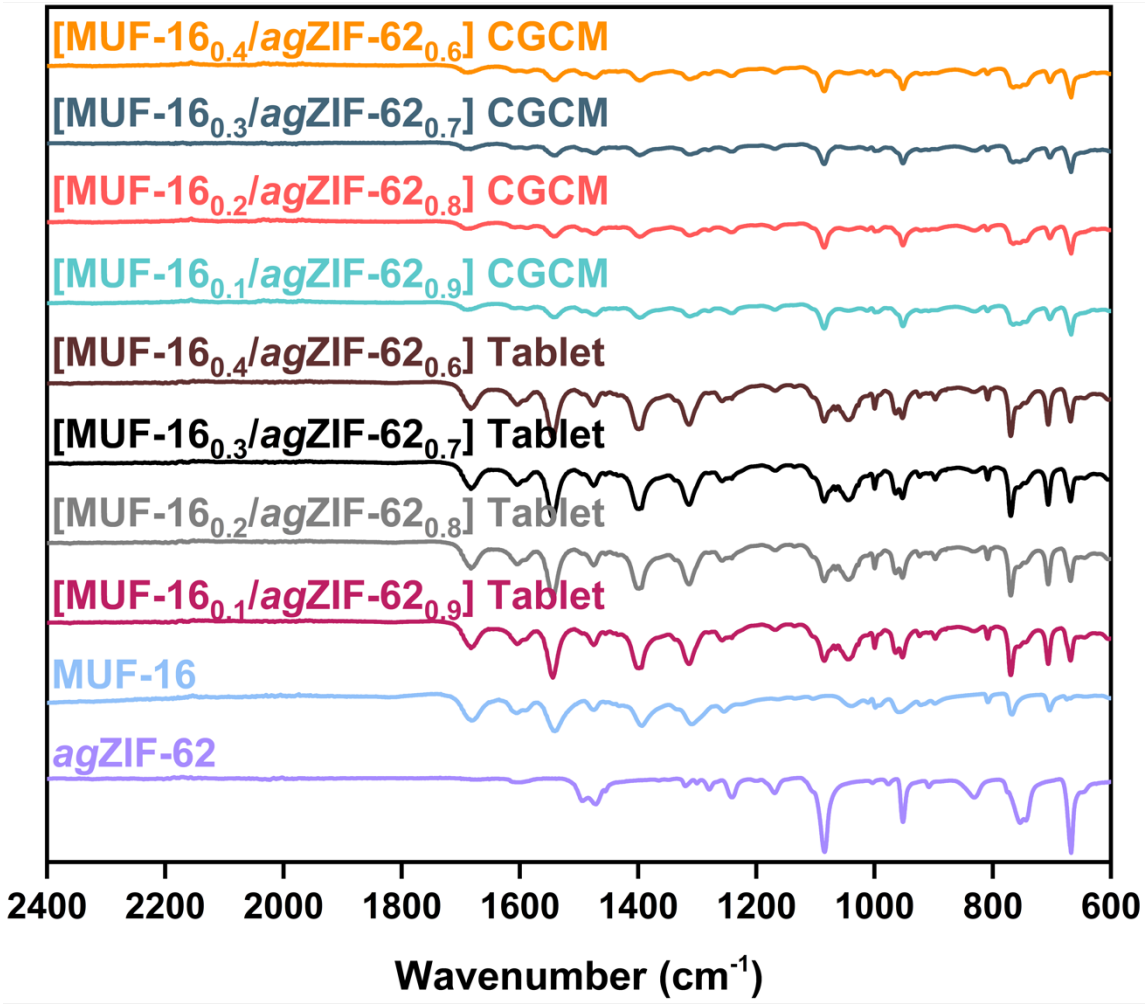


**Figure A. 13** FTIR spectra of *ag*ZIF-62, MUF-16, [MUF-16$_x$/*ag*ZIF-62$_{1-x}$] tablets and [MUF-16$_x$/*ag*ZIF-62$_{1-x}$] CGCM.

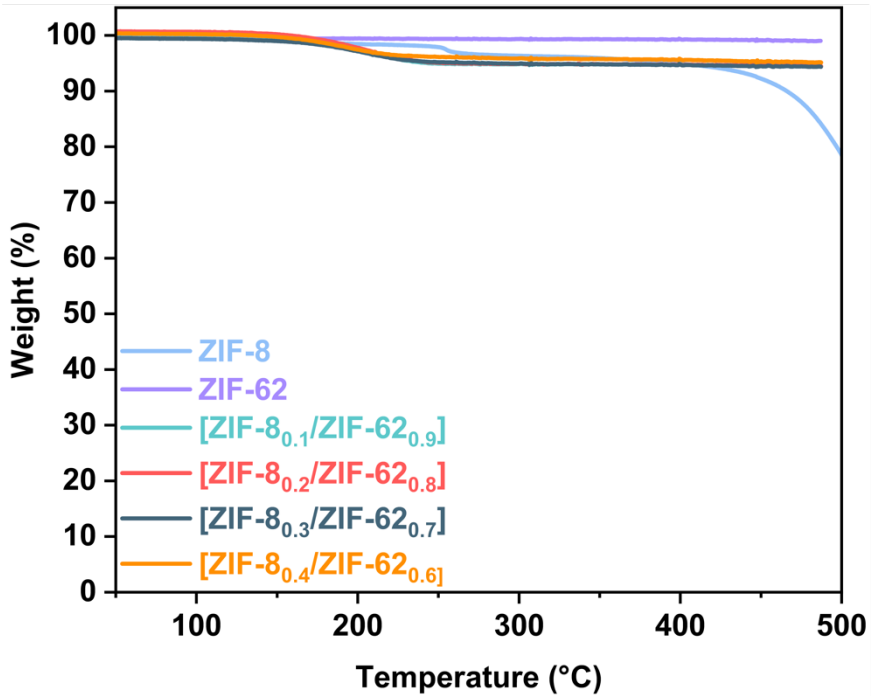


**Figure A. 14** TGA curves ZIF-8, ZIF-62 and [ZIF-8$_x$/ZIF-62$_{1-x}$] composites.

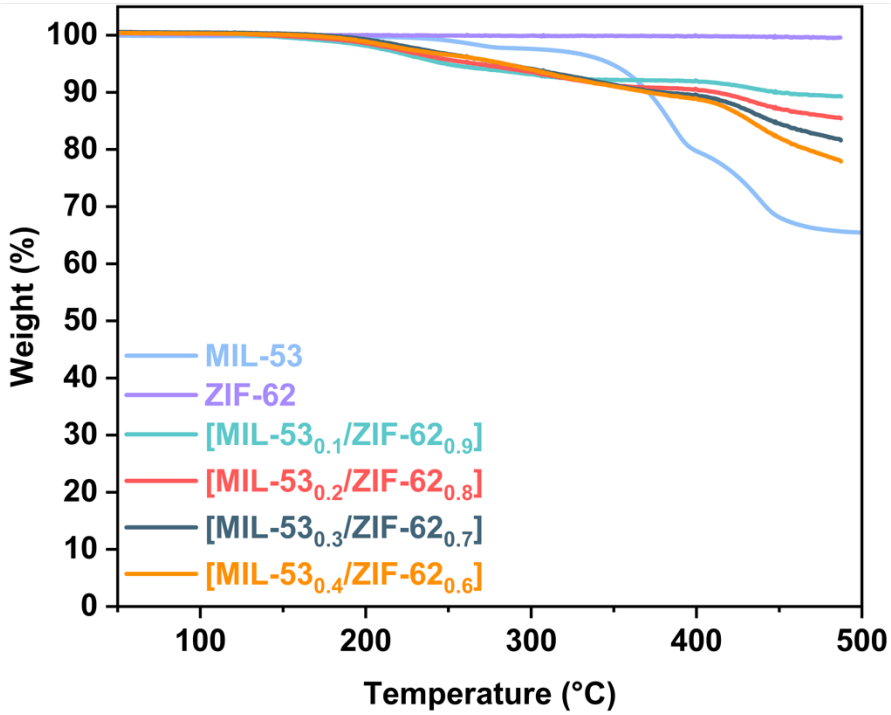


**Figure A. 15** TGA curves of MIL-53, ZIF-62 and [MIL-53$_x$/ZIF-62$_{1-x}$] composites.

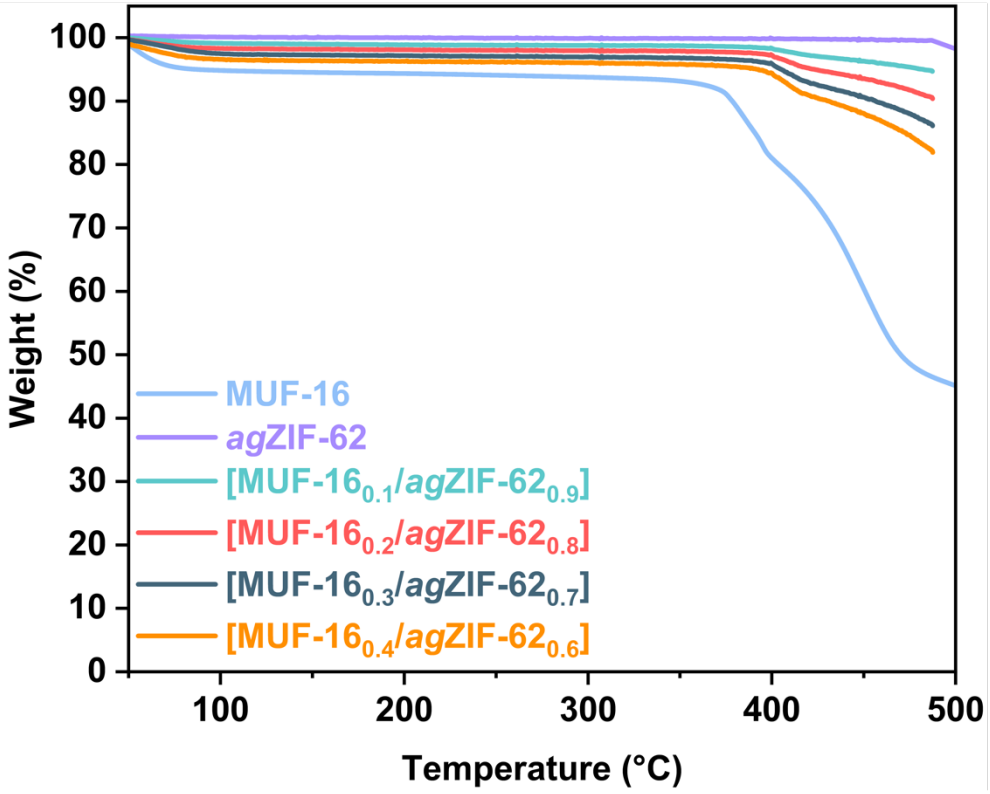


**Figure A. 16** TGA curves of MUF-16, *ag*ZIF-62 and [MUF-16$_x$/*ag*ZIF-62$_{1-x}$] composites.

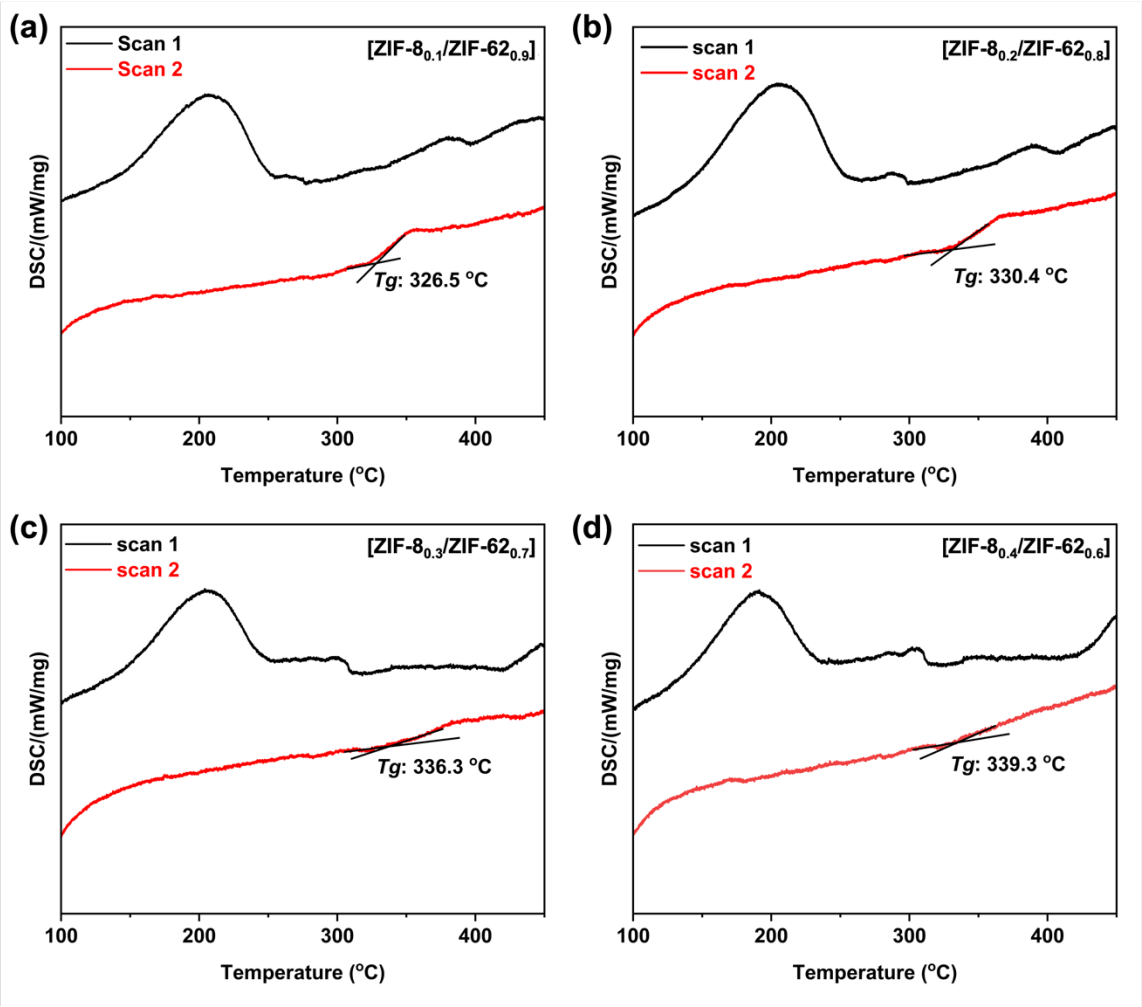


**Figure A. 17** DSC curves of (a) [ZIF-8$_{0.1}$/ZIF-62$_{0.9}$], (b) [ZIF-8$_{0.2}$/ZIF-62$_{0.8}$], (c) [ZIF-8$_{0.3}$/ZIF-62$_{0.7}$] and (d) [ZIF-8$_{0.4}$/ZIF-62$_{0.6}$] CGCs.

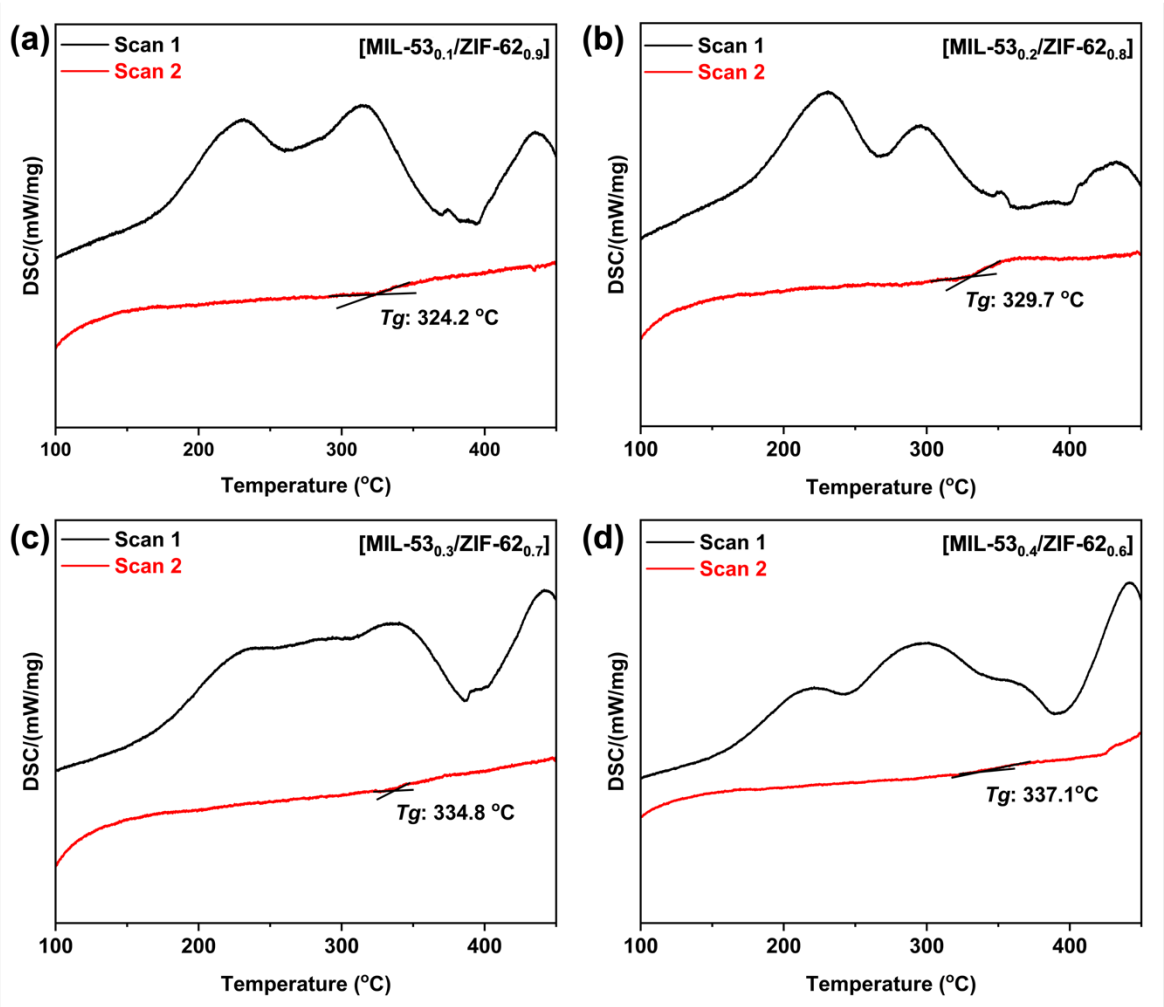


**Figure A. 18** DSC curves of (a) [MIL-53$_{0.1}$/ZIF-62$_{0.9}$], (b) [MIL-53$_{0.2}$/ZIF-62$_{0.8}$], (c) [MIL-53$_{0.3}$/ZIF-62$_{0.7}$] and (d) [MIL-53$_{0.4}$/ZIF-62$_{0.6}$] CGCs.

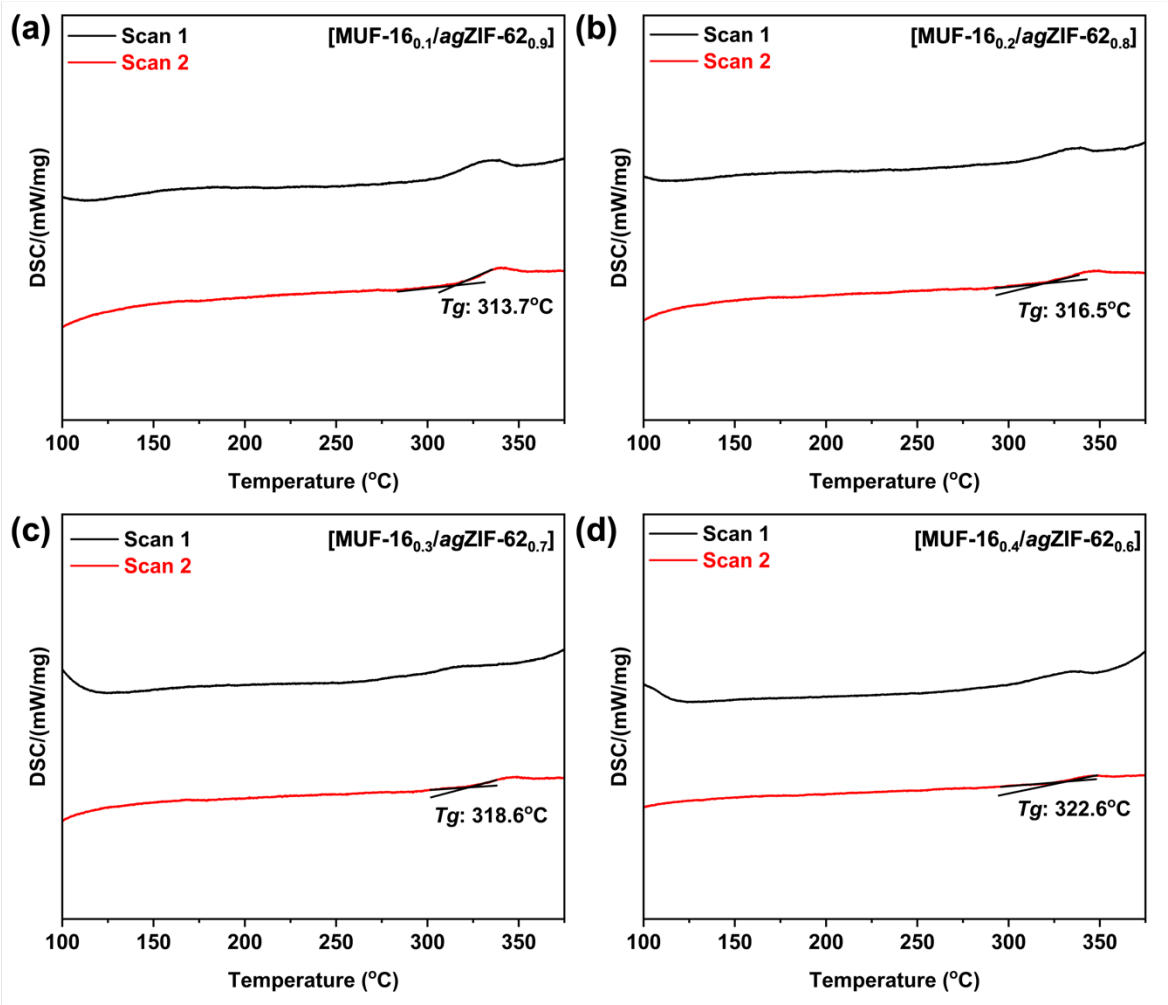


**Figure A. 19** DSC curves of (a) [MUF-16$_{0.1}$/*ag*ZIF-62$_{0.9}$], (b) [MUF-16$_{0.2}$/*ag*ZIF-62$_{0.8}$], (c) [MUF-16$_{0.3}$/*ag*ZIF-62$_{0.7}$] and (d) [MUF-16$_{0.4}$/*ag*ZIF-62$_{0.6}$] CGCs.

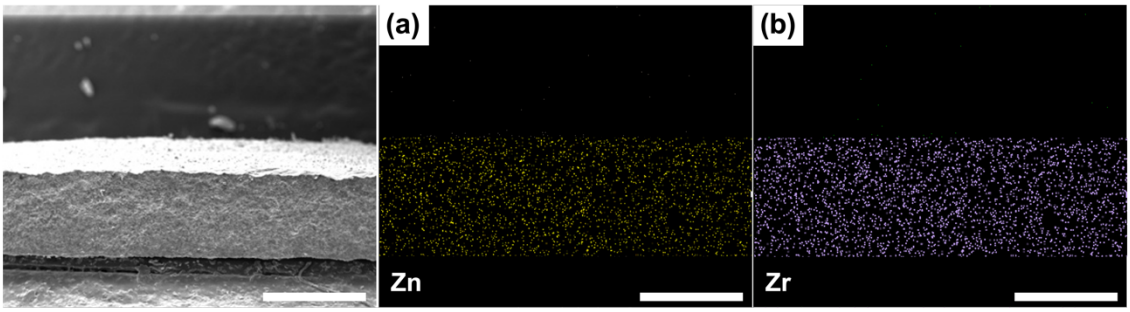


**Figure A. 20** EDS mapping of (a) Zn and (b) Zr for cross-sectional [UiO-66$_{0.4}$/ZIF-62$_{0.6}$] CGCM (scale bar: 500 um).

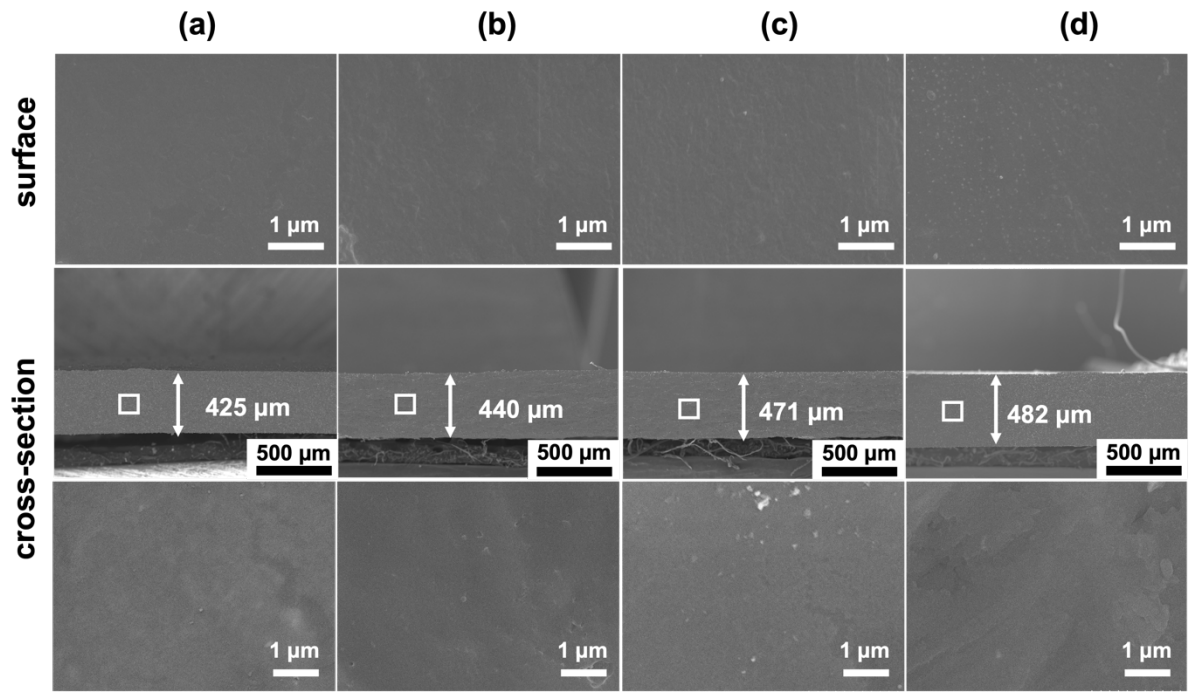


**Figure A. 21** Surface and cross-sectional SEM images of (a) [ZIF-$8_{0.1}$/*ag*ZIF-$62_{0.9}$] CGCM, (b) [ZIF-$8_{0.2}$/*ag*ZIF-$62_{0.8}$] CGCM, (c) [ZIF-$8_{0.3}$/*ag*ZIF-$62_{0.7}$] CGCM and (d) [ZIF-$8_{0.4}$/*ag*ZIF-$62)_{0.6}$] CGCM. The corresponding high resolution cross-sectional SEM images from the white box are included.

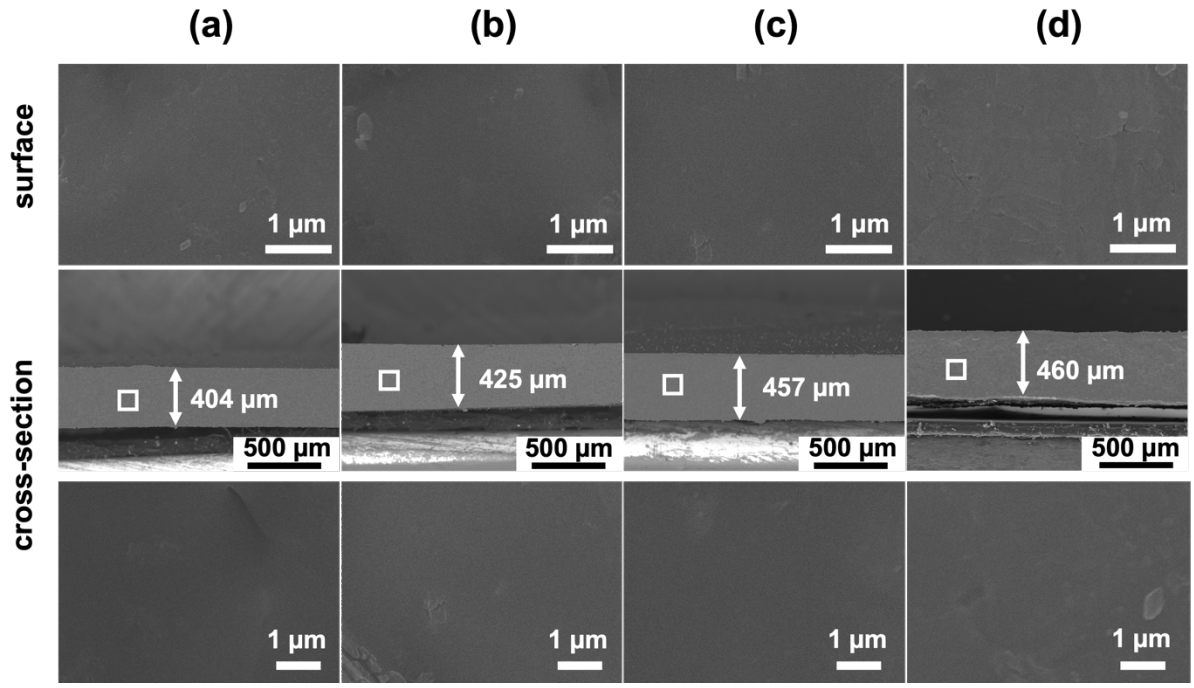


**Figure A. 22** Surface and cross-sectional SEM images of (a) [MIL-53$_{0.1}$/*ag*ZIF-62$_{0.9}$] CGCM, (b) [MIL-53$_{0.2}$/*ag*ZIF-62$_{0.8}$] CGCM, (c) [MIL-53$_{0.3}$/*ag*ZIF-62$_{0.7}$] CGCM and (d) [MIL-53$_{0.4}$/*ag*ZIF-62$_{0.6}$] CGCM. The corresponding high resolution cross-sectional SEM images from the white box are included.

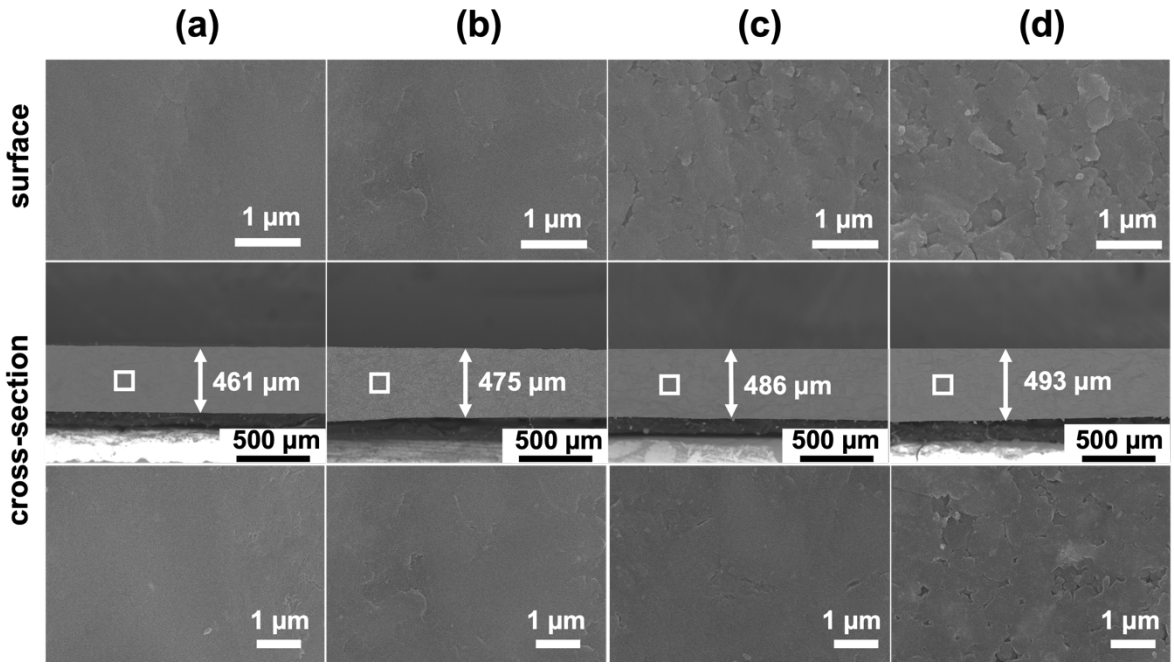


**Figure A. 23** Surface and cross-sectional SEM images of (a) [MUF-16$_{0.1}$/*ag*ZIF-62$_{0.9}$] CGCM, (b) [MUF-16$_{0.2}$/*ag*ZIF-62$_{0.8}$] CGCM, (c) [MUF-16$_{0.3}$/*ag*ZIF-62$_{0.7}$] CGCM and (d) [MUF-16$_{0.4}$/*ag*ZIF-62$_{0.6}$] CGCM. The corresponding high resolution cross-sectional SEM images from the white box are included.

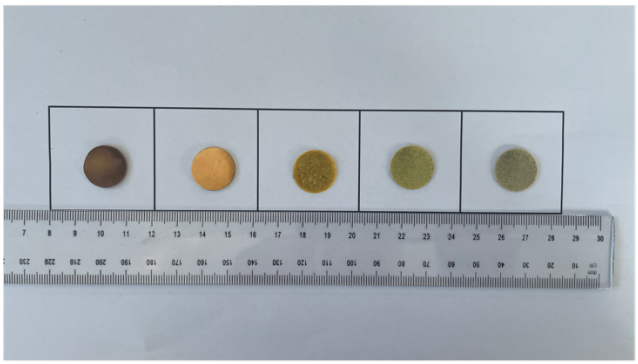

**Figure A. 24** Optical photographs the prepared membranes from left to right are: *ag*ZIF-62, [UiO-66$_{0.1}$/*ag*ZIF-62$_{0.9}$], [UiO-66$_{0.2}$/*ag*ZIF-62$_{0.8}$], [UiO-66$_{0.3}$/*ag*ZIF-62$_{0.7}$] and [UiO-66$_{0.4}$/*ag*ZIF-62$_{0.6}$], respectively.

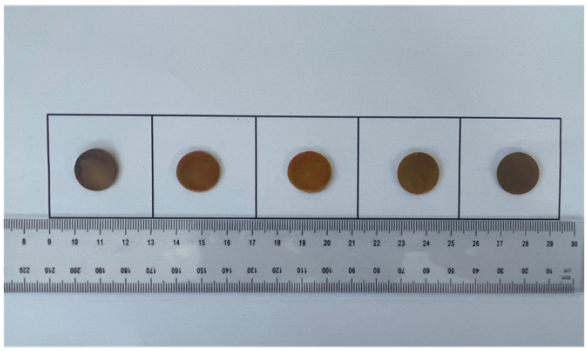

**Figure A. 25** Optical photographs the prepared membranes from left to right are: *ag*ZIF-62, [ZIF-8$_{0.1}$/*ag*ZIF-62$_{0.9}$], [ZIF-8$_{0.2}$/*ag*ZIF-62$_{0.8}$], [ZIF-8$_{0.3}$/*ag*ZIF-62$_{0.7}$] and [ZIF-8$_{0.4}$/*ag*ZIF-62$_{0.6}$], respectively.

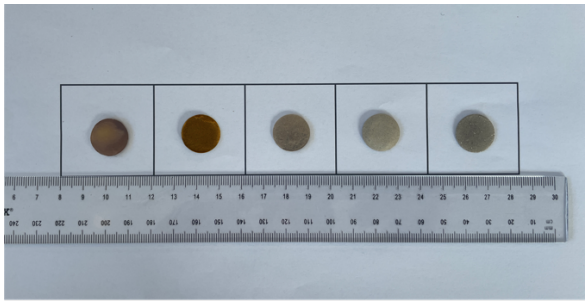

**Figure A. 26** Optical photographs the prepared membranes from left to right are: *ag*ZIF-62, [MIL-53$_{0.1}$/*ag*ZIF-62$_{0.9}$], [MIL-53$_{0.2}$/*ag*ZIF-62$_{0.8}$], [MIL-53$_{0.3}$/*ag*ZIF-62$_{0.7}$] and [MIL-53$_{0.4}$/*ag*ZIF-62$_{0.6}$], respectively.

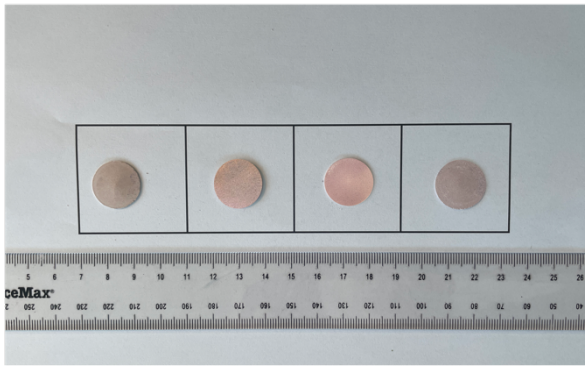

**Figure A. 27** Optical photographs the prepared membranes from left to right are: [MUF-16$_{0.1}$/*ag*ZIF-62$_{0.9}$], [MUF-16$_{0.2}$/*ag*ZIF-62$_{0.8}$], [MUF-16$_{0.3}$/*ag*ZIF-62$_{0.7}$] and [MUF-16$_{0.4}$/*ag*ZIF-62$_{0.6}$], respectively.

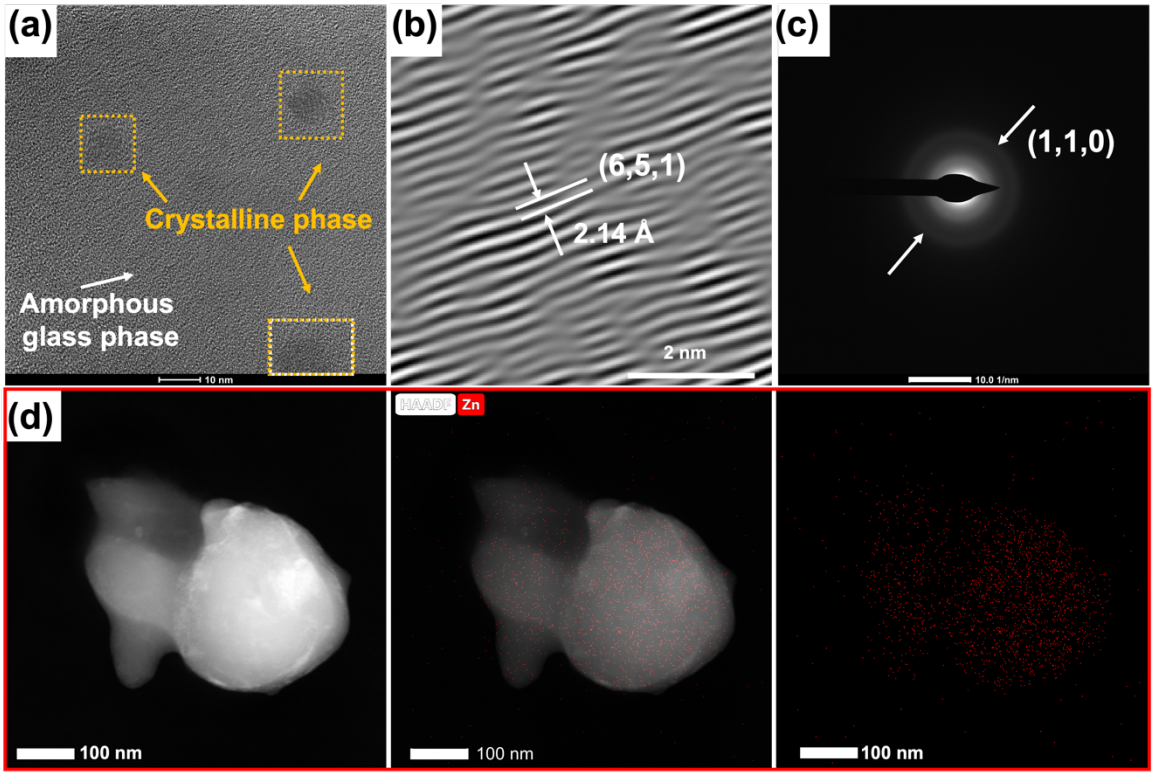


**Figure A. 28** (a) HR-TEM images of [ZIF-$8_{0.4}$/*ag*ZIF-$62_{0.6}$] CGCM, the yellow dashed boxes show the crystal phase, and the other regions are the amorphous phase. (b) Enlarged HR-TEM image of the crystal phase, and the crystal plane spacing d = 2.14 Å, corresponding to (6,5,1) spacing for ZIF-8. (c) SAED patterns of ZIF-8 at other positions. Line scans across the spots, indicated with white arrows, correspond to (110) spacing for ZIF-8. (d) EDX mapping of Zn and Zr in [ZIF-$8_{0.4}$/*ag*ZIF-$62_{0.6}$] CGCM membrane.

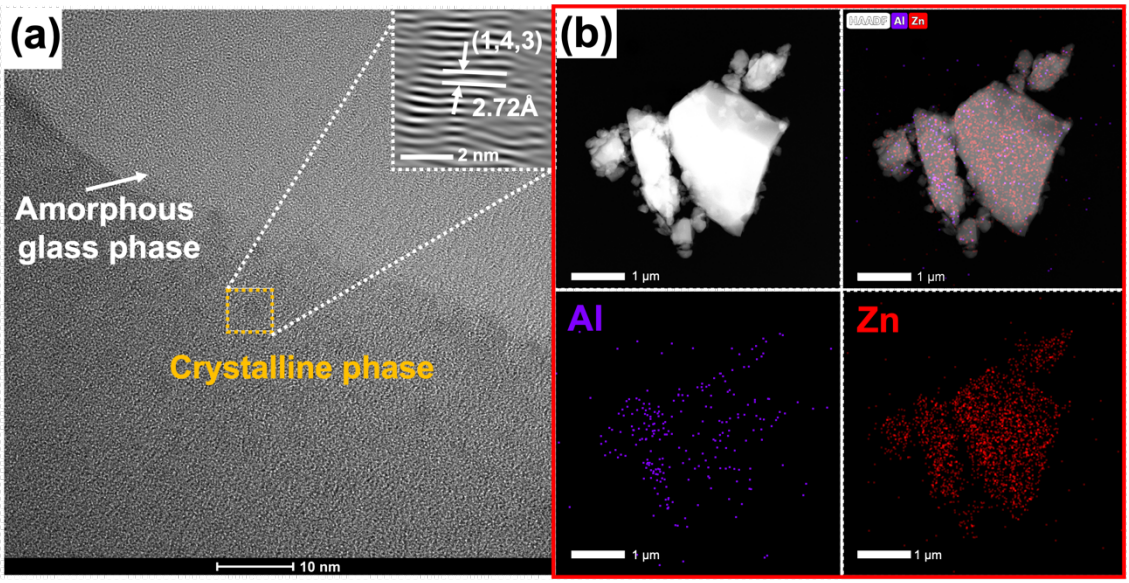


**Figure A. 29** (a) HR-TEM images of [MIL-53$_{0.4}$/*ag*ZIF-62$_{0.6}$] CGCM, the yellow dashed boxes show the crystal phase, and the other regions are the amorphous phase. And the crystal plane spacing d = 2.72 Å, corresponding to (1,4,3) spacing for MIL-53. (b) EDX mapping of Zn and Zr in [MIL-53$_{0.4}$/*ag*ZIF-62$_{0.6}$] CGCM.

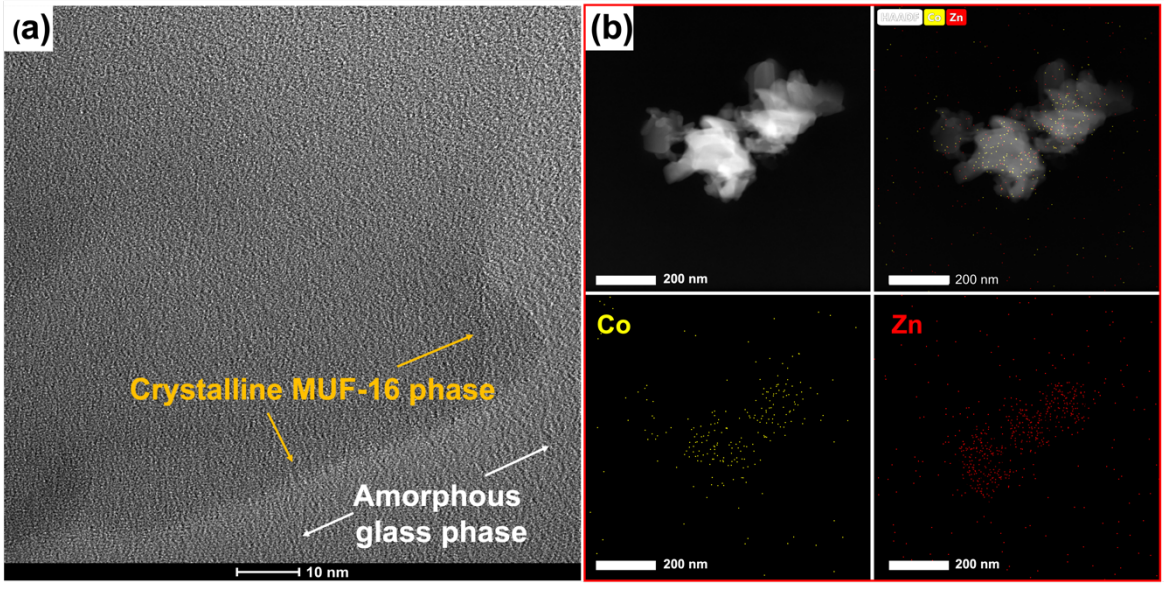


**Figure A. 30** (a) HR-TEM images of [MUF-16$_{0.4}$/*ag*ZIF-62$_{0.6}$] CGCM, the yellow arrows show the crystal phase, and the other regions are the amorphous phase. (b) EDX mapping of Co and Zn in [MUF-16$_{0.4}$/*ag*ZIF-62$_{0.6}$] CGCM.

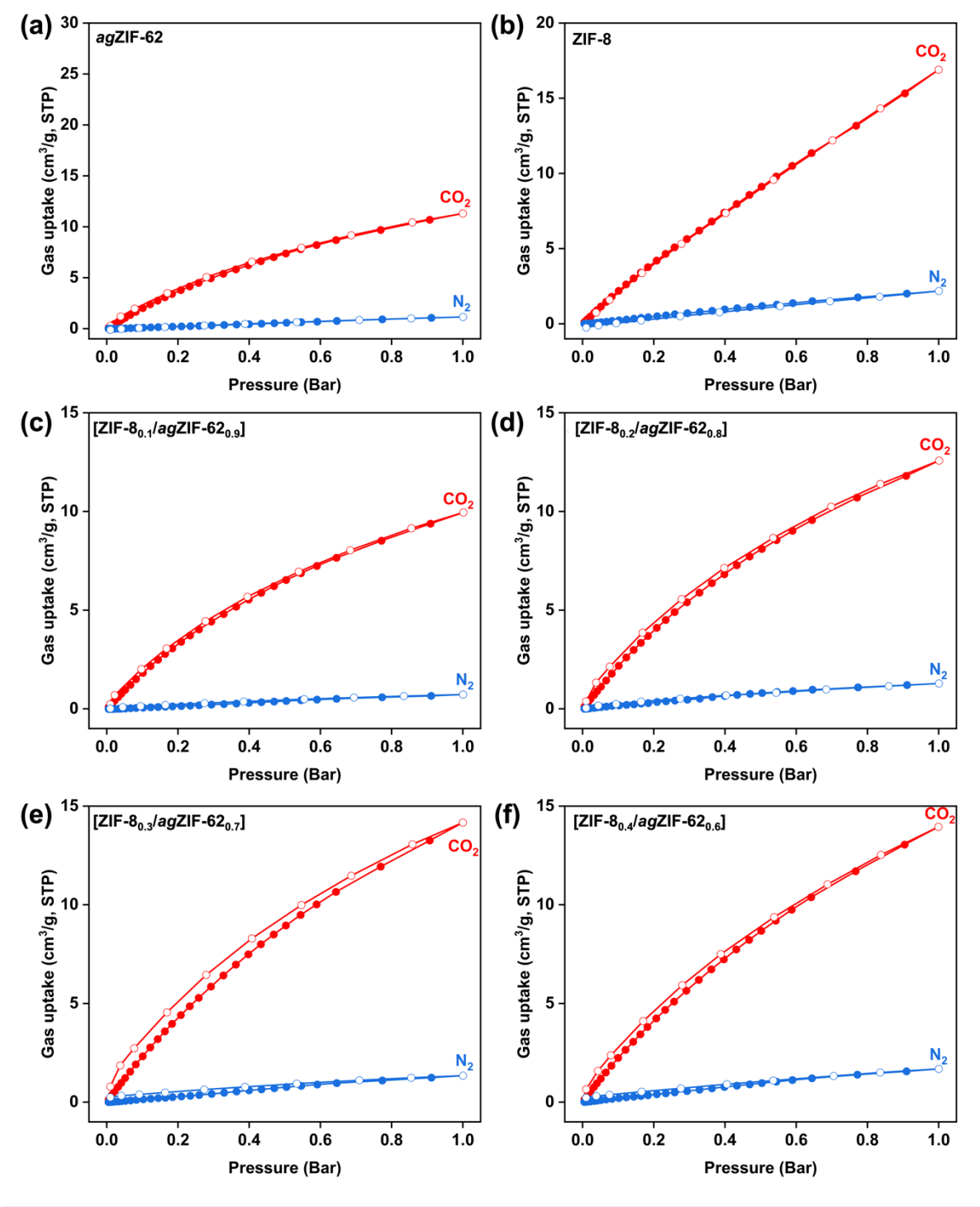


**Figure A. 31** $CO_2$ and $N_2$ adsorption (filled circles) and desorption (open circles) isotherms of (a) *ag*ZIF-62, (b) ZIF-8, (c) [ZIF-8$_{0.1}$/*ag*ZIF-62$_{0.9}$] CGCM, (d) [ZIF-8$_{0.2}$/*ag*ZIF-62$_{0.8}$] CGCM, (e) [ZIF-8$_{0.3}$/*ag*ZIF-62$_{0.7}$] CGCM and (f) [ZIF-8$_{0.4}$/*ag*ZIF-62$_{0.6}$] CGCM at 293K.

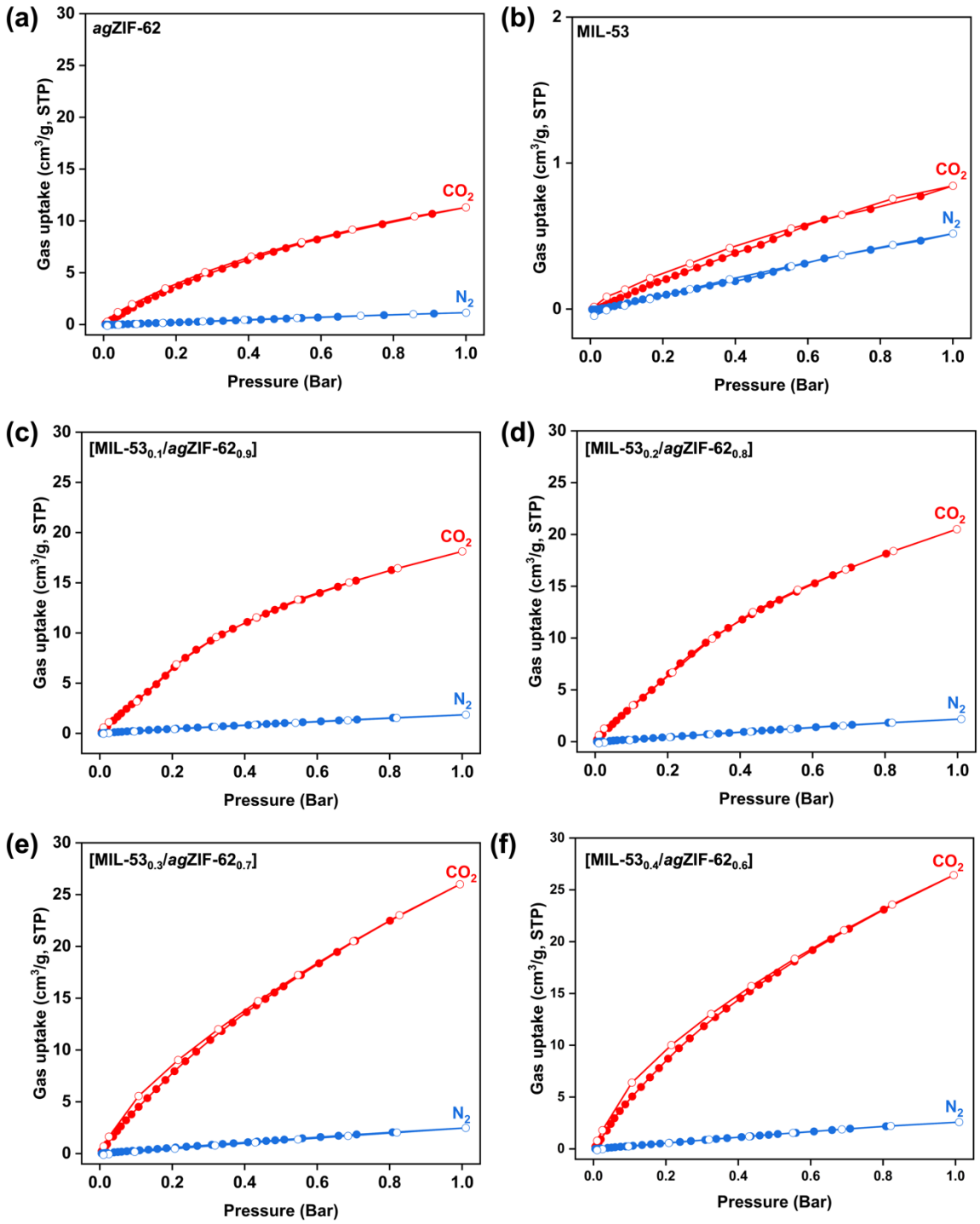


**Figure A. 32** $CO_2$ and $N_2$ adsorption (filled circles) and desorption (open circles) isotherms of (a) *ag*ZIF-62, (b) MIL-53, (c) [MIL-$53_{0.1}$/*ag*ZIF-$62_{0.9}$] CGCM, (d) [MIL-$53_{0.2}$/*ag*ZIF-$62)_{0.8}$] CGCM, (e) [MIL-$53_{0.3}$/*ag*ZIF-$62_{0.7}$] CGCM and (f) [MIL-$53_{0.4}$/*ag*ZIF-$62_{0.6}$] CGCM at 293K.

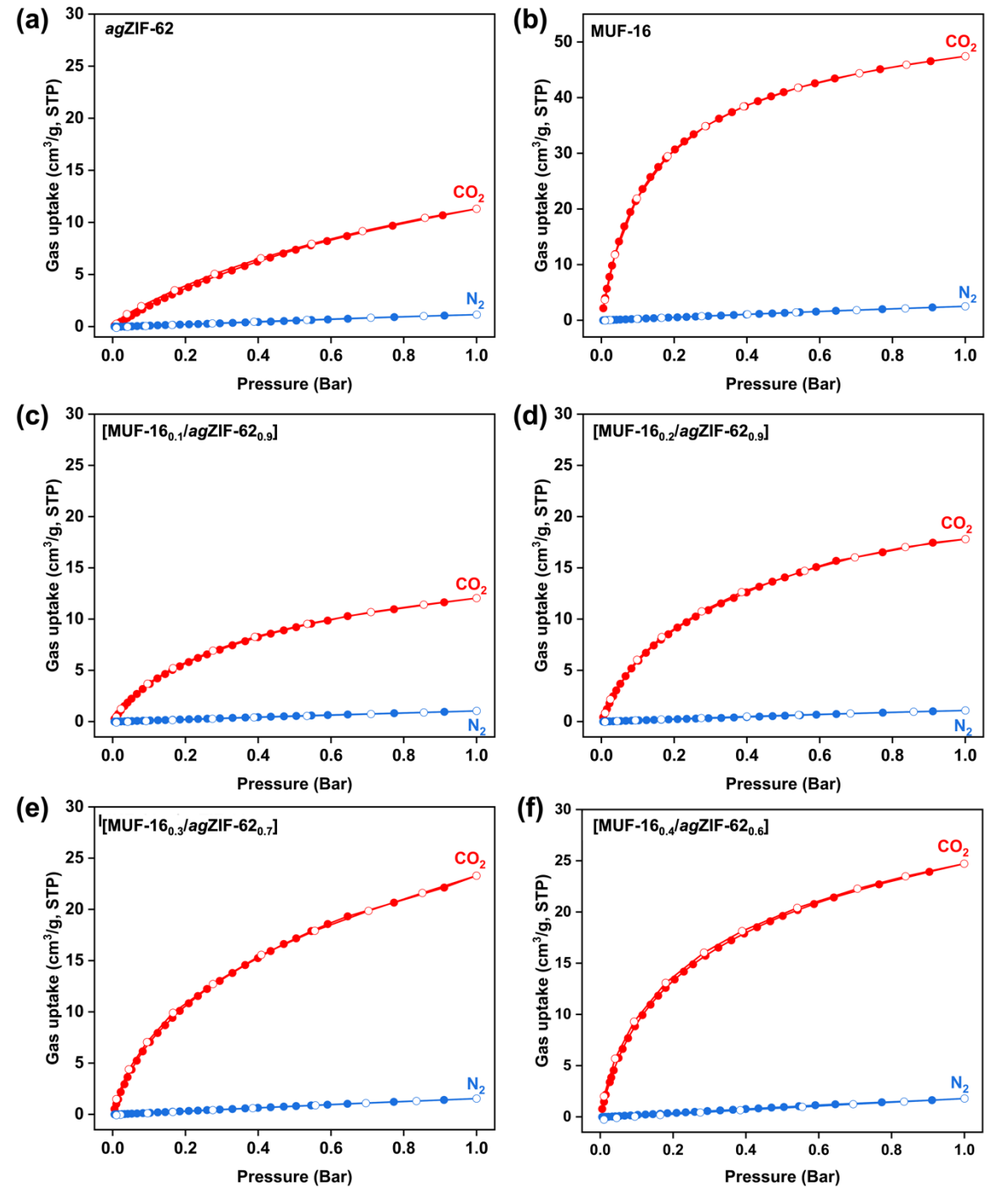


**Figure A. 33** $CO_2$ and $N_2$ adsorption (filled circles) and desorption (open circles) isotherms of (a) *ag*ZIF-62, (b) MUF-16, (c) [MUF-16$_{0.1}$/*ag*ZIF-62)$_{0.9}$] CGCM, (d) [MUF-16$_{0.2}$/*ag*ZIF-62)$_{0.8}$] CGCM, (e) [MUF-16$_{0.3}$/*ag*ZIF-62)$_{0.7}$] CGCM and (f) [MUF-16$_{0.4}$/*ag*ZIF-62$_{0.6}$] CGCM at 293K.

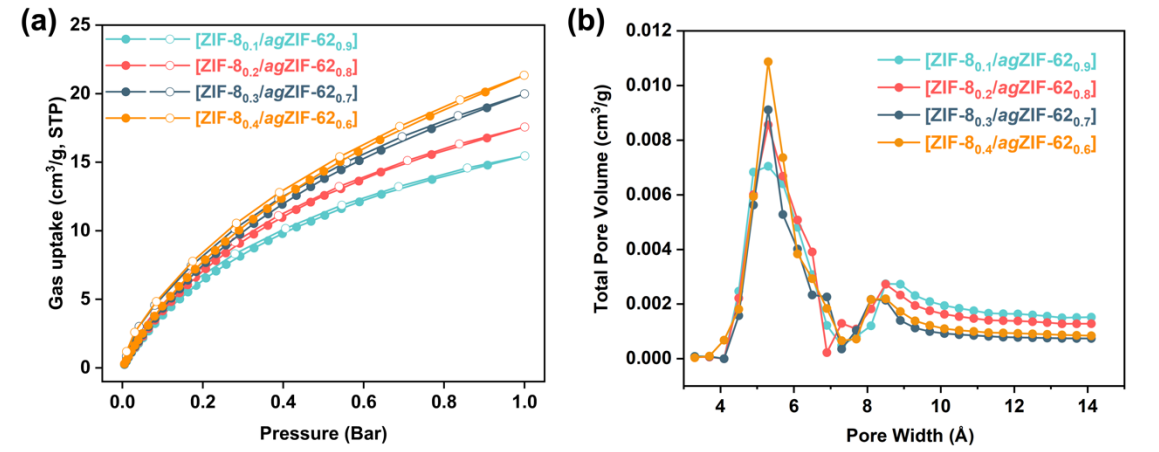


**Figure A. 34** (a) $CO_2$ adsorption–desorption isothermal curves of ZIF-8 CGCMs at 273 K. (b) Micropore size distribution of ZIF-8 CGCMs calculated by the NLDFT method using $CO_2$ adsorption isotherm curves.

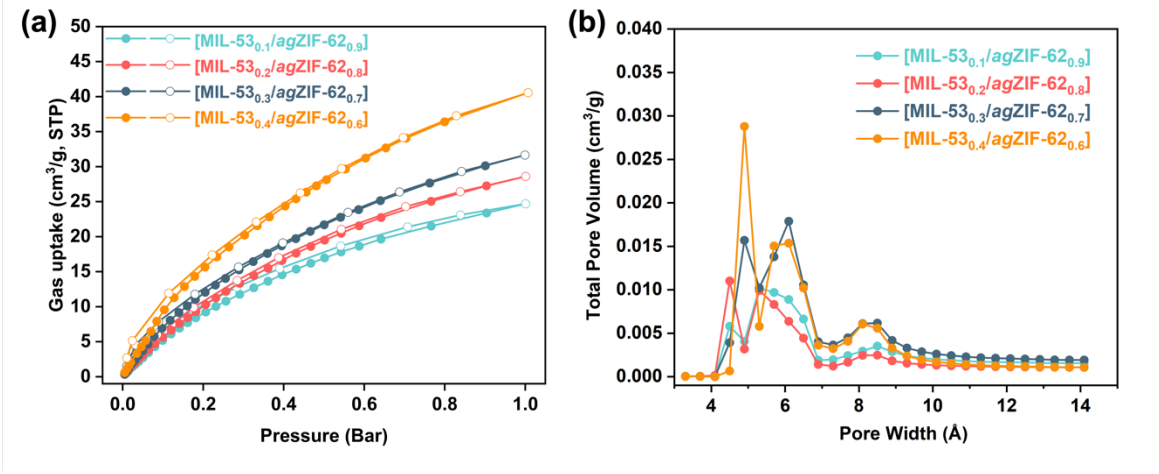


**Figure A. 35** (a) $CO_2$ adsorption–desorption isothermal curves of MIL-53 CGCMs at 273 K. (b) Micropore size distribution of MIL-53 CGCMs calculated by the NLDFT method using $CO_2$ adsorption isotherm curves.

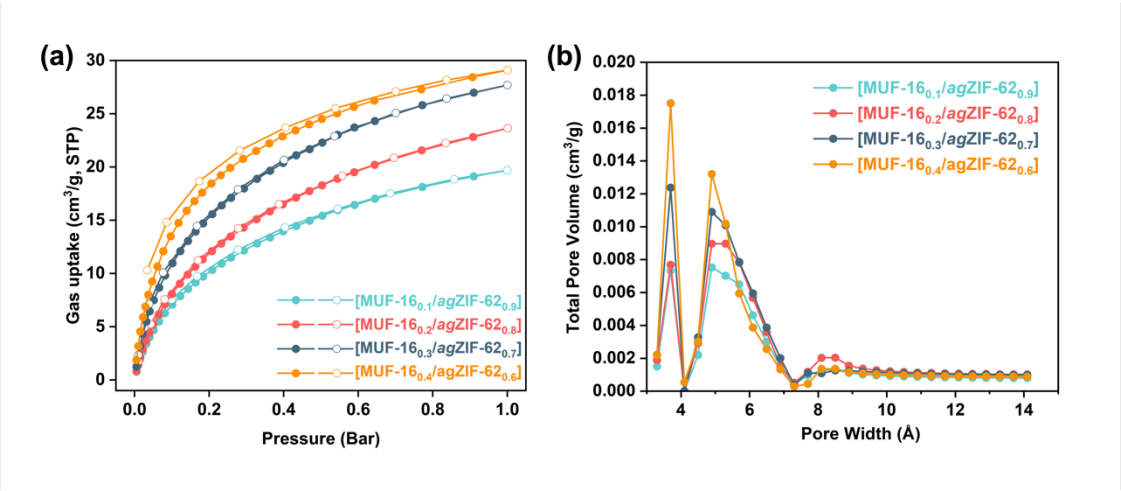


**Figure A. 36** (a) $CO_2$ adsorption–desorption isothermal curves of MUF-16 CGCMs at 273 K. (b) Micropore size distribution of MUF-16 CGCMs calculated by the NLDFT method using $CO_2$ adsorption isotherm curves.

**Table A. 5** $CO_2$ and $N_2$ adsorption uptake values at 1 bar and $CO_2/N_2$ IAST selectivity of [UiO-66$_x$/*ag*ZIF-62$_{1-x}$] CGCMs ($CO_2/N_2$ = 50/50) calculated for CGCMs at 1 bar under 293 K.

| Membranes | Loading x (wt.%) | Gas Uptake (g/cm$^3$ STP) | | IAST at 1bar 293K |
|---|---|---|---|---|
| | | $CO_2$ | $N_2$ | $CO_2/N_2$ |
| Pristine *ag*ZIF-62 | 0 | 11.31 | 1.15 | 9.87 |
| [UiO-66$_x$/*ag*ZIF-62$_{1-x}$] | 10 | 12.86 | 1.04 | 12.33 |
| | 20 | 15.72 | 1.39 | 11.30 |
| | 30 | 17.74 | 1.94 | 9.15 |
| | 40 | 19.88 | 2.04 | 9.73 |
| Pure UiO-66 | 100 | 30.90 | 2.40 | 12.88 |

**Table A. 6** $CO_2$ and $N_2$ adsorption uptake values at 1 bar and $CO_2/N_2$ IAST selectivity of [ZIF-$8_x$/*ag*ZIF-$62_{1-x}$] CGCMs ($CO_2/N_2$ = 50/50) calculated for CGCMs at 1 bar under 293 K.

| Membranes | Loading x (wt.%) | Gas Uptake ($g/cm^3$ STP) | | IAST at 1bar 293K |
|---|---|---|---|---|
| | | $CO_2$ | $N_2$ | $CO_2/N_2$ |
| Pristine *ag*ZIF-62 | 0 | 11.31 | 1.15 | 9.87 |
| [ZIF-$8_x$/*ag*ZIF-$62_{1-x}$] | 10 | 9.95 | 0.72 | 13.74 |
| | 20 | 12.58 | 1.28 | 9.79 |
| | 30 | 14.18 | 1.34 | 10.55 |
| | 40 | 13.95 | 1.69 | 8.27 |
| Pure ZIF-8 | 100 | 16.90 | 2.18 | 7.76 |

**Table A. 7** $CO_2$ and $N_2$ adsorption uptake values at 1 bar and $CO_2/N_2$ IAST selectivity of [MIL-$53_x$/*ag*ZIF-$62_{1-x}$] CGCMs ($CO_2/N_2$ = 50/50) calculated for CGCMs at 1 bar under 293 K.

| Membranes | Loading x (wt.%) | Gas Uptake ($g/cm^3$ STP) | | IAST at 1bar 293K |
|---|---|---|---|---|
| | | $CO_2$ | $N_2$ | $CO_2/N_2$ |
| Pristine *ag*ZIF-62 | 0 | 11.31 | 1.15 | 9.87 |
| [MIL-$53_x$/*ag*ZIF-$62_{1-x}$] | 10 | 18.13 | 1.86 | 9.73 |
| | 20 | 20.51 | 2.19 | 9.38 |
| | 30 | 25.99 | 2.48 | 10.47 |
| | 40 | 26.43 | 2.59 | 10.21 |
| Pure MIL-53 | 100 | 0.84 | 0.52 | 1.63 |

**Table A. 8** $CO_2$ and $N_2$ adsorption uptake values at 1 bar and $CO_2/N_2$ IAST selectivity of [MUF-$16_x$/*ag*ZIF-$62_{1-x}$] CGCMs ($CO_2/N_2$ = 50/50) calculated for CGCMs at 1 bar under 293 K.

| Membranes | Loading x (wt.%) | Gas Uptake ($g/cm^3$ STP) | | IAST at 1bar 293K |
|---|---|---|---|---|
| | | $CO_2$ | $N_2$ | $CO_2/N_2$ |
| Pristine *ag*ZIF-62 | 0 | 11.31 | 1.15 | 9.87 |
| [MUF-$16_x$/*ag*ZIF-$62_{1-x}$] | 10 | 12.05 | 1.04 | 11.58 |
| | 20 | 17.80 | 1.09 | 16.36 |
| | 30 | 23.29 | 1.54 | 15.16 |
| | 40 | 24.72 | 1.78 | 14.65 |
| Pure MUF-16 | 100 | 47.43 | 2.52 | 18.83 |

**Table A. 9** Pore size distribution results of *ag*ZIF-62 and [UiO-$66_x$/*ag*ZIF-$62_{1-x}$] CGCMs.

| *ag*ZIF-62 | | [UiO-$66_{0.1}$/*ag*ZIF-$62_{0.9}$] | | [UiO-$66_{0.2}$/*ag*ZIF-$62_{0.8}$] | | [UiO-$66_{0.3}$/*ag*ZIF-$62_{0.7}$] | | [UiO-$66_{0.4}$/*ag*ZIF-$62_{0.6}$] | |
|---|---|---|---|---|---|---|---|---|---|
| Pore Width (Å) | Total Pore Volume ($cm^3/g$) | Pore Width (Å) | Total Pore Volume ($cm^3/g$) | Pore Width (Å) | Total Pore Volume ($cm^3/g$) | Pore Width (Å) | Total Pore Volume ($cm^3/g$) | Pore Width (Å) | Total Pore Volume ($cm^3/g$) |
| 3.3 | 9.00E-05 | 3.3 | 9.00E-05 | 3.3 | 9.00E-05 | 3.3 | 9.00E-05 | 3.3 | 9.00E-05 |
| 3.7 | 9.00E-05 | 3.7 | 9.00E-05 | 3.7 | 7.00E-05 | 3.7 | 8.00E-05 | 3.7 | 1.00E-04 |
| 4.1 | 1.45E-06 | 4.1 | 0.00E+00 | 4.1 | 0.00E+00 | 4.1 | 0.00E+00 | 4.1 | 0.00E+00 |
| 4.5 | 2.47E-03 | 4.5 | 1.78E-03 | 4.5 | 2.36E-03 | 4.5 | 2.54E-03 | 4.5 | 2.67E-03 |
| 4.9 | 6.83E-03 | 4.9 | 8.22E-03 | 4.9 | 6.23E-03 | 4.9 | 7.47E-03 | 4.9 | 6.75E-03 |
| 5.3 | 7.05E-03 | 5.3 | 8.86E-03 | 5.3 | 1.01E-02 | 5.3 | 1.21E-02 | 5.3 | 1.43E-02 |
| 5.7 | 6.41E-03 | 5.7 | 7.46E-03 | 5.7 | 5.96E-03 | 5.7 | 7.68E-03 | 5.7 | 7.37E-03 |
| 6.1 | 4.81E-03 | 6.1 | 5.84E-03 | 6.1 | 7.57E-03 | 6.1 | 6.74E-03 | 6.1 | 5.06E-03 |
| 6.5 | 3.08E-03 | 6.5 | 3.68E-03 | 6.5 | 2.38E-03 | 6.5 | 4.09E-03 | 6.5 | 3.94E-03 |
| 6.9 | 1.22E-03 | 6.9 | 1.45E-03 | 6.9 | 2.28E-03 | 6.9 | 1.35E-03 | 6.9 | 8.06E-04 |
| 7.3 | 4.87E-04 | 7.3 | 5.19E-04 | 7.3 | 4.16E-04 | 7.3 | 6.65E-04 | 7.3 | 5.66E-04 |
| 7.7 | 8.18E-04 | 7.7 | 9.68E-04 | 7.7 | 1.50E-03 | 7.7 | 1.94E-03 | 7.7 | 1.31E-03 |
| 8.1 | 1.21E-03 | 8.1 | 2.18E-03 | 8.1 | 2.91E-03 | 8.1 | 2.33E-03 | 8.1 | 1.96E-03 |
| 8.5 | 2.74E-03 | 8.5 | 2.67E-03 | 8.5 | 2.81E-03 | 8.5 | 2.06E-03 | 8.5 | 2.06E-03 |
| 8.9 | 2.73E-03 | 8.9 | 2.07E-03 | 8.9 | 1.85E-03 | 8.9 | 1.47E-03 | 8.9 | 1.49E-03 |
| 9.3 | 2.31E-03 | 9.3 | 1.75E-03 | 9.3 | 1.44E-03 | 9.3 | 1.25E-03 | 9.3 | 1.27E-03 |
| 9.7 | 2.09E-03 | 9.7 | 1.59E-03 | 9.7 | 1.26E-03 | 9.7 | 1.15E-03 | 9.7 | 1.16E-03 |
| 10.1 | 1.95E-03 | 10.1 | 1.48E-03 | 10.1 | 1.15E-03 | 10.1 | 1.09E-03 | 10.1 | 1.10E-03 |
| 10.5 | 1.85E-03 | 10.5 | 1.41E-03 | 10.5 | 1.10E-03 | 10.5 | 1.05E-03 | 10.5 | 1.05E-03 |
| 10.9 | 1.76E-03 | 10.9 | 1.36E-03 | 10.9 | 1.06E-03 | 10.9 | 1.02E-03 | 10.9 | 1.02E-03 |
| 11.3 | 1.67E-03 | 11.3 | 1.31E-03 | 11.3 | 1.01E-03 | 11.3 | 9.90E-04 | 11.3 | 9.93E-04 |
| 11.7 | 1.65E-03 | 11.7 | 1.28E-03 | 11.7 | 9.72E-04 | 11.7 | 9.66E-04 | 11.7 | 9.69E-04 |
| 12.1 | 1.64E-03 | 12.1 | 1.27E-03 | 12.1 | 9.66E-04 | 12.1 | 9.55E-04 | 12.1 | 9.55E-04 |
| 12.5 | 1.60E-03 | 12.5 | 1.25E-03 | 12.5 | 9.48E-04 | 12.5 | 9.44E-04 | 12.5 | 9.43E-04 |
| 12.9 | 1.56E-03 | 12.9 | 1.23E-03 | 12.9 | 9.27E-04 | 12.9 | 9.33E-04 | 12.9 | 9.32E-04 |
| 13.3 | 1.50E-03 | 13.3 | 1.20E-03 | 13.3 | 9.14E-04 | 13.3 | 9.25E-04 | 13.3 | 9.19E-04 |
| 13.7 | 1.51E-03 | 13.7 | 1.20E-03 | 13.7 | 9.21E-04 | 13.7 | 9.27E-04 | 13.7 | 9.16E-04 |
| 14.1 | 1.52E-03 | 14.1 | 1.19E-03 | 14.1 | 9.26E-04 | 14.1 | 9.28E-04 | 14.1 | 9.13E-04 |

**Table A. 10** Pore size distribution results of [ZIF-$8_x$/*ag*ZIF-$62_{1-x}$] CGCMs.

| [ZIF-$8_{0.1}$/*ag*ZIF-$62_{0.9}$] | | [ZIF-$8_{0.2}$/*ag*ZIF-$62_{0.8}$] | | [ZIF-$8_{0.3}$/*ag*ZIF-$62_{0.7}$] | | [ZIF-$8_{0.4}$/*ag*ZIF-$62_{0.6}$] | |
|---|---|---|---|---|---|---|---|
| Pore Width (Å) | Total Pore Volume ($cm^3/g$) | Pore Width (Å) | Total Pore Volume ($cm^3/g$) | Pore Width (Å) | Total Pore Volume ($cm^3/g$) | Pore Width (Å) | Total Pore Volume ($cm^3/g$) |
| 3.3 | 9.00E-05 | 3.3 | 6.30E-05 | 3.3 | 8.01E-05 | 3.3 | 3.69E-05 |
| 3.7 | 9.00E-05 | 3.7 | 6.30E-05 | 3.7 | 8.01E-05 | 3.7 | 9.48E-05 |
| 4.1 | 1.45E-06 | 4.1 | 0.00E+00 | 4.1 | 0.00E+00 | 4.1 | 6.82E-04 |
| 4.5 | 2.47E-03 | 4.5 | 2.22E-03 | 4.5 | 1.58E-03 | 4.5 | 1.82E-03 |
| 4.9 | 6.83E-03 | 4.9 | 6.01E-03 | 4.9 | 5.63E-03 | 4.9 | 5.94E-03 |
| 5.3 | 7.05E-03 | 5.3 | 8.56E-03 | 5.3 | 9.12E-03 | 5.3 | 1.09E-02 |
| 5.7 | 6.41E-03 | 5.7 | 6.68E-03 | 5.7 | 5.28E-03 | 5.7 | 7.36E-03 |
| 6.1 | 4.81E-03 | 6.1 | 5.08E-03 | 6.1 | 4.02E-03 | 6.1 | 3.84E-03 |
| 6.5 | 3.08E-03 | 6.5 | 3.91E-03 | 6.5 | 2.34E-03 | 6.5 | 2.93E-03 |
| 6.9 | 1.22E-03 | 6.9 | 2.25E-04 | 6.9 | 2.26E-03 | 6.9 | 1.84E-03 |
| 7.3 | 4.87E-04 | 7.3 | 1.29E-03 | 7.3 | 3.59E-04 | 7.3 | 6.63E-04 |
| 7.7 | 8.18E-04 | 7.7 | 1.09E-03 | 7.7 | 1.04E-03 | 7.7 | 7.21E-04 |
| 8.1 | 1.21E-03 | 8.1 | 1.83E-03 | 8.1 | 2.17E-03 | 8.1 | 2.17E-03 |
| 8.5 | 2.74E-03 | 8.5 | 2.73E-03 | 8.5 | 2.14E-03 | 8.5 | 2.20E-03 |
| 8.9 | 2.73E-03 | 8.9 | 2.33E-03 | 8.9 | 1.40E-03 | 8.9 | 1.73E-03 |
| 9.3 | 2.31E-03 | 9.3 | 1.95E-03 | 9.3 | 1.13E-03 | 9.3 | 1.39E-03 |
| 9.7 | 2.09E-03 | 9.7 | 1.76E-03 | 9.7 | 9.99E-04 | 9.7 | 1.22E-03 |
| 10.1 | 1.95E-03 | 10.1 | 1.63E-03 | 10.1 | 9.22E-04 | 10.1 | 1.10E-03 |
| 10.5 | 1.85E-03 | 10.5 | 1.55E-03 | 10.5 | 8.82E-04 | 10.5 | 1.04E-03 |
| 10.9 | 1.76E-03 | 10.9 | 1.48E-03 | 10.9 | 8.53E-04 | 10.9 | 1.00E-03 |
| 11.3 | 1.67E-03 | 11.3 | 1.41E-03 | 11.3 | 8.20E-04 | 11.3 | 9.59E-04 |
| 11.7 | 1.65E-03 | 11.7 | 1.39E-03 | 11.7 | 7.91E-04 | 11.7 | 9.47E-04 |
| 12.1 | 1.64E-03 | 12.1 | 1.38E-03 | 12.1 | 7.81E-04 | 12.1 | 9.32E-04 |
| 12.5 | 1.60E-03 | 12.5 | 1.36E-03 | 12.5 | 7.69E-04 | 12.5 | 9.14E-04 |
| 12.9 | 1.56E-03 | 12.9 | 1.33E-03 | 12.9 | 7.57E-04 | 12.9 | 8.96E-04 |
| 13.3 | 1.50E-03 | 13.3 | 1.28E-03 | 13.3 | 7.46E-04 | 13.3 | 8.72E-04 |
| 13.7 | 1.51E-03 | 13.7 | 1.28E-03 | 13.7 | 7.45E-04 | 13.7 | 8.56E-04 |
| 14.1 | 1.52E-03 | 14.1 | 1.28E-03 | 14.1 | 7.44E-04 | 14.1 | 8.43E-04 |

**Table A. 11** Pore size distribution results of [MIL-$53_x$/*ag*ZIF-$62_{1-x}$] CGCMs.

| [MIL-$53_{0.1}$/*ag*ZIF-$62_{0.9}$] | | [MIL-$53_{0.2}$/*ag*ZIF-$62_{0.8}$] | | [MIL-$53_{0.3}$/*ag*ZIF-$62_{0.7}$] | | [MIL-$53_{0.4}$/*ag*ZIF-$62_{0.6}$] | |
|---|---|---|---|---|---|---|---|
| Pore Width (Å) | Total Pore Volume ($cm^3/g$) | Pore Width (Å) | Total Pore Volume ($cm^3/g$) | Pore Width (Å) | Total Pore Volume ($cm^3/g$) | Pore Width (Å) | Total Pore Volume ($cm^3/g$) |
| 3.3 | 5.69E-05 | 3.3 | 5.69E-05 | 3.3 | 4.22E-05 | 3.3 | 3.69E-05 |
| 3.7 | 5.69E-05 | 3.7 | 5.69E-05 | 3.7 | 4.22E-05 | 3.7 | 3.79E-05 |
| 4.1 | 0.00E+00 | 4.1 | 1.45E-04 | 4.1 | 0.00E+00 | 4.1 | 0.00E+00 |
| 4.5 | 5.81E-03 | 4.5 | 1.10E-02 | 4.5 | 3.92E-03 | 4.5 | 6.63E-04 |
| 4.9 | 4.06E-03 | 4.9 | 3.17E-03 | 4.9 | 1.57E-02 | 4.9 | 2.88E-02 |
| 5.3 | 1.02E-02 | 5.3 | 9.93E-03 | 5.3 | 1.02E-02 | 5.3 | 5.80E-03 |
| 5.7 | 9.70E-03 | 5.7 | 8.31E-03 | 5.7 | 1.38E-02 | 5.7 | 1.50E-02 |
| 6.1 | 8.88E-03 | 6.1 | 6.38E-03 | 6.1 | 1.79E-02 | 6.1 | 1.54E-02 |
| 6.5 | 6.63E-03 | 6.5 | 4.44E-03 | 6.5 | 1.06E-02 | 6.5 | 1.02E-02 |
| 6.9 | 1.90E-03 | 6.9 | 1.42E-03 | 6.9 | 4.02E-03 | 6.9 | 3.63E-03 |
| 7.3 | 1.97E-03 | 7.3 | 1.21E-03 | 7.3 | 3.65E-03 | 7.3 | 3.23E-03 |
| 7.7 | 2.43E-03 | 7.7 | 1.67E-03 | 7.7 | 4.48E-03 | 7.7 | 4.08E-03 |
| 8.1 | 2.95E-03 | 8.1 | 2.45E-03 | 8.1 | 6.11E-03 | 8.1 | 6.06E-03 |
| 8.5 | 3.53E-03 | 8.5 | 2.48E-03 | 8.5 | 6.17E-03 | 8.5 | 5.59E-03 |
| 8.9 | 2.87E-03 | 8.9 | 1.83E-03 | 8.9 | 4.17E-03 | 8.9 | 3.29E-03 |
| 9.3 | 2.39E-03 | 9.3 | 1.55E-03 | 9.3 | 3.30E-03 | 9.3 | 2.39E-03 |
| 9.7 | 2.15E-03 | 9.7 | 1.41E-03 | 9.7 | 2.87E-03 | 9.7 | 1.95E-03 |
| 10.1 | 1.99E-03 | 10.1 | 1.32E-03 | 10.1 | 2.60E-03 | 10.1 | 1.69E-03 |
| 10.5 | 1.89E-03 | 10.5 | 1.26E-03 | 10.5 | 2.43E-03 | 10.5 | 1.54E-03 |
| 10.9 | 1.80E-03 | 10.9 | 1.22E-03 | 10.9 | 2.30E-03 | 10.9 | 1.42E-03 |
| 11.3 | 1.72E-03 | 11.3 | 1.18E-03 | 11.3 | 2.19E-03 | 11.3 | 1.32E-03 |
| 11.7 | 1.69E-03 | 11.7 | 1.15E-03 | 11.7 | 2.13E-03 | 11.7 | 1.25E-03 |
| 12.1 | 1.67E-03 | 12.1 | 1.14E-03 | 12.1 | 2.08E-03 | 12.1 | 1.21E-03 |
| 12.5 | 1.64E-03 | 12.5 | 1.12E-03 | 12.5 | 2.04E-03 | 12.5 | 1.18E-03 |
| 12.9 | 1.60E-03 | 12.9 | 1.11E-03 | 12.9 | 2.00E-03 | 12.9 | 1.14E-03 |
| 13.3 | 1.56E-03 | 13.3 | 1.08E-03 | 13.3 | 1.94E-03 | 13.3 | 1.10E-03 |
| 13.7 | 1.56E-03 | 13.7 | 1.08E-03 | 13.7 | 1.93E-03 | 13.7 | 1.09E-03 |
| 14.1 | 1.56E-03 | 14.1 | 1.08E-03 | 14.1 | 1.92E-03 | 14.1 | 1.08E-03 |

**Table A. 12** Pore size distribution results of [MUF-$16_x$/*ag*ZIF-$62_{1-x}$] CGCMs.

| [MUF-$16_{0.1}$/*ag*ZIF-$62_{0.9}$] | | [MUF-$16_{0.2}$/*ag*ZIF-$62_{0.8}$] | | [MUF-$16_{0.3}$/*ag*ZIF-$62_{0.7}$] | | [MUF-$16_{0.4}$/*ag*ZIF-$62_{0.6}$] | |
|---|---|---|---|---|---|---|---|
| Pore Width (Å) | Total Pore Volume ($cm^3/g$) | Pore Width (Å) | Total Pore Volume ($cm^3/g$) | Pore Width (Å) | Total Pore Volume ($cm^3/g$) | Pore Width (Å) | Total Pore Volume ($cm^3/g$) |
| 3.3 | 0.00151 | 3.3 | 0.00188 | 3.3 | 0.00221 | 3.3 | 0.00218 |
| 3.7 | 0.00734 | 3.7 | 0.00769 | 3.7 | 0.01238 | 3.7 | 0.01752 |
| 4.1 | 0.00E+00 | 4.1 | 0.00E+00 | 4.1 | 0.00E+00 | 4.1 | 5.45E-04 |
| 4.5 | 2.20E-03 | 4.5 | 2.91E-03 | 4.5 | 3.28E-03 | 4.5 | 3.00E-03 |
| 4.9 | 7.53E-03 | 4.9 | 8.97E-03 | 4.9 | 1.09E-02 | 4.9 | 1.32E-02 |
| 5.3 | 7.02E-03 | 5.3 | 8.98E-03 | 5.3 | 1.01E-02 | 5.3 | 1.02E-02 |
| 5.7 | 6.50E-03 | 5.7 | 7.81E-03 | 5.7 | 7.86E-03 | 5.7 | 5.94E-03 |
| 6.1 | 4.62E-03 | 6.1 | 5.67E-03 | 6.1 | 5.95E-03 | 6.1 | 3.87E-03 |
| 6.5 | 3.01E-03 | 6.5 | 3.58E-03 | 6.5 | 3.87E-03 | 6.5 | 2.56E-03 |
| 6.9 | 1.51E-03 | 6.9 | 1.55E-03 | 6.9 | 2.01E-03 | 6.9 | 1.32E-03 |
| 7.3 | 4.27E-04 | 7.3 | 5.14E-04 | 7.3 | 3.91E-04 | 7.3 | 2.83E-04 |
| 7.7 | 9.60E-04 | 7.7 | 1.18E-03 | 7.7 | 1.10E-03 | 7.7 | 4.44E-04 |
| 8.1 | 1.27E-03 | 8.1 | 2.03E-03 | 8.1 | 1.09E-03 | 8.1 | 1.36E-03 |
| 8.5 | 1.31E-03 | 8.5 | 2.04E-03 | 8.5 | 1.26E-03 | 8.5 | 1.37E-03 |
| 8.9 | 1.11E-03 | 8.9 | 1.55E-03 | 8.9 | 1.24E-03 | 8.9 | 1.16E-03 |
| 9.3 | 1.02E-03 | 9.3 | 1.37E-03 | 9.3 | 1.20E-03 | 9.3 | 1.08E-03 |
| 9.7 | 9.61E-04 | 9.7 | 1.27E-03 | 9.7 | 1.15E-03 | 9.7 | 1.03E-03 |
| 10.1 | 9.22E-04 | 10.1 | 1.21E-03 | 10.1 | 1.12E-03 | 10.1 | 9.99E-04 |
| 10.5 | 8.93E-04 | 10.5 | 1.17E-03 | 10.5 | 1.09E-03 | 10.5 | 9.73E-04 |
| 10.9 | 8.72E-04 | 10.9 | 1.13E-03 | 10.9 | 1.07E-03 | 10.9 | 9.53E-04 |
| 11.3 | 8.54E-04 | 11.3 | 1.11E-03 | 11.3 | 1.05E-03 | 11.3 | 9.37E-04 |
| 11.7 | 8.38E-04 | 11.7 | 1.08E-03 | 11.7 | 1.03E-03 | 11.7 | 9.22E-04 |
| 12.1 | 8.26E-04 | 12.1 | 1.07E-03 | 12.1 | 1.02E-03 | 12.1 | 9.10E-04 |
| 12.5 | 8.18E-04 | 12.5 | 1.05E-03 | 12.5 | 1.01E-03 | 12.5 | 9.02E-04 |
| 12.9 | 8.11E-04 | 12.9 | 1.05E-03 | 12.9 | 1.01E-03 | 12.9 | 8.96E-04 |
| 13.3 | 8.02E-04 | 13.3 | 1.03E-03 | 13.3 | 9.96E-04 | 13.3 | 8.86E-04 |
| 13.7 | 7.97E-04 | 13.7 | 1.03E-03 | 13.7 | 9.92E-04 | 13.7 | 8.82E-04 |
| 14.1 | 7.94E-04 | 14.1 | 1.02E-03 | 14.1 | 9.88E-04 | 14.1 | 8.79E-04 |

**Table A. 13** Single gas permeance test and ideal $CO_2/N_2$ selectivity of [UiO-$66_x$/*ag*ZIF-$62_{1-x}$] CGCM.

| Membrane | Gas Permeance ($10^4$ GPU) | | Selectivity |
|---|---|---|---|
| | $CO_2$ | $N_2$ | $CO_2/N_2$ |
| *ag*ZIF-62 | 1.97 | 1.05 | 1.9 |
| [UiO-$66_{0.1}$/*ag*ZIF-$62_{0.9}$] | 11.6 | 4.65 | 2.5 |
| [UiO-$66_{0.2}$/*ag*ZIF-$62_{0.8}$] | 14.0 | 4.51 | 3.1 |
| [UiO-$66_{0.3}$/*ag*ZIF-$62_{0.7}$] | 16.5 | 4.33 | 3.8 |
| [UiO-$66_{0.4}$/*ag*ZIF-$62_{0.6}$] | 17.6 | 3.71 | 4.7 |

**Table A. 14** Single gas permeance test and ideal $CO_2/N_2$ selectivity of [ZIF-$8_x$/*ag*ZIF-$62_{1-x}$] CGCM.

| Membrane | Gas Permeance ($10^4$ GPU) | | Selectivity |
|---|---|---|---|
| | $CO_2$ | $N_2$ | $CO_2/N_2$ |
| [ZIF-$8_{0.1}$/*ag*ZIF-$62_{0.9}$] | 8.32 | 1.80 | 4.6 |
| [ZIF-$8_{0.2}$/*ag*ZIF-$62_{0.8}$] | 9.08 | 1.46 | 6.2 |
| [ZIF-$8_{0.3}$/*ag*ZIF-$62_{0.7}$] | 10.6 | 1.88 | 5.6 |
| [ZIF-$8_{0.4}$/*ag*ZIF-$62_{0.6}$] | 10.9 | 2.02 | 5.4 |

**Table A. 15** Single gas permeance test and ideal $CO_2/N_2$ selectivity of [MIL-$53_x$/*ag*ZIF-$62_{1-x}$] CGCM.

| Membrane | Gas Permeance ($10^4$ GPU) | | Selectivity |
|---|---|---|---|
| | $CO_2$ | $N_2$ | $CO_2/N_2$ |
| [MIL-$53_{0.1}$/*ag*ZIF-$62_{0.9}$] | 10.3 | 3.89 | 2.6 |
| [MIL-$53_{0.2}$/*ag*ZIF-$62_{0.8}$] | 11.3 | 4.21 | 2.7 |
| [MIL-$53_{0.3}$/*ag*ZIF-$62_{0.7}$] | 17.5 | 5.36 | 3.2 |
| [MIL-$53_{0.4}$/*ag*ZIF-$62_{0.6}$] | 17.1 | 6.50 | 2.6 |

**Table A. 16** Single gas permeance test and ideal $CO_2/N_2$ selectivity of [MUF-$16_x$/*ag*ZIF-$62_{1-x}$] CGCM.

| Membrane | Gas Permeance ($10^4$ GPU) | | Selectivity |
|---|---|---|---|
| | $CO_2$ | $N_2$ | $CO_2/N_2$ |
| [MUF-$16_{0.1}$/*ag*ZIF-$62_{0.9}$] | 14.2 | 5.55 | 2.6 |
| [MUF-$16_{0.2}$/*ag*ZIF-$62_{0.8}$] | 15.0 | 4.52 | 3.3 |
| [MUF-$16_{0.3}$/*ag*ZIF-$62_{0.7}$] | 17.2 | 3.95 | 4.4 |
| [MUF-$16_{0.4}$/*ag*ZIF-$62_{0.6}$] | 20.4 | 3.56 | 5.7 |

**Table A. 17** Mixed gas permeance test and $CO_2/N_2$ selectivity of all CGCMs with 40 wt.% MOF loading.

| Membrane | $CO_2$ Permeance ($10^4$ GPU) | $CO_2/N_2$ |
|---|---|---|
| [UiO-$66_{0.4}$/*ag*ZIF-$62_{0.6}$] | 16.3 | 4.2 |
| [ZIF-$8_{0.4}$/*ag*ZIF-$62_{0.6}$] | 9.6 | 4.7 |
| [MIL-$53_{0.4}$/*ag*ZIF-$62_{0.6}$] | 16.5 | 2.1 |
| [MUF-$16_{0.4}$/*ag*ZIF-$62_{0.6}$] | 19.2 | 5.0 |

# Appendix B for Chapter 3

## 1. Experimental section

### Materials

Cobalt(II) acetate tetrahydrate (99.99%) and 5-aminoisophthalic acid ($H_2$aip, 99 %) were purchased from Sigma-Aldrich. Methanol (MeOH, 99.9%) and ethanol (EtOH, 99.9%) were purchased from Fisher Chemicals. Commercial Pebax-1657 (consisting of 60 wt% polyether segments and 40 wt% polyamide segments) was purchased from Arkema Inc. Deionized (DI) water was produced from a home-made reverse osmosis water treatment.

### Synthesis of MUF-16

A mixture of $Co(OAc)_2 \cdot 4H_2O$ (0.625 g), $H_2$aip (1.80 g), methanol (80 mL), and DI water (5 mL) was sonicated for 20 minutes in a sealed 1000 mL Schott bottle, which was then heated in a pre-heated oven at 85 ºC for 2 hours. After cooling to room temperature, the resulting pink crystals were isolated by decanting off the mother liquor, washed with methanol several times, then dried under vacuum at 130 ºC for 20 hours.

### *ns*MUF-16 fabrication via ball mill

MUF-16 (2.0 g) was added to a 50 mL grinding jar with 10 × 4 mm zirconium grinding balls and then ground at 30 Hz in a Vertical Planetary Ball Mill (Semi-circle Type) at a frequency of 30 Hz for 60 min. The nano-sized MUF-16 (referred to as *ns*MUF-16) powder was collected for further use.

### Characterization methods

The X-ray diffraction (XRD) of crystalline MUF-16 and MMMs was performed on a Bruker D8 Venture Diffractometer using $Cu_\alpha$ radiation (wavelength = 1.54018 Å), with a diamond microfocus X-ray source and a Photon III 28 detector. The collection of 1D diffractograms was processed using APEX3. Scanning electron microscope (SEM) images were taken on a FEI Quanta 200 Environmental with EDAX module. Transmission Electron Microscope (TEM) images were taken on a FEI Tecnai G2 Biotwin with tomography unit. Attenuated total reflection flourier transformed infrared spectroscopy (ATR-FTIR) measurements were performed on Nicolet iS5 IR with iD7 ATR Accessory, and the spectra were collected in the range of wavenumbers from 4000 to 500 $cm^{-1}$ with a scan per sample.

Thermogravimetric analysis (TGA) was carried out using a TA Q50 instrument at a heating rate of 10 °C/min from 20 to 600 °C with the $N_2$ flow rate of 60 mL/min. Gas sorption isotherms for $CO_2$, $N_2$, $CH_4$ were measured using a Quantachrome Autosorb iQ2 instrument at 293 K using ultra-high purity gases.

**Table B. 1** Parameters of gas permeability (*P*), solubility coefficient (*S*), diffusion coefficient (*D*), $C_{sat}$, $b_i$ and $k_{D,i}$.

| Membranes | | P (Barrer) | S ($10^{-2}$cm$^3$(STP) cm$^{-3}$cmHg$^{-1}$) | D ($10^{-8}$cm$^2$s$^{-1}$) | $c_{sat}$ | $b_i$ | $k_{D,i}$ |
|---|---|---|---|---|---|---|---|
| Pure Pebax | $CO_2$ | 84.99 | 3.17 | 26.81 | -- | -- | 3.17276 ± 0.01329 |
| | $N_2$ | 2.10 | 0.99 | 2.12 | -- | -- | 0.9918 ± 0.01292 |
| | $CH_4$ | 4.23 | 1.26 | 3.36 | -- | -- | 1.25978 ± 0.01657 |
| Pebax/40 wt.% *ns*MUF-16 | $CO_2$ | 231.0 | 4.09 | 56.48 | | | -- |
| | $N_2$ | 0.80 | 0.29 | 2.77 | -- | -- | 0.29435± 0.00461 |
| | $CH_4$ | 0.96 | 0.28 | 3.44 | -- | -- | 0.28717± 0.00386 |

## 2. Appendix Figures

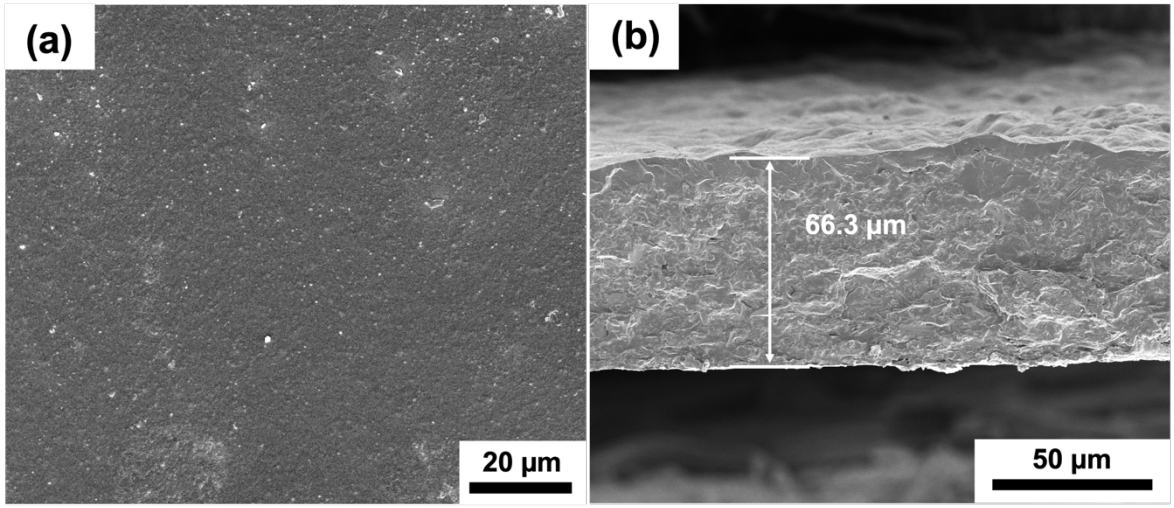


**Figure B. 1** SEM images of (a) surface and (b) cross- sectional morphologies of the membrane with 25.0 wt.% *ns*MUF-16 loading.

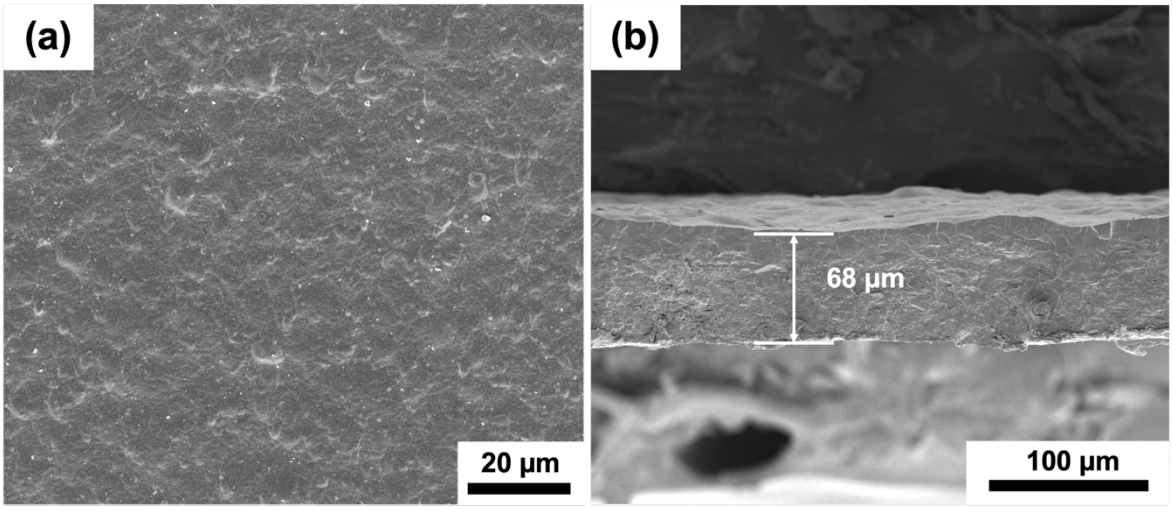


**Figure B. 2** SEM images of (a) surface and (b) cross- sectional morphologies of the membrane with 33.3 wt.% *ns*MUF-16 loading.

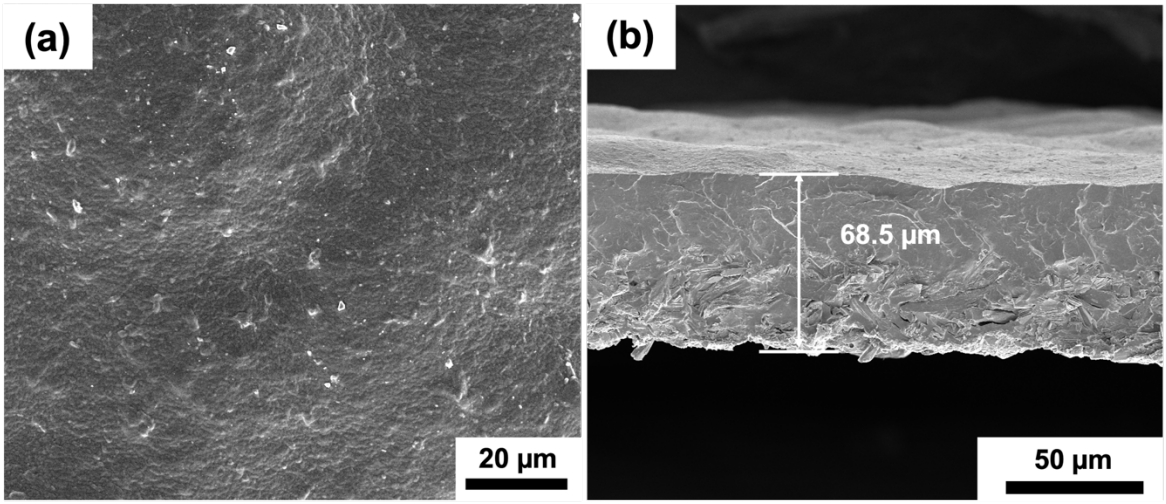


**Figure B. 3** SEM images of (a) surface and (b) cross- sectional morphologies of the membrane with 37.5 wt.% *ns*MUF-16 loading.

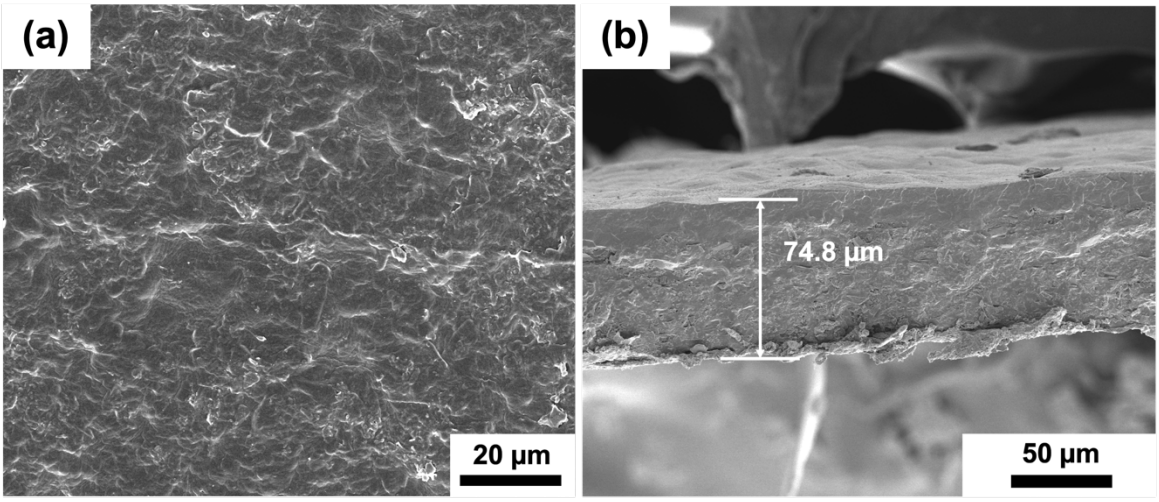


**Figure B. 4** SEM images of (a) surface and (b) cross- sectional morphologies of the membrane with 43.4 wt.% *ns*MUF-16 loading.

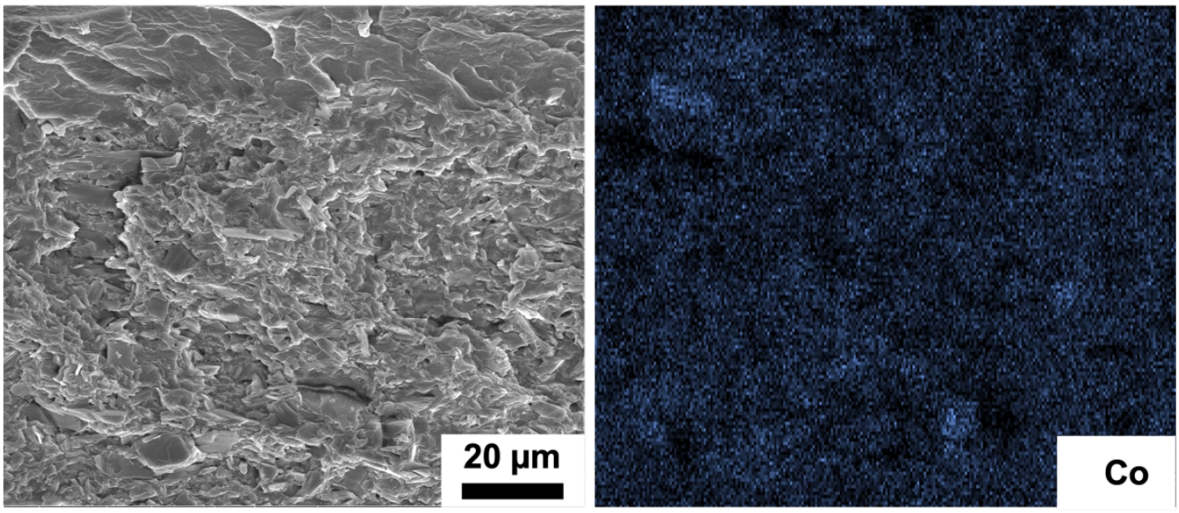


**Figure B. 5** EDS mapping of the membrane with 40.0 wt.% *ns*MUF-16 loading.

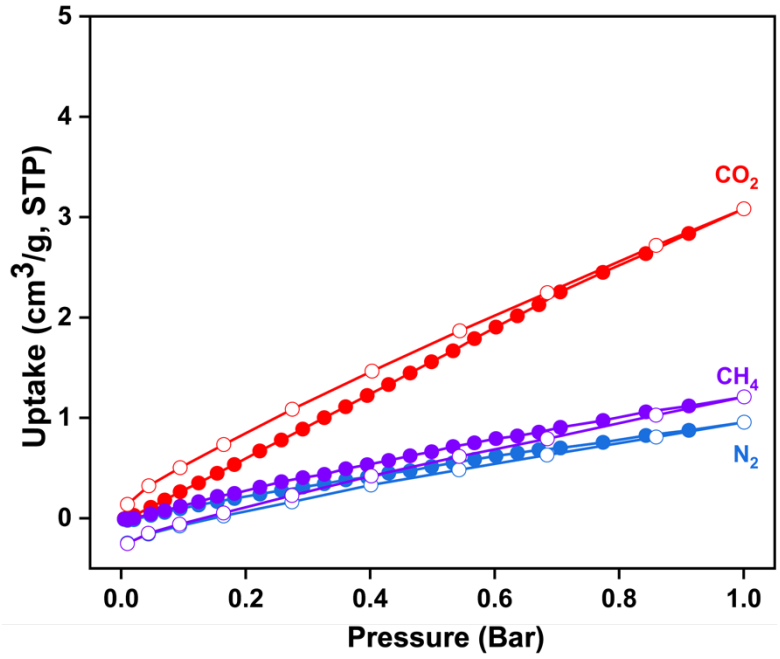


**Figure B. 6** $CO_2$, $CH_4$ and $N_2$ adsorption (filled circles) and desorption (open circles) isotherms of pure Pebax membrane measured at 293 K. The negative uptake values are artefacts of the measurement process caused by the low uptake amounts.

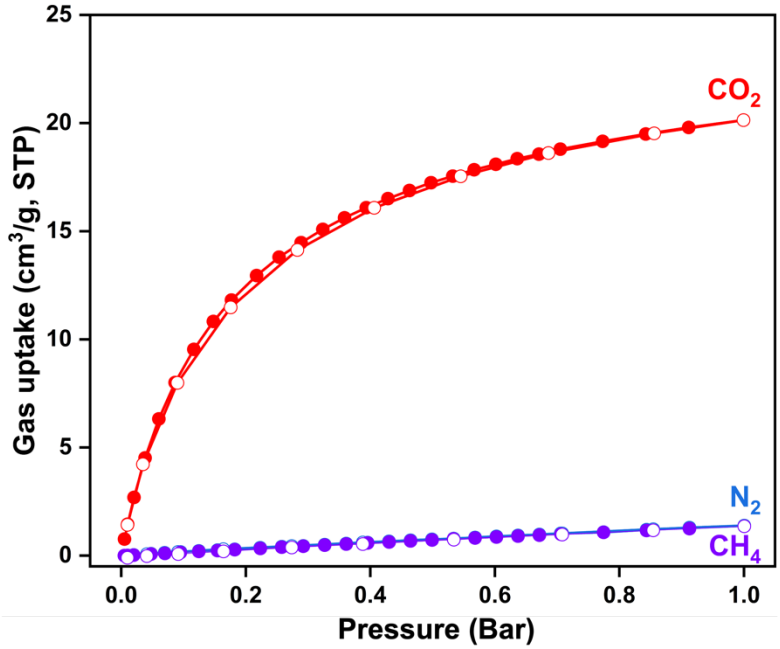


**Figure B. 7** $CO_2$, $CH_4$ and $N_2$ adsorption (filled circles) and desorption (open circles) isotherms of Pebax membrane with 40 wt.% *ns*MUF-16 loading measured at 293 K.

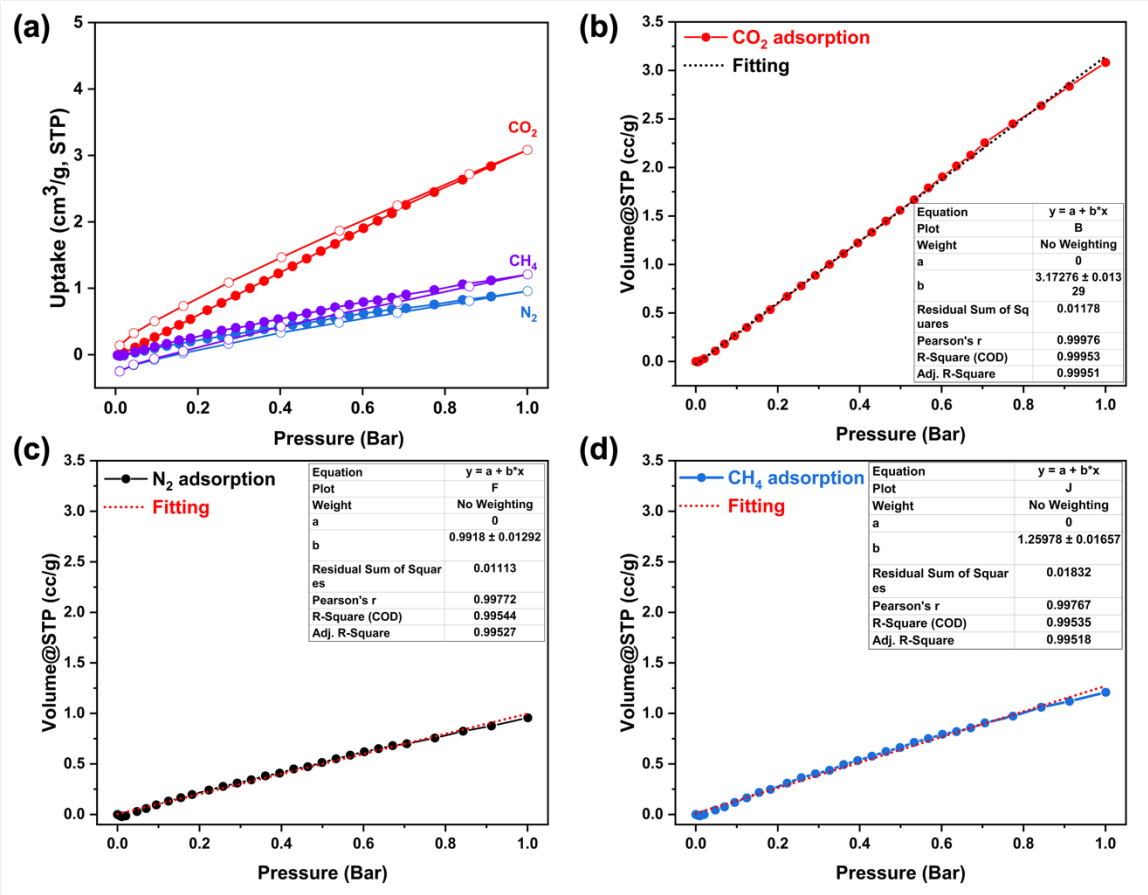


**Figure B. 8** Adsorption isotherms of $CO_2$, $N_2$ and $CH_4$ on a pure Pebax membrane at 293 K.

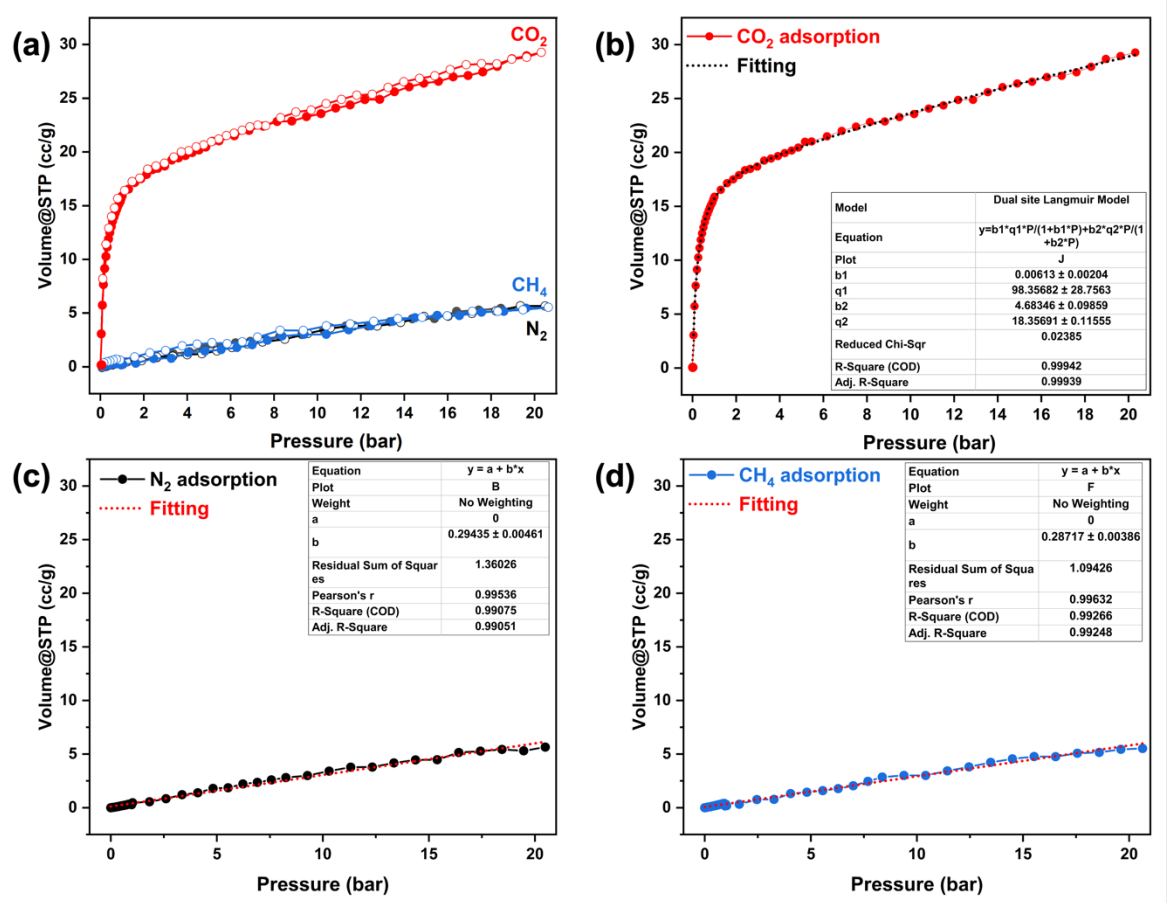


**Figure B. 9** Adsorption isotherms of $CO_2$, $N_2$ and $CH_4$ on a Pebax membrane with 40 wt.% *ns*MUF-16 loading measured at 293 K.

# Appendix C for Chapter 4

## 1. Experimental section

### Materials

Cobalt(II) acetate tetrahydrate (99.99 %) and 5-aminoisophthalic acid ($H_2$aip, 99 %) were purchased from QINGDAO SIGMACHEMICAL CO., LTD. Methanol (MeOH, 99.9 %), ethanol (EtOH, 99.9 %) and chloroform ($CHCl_3$, 99.9 %) were purchased from Fisher Chemicals. Deionized (DI) water was produced from a home-made reverse osmosis water treatment and used throughout the experiment. All the reagents were analytical grade and were used without further purification. Polyimide 6FDA-DAM (Mw = 326 kDa, PDI = 2.95), and 6FDA-Durene (Mw = 247 kDa, PDI = 2.75) were purchased from Akron Polymer Systems. Inc. $CO_2$, $N_2$, $CH_4$ and He cylinders were purchased from BOC company.

### Synthesis of MUF-16

A mixture of $Co(OAc)_2{\cdot}4H_2O$ (0.625 g, 1.0 mmol), $H_2$aip (1.80 g, 4.0 mmol), methanol (80 mL), and DI water (5 mL) was sonicated for 20 min in a sealed 1000 mL Schott bottle, which was then heated in a preheated oven at 85 °C for 2 hours. After cooling to room temperature, the resulting pink crystals were isolated by decanting off the mother liquor, washed several times with methanol, then dried under vacuum at 130 °C for 20 hours.

### Ball mill synthesis of MUF-16 (*bm*MUF-16)

$Co(OAc)_2{\cdot}4H_2O$ (100.0 mg, 0.2 mmol), $H_2$aip (146.0 mg, 0.8 mmol), and grinding balls were added to the grinding jars, which were then preheated in an oven at 120 °C for 1 hour. EtOH was then immediately added into the grinding jars. After shaking at 30 Hz for 2 hours, the resulting MUF-16 was collected and then washed several times with EtOH. Finally, the *bm*MUF-16 was dried in an oven at 80 °C for further use.

### Post-treatment of MUF-16 via ball mill (*ns*MUF-16)

The as-fabricated MUF-16 (2.0 g) was added to a 50 mL grinding jar, followed by 10 × 4 mm (zirconium grinding balls). The grinding jars were sealed and spun in a ball mill at 30 Hz for 2 hours. The nanosized-MUF-16 (*ns*MUF-16) powder was collected for further use.

### Membrane fabrications

**Fabrication of PI based MMMs**

6FDA-DAM and MUF-16 (hydrothermal synthesis, ball mill synthesis and ball mill post treatment) were added to the $CHCl_3$ solution, respectively. After stirring overnight at room temperature, the viscous casting solution was formed. The casting solution was then poured into a glass Petri dish on a level surface in a $CHCl_3$ atmosphere at room temperature overnight. Finally, the resulting MMM was peeled off from the dish and treated in a vacuum oven at 130 $^oC$ for 24 hours to remove the residual solvent. In this manner, 6FDA-DAM based MMMs with different MUF-16 morphologies (hydrothermal synthesis, ball-mill synthesis, and ball-mill post-treatment) were fabricated with the same loading. similarly, 6FDA-Durene based MUF-16 with different crystal sizes were prepared.

**Characterization methods**

The X-ray diffraction (XRD) of crystalline MUF-16 and MMMs was performed on a Bruker D8 Venture Diffractometer using $Cu_\alpha$ radiation (wavelength = 1.54018 Å), with a diamond microfocus X-ray source and a Photon III 28 detector. The collection 1D diffractograms was processed using APEX3. Scanning electron microscope (SEM) images were taken on a FEI Quanta 200 Environmental with EDAX module. Transmission Electron Microscope (TEM) images were taken on a FEI Tecnai G2 Biotwin with tomography unit. Attenuated total reflection flourier transformed infrared spectroscopy (ATR-FTIR) measurements were performed on Nicolet iS5 IR with iD7 ATR Accessory, and the spectra were collected in the range of wavenumbers from 4000 to 500 $cm^{-1}$ with one scan per sample. Thermogravimetric analysis (TGA) was carried out using a TA Q50 instrument at a heating rate of 10 °C/min from 20 to 600 °C with an $N_2$ flow rate of 60 mL/min. Gas sorption isotherms for $CO_2$, $N_2$, $CH_4$ of MMMs were measured using a Quantachrome Autosorb iQ2 instrument at 293 K. All adsorption measurements were performed using ultra-high purity gases. In addition, MUF-16 crystals were ground at 30 HZ using a vertical planetary ball mill (semi-circle type) at a frequency of 30 Hz for 60 min. Viscosity testing was carried out using an AR-G2 rheometer (TA Instruments), and the polymer-MOF suspension was stirred for 2 hours for further relative viscosity testing.

## 2. Appendix Figures

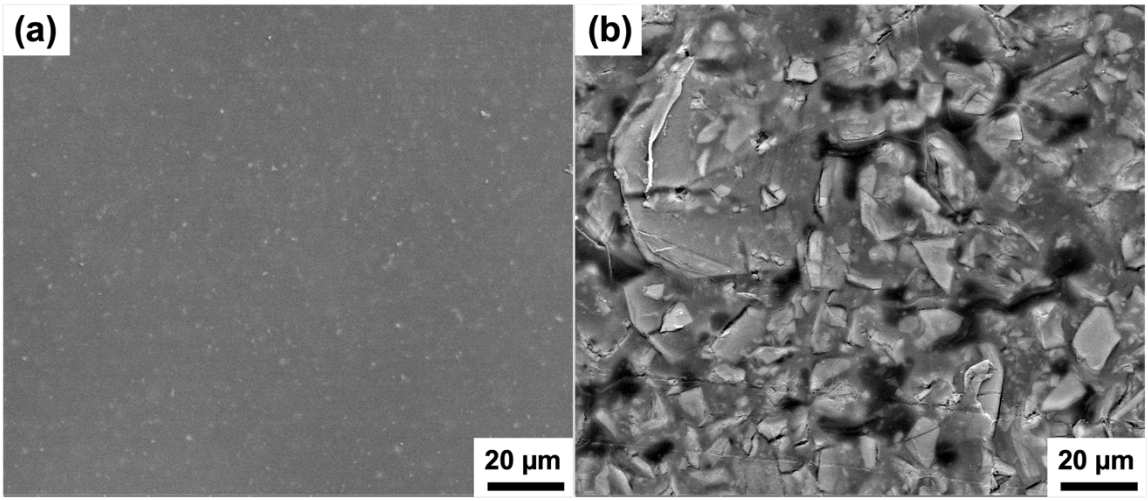


**Figure C. 1** Surface morphologies of (a) top side and (b) bottom side of 6FDA-DAM loaded with 40 wt.% MUF-16 loading.

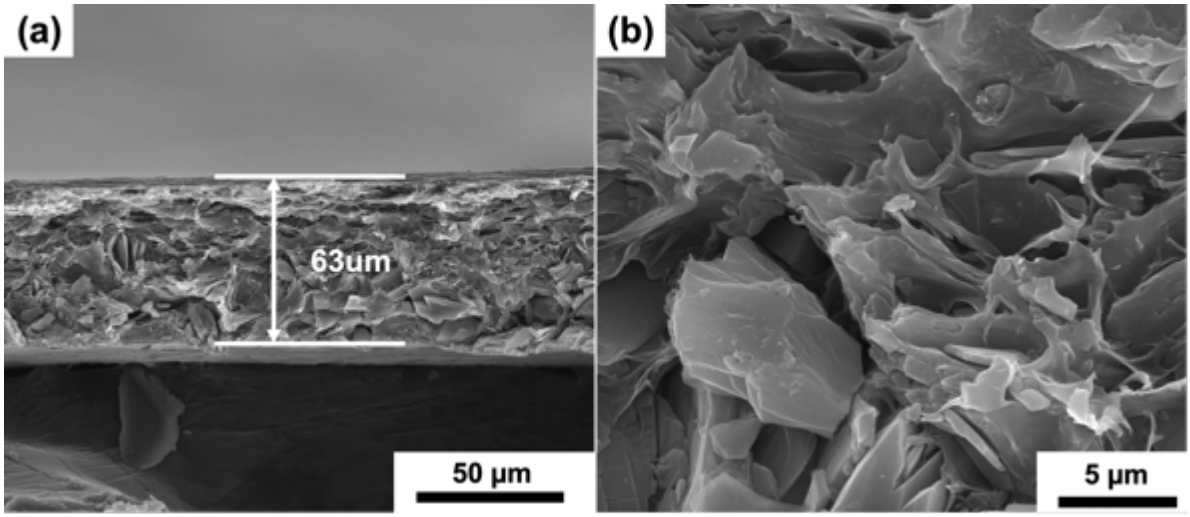


**Figure C. 2** Cross-sectional morphologies of 6FDA-DAM loaded with 40 wt.% MUF-16 loading at different magnifications (clear sediment can be observed).

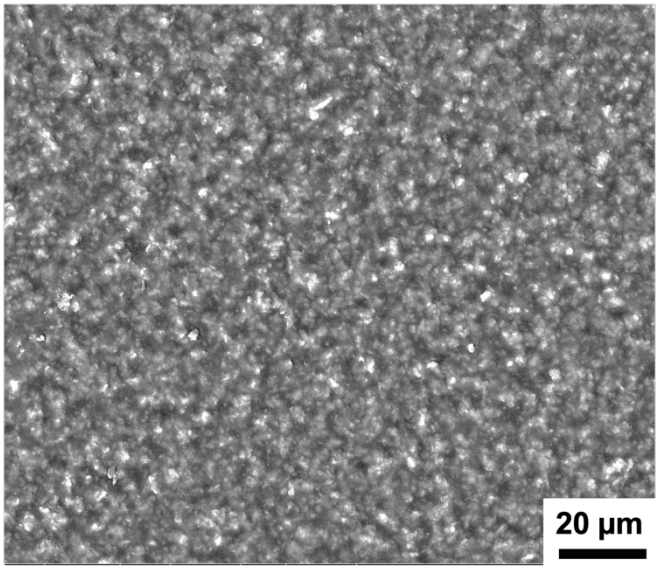


**Figure C. 3** Surface morphologies of 6FDA-DAM loaded with 40 wt.% *bm*MUF-16 loading.

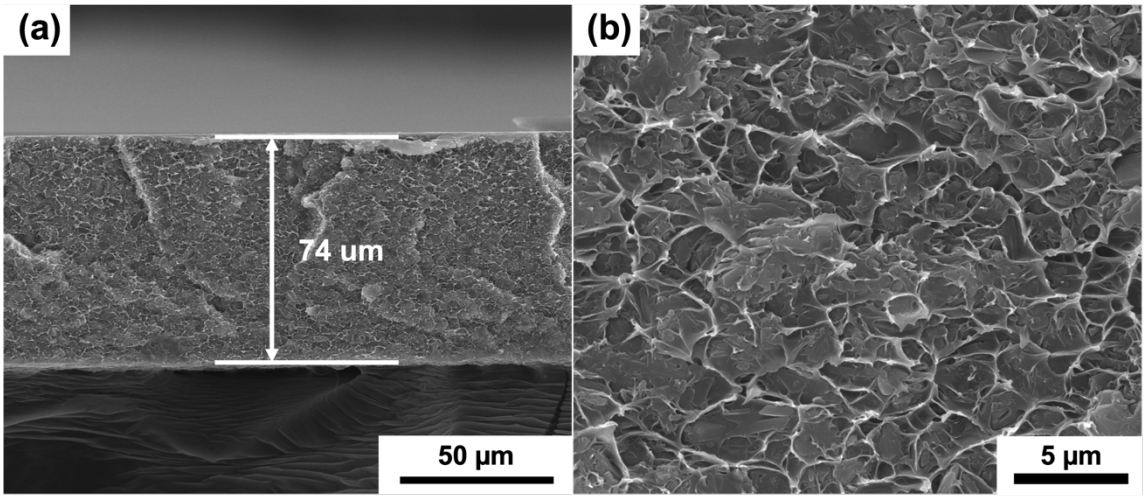


**Figure C. 4** Cross-sectional morphologies of 6FDA-DAM loaded with 40 wt.% *bm*MUF-16 loading with different magnifications.

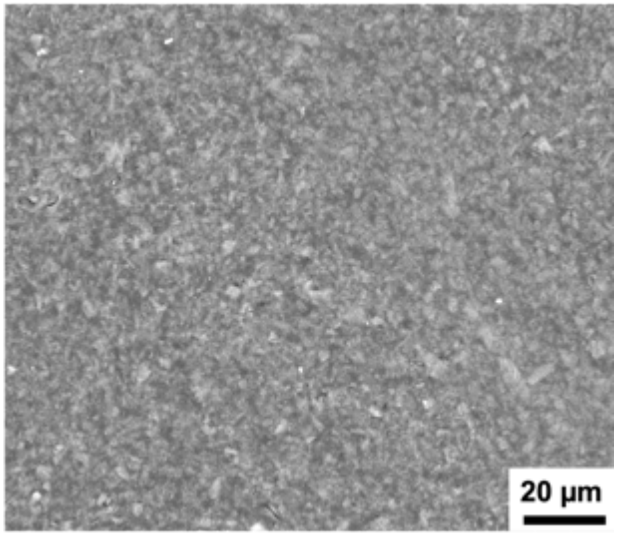


**Figure C. 5** Surface morphologies of 6FDA-DAM loaded with 40 wt.% *ns*MUF-16 loading.

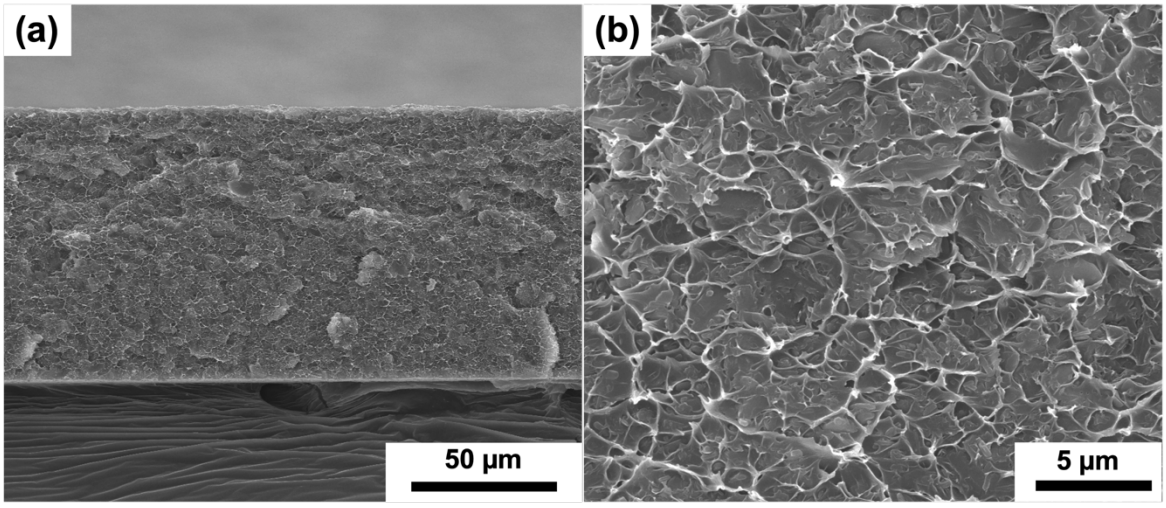


**Figure C. 6** Cross-sectional morphologies of 6FDA-DAM loaded with 40 wt.% *bm*MUF-16 loading with different magnifications.

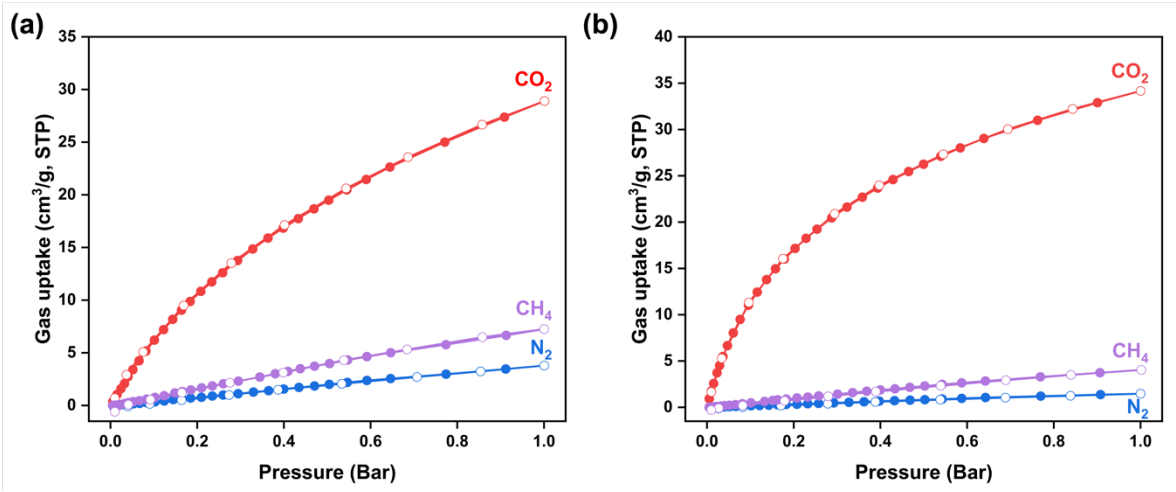


**Figure C. 7** $CO_2$, $CH_4$ and $N_2$ adsorption (filled circles) and desorption (open circles) isotherms of (a) 6FDA-DAM and (b) 6FDA-DAM with 40 wt.% *ns*MUF-16 loading.

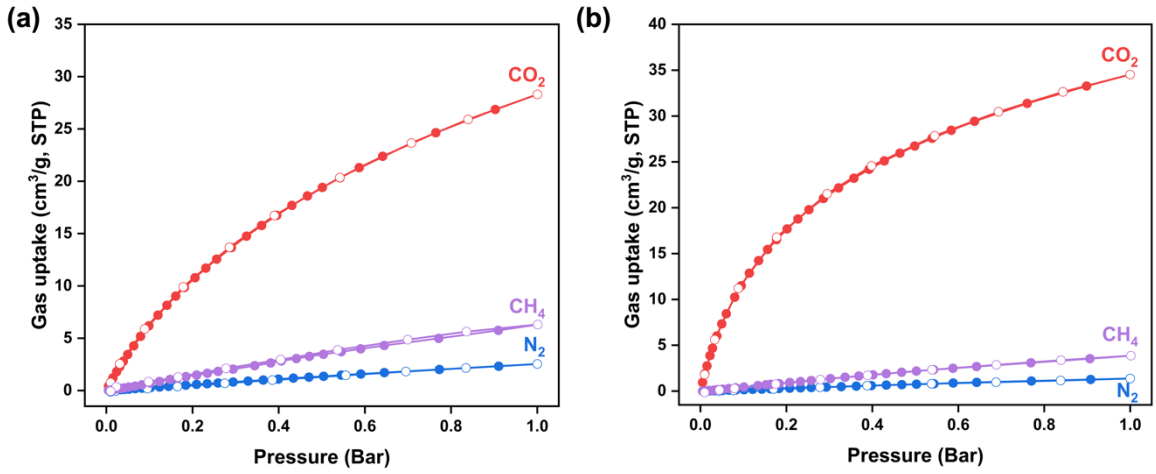


**Figure C. 8** $CO_2$, $CH_4$ and $N_2$ adsorption (filled circles) and desorption (open circles) isotherms of (a) 6FDA-Durene and (b) 6FDA-Durene with 40 wt.% *ns*MUF-16 loading.

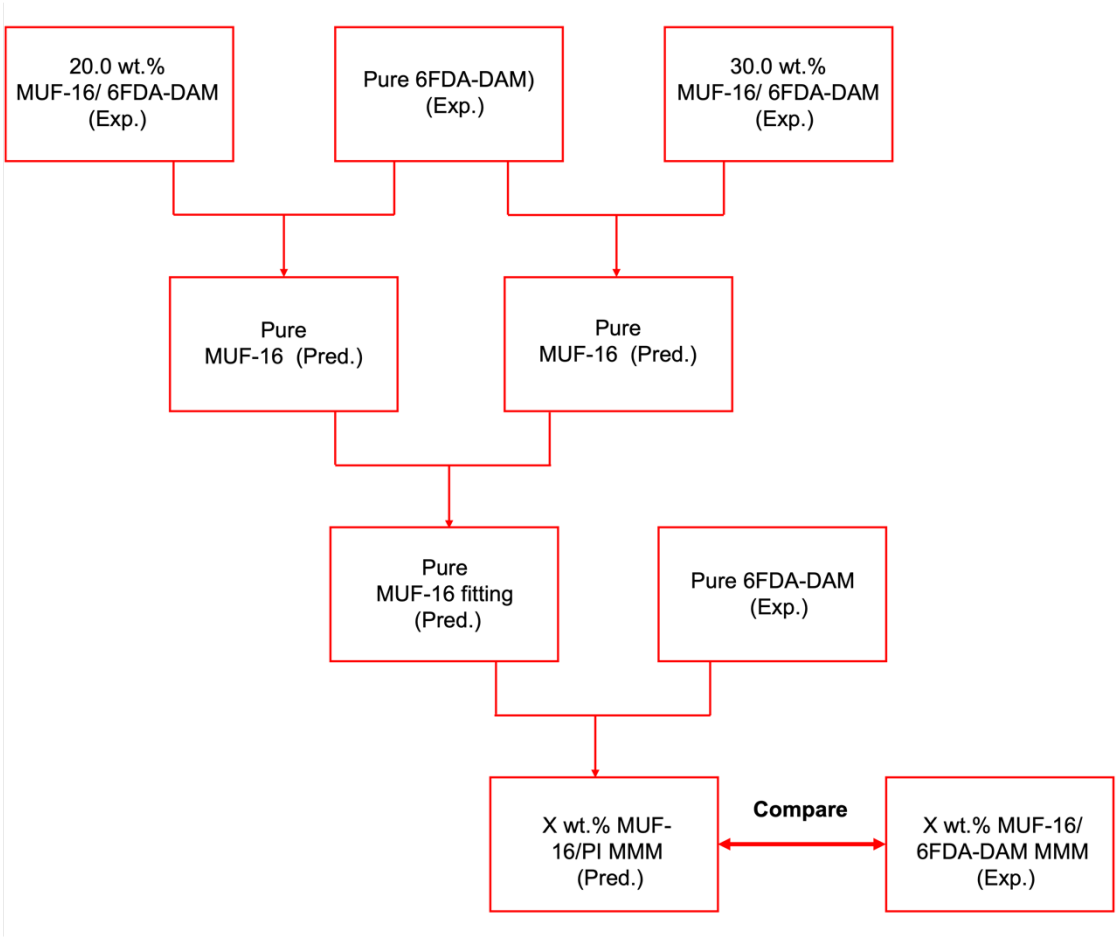


**Figure C. 9** Theoretical prediction of the permeation performance of mixed matrix membranes based on the measured performance of pure 6FDA-DAM (or 6FDA-Durene) membrane and *ns*MUF-16/6FDA-DAM mixed matrix membranes (Exp.: measured pure-gas permeability and selectivity; Pred: Maxwell predicted pure-gas permeability and selectivity. Polymer: 6FDA-DAM, 6FDA-Durene; X%: MOF loading ranging from 0 to 40 wt.%). Note: the pure MUF-16 membrane permeability was predicted by fitting the permeability values of membranes with different MUF-16 loading.

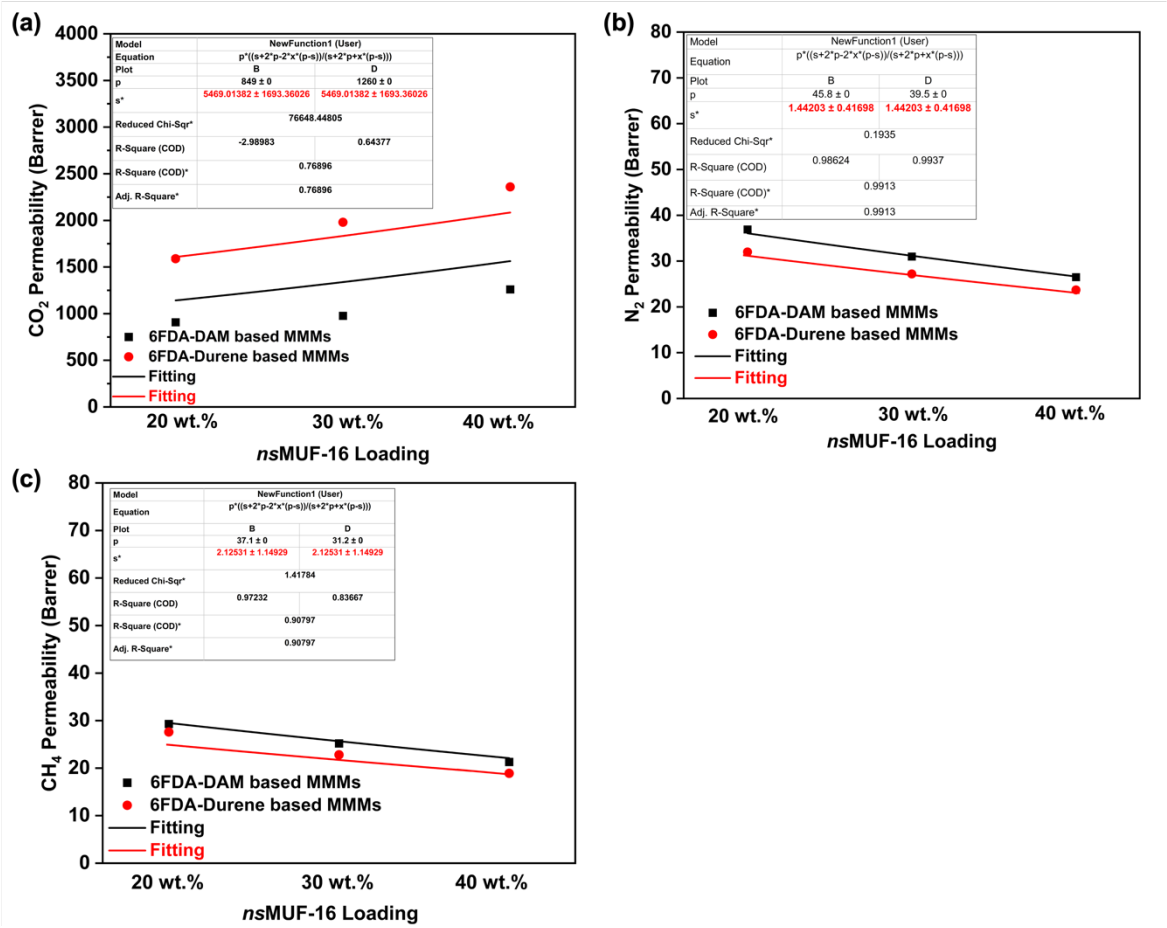


**Figure C. 10** (a) $CO_2$ (b) $N_2$ and (c) $CH_4$ permeabilities of pure MUF-16 membrane obtained by fitting the predicted gas permeability of membranes with 20 wt.%, 30 wt.% and 40 wt. % *ns*MUF-16 loading using maxwell model.

**Table C. 1** Comparison of predicted gas separation performance of other pure MOFs using Maxwell Model.

| MOFs | $CO_2$ Permeability (Barrer) | $CO_2/N_2$ | $CO_2/CH_4$ | Ref. |
|---|---|---|---|---|
| ZIF-8 | 1192 | 2.60 | 2.80 | [306] |
| ZIF-90 | 8000 | -- | 250 | [278] |
| UiO-66-$NH_2$ | 3515 | 20.3 | 21.8 | [202] |
| (001)-AlFFIVE-1-Ni | 2035 | -- | 354 | [154] |
| MIL-53(Al)-$NH_2$ | 90.0 | -- | 25.7 | [307] |
| ZMOF | 10000 | -- | 180 | [279] |
| MUF-16 | 5649 | 3922 | 2556 | This work |

# Appendix D for Chapter 5

## 1. Experimental section

### Materials

Cobalt(II) acetate tetrahydrate (99.99 %) and isophthalic acid ($H_2$aip, 99 %) were purchased from Sigma-Aldrich. Methanol (MeOH, 99.9 %) was purchased from Fisher Chemicals. The polyimide 6FDA-DAM (Mw ~ 326000, PDI ~ 2.68) was supplied by Akron Polymer Systems. DCM was purchased from Sigma-Aldrich. Deionized (DI) water was produced from a home-made reverse osmosis water treatment, which was used in the whole experiment. All the reagents were analytical grade and were used without further purification.

### Characterization

X-ray diffraction (XRD) patterns were recorded on a Bruker D8 Venture diffractometer with $Cu_\alpha$ radiation (wavelength = 1.54018 Å), with a diamond microfocus X-ray source and a Photon III 28 detector. Scanning Electron Microscope (SEM) images were taken on a FEI Quanta 200 Environmental with EDAX module. Thermogravimetric analysis (TGA) data were collected using the TA Q50 instrument at a heating rate of 10 °C/min from 50 to 600 °C with a $N_2$ flow rate of 40 mL/min. ATR-FTIR measurements used a Nicolet iS5 IR with iD7 ATR Accessory. Gas adsorption isotherms were measured on a Quantachrome Autosorb iQ2 instrument using ultra-high purity gases.

### Synthesis of MUF-15 and its analogues

Four different isophthalic acid ligands with fluoro (-F), bromo (-Br), nitro (-$NO_2$) and methyl ($CH_3$) functional groups can react with cobalt(II) acetate in methanol under solvothermal conditions. The analogues of MUF-15 were synthesized according to Figure 5.4.

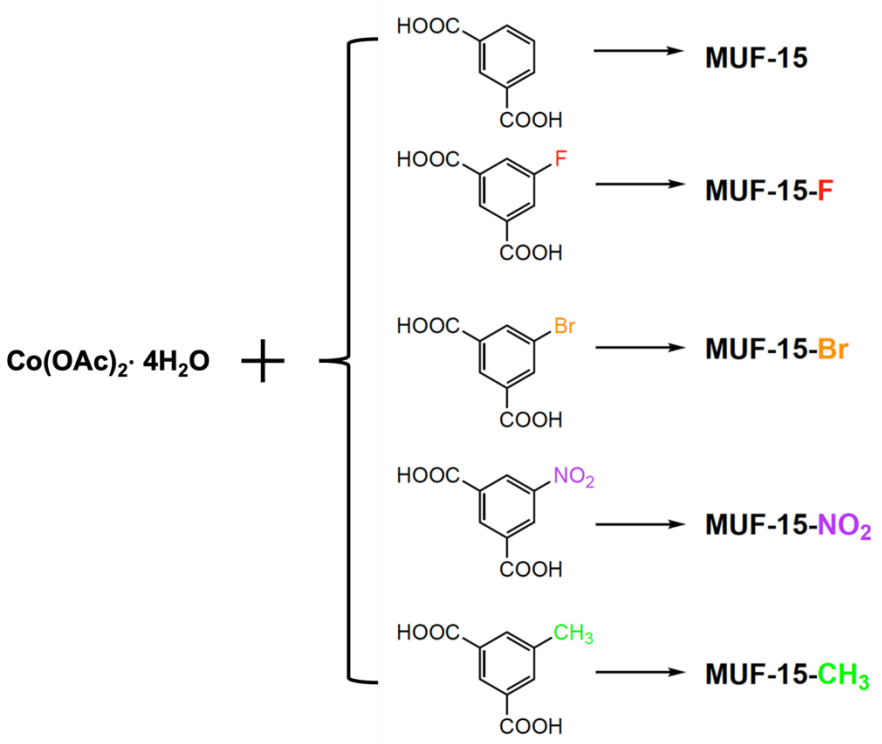


**Figure D. 1** Scheme of the synthetic routes to MUF-15 and its analogues.

A mixture of $Co(OAC)_2 \cdot 4H_2O$ (125 mg, 0.50 mmol), ligands, MeOH (6 mL), and $H_2O$ (0.5 mL) required for MUF-15 and its analogues synthesis were sonicated for 10 min and sealed into a 25 mL Teflon-lined autoclave, then heated to the target temperature (Table D. 1). After cooling to room temperature, the crystals were collected and washed with MeOH three times and then stored in MeOH for further use.

**Table D. 1** Synthesis of MUF-15 and its analogues.

| MOF | Salt | Ligand | Ligand/salt (mol/mol) | Reaction temperature (°C) | Reaction time (h) |
|---|---|---|---|---|---|
| MUF-15 | $Co(OAc)_2 \cdot 4H_2O$ | $H_2ipa$ | 2 | 120 | 48 |
| MUF-15-F | $Co(OAc)_2 \cdot 4H_2O$ | $H_2ipa$-F | 1.75 | 120 | 24 |
| MUF-15-Br | $Co(OAc)_2 \cdot 4H_2O$ | $H_2ipa$-Br | 2 | 120 | 48 |
| MUF-15-$NO_2$ | $Co(OAc)_2 \cdot 4H_2O$ | $H_2ipa$-$NO_2$ | 1.75 | 120 | 48 |
| MUF-15-$CH_3$ | $Co(OAc)_2 \cdot 4H_2O$ | $H_2ipa$-$CH_3$ | 1.75 | 140 | 36 |

**Membrane fabrication**

The MUF-15 crystals stored in MeOH was first centrifuged to remove the solvent and then washed with DCM three times. Subsequently, a certain amount of MUF-15 was added into DCM (3 mL) and stirred overnight. Then 6FDA-DAM was added into the above mixed solution and stirred for another 12 hours. The casting solution was then poured into a glass Petri dish on a level surface in a desiccator (30 cm in diameter) with a $CHCl_3$ atmosphere at room temperature overnight. Finally, the resulting MMM was peeled off from the dish and treated in a vacuum oven at 130 °C for 2 hours to remove the residual solvent. And the prepared membrane was immediately used to the gas permeability test.

**Solubility and diffusion calculation**

The $CO_2$ and $CH_4$ adsorption isotherms were fitted by a dual-site Langmuir model as listed in equation below:

$$q = \frac{q_{sat,1} \times b_1 \times p}{1 + b_1 \times p} + \frac{q_{sat,2} \times b_2 \times p}{1 + b_2 \times p}$$

where $q$ represents the gas concentration adsorbed, $p$ represents the testing pressure, $q_{sat}$ represents the saturation loadings for different sites, and $b_1$ and $b_2$ represent the Langmuir parameters for different sites, respectively.

The gas solubility ($S$) in the membrane was calculated using equation below:

$$S_i = \frac{q_i}{p_i}$$

The gas transportation through the membranes follows a solution-diffusion mechanism, therefore the gas diffusivity in the membranes is given by:

$$D_i = \frac{P_i}{S_i}$$

**Table D. 2** Fitting parameters for the adsorption isotherms.

| Gas | Sample | Fitting Parameters | | | | |
|---|---|---|---|---|---|---|
| | | $q_{sat,1}$ ($cm^3/g$) | $b_1$ ($bar^{-1}$) | $q_{sat,2}$ ($cm^3/g$) | $b_2$ ($bar^{-1}$) | $R^2$ |
| $CO_2$ | 6FDA-DAM | 1840 | 0.0051 | 28.1 | 2.20 | 0.9999 |
| | 30 wt.% MUF-15 MMM | 57.8 | 1.31 | -- | -- | 0.9997 |
| | 30 wt.% MUF-15-F MMM | 66.6 | 0.70 | 9.13 | 5.90 | 0.9999 |
| $CH_4$ | 6FDA-DAM | 78.2 | 0.0392 | 121.6 | 0.039 | 0.9990 |
| | 30 wt.% MUF-15 MMM | 35.7 | 0.21 | 12.2 | 0.21 | 0.9999 |
| | 30 wt.% MUF-15-F MMM | 77.4 | 0.13 | -- | -- | 0.9987 |

MASSEY UNIVERSITY
TE KUNENGA KI PŪREHUROA
UNIVERSITY OF NEW ZEALAND

GRADUATE RESEARCH SCHOOL

# STATEMENT OF CONTRIBUTION
# DOCTORATE WITH PUBLICATIONS/MANUSCRIPTS

We, the student and the student's main supervisor, certify that all co-authors have consented to their work being included in the thesis and they have accepted the student's contribution as indicated below in the Statement of Originality.

| | |
|---|---|
| Student name: | Yiming Zhang |
| Name and title of main supervisor: | Prof Shane G. Telfer |
| In which chapter is the manuscript/published work? | Chapter 2 |
| What percentage of the manuscript/published work was contributed by the student? | 100 % |

Describe the contribution that the student has made to the manuscript/published work:

Yiming Zhang performed the experiments, analyzed the data, and has written a draft of the paper.

Please select one of the following three options:

- ○ The manuscript/published work is published or in press
  Please provide the full reference of the research output:
- ○ The manuscript is currently under review for publication
  Please provide the name of the journal:
- ◉ It is intended that the manuscript will be published, but it has not yet been submitted to a journal

| | | | |
|---|---|---|---|
| Student's signature: | Yiming Zhang Digitally signed by Yiming Zhang Date: 2024.04.27 04:48:08 +08'00' | Main supervisor's signature: | SGTelfer Digitally signed by Shane Telfer Date: 2024.04.29 09:20:08 +12'00' |

*This form should appear at the end of each thesis chapter/section/appendix submitted as a manuscript/ publication or collected as an appendix at the end of the thesis.*

MASSEY UNIVERSITY
TE KUNENGA KI PŪREHUROA
UNIVERSITY OF NEW ZEALAND

GRADUATE RESEARCH SCHOOL

# STATEMENT OF CONTRIBUTION
# DOCTORATE WITH PUBLICATIONS/MANUSCRIPTS

We, the student and the student's main supervisor, certify that all co-authors have consented to their work being included in the thesis and they have accepted the student's contribution as indicated below in the Statement of Originality.

| | |
|---|---|
| Student name: | Yiming Zhang |
| Name and title of main supervisor: | Prof Shane G. Telfer |
| In which chapter is the manuscript/published work? | Chapter 3 |
| What percentage of the manuscript/published work was contributed by the student? | 100 % |

Describe the contribution that the student has made to the manuscript/published work:

Yiming Zhang performed the experiments, analyzed the data, and has written a draft of the paper.

Please select one of the following three options:

- ○ **The manuscript/published work is published or in press**
  Please provide the full reference of the research output:
- ○ **The manuscript is currently under review for publication**
  Please provide the name of the journal:
- ◉ **It is intended that the manuscript will be published, but it has not yet been submitted to a journal**

| | | | |
|---|---|---|---|
| Student's signature: | Yiming Zhang Digitally signed by Yiming Zhang Date: 2024.04.27 04:48:08 +08'00' | Main supervisor's signature: | SGTelfer Digitally signed by Shane Telfer Date: 2024.04.29 09:20:59 +12'00' |

*This form should appear at the end of each thesis chapter/section/appendix submitted as a manuscript/ publication or collected as an appendix at the end of the thesis.*

MASSEY UNIVERSITY
TE KUNENGA KI PŪREHUROA
UNIVERSITY OF NEW ZEALAND

GRADUATE RESEARCH SCHOOL

# STATEMENT OF CONTRIBUTION
# DOCTORATE WITH PUBLICATIONS/MANUSCRIPTS

We, the student and the student's main supervisor, certify that all co-authors have consented to their work being included in the thesis and they have accepted the student's contribution as indicated below in the Statement of Originality.

| | |
|---|---|
| Student name: | Yiming Zhang |
| Name and title of main supervisor: | Prof Shane G. Telfer |
| In which chapter is the manuscript/published work? | Chapter 4 |
| What percentage of the manuscript/published work was contributed by the student? | 100 % |

Describe the contribution that the student has made to the manuscript/published work:

Yiming Zhang performed the experiments, analyzed the data, and has written a draft of the paper.
Elnaz Jangodaz assisted with the Maxwell fitting and analysis presented in Chapter 4.

Please select one of the following three options:

- ○ **The manuscript/published work is published or in press**
  Please provide the full reference of the research output:
- ○ **The manuscript is currently under review for publication**
  Please provide the name of the journal:
- ◉ **It is intended that the manuscript will be published, but it has not yet been submitted to a journal**

| | | | |
|---|---|---|---|
| Student's signature: | Yiming Zhang Digitally signed by Yiming Zhang Date: 2024.04.27 04:48:08 +08'00' | Main supervisor's signature: | SGTelfer Digitally signed by Shane Telfer Date: 2024.04.29 09:21:54 +12'00' |

*This form should appear at the end of each thesis chapter/section/appendix submitted as a manuscript/ publication or collected as an appendix at the end of the thesis.*

MASSEY UNIVERSITY
TE KUNENGA KI PŪREHUROA
UNIVERSITY OF NEW ZEALAND

GRADUATE RESEARCH SCHOOL

# STATEMENT OF CONTRIBUTION
# DOCTORATE WITH PUBLICATIONS/MANUSCRIPTS

We, the student and the student's main supervisor, certify that all co-authors have consented to their work being included in the thesis and they have accepted the student's contribution as indicated below in the Statement of Originality.

| | |
|---|---|
| Student name: | Yiming Zhang |
| Name and title of main supervisor: | Prof Shane G. Telfer |
| In which chapter is the manuscript/published work? | Chapter 5 |
| What percentage of the manuscript/published work was contributed by the student? | 100 % |

Describe the contribution that the student has made to the manuscript/published work:

Yiming Zhang performed the experiments, analyzed the data, and wrote a draft of the paper.

Please select one of the following three options:

- ○ The manuscript/published work is published or in press
  Please provide the full reference of the research output:
- ◉ The manuscript is currently under review for publication
  Please provide the name of the journal:
  Chemical Communications
- ○ It is intended that the manuscript will be published, but it has not yet been submitted to a journal

| | | | |
|---|---|---|---|
| Student's signature: | Yiming Zhang Digitally signed by Yiming Zhang Date: 2024.04.27 04:48:08 +08'00' | Main supervisor's signature: | SGTelfer Digitally signed by Shane Telfer Date: 2024.04.29 09:22:53 +12'00' |

*This form should appear at the end of each thesis chapter/section/appendix submitted as a manuscript/ publication or collected as an appendix at the end of the thesis.*